

IntechOpen

The Nonlinear Schrödinger Equation

Edited by Nalan Antar and İlkey Bakırtaş



The Nonlinear Schrödinger Equation

Edited by Nalan Antar and İlkay Bakırtaş

Published in London, United Kingdom



IntechOpen





Supporting open minds since 2005



The Nonlinear Schrödinger Equation

<http://dx.doi.org/10.5772/intechopen.95650>

Edited by Nalan Antar and İlkey Bakırtaş

Contributors

Francis T. S. Yu, Lothar Moeller, Saïdou Abdoukary, Alidou Mohamadou, Gérard Gouesbet, Mir Asma, Khalil S. Al-Ghafri, Mati Youssoufa, Ousmanou Dafounansou, Camus Gaston Latchio Tiofack, Nalan Antar, Mahmut Bağcı, Theodoros Horikis, İlkey Bakırtaş

© The Editor(s) and the Author(s) 2022

The rights of the editor(s) and the author(s) have been asserted in accordance with the Copyright, Designs and Patents Act 1988. All rights to the book as a whole are reserved by INTECHOPEN LIMITED. The book as a whole (compilation) cannot be reproduced, distributed or used for commercial or non-commercial purposes without INTECHOPEN LIMITED's written permission. Enquiries concerning the use of the book should be directed to INTECHOPEN LIMITED rights and permissions department (permissions@intechopen.com).

Violations are liable to prosecution under the governing Copyright Law.



Individual chapters of this publication are distributed under the terms of the Creative Commons Attribution 3.0 Unported License which permits commercial use, distribution and reproduction of the individual chapters, provided the original author(s) and source publication are appropriately acknowledged. If so indicated, certain images may not be included under the Creative Commons license. In such cases users will need to obtain permission from the license holder to reproduce the material. More details and guidelines concerning content reuse and adaptation can be found at <http://www.intechopen.com/copyright-policy.html>.

Notice

Statements and opinions expressed in the chapters are these of the individual contributors and not necessarily those of the editors or publisher. No responsibility is accepted for the accuracy of information contained in the published chapters. The publisher assumes no responsibility for any damage or injury to persons or property arising out of the use of any materials, instructions, methods or ideas contained in the book.

First published in London, United Kingdom, 2022 by IntechOpen

IntechOpen is the global imprint of INTECHOPEN LIMITED, registered in England and Wales, registration number: 11086078, 5 Princes Gate Court, London, SW7 2QJ, United Kingdom
Printed in Croatia

British Library Cataloguing-in-Publication Data

A catalogue record for this book is available from the British Library

Additional hard and PDF copies can be obtained from orders@intechopen.com

The Nonlinear Schrödinger Equation

Edited by Nalan Antar and İlkey Bakırtaş

p. cm.

Print ISBN 978-1-83969-978-8

Online ISBN 978-1-83969-979-5

eBook (PDF) ISBN 978-1-83969-980-1

We are IntechOpen, the world's leading publisher of Open Access books Built by scientists, for scientists

5,900+

Open access books available

144,000+

International authors and editors

180M+

Downloads

156

Countries delivered to

Our authors are among the
Top 1%

most cited scientists

12.2%

Contributors from top 500 universities



WEB OF SCIENCE™

Selection of our books indexed in the Book Citation Index (BKCI)
in Web of Science Core Collection™

Interested in publishing with us?
Contact book.department@intechopen.com

Numbers displayed above are based on latest data collected.
For more information visit www.intechopen.com



Meet the editors



Dr. Nalan Antar is a Professor of Applied Mathematics, Department of Mathematical Engineering, Istanbul Technical University, Turkey. She received her Ph.D. in Mechanics from the same university in 1999. She completed her post-doctoral studies at the Department of Mathematics and Statistics, University of Alberta, Canada, and later participated in academic research projects at the University of Colorado at Boulder, USA. She has published thirty-two research papers in peer-reviewed journals, thirteen conference proceedings, and one book chapter in the fields of nonlinear wave propagation in arteries, optical solitons in nonlinear optics, and water waves problems, in particular gravity currents. She has also edited one book, *Nonlinear Optics - From Solitons to Similaritons*. She has supervised many graduate students in applied mathematics. Dr. Antar is a member of the Scientific Committee of the Turkish National Committee of Theoretical and Applied Mechanics (TUMTMK).



Dr. İlkey Bakırtaş is a Professor of Applied Mathematics, Department of Mathematics, Istanbul Technical University (ITU), Turkey. She received her Ph.D. in Mechanics from the same university in 2003. She completed her postdoctoral studies at the University of Colorado at Boulder, USA. She has published eighteen research papers in peer-reviewed journals, four book chapters, and twenty-one conference proceedings in the fields of perturbation methods, nonlinear wave propagation in arteries, optical solitons and wave collapse in optics, and water waves problems. She is the editor of the books *Perturbation Methods with Applications in Science and Engineering* and *Nonlinear Optics - From Solitons to Similaritons*. Dr. Bakırtaş is a member of the Scientific Committee of the Turkish National Committee of Theoretical and Applied Mechanics (TUMTMK). She was awarded the 2004 Dr. Serhat Ozyar Young Scientist of the Year Award and the 2003 Best Ph.D. Dissertation Award from TUMTMK.

Contents

Preface	XIII
Chapter 1 Perspective Chapter: Lattice Solitons in a Nonlocal Nonlinear Medium with Self-Focusing and Self-Defocusing Quintic Nonlinearity <i>by Mahmut Bağcı, Theodoros P. Horikis, İlkyay Bakırtaş and Nalan Antar</i>	1
Chapter 2 Soliton Like-Breather Induced by Modulational Instability in a Generalized Nonlinear Schrödinger Equation <i>by Saïdou Abdoulkary and Alidou Mohamadou</i>	19
Chapter 3 A Comparison of the Undetermined Coefficient Method and the Adomian Decomposition Method for the Solutions of the Sasa-Satsuma Equation <i>by Mir Asma</i>	31
Chapter 4 Resonant Optical Solitons in $(3 + 1)$ -Dimensions Dominated by Kerr Law and Parabolic Law Nonlinearities <i>by Khalil S. Al-Ghafri</i>	53
Chapter 5 Traveling Wave Solutions and Chaotic Motions for a Perturbed Nonlinear Schrödinger Equation with Power-Law Nonlinearity and Higher-Order Dispersions <i>by Mati Youssoufa, Ousmanou Dafounansou, Camus Gaston Latchio Tiofack and Alidou Mohamadou</i>	69
Chapter 6 Non-Manakovian Propagation in Optical Fiber <i>by Lothar Moeller</i>	87
Chapter 7 Nonlinear Generalized Schrödinger's Equations by Lifting Hamilton-Jacobi's Formulation of Classical Mechanics <i>by Gérard Gouesbet</i>	115
Chapter 8 From Schrödinger Equation to Quantum Conspiracy <i>by Francis T.S. Yu</i>	131

Preface

The nonlinear Schrödinger equation is a well-known equation that arises for a wide range of scientific purposes, including optical fiber communication systems, quantum mechanics, thermodynamics, ocean acoustic performance, biomedical dynamics, and quantum physics.

In this book, we present exact and numerical solutions to the nonlinear Schrödinger equation and its applications from various perspectives.

This book is a collection of selectively chosen chapters written by some of the world's leading researchers in quantum mechanics and nonlinear optics, particularly concerning the nonlinear Schrödinger equation.

Chapter 1 investigates the existence and stability properties of fundamental lattice solitons in a nonlocal nonlinear medium with self-focusing and self-defocusing quintic nonlinearity.

In Chapter 2, linear stability analysis is used to study the modulation instability gain for a generalized nonlinear Schrödinger equation with rational nonlinear terms.

Chapter 3 presents different types of soliton solutions, such as bright, dark, singular, and *W*-shaped solitons, for the extended non-trivial version of the nonlinear Schrödinger equation. The Adomian decomposition method is used to compare the soliton solutions obtained using the indeterminate coefficient method.

In Chapter 4, the Projective Riccati equation technique is used to find various types of exact resonant optical soliton solutions, such as bright, dark, singular, king, dark-singular, and combined singular solitons, for the $(3 + 1)$ dimensional resonant nonlinear Schrödinger equation with Kerr and parabolic nonlinearities.

Chapter 5 investigates the existence and stability properties of traveling wave solutions for the perturbed nonlinear Schrödinger equation with power-law nonlinearity and higher-order dispersions in a nano-optical fiber.

Chapter 6 discusses the non-Manakovian transmission phenomena for nonlinear depolarization of light governed by coupled nonlinear Schrödinger equation in optical fiber.

Chapter 7 presents a set of generalized Schrödinger's equations using the Hamilton–Jacobi equation and lifting principle. The classical Schrödinger's equation is demonstrated to be the simplest of this set.

Finally, Chapter 8 investigates the paradox of Schrödinger's cat and double-slit postulation. The author gives a different perspective on questions about the Schrödinger equation and the quantum conspiracy that physicists have debated for many years.

This book is a useful resource for scientists, researchers, and postgraduate students from various backgrounds.

Dr. Nalan Antar and Dr. İlky Bakırtaş
Department of Mathematics Engineering,
Istanbul Technical University,
İstanbul, Türkiye

Perspective Chapter: Lattice Solitons in a Nonlocal Nonlinear Medium with Self-Focusing and Self-Defocusing Quintic Nonlinearity

*Mahmut Bağcı, Theodoros P. Horikis, İlkey Bakırtaş
and Nalan Antar*

Abstract

The fundamental lattice solitons are explored in a nonlocal nonlinear medium with self-focusing and self-defocusing quintic nonlinearity. The band-gap boundaries, soliton profiles, and stability domains of fundamental solitons are investigated comprehensively by the linear stability spectra and nonlinear evolution of the solitons. It is demonstrated that fundamental lattice solitons can stay stable for a wide range of parameters with the weak self-focusing and self-defocusing quintic nonlinearity, while strong self-focusing and self-defocusing quintic nonlinearities are shortened the propagation distance of evolved solitons. Furthermore, it is observed that when the instability emerges from strong quintic nonlinearity, increasing anisotropy of the medium and modification of lattice depth can be considered as a collapse arrest mechanism.

Keywords: lattice solitons, nonlinear response, nonlocal nonlinear medium, quintic nonlinearity, focusing and defocusing media

1. Introduction

Optical solitons arise as localized optical fields that preserve their shapes during propagation when the medium's diffraction and self-phase modulation are balanced [1]. Since they were first observed experimentally in 2003 [2], spatial solitons [3] in nonlinear optical systems with additional optical lattices have received a significant interest. Currently, fundamental solitons and vortices on a variety of lattices including real and complex structures in the media with cubic (Kerr) [4, 5], saturable [6] and with competing nonlinearities [7] have been studied. Solitons may also exist in aperiodic or quasicrystal lattices [8–12] and in lattices with defects [13] and dislocations [14, 15].

In the studies above, the governing equations are nonlinear cubic Schrödinger (NLS) equation and their variants, e.g., NLS with additional terms and/or with external lattices. On the other hand, numerous optical materials, such as potassium

niobate (KNbO₃) [16] or lithium niobate (LiNbO₃) [17], acquire quadratic nonlinear responses as well [18–24]. NLS equation with coupling to a mean term (NLSM) system governs the pulse dynamics in quadratically polarized media. The general NLSM system is given by [18, 25, 26].

$$iu_z + \Delta u + |u|^2 u - \rho u \phi = 0, \quad \phi_{xx} + \nu \phi_{yy} = \left(|u|^2 \right)_{xx} \quad (1)$$

Here $u(x, y)$ is the normalized amplitude of the envelope of the static electric field propagating in the z direction. $\Delta u \equiv u_{xx} + u_{yy}$ corresponds to diffraction, and the nonlinear cubic term comes from the nonlinear Kerr effect. The parameter ρ is a coupling constant that emerges from the combined optical rectification and electro-optic effects formed by the $\phi(x, y)$ field, and ν is the coefficient that originates from the anisotropy of the material [26]. These equations arise due to the interaction between the fundamental and dc fields when second-harmonic-generation is not phase-matched. In such a situation, the second harmonic component can be solved explicitly and generates an additional self-phase modulation contribution due to cascaded nonlinearity. Consequently, the NLSM system is obtained as a result of the nonlocal nonlinear coupling between the first field (with the cascaded effect from the second harmonic) and a static field that arises from the zeroth harmonic (mean term). We would like to note that solitons of a media with solely quadratic nonlinear response can also be governed by the NLSM type Equations [25, 26].

NLSM equations were derived by Benney and Roskes [27] for a finite water depth, neglecting the surface tension. In 1974, Davey and Stewartson [28] investigated the evolution of a three-dimensional wave packet for a finite water depth and obtained an equivalent form of these equations. The integrability of the NLSM equations that were derived for the shallow water limit was studied by Ablowitz and Haberman [29]. Djordevic and Reddekopp [30] improved the study of Benney and Roskes by including the surface tension in 1977. Later, Ablowitz et al. [18, 25, 26] derived from first principles that NLSM type equations model the evolution of the electromagnetic field in a quadratically polarized media.

One major drawback of the dynamics of solitons under the NLS equation in 2D is that they exhibit collapse. As a matter of fact, in [31], it was revealed that the collapse dynamics of NLSM solitons are similar to the collapse of NLS solitons. Possible collapse arrest mechanisms have been studied extensively in nonlinear optics, e.g., nonlinear saturation [32, 33]. Merle and Raphael [34] investigated the collapse of the NLS solitons and its variants in depth. Furthermore, Gaeta and coworkers [35] carried out detailed experiments in order to expose the nature of the singularity formation in cubic optical media and demonstrated experimentally that collapse occurs with a self-similar profile.

Recently, wave collapse in the NLSM system was studied in [36] and it is shown that in both water waves and optics, collapse occurs with a quasi self-similar profile. By evolving the NLSM solutions that are computed by the Spectral Renormalization method which is essentially a fixed point iteration scheme. In this study, it is also revealed that the NLSM solitons have astigmatic profiles and their collapse can be arrested by adding nonlinear saturation into the system. Wave self-rectification and beam ellipticity as a collapse arrest mechanism for NLSM solitons was put forward by in [16]. In the aforementioned work, for simplicity, the authors considered Gaussian profiles with various input powers and astigmatism and then evolve these profiles for long distances. More recently, wave collapse in the NLSM system was arrested by adding a periodic external lattice in [23] and it has been shown that deeper lattices may serve as a collapse arrest mechanism.

In this chapter, the NLSM model (1) is extended by adding a quintic term and an external lattice. Using this new model, the dynamics of the fundamental lattice solitons in a nonlocal nonlinear medium with quintic nonlinearity are explored. The study is concentrated on effects formed by the imposed lattice depth and the strength of quintic nonlinearity. The stability of the obtained lattice solitons is examined by the nonlinear evolution and linear spectra. In the light of the conducted numerical analysis, it is confirmed that fundamental lattice solitons can exist in nonlocal nonlinear media with both self-focusing and self-defocusing quintic nonlinearities and stability of these solitons is achieved for a broad range of system parameters. Since many optical materials such as chalcogenide glasses are engineered to reveal fifth and seventh-order effects in addition to cubic nonlinear effects [37], and high-order nonlinearities can arise even with pure Kerr materials [38–40], it is crucial to consider the soliton dynamics consists of higher-order nonlinearities.

The outline of the chapter is as follows: In Section 2, we present the model equations and compute the periodic lattice solitons numerically. In Section 3, we explore the linear spectra and nonlinear evolution of the solitons. Results are outlined in Section 4.

2. The model and its soliton solutions

It is known that, the steady-state solutions of the NLSM system (1) collapse [36], and the collapse of solitons can be arrested by adding external lattices [23]. The NLSM model (1) is extended as follows to describe the nonlocal cubic-quintic nonlinear medium with an external lattice,

$$iu_z + \frac{1}{2} \Delta u + \beta |u|^2 u - \rho u \phi + \gamma |u|^4 u - V(x, y)u = 0, \quad \phi_{xx} + \nu \phi_{yy} = \left(|u|^2 \right)_{xx} \quad (2)$$

where γ denotes the strength of quintic nonlinearity and $V(x, y)$ shows the optical lattice. We consider lattices that are created by the sum of N phase-modulated plane waves [8].

$$V(x, y) = \frac{V_0}{N^2} \left| \sum_{n=0}^{N-1} e^{i(k_x^n x + k_y^n y)} \right|^2 \quad (3)$$

where $V_0 > 0$ is the depth of lattice and the wave vector $(k_x^n, k_y^n) = [K \cos(2\pi n/N), K \sin(2\pi n/N)]$. The lattices for $N = 2, 3, 4, 6$ correspond to crystal (periodic) structures, while $N = 5, 7$ correspond to aperiodic (Penrose) quasi-crystals. Contour plot and diagonal cross-section of the lattice $V(x, y)$ is displayed in **Figure 1** for $V_0 = 12.5, N = 4$ and $k_x = k_y = 2\pi$. It can be seen that the lattice is periodic, and the center $((x, y) = (0, 0))$ of lattice is a local maximum.

2.1 Numerical solution for the fundamental solitons

The squared operator (SOM) method (that was proposed by Yang and Lakoba [41]) is utilized to calculate the soliton solutions of the $(2 + 1)$ D NLSM model (2). The SOM method is based on integrating squared-operators of evolution equations. Derivation of these operators and the scheme of the method are explained below.

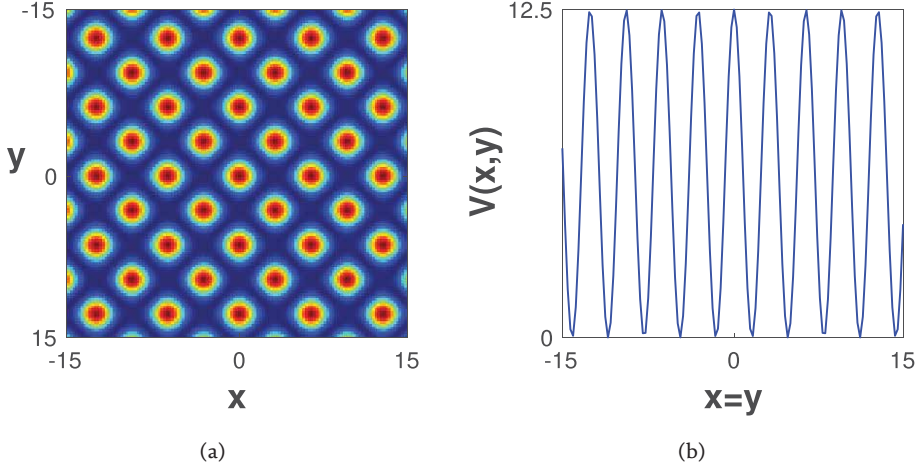


Figure 1. The top view and diagonal cross-section of the lattice $V(x,y)$ when $V_o = 12.5, N = 4$ and $(x,y) \in [-15, 15]$.

A real-valued nonlinear evolution equation can be presented in the following form

$$\mathbf{L}_0 \mathbf{u}(\mathbf{x}) = 0 \quad (4)$$

where \mathbf{x} is the multidimensional spatial variable, $\mathbf{u}(\mathbf{x})$ is a real valued function and the operator \mathbf{L}_0 includes the solitary wave's propagation constant. Let the operator \mathbf{L}_1 denotes linearization of Eq. (4) around the solution \mathbf{u} , and given by

$$\mathbf{L}_1(\mathbf{u} + \tilde{\mathbf{u}}) = \mathbf{L}_1 \tilde{\mathbf{u}} + O(\tilde{\mathbf{u}}^2) \quad (5)$$

where $\tilde{\mathbf{u}} \ll 1$. In order to get a solitary wave solution, the following time-dependent squared operator evolution equation will be integrated

$$\mathbf{u}_t = -\mathbf{M}^{-1} \mathbf{L}_1^\dagger \mathbf{M}^{-1} \mathbf{L}_0 \mathbf{u} \quad (6)$$

here \mathbf{L}_1^\dagger denotes the Hermitian of the operator and \mathbf{M} is a real valued positive definite Hermitian operator that is introduced to accelerate the convergence. Using the forward Euler method, the solitary wave solution \mathbf{u} will be calculated by the following iteration.

$$\mathbf{u}_{n+1} = \mathbf{u}_n - [\mathbf{M}^{-1} \mathbf{L}_1^\dagger \mathbf{M}^{-1} \mathbf{L}_0 \mathbf{u}]_{\mathbf{u}=\mathbf{u}_n} \Delta t. \quad (7)$$

It was shown that the SOM method converges to a solitary wave solution for a broad-range of nonlinear evolution equations when a convenient initial condition is given and time step Δt is small enough [41, 42].

To calculate a solitary wave solution of the model Eq. (2) by the SOM, the following scheme is constructed. Inserting the solution suggestion $u = U(x,y) \exp(i\mu z)$ into the model (2), the following sub-operators are obtained

$$\begin{aligned} F_0 &= -\mu + \beta|U|^2 - \rho\phi + \gamma|U|^4 - V(x,y), & \phi_{xx} + \nu\phi_{yy} &= \left(|U|^2\right)_{xx} \\ F_1 &= -\mu + 3\beta U^2 - \rho\phi + 5\gamma U^4 - V(x,y) \end{aligned} \quad (8)$$

where μ is propagation constant. Using F_0 and F_1 , we get L_0 and L_1 operators as follows:

$$\begin{aligned} L_0 U &= \frac{1}{2} \Delta U + F_0 U, & M_0 &= \mathcal{F}^{-1} \left(\frac{\mathcal{F}(L_0 U)}{K^2 + c} \right), \\ L_1 U &= \frac{1}{2} \Delta M_0 + F_1 M_0, & M_1 &= \mathcal{F}^{-1} \left(\frac{\mathcal{F}(L_1 U)}{K^2 + c} \right) \end{aligned} \quad (9)$$

where

$$\mathcal{F}\{f(x, y)\} = \hat{f}(k_x, k_y) = \int_{-\infty}^{\infty} f(x, y) e^{i(k_x x + k_y y)} dx dy \quad (10)$$

$$\mathcal{F}^{-1}\{\hat{f}(k_x, k_y)\} = f(x, y) = \frac{1}{2\pi} \int_{-\infty}^{\infty} \hat{f}(k_x, k_y) e^{-i(k_x x + k_y y)} dk_x dk_y, \quad (11)$$

$K^2 = k_x^2 + k_y^2$ and the parameter c that has a considerable effect on convergence of the SOM method is utilized for parametrizing the numerical procedure.

After obtaining M_1 , the iteration scheme is executed as follows,

$$U_{n+1} = U_n - M_1 \Delta t. \quad (12)$$

while the mean term $\phi(x, y)$ is calculated by

$$\phi_n = \mathcal{F}^{-1} \left(\frac{k_x^2}{k_x^2 + \nu k_y^2} \mathcal{F}(|U_n|^2) \right). \quad (13)$$

In order to avoid division by zero error, the first element of K^2 is set to be 1. Starting from an initial guess, this numerical scheme is iterated until the error $E = \sqrt{\|U_{n+1} - U_n\|^2} < 10^{-8}$. It is noted that c and Δt are chosen heuristically as positive real numbers to obtain a convergent solution, and we take $c = 1.3$ and $\Delta t = 0.2$ in this chapter. The initial condition of the SOM method is chosen as a Gaussian $u(x, y) = \exp\left(-\left[(x - x_0)^2 + (y - y_0)^2\right]\right)$. The location of the initial condition is determined by x_0 and y_0 . In previous studies [8, 15, 23], it was shown that the solitons centered at the maxima of the lattices cannot stay stable. Thus, in this study, the initial condition is located on a local minimum of the periodic lattice where $(x_0, y_0) = (\pi, 0)$ (that is shown in **Figure 1**). Unless otherwise stated, the parameters in the model (2) are fixed to the following values

$$(\mu, \rho, \nu, \beta, \gamma, V_0) = (-0.1, 0.5, 1.5, 2, \pm 0.2, 12.5). \quad (14)$$

It should be noted that $\rho = 0.5$ and $\nu = 1.5$ are specifically chosen to characterize the electro-optical effects in potassium niobate (KNbO₃) [16], and $\gamma = 0.2$ and $\gamma = -0.2$ cases are chosen to investigate soliton dynamics with self-focusing and self-defocusing quintic nonlinearity, respectively.

The fundamental solitons of the NLSM model (2) are obtained by the SOM method for the considered parameters (14) and are shown in **Figure 2**.

As shown in previous studies [23, 24, 36], fundamental solitons of the NLSM system (2) (with or without lattice) are not radially symmetric due to the anisotropy in the medium. To investigate the effect of the quintic nonlinearity on the level

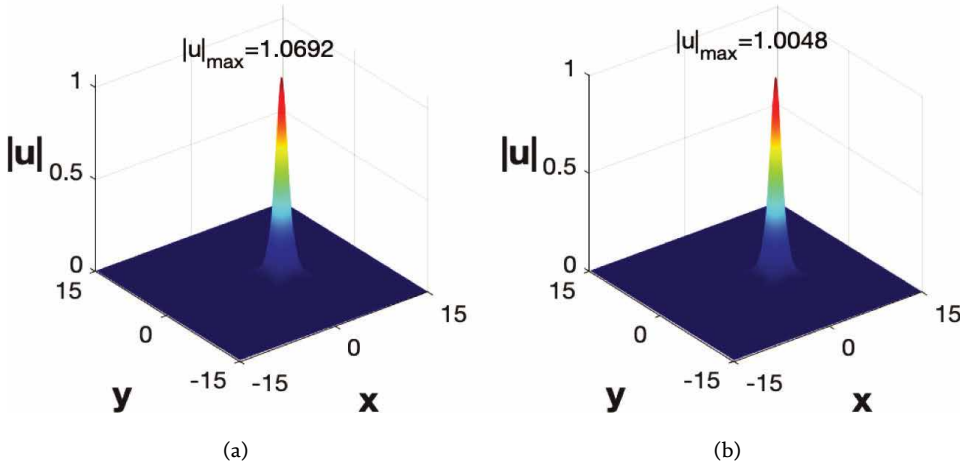


Figure 2. 3D profiles (first column), top views (second column) of fundamental solitons that are obtained (a) for $\gamma = -0.2$ (self-defocusing) and (b) for $\gamma = 0.2$ (self-focusing) quintic nonlinearity. All other parameters are taken as in Eq. (14).

of astigmatism in the solitons, the following formulation is defined as a measure of astigmatism

$$e = \frac{\text{radius along } y - \text{axis}}{\text{radius along } x - \text{axis}}. \quad (15)$$

Here, $e = 1$ when the soliton is radially symmetric, and if $e < 1$ and $e > 1$ the obtained solitons are comparatively wider along the x and y axes, respectively. Thus, the solitons are elliptical if $e \neq 1$.

Contour plots of solitons are depicted in **Figure 3** for $\rho = 0$, $\rho = 0.5$ and $\rho = 1$ when the quintic nonlinearity coefficient $\gamma = -0.5$, $\gamma = 0$ and $\gamma = 0.5$. **Figure 3** shows that astigmatism along the x -axis is emphasized when the fundamental solitons are obtained with a larger coupling parameter ρ (see the first column). It is also observed that the fundamental soliton becomes less astigmatic along x -axis with a larger quintic nonlinearity parameter γ (for a fixed ρ), and when $\rho = 0$ and the quintic nonlinearity is self-focusing (i.e., when $\gamma > 0$) the solitons become comparatively wider along y -axis (see the first row).

To see the impact of the anisotropy parameter ν on the soliton profile, the on-axes amplitudes and contour images of fundamental solitons are displayed in **Figure 4**. **Figure 4** shows that the amplitude of fundamental solitons are decreasing with increasing ν (from 0 to 3), and solitons become more extended along x -axis with larger ν values.

Comparing the contour images in **Figures 3** and **4**, it is seen that the astigmatism of the fundamental solitons changes significantly with ρ , whereas it depends weakly on ν .

3. Stability analysis

The stability properties of fundamental solitons (that are obtained by the SOM method) are examined by the linear eigenvalue spectra and the direct simulation of the nonlinear model (2).

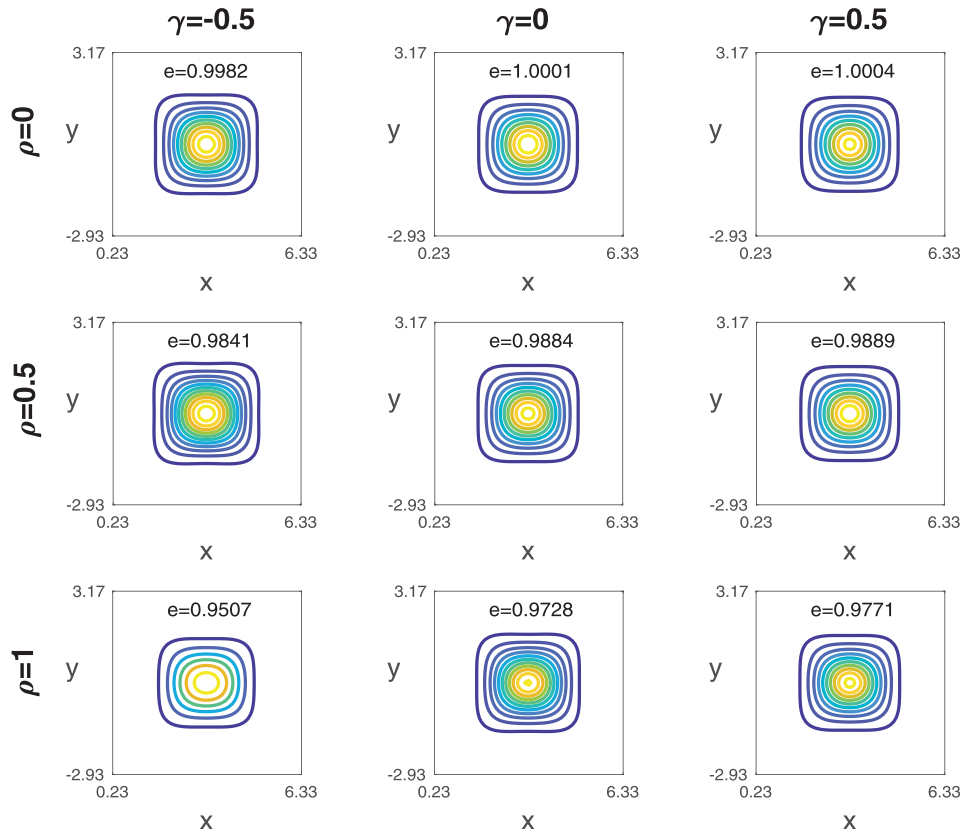


Figure 3. Contour image of fundamental solitons that are obtained for $\rho = 0$ (the first row), $\rho = 0.5$ (the second row) and $\rho = 1$ (the third row) while $\gamma = -0.5$ (the first column), $\gamma = 0$ (the second column) and $\gamma = 0.5$ (the third column). All other parameters are taken as in Eq. (14) and e shows the degree of astigmatism for each soliton.

The linear stability of solitons are studied by the linear spectra of fundamental solitons. To obtain the linear spectrum, the fundamental soliton is perturbed as follows

$$U = e^{i\mu z} [u_0(x, y) + g(x, y)e^{\lambda z} + h^*(x, y)e^{\lambda^* z}] \quad (16)$$

where $u_0(x, y)$ is the fundamental soliton and $g, h \ll 1$ are infinitesimal perturbations. Substituting the solution U into (2) and linearizing, it is found that these normal modes satisfy the following linear eigenvalue problem

$$\mathcal{L}\mathbf{V} = \lambda\mathbf{V} \quad (17)$$

where

$$\mathcal{L} = i \begin{pmatrix} 0 & \mathcal{L}_+ \\ \mathcal{L}_- & 0 \end{pmatrix}, \quad \mathbf{V} = \begin{pmatrix} g \\ h \end{pmatrix}$$

and the matrix coefficients of \mathcal{L} are

$$\begin{aligned} \mathcal{L}_+ &= -\mu + \frac{1}{2}\Delta - \rho\phi + 3\beta u^2 + 5\gamma u^4 - V, \\ \mathcal{L}_- &= -\mu + \frac{1}{2}\Delta - \rho\phi + \beta u^2 + \gamma u^4 - V. \end{aligned} \quad (18)$$

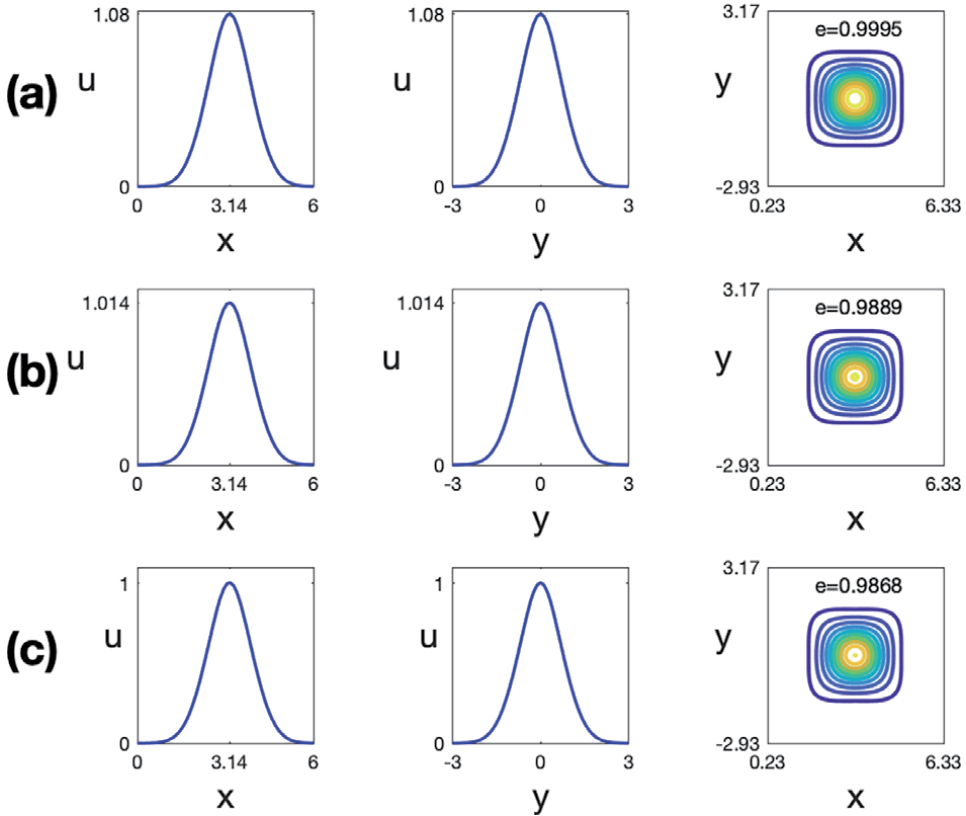


Figure 4. The on-axes amplitudes of fundamental solitons along x -axis (first column), along y -axis (second column) and contour image of solitons (third row) (a) for $\nu = 0$; (b) for $\nu = 1.5$ and (c) $\nu = 3$. All other parameters are taken as in Eq. (14) and e shows the degree of astigmatism for each soliton.

We can solve this eigenvalue problem by the Fourier collocation method [42]. Any eigenvalue with a positive real part in the spectrum indicates the linear instability of the fundamental soliton considered.

The power (or energy in some other contexts) of solitons can be computed by $P = \iint_{-\infty}^{\infty} |u|^2 dx dy$. In [43], Vakhitov and Kolokolov (VK) demonstrated that there is a critical power value above which the solitons cannot be linearly stable, and a soliton can be linearly stable only if its power increases as the propagation constant μ is increased, i.e.,

$$dP/d\mu > 0. \quad (19)$$

Moreover, in [44, 45], it was shown that the solitons can be stable nonlinearly only if the slope condition (19) is satisfied.

In the light of these results, prior to the nonlinear stability analysis, the power and linear stability of solitons are studied in **Figure 5**. These power-eigenvalue diagrams are calculated for the parameters that are given in Eq. (14), and the linear (in)stability intervals of gap solitons are determined via the computation of eigenvalue spectra of the solitons at each point of the power curves (see **Figure 5 (a1)–(b1)**). Furthermore, the maximum real part in the eigenvalue spectra (spectral radius) is examined in **Figure 5(a2)–(b2)** for the gap solitons. The solitons are found to be linearly stable for self-defocusing quintic nonlinearity ($\gamma = -0.2$) when the power $P \in [1.61, 2.39]$ and propagation constant $\mu \in [-0.35, 0]$

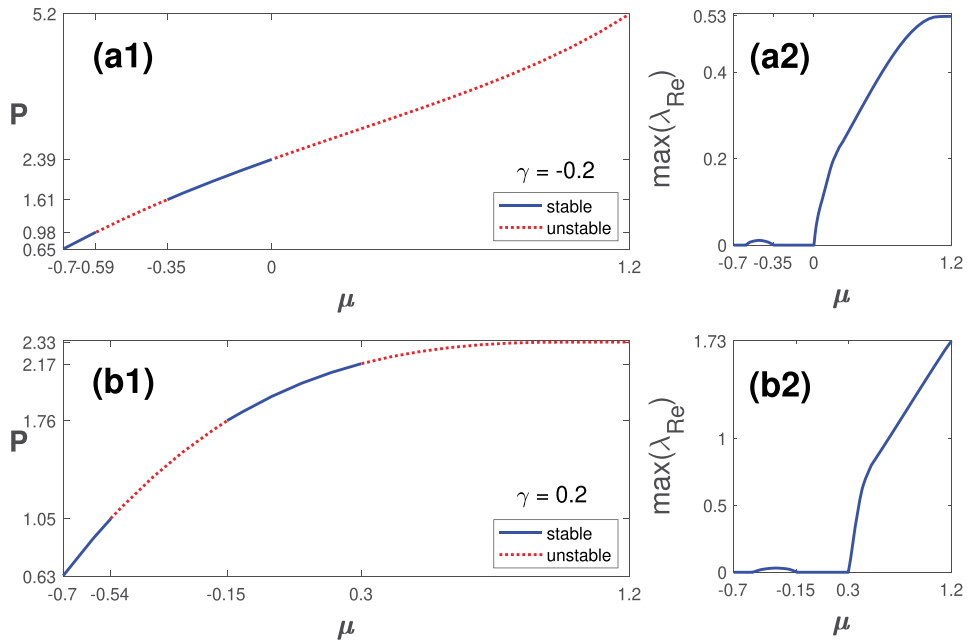


Figure 5. The power-eigenvalue ($P - \mu$) diagram of lattice solitons (a1) for $\gamma = -0.2$ (self-defocusing) and (b1) for $\gamma = 0.2$ (self-focusing). Maximum real part (spectral radius) of the eigenvalue spectra of solitons (a2) for $\gamma = -0.2$ and (b2) for $\gamma = 0.2$. Solid blue and red dotted lines show stable and unstable regions for the gap solitons, respectively.

(see **Figure 5(a1)–(a2)**), and the solitons are linearly stable when $P \in [1.76, 2.17]$ and $\mu \in [-0.15, 0.3]$ for self-focusing ($\gamma = 0.2$) quintic nonlinearity (see **Figure 5(b1)–(b2)**). These results are consistent with VK stability criterion since the slope of both power-eigenvalue diagrams is positive.

In addition to the power-eigenvalue diagram, the power and linear stability of solitons are studied in **Figure 6** for varied values of γ, ρ and β . The x -axis of each panel shows the existence domain for the varied parameter when other parameters are fixed to the values in Eq. (14). For instance, when $\mu = -0.1, \rho = 0.5, \nu = 1.5, \beta = 2$ and $V_0 = 12.5$, fundamental solitons can be generated for $\gamma \in [-0.7, 25.1]$ (see the left panel in **Figure 6(a)**). In **Figure 6(a)**, stable (solid blue line) and unstable (red dotted line) regions are determined in the left panel, and in the right panel zoom-in view of the black rectangular region in the left panel is depicted.

Figure 6 shows that the power of solitons is decreased as γ and β are increased. The right panel in **Figure 6(a)** shows that solitons are linearly stable when γ is between -0.24 and 0.26 , and comparing the left and right panels in **Figure 6(b)** and **(c)**, it is seen that stability regions of ρ and β parameters for self-focusing ($\gamma = 0.2$) case of quintic nonlinearity is narrow than that of self-defocusing ($\gamma = -0.2$) case.

To confirm obtained linear stability results, we study nonlinear evolution of solitons by means of direct simulation of the governing Eq. (2). To this end, using the fourth-order Runge–Kutta (RK4) scheme fundamental soliton is advanced in z direction, and the spatial domain (x, y) is discretized by the finite-difference method. It should be noted that the RK4 method is widely used for numerical analysis of nonlinear evolution equations, in this regard we apply RK4 to compare the results of this chapter with previous studies. The starting point of nonlinear evolution is chosen as the fundamental soliton, and 1% random noise is inserted to amplitude of the soliton to test the nonlinear stability under perturbations.

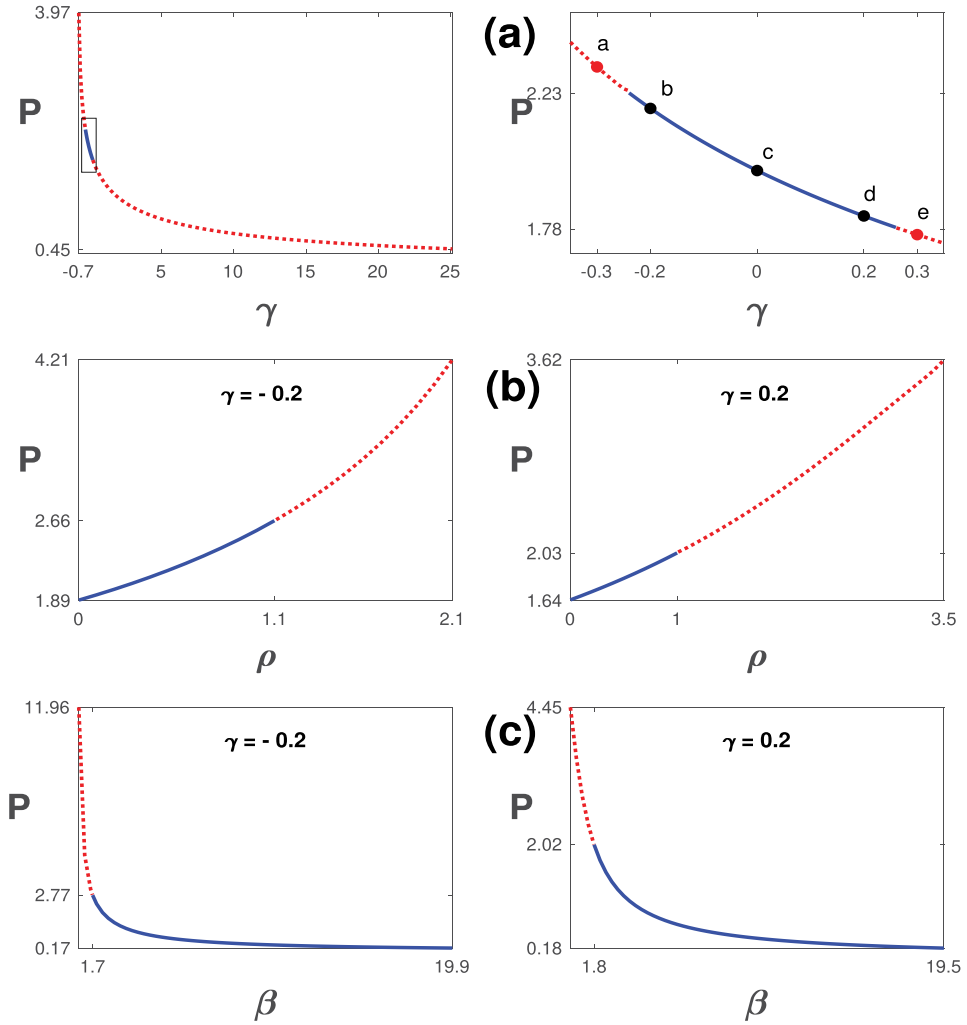


Figure 6. (a) Soliton power for varying quintic nonlinearity coefficient γ , left panel shows the domain of existence, and right panel shows zoom-in view of the black rectangular region. Soliton powers for $\gamma = -0.2$ (left panel) and $\gamma = 0.2$ (right panel) (b) with varying ρ and (c) with varying β parameters. The linear stability and instability regions are shown by solid blue and red dotted lines, respectively.

In **Figure 7**, linear stability spectrum (first column), nonlinear evolution of the peak amplitude (second column), the evolution of soliton power (third column), and 3D view of the evolved soliton (fourth column) are plotted for the fundamental solitons that correspond to “a”, “b”, “c”, “d” and “e” points in the right panel of **Figure 6(a)**. Here, the impact of quintic nonlinearity is examined by increasing γ from -0.3 to 0.3 .

In **Figure 7(b)–(d)**, it is shown that the linear spectrum of the fundamental soliton is purely-imaginary (none of their eigenvalues have a real part), and the peak amplitudes oscillate during the propagation, thus stable evolution can be achieved for the considered solitons in the quadratic-cubic-quintic nonlinear medium when $\gamma = -0.2$, $\gamma = 0$ and $\gamma = 0.2$. On the other hand, when the coefficient of quintic nonlinearity is increased, there are eigenvalues with positive real part in linear stability spectra, and the peak amplitudes blow-up after a short propagation distance for $\gamma = -0.3$ and $\gamma = 0.3$ as shown in **Figure 7(a)** and **(e)**, respectively.

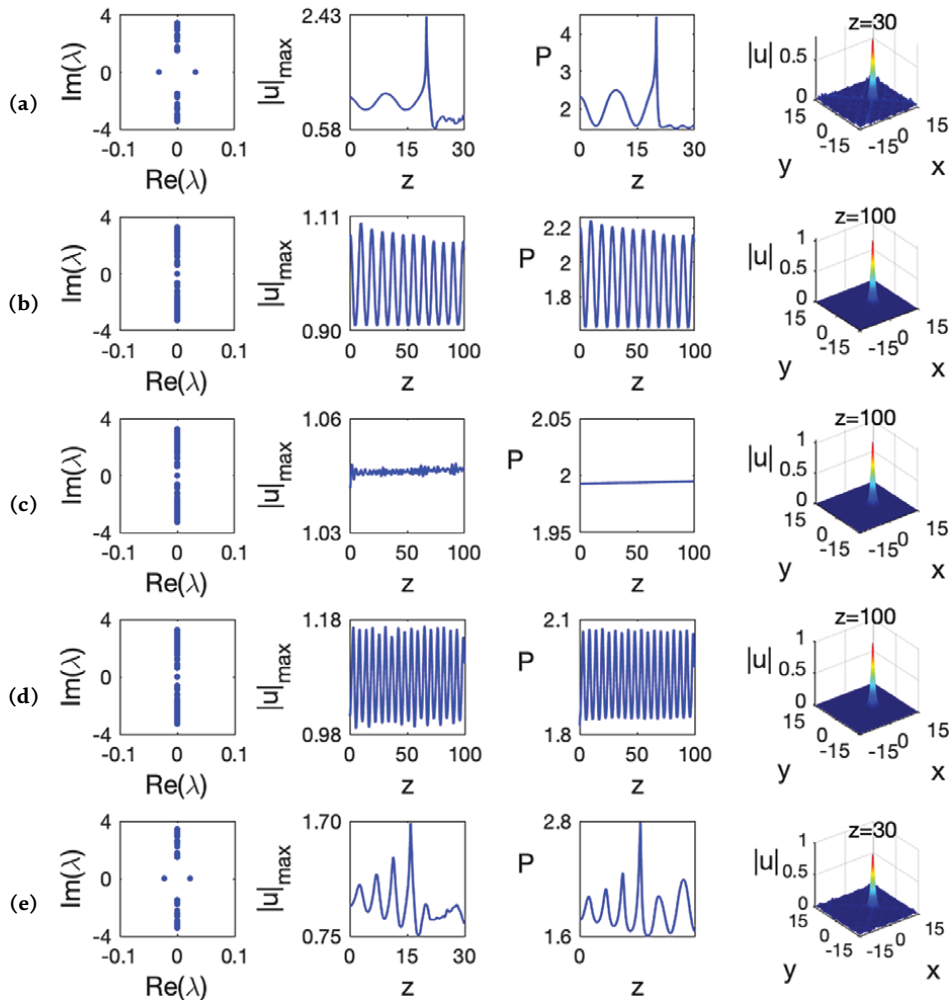
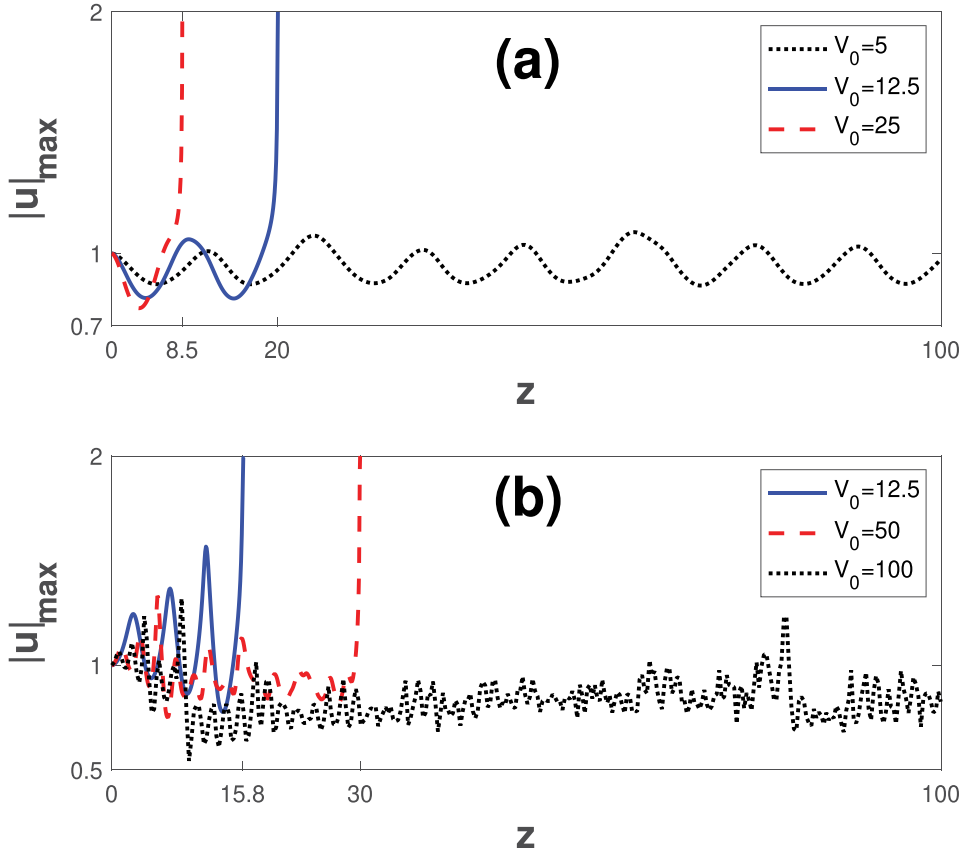


Figure 7. Linear spectra (first column), nonlinear evolution of peak amplitudes (second column), the evolution of soliton power (third column), and 3D view of the soliton after evolution (fourth column) for (a) $\gamma = -0.3$; (b) $\gamma = -0.2$; (c) $\gamma = 0$; (d) $\gamma = 0.2$; and (e) $\gamma = 0.3$. All other parameters are fixed to the values in Eq. (14).

This fact reveals that both strong self-focusing and self-defocusing quintic nonlinearities have an adverse effect on the stability of fundamental solitons.

From previous studies, it is known that increasing potential depth V_0 improves the stability of solitons in quadratic [23] and cubic (Kerr) medium [4]. In **Figure 8**, to examine the impact of the deeper lattice on the soliton stability in the quadratic-cubic-quintic nonlinear medium when $\gamma = -0.3$ (see panel (a)) and $\gamma = 0.3$ (see panel (b)), the evolution of the peak amplitudes are displayed for varied potential depths. To compare the propagation distance, the amplitude of solitons are divided by their peak amplitudes. **Figure 8** shows that larger lattice depth V_0 supports the stability of solitons for $\gamma = 0.3$ (self-focusing), whereas shallow potential extends and eventually stabilizes the soliton for $\gamma = -0.3$ (self-defocusing). Thus, when the instability emerges from strong self-focusing nonlinearity, a deeper lattice can be utilized to arrest (or delay) the collapse. This result is consistent with the previous studies, and it is meaningful because the potential in our model (2) is defocusing and it must be balanced with a self-focusing term to obtain stable modes.

Furthermore, it is known that increasing anisotropy parameter ν assists the stability of solitons when quadratic electro-optic effects are strong [23, 46, 47]. In


Figure 8.

Peak amplitude of the evolved solitons for varying lattice depths when the fundamental soliton is obtained for (a) $\gamma = -0.3$; and (b) $\gamma = 0.3$.

order to investigate the impact of anisotropy on soliton dynamics, we plot the evolution of peak amplitude when ν is varying between 0 and 1000 in **Figure 9**. As shown in **Figure 9**, increasing the anisotropy coefficient ν (from 0.001 to 100) extends the propagation distance of the evolved solitons, and it stabilizes the soliton in the medium with a strong self-defocusing nonlinearity (when $\gamma = -0.3$) eventually (see black dotted line in panel (a)). Similarly, increased ν supports the stability of the solitons for strong self-focusing nonlinearity (when $\gamma = 0.3$), and although it cannot stabilize the soliton robustly, it provides a significant extension of propagation distance when $\nu = 1000$ (see black dotted line in panel (b)).

It must be noted that even though soliton solutions of the NLSM system (2) can be obtained when $\nu \in (0, \infty)$ and stability of solitons are improved by higher values of ν , they cannot be utilized in practical optical applications, due to the fact that ρ and ν are predetermined constants associated with the type of optical materials.

4. Conclusions

Fundamental lattice solitons were obtained in a nonlocal nonlinear medium with self-focusing and self-defocusing quintic nonlinearity. The steady-state solutions are calculated by the SOM algorithm and the stability properties of solitons have been explored by linear spectra and nonlinear evolution of the amplitude by direct simulation of the nonlinear model. The band-gap boundaries and stability intervals

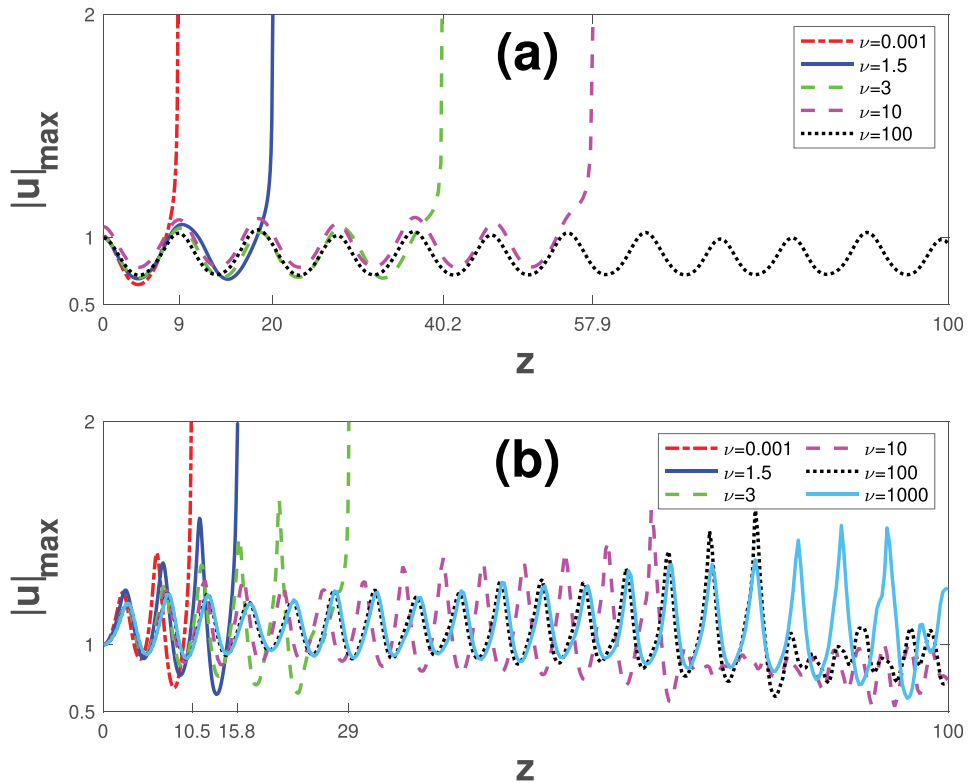


Figure 9. Peak amplitude of the evolved solitons for varying anisotropy coefficients (ν) between 0.001 and 1000 when the fundamental soliton is obtained for (a) $\gamma = -0.3$; and (b) $\gamma = 0.3$.

of solitons were found and the power of solitons was investigated for varied ρ , β and γ parameters. It has been seen that the power of fundamental solitons is decreased by increasing cubic (β) and quintic (γ) nonlinearity, while the power is increasing as the quadratic nonlinear response (ρ) is increased, and stability regions of ρ and β parameters for self-focusing ($\gamma = 0.2$) case of quintic nonlinearity is narrow than that of self-defocusing ($\gamma = -0.2$) case.

The stability analysis showed that fundamental lattice solitons can stay stable for the weak self-focusing and self-defocusing quintic nonlinearity. Strong self-focusing ($\gamma = 0.3$) and self-defocusing ($\gamma = -0.3$) quintic nonlinearities shortened the propagation distance of evolved solitons.

Furthermore, it has been observed that when the quintic nonlinearity is strong in the medium, solitons collapse, and the collapse of solitons can be arrested by a deeper lattice for self-focusing quintic nonlinearity ($\gamma = 0.3$), whereas unstable solitons can be stabilized by shallow lattice for strong self-defocusing quintic nonlinearity ($\gamma = -0.3$).

In conclusion, the numerical existence and stability of fundamental lattice solitons have been presented in a nonlocal nonlinear medium with the quintic nonlinear response, and it has been demonstrated that stability of unstable solitons can be improved by modification of potential depth and strong anisotropy coefficient.

Conflict of interest

The authors declare no conflict of interest.

Author details

Mahmut Bağcı^{1*†}, Theodoros P. Horikis^{2†}, İlkey Bakırtaş^{3†} and Nalan Antar^{3†}

1 Department of Management Information Systems, Marmara University, Istanbul, Turkey

2 Department of Mathematics, University of Ioannina, Ioannina, Greece

3 Department of Mathematics Engineering, Istanbul Technical University, Istanbul, Turkey

*Address all correspondence to: bagcimahmut@gmail.com

† These authors contributed equally.

IntechOpen

© 2022 The Author(s). Licensee IntechOpen. This chapter is distributed under the terms of the Creative Commons Attribution License (<http://creativecommons.org/licenses/by/3.0>), which permits unrestricted use, distribution, and reproduction in any medium, provided the original work is properly cited. 

References

- [1] Stegeman GIA, Christodoulides DN, Segev M. Optical spatial solitons: Historical perspectives. *IEEE Journal of Selected Topics in Quantum Electronics*. 2000;**6**:1419-1427
- [2] Fleischer JW, Segev M, Efremidis NK, Christodoulides DN. Observation of two-dimensional discrete solitons in optically induced nonlinear photonic lattices. *Nature*. 2003;**422**:147-150
- [3] Chen Z, Segev M, Christodoulides DN. Optical spatial solitons: Historical overview and recent advances. *Reports on Progress in Physics*. 2012;**75**:086401
- [4] Ablowitz MJ, Antar N, Bakrtaş İ, Ilan B. Band-gap boundaries and fundamental solitons in complex two-dimensional nonlinear lattices. *Physical Review A*. 2010;**81**:033834
- [5] Christodoulides DN, Yang J, editors. *Parity-Time Symmetry and its Applications*. Singapore: Springer; 2018
- [6] Göksel I, Bakrtaş I, Antar N. Nonlinear lattice solitons in Saturable media. *Applied Mathematics & Information Sciences*. 2014;**9**: 377-385
- [7] Göksel I, Antar N, Bakrtaş I. Two-dimensional solitons in PT-symmetric optical media with competing nonlinearity. *Optik*. 2018;**156**:470-478
- [8] Ablowitz MJ, Ilan B, Schonbrun E, Piestun R. Solitons in two-dimensional lattices possessing defects, dislocations, and quasicrystal structures. *Physical Review E*. 2006;**74**:035601
- [9] Ablowitz MJ, Antar N, Bakrtaş İ, Ilan B. Vortex and dipole solitons in complex two-dimensional nonlinear lattices. *Physical Review A*. 2012;**86**: 033804
- [10] Fu Q, Wang P, Huang C, Kartashov YV, Torner L, Konotop VV, et al. Optical soliton formation controlled by angle twisting in photonic moiré lattices. *Nature Photon*. 2020;**14**: 663-668
- [11] Wang P, Zheng Y, Chen X, Huang C, Kartashov YV, Torner L, et al. Localization and delocalization of light in photonic moiré lattices. *Nature*. 2020; **577**:42-46
- [12] Huang C, Ye F, Chen X, Kartashov YV, Konotop VV, Torner L. Localization-delocalization wavepacket transition in Pythagorean aperiodic potentials. *Scientific Reports*. 2016;**6**: 32546
- [13] Bağcı M, Bakrtaş İ, Antar N. Fundamental solitons in parity-time symmetric lattice with a vacancy defect. *Optics Communication*. 2015;**356**: 472-481
- [14] Martin H, Eugenieva ED, Chen Z, Christodoulides DN. Discrete solitons and soliton-induced dislocations in partially coherent photonic lattices. *Physical Review Letters*. 2004;**92**: 123902
- [15] Bağcı M, Bakrtaş İ, Antar N. Vortex and dipole solitons in lattices possessing defects and dislocations. *Optics Communication*. 2014;**331**: 204-218
- [16] Crasovan LC, Torres JP, Mihalache D, Torner L. Arresting wave collapse by wave self-rectification. *Physical Review Letters*. 2003;**91**: 063904
- [17] Schiek R, Pertsch T. Absolute measurement of the quadratic nonlinear susceptibility of lithium niobate in waveguides. *Optical Materials Express*. 2012;**2**:126-139

- [18] Ablowitz MJ, Biondini G, Blair S. Localized multi-dimensional optical pulses in non-resonant quadratic materials. *Mathematics and Computers in Simulation*. 2001;**56**: 511-519
- [19] Hayata K, Koshiba M. Multidimensional solitons in quadratic nonlinear media. *Physical Review Letters*. 1993;**71**:3275-3278
- [20] Torruellas WE, Wang Z, Hagan DJ, VanStryland EW, Stegeman GI, Torner L, et al. Observation of two-dimensional spatial solitary waves in a quadratic medium. *Physical Review Letters*. 1995;**74**:5036-5039
- [21] Torner L, Sukhorukov AP. Quadratic Solitons. *Optics & Photonics News*. 2002;**13**:42-47
- [22] Buryak AV, Trapani PD, Skryabin DV, Trillo S. Optical solitons due to quadratic nonlinearities: From basic physics to futuristic applications. *Physics Reports*. 2002;**370**: 63-235
- [23] Bağcı M, Bakırtaş İ, Antar N. Lattice solitons in nonlinear Schrödinger equation with coupling-to-a-mean-term. *Optics Communication*. 2017;**383**: 330-340
- [24] Bağcı M, Kutz JN. Spatiotemporal mode locking in quadratic nonlinear media. *Physical Review E*. 2020;**102**: 022205
- [25] Ablowitz MJ, Biondini G, Blair S. Multi-dimensional pulse propagation in non-resonant $\chi^{(2)}$ materials. *Physics Letters A*. 1997;**236**:520-524
- [26] Ablowitz MJ, Biondini G, Blair S. Nonlinear Schrödinger equations with mean terms in nonresonant multidimensional quadratic materials. *Physical Review E*. 2001;**63**: 046605
- [27] Benney DJ, Roskes GJ. Wave instabilities. *Studies in Applied Mathematics*. 1969;**48**:377-385
- [28] Davey A, Stewartson K. On three-dimensional packets of surface waves. *Proceedings of the Royal Society A*. 1974;**338**:101-110
- [29] Ablowitz MJ, Haberman R. Nonlinear evolution equations—Two and three dimensions. *Physical Review Letters*. 1975;**35**:1185-1188
- [30] Djordjevic VD, Redekopp LG. On two-dimensional packets of capillary-gravity waves. *Journal of Fluid Mechanics*. 1977;**79**:703-714
- [31] Papanicolaou G, McLaughlin D, Weinstein M. Focusing singularity for the nonlinear schrodinger equation. In: Fujita H, Lax PD, Strang G, editors. *Nonlinear Partial Differential Equations in Applied Science; Proceedings of The U.S.-Japan Seminar, Tokyo, 1982*. Vol. 81. North-Holland Mathematics Studies. North-Holland; 1983. pp. 253-257. DOI: 10.1016/S0304-0208(08)72095-4
- [32] Ghidaglia JM, Saut JC. On the initial value problem for the Davey-Stewartson systems. *Nonlinearity*. 1990; **3**:475-506
- [33] Fibich G, Papanicolaou G. Self-focusing in the perturbed and unperturbed nonlinear Schrödinger equation in critical dimension. *SIAM Journal on Applied Mathematics*. 1999; **60**:183-240
- [34] Merle FH, Raphael P. On universality of blow-up profile for L^2 critical nonlinear Schrödinger equation. *Inventiones Mathematicae*. 2004;**156**: 565-672
- [35] Moll KD, Gaeta AL, Fibich G. Self-similar optical wave collapse: Observation of the Townes profile. *Physical Review Letters*. 2003;**90**: 203902

- [36] Ablowitz MJ, Bakrtaş İ, Ilan B. Wave collapse in a class of nonlocal nonlinear Schrödinger equations. *Physica D: Nonlinear Phenomena*. 2005; **207**:230-253
- [37] Chen YF, Beckwitt K, Wise FW, Aitken BG, Sanghera JS, Aggarwal ID. Measurement of fifth- and seventh-order nonlinearities of glasses. *Journal of the Optical Society of America B: Optical Physics*. 2006; **23**:347-352
- [38] Komarov A, Leblond H, Sanchez F. Quintic complex Ginzburg-Landau model for ring fiber lasers. *Physical Review E*. 2005; **72**:025604
- [39] Mohamadou A, LatchioTiofack CG, Kofané TC. Wave train generation of solitons in systems with higher-order nonlinearities. *Physical Review E*. 2010; **82**:016601
- [40] Azzouzi F, Triki H, Grelu P. Dipole soliton solution for the homogeneous high-order nonlinear Schrödinger equation with cubic-quintic-septic non-Kerr terms. *Applied Mathematical Modelling*. 2015; **39**:1300-1307
- [41] Yang J, Lakoba TI. Universally-convergent squared-operator iteration methods for solitary waves in general nonlinear wave equations. *Studies in Applied Mathematics*. 2007; **118**: 153-197
- [42] Yang J. *Nonlinear Waves in Integrable and Nonintegrable Systems*. Philadelphia: SIAM; 2010
- [43] Vakhitov NG, Kolokolov AA. Stationary solutions of the wave equation in a medium with nonlinearity saturation. *Radiophysics and Quantum Electronics*. 1973; **16**:783-789
- [44] Weinstein MI. Modulational stability of ground states of nonlinear Schrödinger equations. *SIAM Journal on Mathematical Analysis*. 1985; **16**: 472-491
- [45] Rose HA, Weinstein MI. On the bound states of the nonlinear schrödinger equation with a linear potential. *Physica D: Nonlinear Phenomena*. 1988; **30**:207-218
- [46] Bağcı M. Soliton dynamics in quadratic nonlinear media with two-dimensional Pythagorean aperiodic lattices. *Journal of the Optical Society of America B: Optical Physics*. 2021; **38**: 1276-1282
- [47] Bağcı M. Partially \mathcal{PT} -symmetric lattice solitons in quadratic nonlinear media. *Physical Review A*. 2021; **103**: 023530

Soliton Like-Breather Induced by Modulational Instability in a Generalized Nonlinear Schrödinger Equation

Saïdou Abdoulkary and Alidou Mohamadou

Abstract

We consider the nonlinear Schrödinger equation modified by a rational nonlinear term. The model appears in various studies often in the context of the Ginzburg-Landau equation. We investigate modulational instability by means of a linear stability analysis and show how the nonlinear terms affect the growth rate. This analytical result is confirmed by a numerical simulation. The latter analysis shows that breather-like solitons are generated from the instability, and the effects of the nonlinear terms are again clearly seen. Moreover, by employing an auxiliary-equation method we obtain kink and anti-kink soliton as analytical solutions. Our theoretical solution is in good agreement with our numerical investigation.

Keywords: generalized nonlinear schrödinger, modulational instability, breather like-soliton

1. Introduction

The nonlinear Schrödinger equation (NLSE) is the main equation which governs the propagation of pulses in various fields such as nonlinear optical systems, plasmas, fluid dynamics, Bose-Einstein condensation, and condensed matter physics. It has been shown to govern the evolution of a wave packets in weakly nonlinear and dispersive media and has thus arisen in such diverse fields. One other application of this equation is in pattern formation, where it has been used to model some nonequilibrium pattern forming systems. Most notable is the role it plays in understanding the propagation of electromagnetic waves in glass fibers and other optical waveguides [1].

In this paper we consider a NLS equation with inverse nonlinear terms. Inverse nonlinear term has been introduced for the first time by Malomed and al. [2] which has been later studied by [3, 4] in the case of the Ginzburg-Landau equation.

$$iu_z + pu_{xx} + \gamma_1 \frac{|\frac{\partial u}{\partial x}|^2}{|u|^2} u + \gamma_2 \frac{1}{|u|^2} u + \gamma_3 |u|^2 u = 0, \quad (1)$$

where u is a complex amplitude that depends on z and x , γ_i ($i = 1, 2, 3$) is a real constant and represents the nonlinear coefficient, p is a real constant and supposes

to be the group-velocity dispersion (GVD) coefficient. Notice that Eq. (1) especially with $\gamma_1 = \gamma_2 = 0$ appears in many contemporary work in physics and has been shown to be completely integrable [5] and to admit optical solitons by balancing the GVD and Kerr nonlinearity γ_3 (the self-focusing interaction and defocusing interaction corresponding to bright and dark solitons, respectively). However, in many applications it contains also some small additional terms which destroy these properties. It describes either the propagation of a continuous wave (CW) beam in a planar waveguide or propagation of an optical pulse inside optical fiber, and show that this equation admits analytical solitary solution and exhibits a modulation instability (MI). This instability leads to spatial or temporal modulation of a constant-intensity plane wave.

Modulational instability is one of the nonlinear wave equations associated to NLSE and appears in many physical systems. It indicates that due to the competition between nonlinearity and the dispersive effects, a small perturbation of the initial plane wave may induce an exponential growth of the wave amplitude, resulting in the carrier-wave breakup into a train of localized waves [6].

The NLSE is also one of the original nonlinear partial differential equations, the study of which has led to fundamental advances in theoretical physics. The study of NLS was motivated by a large number of theoretical problems ranging from optical pulse propagation in nonlinear fibers to hydrodynamics, condensed matter physics and biophysics. It is now known that NLS is one of the few examples of completely integrable nonlinear partial differential equations [7, 8].

The main objective of this paper is to study MI in a generalized NLSE that includes rational nonlinear terms given by Eq. (1). By means of the linear stability analysis we explicitly investigate the stability condition of a launched plane wave. The results show that the MI gain is strongly dependent on the nonlinear parameters as well as the GVD. Our numerical simulations show that those parameters contribute to the formation and the propagation of the soliton like-breather in the systems. Those parameters can generate either stable or unstable solitons. We also investigate analytical soliton solutions. By employing auxiliary equation method we obtain kink and antikink solutions of Eq. (1).

The rest of the paper is organized as follows. The model is introduced in Section 2, which is followed by the analysis of the MI of the CW solutions in Section 3, direct simulations shown the formation of modulated wave as well as breather like-solitons and their stability in Section 4. Exact analytical kink and antikink soliton solutions are reported in Section 5, and the paper is concluded by Section 6.

2. Modulational instability

The nonlinear Schrodinger Equation Eq. (1) has the simplest solution in the form of a continuous wave as $u = u_0 \exp i(kx - \omega z)$, where u_0 is a constant and k and ω are respectively the the wave-number and the angular frequency and satisfy the dispersion relation $\omega - k^2 p + \gamma_1 k^2 + \frac{\gamma_2}{|u_0|^2} + \gamma_3 |u_0|^2 = 0$. Now we focus our attention on the modulational instability in the system. Therefore, we look at solutions of Eq. (1) in the form of

$$u = u_0(1 + b) \exp i(kx - \omega z), \quad (2)$$

where b represents a small perturbation.

Substituting Eq. (2) into the NLS equation Eq. (1) and linearizing the resulting equations, we obtain a linear equation of b .

$$ib_z + pb_{xx} + 2ikpb_x + i\gamma_1 k(b_x^* - b_x) - \frac{\gamma_2}{|u_0|^2}(b^* + b) + \gamma_3|u_0|^2(b^* + b) = 0, \quad (3)$$

Looking for solutions to this function in the form of plane waves $b = b_1 \exp i(Kx - \Omega z) + b_2^* \exp -i(Kx - \Omega z)$, we obtain the dispersion relation

$$\Omega = (2p - \gamma_1)kK \pm K \sqrt{\gamma_1^2 k^2 + p^2 K^2 + 2 \frac{\gamma_2}{|u_0|^2} p - 2\gamma_3 p |u_0|^2}, \quad (4)$$

where the wave number K and the frequency Ω characterize linear properties of the modulation wave. The dispersion relation given by Eq. (4) determine the condition for the stability of a plane wave with a wave number k in the system. This is the case as long as Ω is real. This stability condition is explicitly depends on the nonlinear parameters γ_1 , γ_2 , and γ_3 . It shows that the CW plane-wave is absolutely stable only in the case $\gamma_1^2 k^2 + p^2 K^2 + 2 \frac{\gamma_2}{|u_0|^2} p - 2\gamma_3 p |u_0|^2 < 0$. That is

$$(\gamma_1^2 k^2 + p^2 K^2) - \sqrt{\Delta} < |u_0|^2 < (\gamma_1^2 k^2 + p^2 K^2) + \sqrt{\Delta}, \quad (5)$$

with $\Delta = (\gamma_1^2 k^2 + p^2 K^2)^2 + 16\gamma_2 \gamma_3 p^2$.

The modulation instability gain is related to the imaginary part of Ω and is given by

$$g = \text{Im} \left[|K| \sqrt{\gamma_1^2 k^2 + p^2 K^2 + 2 \frac{\gamma_2}{|u_0|^2} p - 2\gamma_3 p |u_0|^2} \right], \quad (6)$$

Figure 1 shows the instability gain as a function of the perturbation wave number K for $u_0 = 1$ and 1.5 . The gain exists for both positive and negative values of K in the range $|K| < K_0 = (1/2) \sqrt{-2\gamma_1^2 k^2 |u_0|^2 - 4\gamma_2 p + 4\gamma_3 p |u_0|^4} / (|u_0| p)$. The peak gain occurs for $K = K_0$ and has the value $g_{max} = (1/2) K_0 | \sqrt{2\gamma_1^2 k^2 + 4\gamma_2 p / |u_0|^2 - 4\gamma_3 p |u_0|^2} |$. Now let us study the latter gain. We have plotted a qualitative study of its behavior. **Figure 1a** shows that the peak gain increased with the amplitude u_0 increasing as well as it width. In **Figure 1b** one can see the inverse phenomenon. **Figure 2** shows the evolution of the peak gain as a function of nonlinear parameters γ_2 and γ_3 . Here we are seeing the

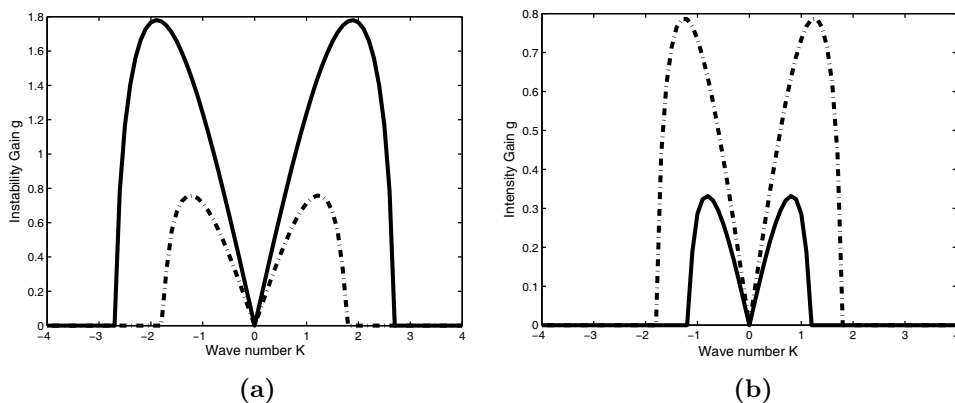


Figure 1. Gain spectrum $g(K)$ of modulation instability as a function of wave number with effect of the background amplitude $u_0 = 1$ (dashed line) and 1.5 (soline) when the GVD is 0.5 for the left-hand panel (a) with $\gamma_1 = 0.1$, $\gamma_2 = 0.4$, $\gamma_3 = 0.8$ and the GVD is -0.5 for the right hand-panel (b) with $\gamma_2 = 0.8$, $\gamma_3 = 0.01$.

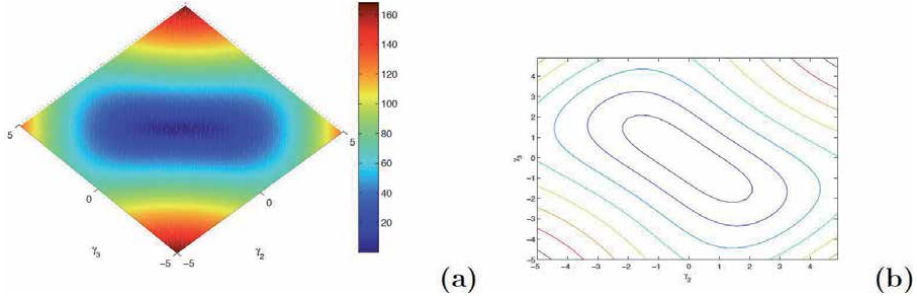


Figure 2. Maximum gain spectrum g_{max} of modulation instability for $u_0 = 1$ versus nonlinear parameters γ_2 and γ_3 (panel (a)), while in panel (b) we show its contour plot.

increasing of the peak with the nonlinear terms (see **Figure 2a**). There is a limit cycle where the peak remains constant for certain values of both γ_2 and γ_3 . This is clearly seen through the contour plot in **Figure 2b**. This aspect is better analyzed in **Figure 3** where the peak gain increased by increasing both γ_2 and γ_3 in the left side of top panel (a) as well as the gain width. This is confirm by fixing one nonlinear parameter (γ_2)

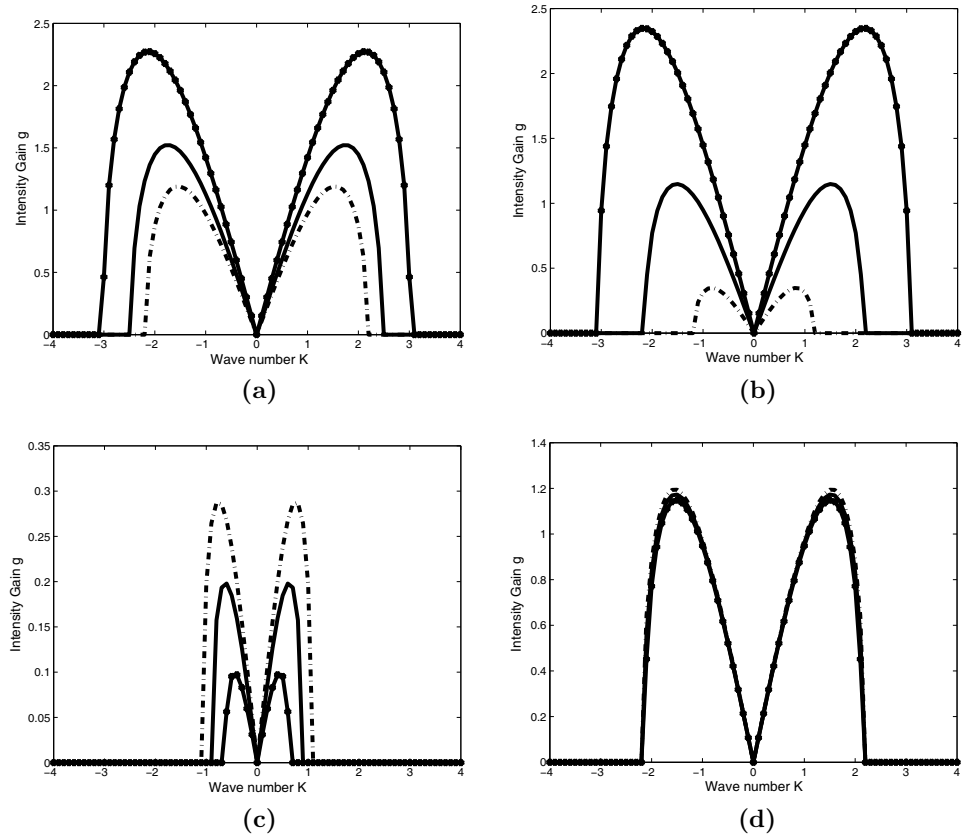


Figure 3. Gain spectrum $g(K)$ of modulation instability as a function of wave number with effect of the nonlinear parameters γ_2, γ_3 . In the top panel (a) on left we set $\gamma_2 = 0.03, \gamma_3 = 0.3$ for dashed line, $\gamma_2 = 0.3, \gamma_3 = 0.4$ for the solid line, $\gamma_2 = 0.5, \gamma_3 = 0.6$ for o-line. On right (b) we set $\gamma_2 = 0.2$, and $\gamma_3 = 0.1, 0.3, 0.6$ (respectively for dashed, solid and o-line). In bottom we got on left panel (c) $\gamma_2 = 0.01, 0.1, 0.2$ (respectively for dashed, solid and o-line) and $\gamma_3 = 0.3$. For all the previous panels we got $u_0 = 1$ and $\gamma_1 = 0.1$. On right panel (d) we consider the same values in (c) when $u_0 = 2$.

when the last one (γ_3) is varying (see panel (b)). One observe the inverse phenomenon by fixing γ_3 when γ_2 increasing (see panel (c)). The last panel (d) is very particular while we are seeing the peak and the width gain are almost constant by varying the nonlinear parameters (γ_2) when the background amplitude $u_0 = 2$.

3. The numerical simulation analysis

Analytical analysis done by linear stability shown the possibility of the formation of modulated waves in the consider system. This prediction can be numerically confirmed. In this way let us launch as initial condition a modulated plane wave: $u(0, x) = 1 + \varepsilon \cos(Kx)$ where fixed boundary conditions are used and the numerical constants used in the calculation are the following: $\varepsilon = 0.01$, $p = 0.5$, $k = 0$, $K = 0.2\pi$, $\gamma_1 = 0.1, 0.2, 0.3$ in $\gamma_2 = 0.01, 0.1, 0.4, 0.6$ and $\gamma_3 = 0.1, 0.3, 0.6, 0.9$ normalized units. The question we are going to answer is the influence of the parameters γ_i on the formation of modulated wave.

From **Figure 4** one can see the formation of bright solitary wave. The left hand top panel shows the generation of a pulse train toward the boundary regions but the intensity is smallest at the center. On right hand panel we can see the bright solitary wave behaves like a breather soliton is forming. This may be a multisoliton quasiperiodic solutions. It can be seen that the breather solutions keep their oscillating shapes, while the wave packets move as periodic solitons along the x -axis for certain values of z . Those breathers are periodic in the x coordinate and aperiodic in the z coordinate. There is more generation of breathers in bottom panels (e) and (f). Comparing panel (b) with panels (e) and (f), one can see that in panels (e) and (f), under the influence of the increasing values of the parameter γ_3 , the number of peaks on the same space interval is increasing when $|x|$ goes up even z . The breathers have compressed in width and peak, and this is clearly seen through the contour plot figures given by panels (c), (d), (g) and (h). Those phenomenon are certainly caused by increasing of the nonlinear parameter γ_3 when γ_2 remains small and constant. We can see the evolution of the peak amplitude of the wave over the z -axis for each case above in **Figure 5**. One can see that in panel (a) the peak amplitude increases gradually and oscillation little beat over the parameter z . The oscillation of the peak is increasing when the nonlinear parameter γ_3 increases and the curve believes sharp. This is perceptible in the rest panels (b, c and d). One can clearly confirms The dynamical process of the spatial pattern formation induced by MI. When γ_3 increases, the rate of MI increases too and the MI occurs earlier. Another interesting phenomenon is the width of the breather which decreases by increasing the consider nonlinear parameter.

There is more breathers when γ_2 is negative. **Figure 6** shows the evolution of the typical intensity profile done by numerical simulations. In panel (a) one can see that there are more breathers that appears more stable than the previous one. This analysis is more perceptible in panel (b) where we plot the contour plot of the consider figure. We are seeing both presence of breathers and bright soliton. This means that the consider parameter is strongly responsible of the formation of those solitons. This is more view in **Figure 7** where panels (a) and (b) shown how breathers are broke and the bright soliton takes place and propagate through the system when the wave vector is small than the previous one (0.01π).

4. Exact analytical solutions to the consider stationary model

We now discuss about the analytical solution to the stationary NLS of Eq. (1). Suppose that

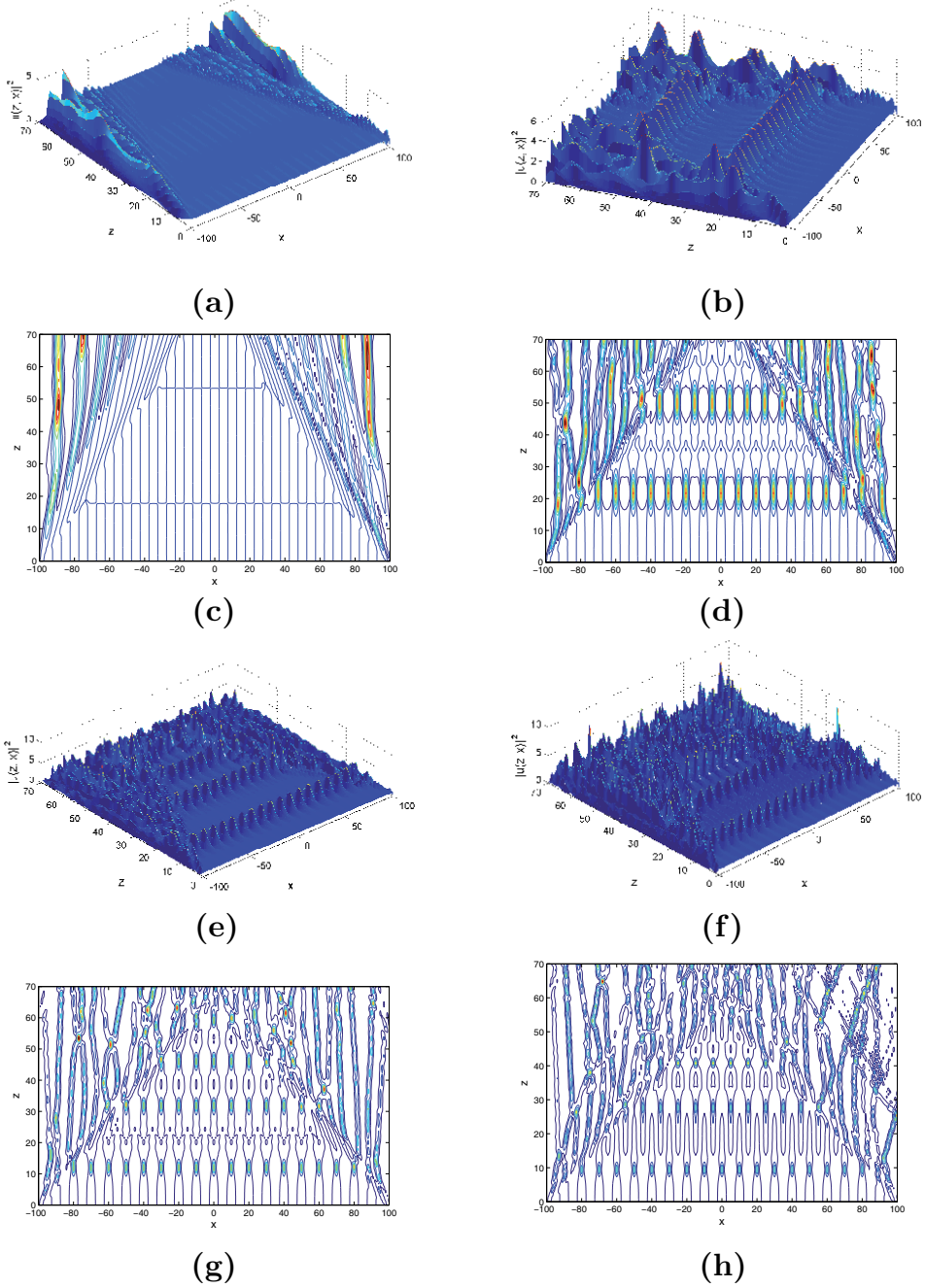


Figure 4. The evolution of the typical intensity profile done by numerical simulation of Eq. (1) when γ_3 is varying (0.1, for (a), 0.3 for (b), 0.6 for (e) and 0.8 for (f)) by fixing $\gamma_1 = 0.1$ and $\gamma_2 = 0.01$, while panels (c), (d), (g) and (h) show their respective contour plots.

$$u(z, x) = V(x) \exp [i\phi(z)], \quad (7)$$

is the solution of Eq. (1) where V is independent of z and ϕ the phase. Substituting Eq. (7) into Eq. (1) we obtain two equations for V and ϕ . The phase equation shows that ϕ should be of the form $\phi(z) = \beta z$, where β is a constant and V equation is

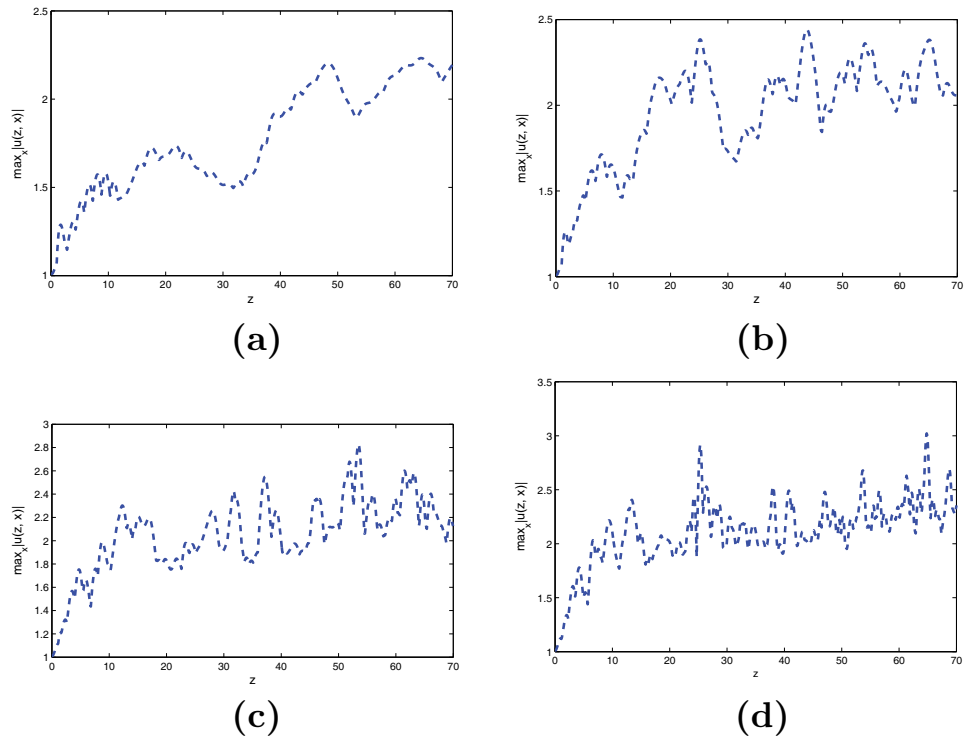


Figure 5. Representation of the maximum amplitude versus z corresponding of each panels (a), (b), (e) and (f) of Figure 4 respectively.

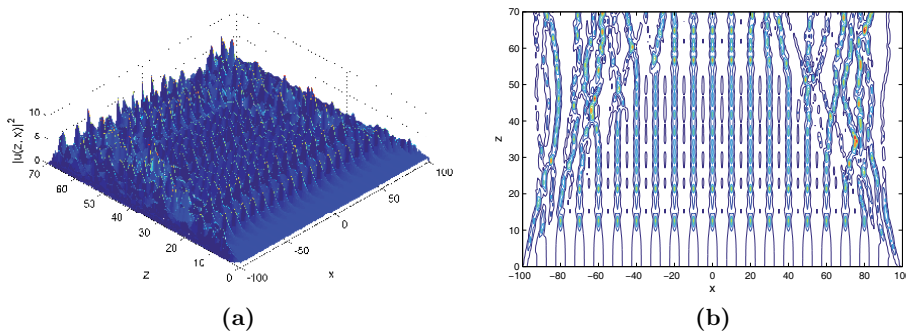


Figure 6. The influence of negative value of γ_2 on the evolution of the typical intensity profile done by numerical simulation of Eq. (1) with $p = 1/2$, $\gamma_1 = 0.1$, $\gamma_2 = -0.2$, $\gamma_3 = 0.4$ showed by panel (a), while panel (b) shows its contour plot.

$$-\beta V + pV_{xx} + \gamma_1 \frac{V^2}{x} + \gamma_2 \frac{1}{V} + \gamma_3 V^3 = 0, \quad (8)$$

For solving this equation we set $V = G^2$ and then the Eq. (8) yields

$$\frac{1}{4}(\gamma_1 - p)\dot{G}^2 + \frac{1}{2}pG\ddot{G} + \gamma_2 G - \beta G^2 + \gamma_3 G^3 = 0, \quad (9)$$

This is a nonlinear ordinary differential equation which can be solve by the auxiliary equation method.

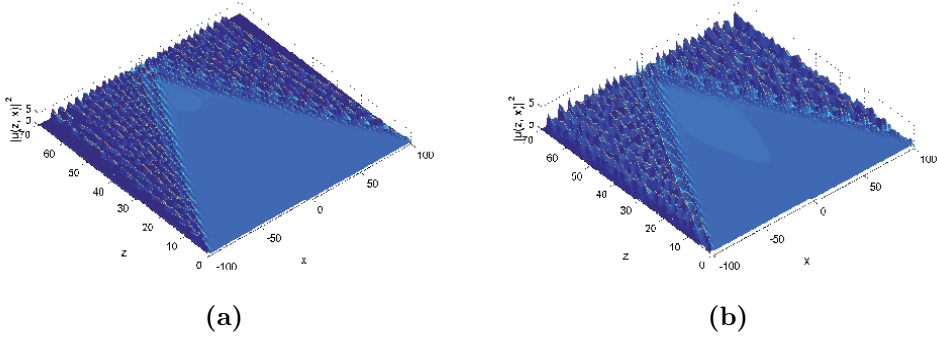


Figure 7. Influence of γ_2 and wave number K on the evolution of the typical intensity profile done by numerical simulation of Eq. (1) when $\gamma_2 = -0.03$ in (a) and $\gamma_2 = 0.03$ (b), the rest of the parameters are $\gamma_1 = 0.1$, $\gamma_3 = 0.5$ and $K = 0.01\pi$.

4.1 The auxiliary equation method

The auxiliary equation method has been defined by [9, 10] while it allows to find more and new multiple solutions for nonlinear partial differential equations. The main steps of using this method is summarized as follows.

For solving equation

$$P(u, u_t, u_x, u_{xx}, u_{xxx}, \dots) = 0, \quad (10)$$

we set $\xi = x + \omega t$ then the nonlinear partial differential equation in two independent variables (x, t) becomes a nonlinear ordinary differential equation

$$Q(u, u', u'', u''', \dots) = 0, \quad (11)$$

We seek for the solutions of Eq. (11) in the following generalized form

$$u(\xi) = \sum_{i=0}^{2M} a_i F^i(\xi), \quad (12)$$

in which a_i ($i = 0, 1, 2, \dots, 2M$) are constants to be determined and $M = 2$. The variable $F(\xi)$ should satisfy the following variable separated ordinary differential equation

$$F'^2(\xi) = aF^2(\xi) + bF^4(\xi) + cF^6(\xi), \quad (13)$$

where a, b, c are parameters to be determined. Substituting Eq. (12) into (11) by taking in account Eq. (13) and equate the coefficients of all powers of $F(\xi)$ to zero yields a set of algebraic equations for unknowns a, b, c, a_i ($i = 0, 1, \dots, 2M$) and ω . We solve the set of algebraic equations by the use of Maple and substitute the solutions obtained in this step back into (12) so as to obtain the exact traveling wave solutions for Eq. (10).

The solution of Eq. (9), balancing GG'' with G^3 gives $M = 2$. Therefore we may choose

$$G'^2 = a_0 + a_1 F(\xi) + a_2 F^2(\xi) + a_3 F^3 + a_4 F^4, \quad (14)$$

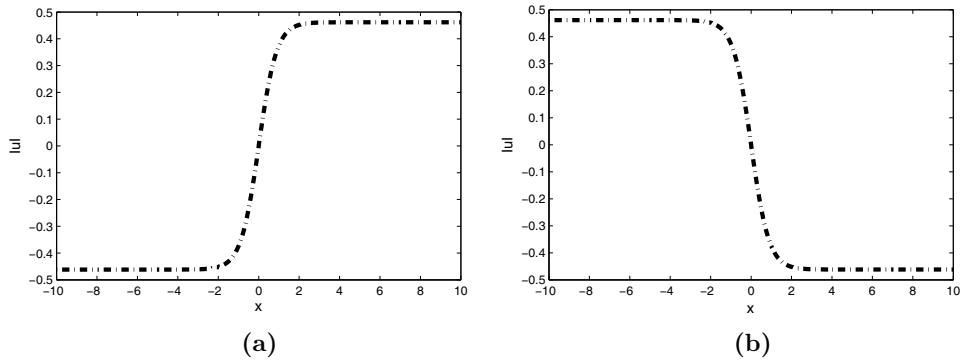


Figure 8. Kink and anti-kink representations of the analytical solutions done by Eq. (16). The following parameter values are used $p = 1/2$, $\gamma_1 = -1.1$, $\gamma_2 = 0.3$ and $\gamma_3 = 0.6$.

where a_0, a_1 and a_2, a_3, a_4 are constants to be determined. By applying the defined method we obtained the following exact kink and anti-kink solutions for the stationary NLSE (9).

$$G = \pm \sqrt{a_0} \tanh(x\sqrt{a}), \quad (15)$$

where $a_0 = \sqrt{\frac{\gamma_2}{\gamma_3} \left(1 + \frac{2p}{\gamma_1}\right)}$ and $a = -\frac{\gamma_2}{\gamma_1 a_0}$. We must have $\gamma_2/\gamma_1 < 0$ in order to ensure that the pulse width \sqrt{a} is real.

Having obtained exact solutions of the stationary NLSE Eq. (9), we will use them together to construct soliton solutions of the NLSE Eq. (1). In this case, the kink-soliton and anti-kink solutions of Eq. (1) can be written in the form

$$u(z, x) = \pm \sqrt{a_0} \tanh(x\sqrt{a}) \exp i\beta z, \quad (16)$$

where $\beta = 2a(\gamma_1 + p)$. **Figure 8** shows the representation of the analytical solution to the stationary NLSE.

5. Conclusion

In the present study a generalized nonlinear Schrödinger equation with particular nonlinearities has been introduced. The model including rational nonlinearity that arise from Malomed model and describes the propagation of nonlinear surface waves on a plasma with a sharp boundary. We explicitly investigated MI gain by means of linear stability analysis. Results reveal that the nonlinear parameters are strongly influences the dynamics of the launched plane wave. We further tested the evolutionary modulate plan wave numerically, which indicates that those parameters allow the formation of breather-like soliton in the system as well as bright soliton. We have investigated analytical kink and anti-kink soliton too.

It would be particularly worthwhile to extend this study to the generalized NLS with time and space modulated nonlinearities and potentials. This could allow more stability and more formation of the breather-like soliton as well as the Akhmediev breather [11], Peregrine rogue wave [12], and Kuznetsov-Ma breather [13, 14] and even high-order rogue waves [15]. MI gain distributions could bring different nonlinear excitation pattern dynamics.

Classification

PACS numbers: 05.45.Yv, 04.20.Jb, 42.65.Tg

Author details

Saïdou Abdoukary^{1*} and Alidou Mohamadou^{2,3}

1 Département des Sciences Fondamentales, FMIP, University of Maroua, Maroua, Cameroon

2 National Advanced School of Engineering of Maroua, Maroua, Cameroon

3 The Abdus Salam International Centre for Theoretical Physics, Trieste, Italy

*Address all correspondence to: elsaidais@yahoo.fr

IntechOpen

© 2021 The Author(s). Licensee IntechOpen. This chapter is distributed under the terms of the Creative Commons Attribution License (<http://creativecommons.org/licenses/by/3.0>), which permits unrestricted use, distribution, and reproduction in any medium, provided the original work is properly cited. 

References

- [1] G. P. Agrawal, *Nonlinear Fiber Optics* (Academic, California, 2001).
- [2] B. A. Malomed, L. Stenflo, *J Phys A: Math Gen* **24** L1149 (1991).
- [3] E. Yomba, T. C. Kofane, *Chaos, Solitons and Fractals* **17** 847 (2003).
- [4] A. Mohamadou et al. *Chaos, Solitons and Fractals* **27** 914–925 (2006).
- [5] V. E. Zakharov and A. B. Shabat, *Zh. Eksp. Teor. Fiz.* **61**, 118 (1971) [*Sov. Phys. JETP* **34**, 62 (1972)].
- [6] L.Q. English, M. Sato, A.J. Sievers, *Phys. Rev. B* **67**, 024403 (2003).
- [7] D. Hennig, G. P. Tsironis, *Physics Reports* **307** (1999) 333-432.
- [8] M. J. Ablowitz, P. A. Clarkson, *Solitons, Nonlinear Evolution Equations and Inverse Scattering*, Cambridge Univ. Press, New York, 1991.
- [9] Sirendareji, *Phys. Lett. A* **356** (2006) 124.
- [10] S. Abdoukary et al., *Appl. Math. Comput.* **233** (2014) 109-115.
- [11] N. Akhmediev and V. I. Korneeov, *Theor. Math. Phys.* **69**, 1089 (1986).
- [12] D. H. Peregrine, *J. Aust. Math. Soc. Ser. B* **25**, **16** (1983).
- [13] E. A. Kuznetsov, *Sov. Phys. Dokl.* **22**,507(1977).
- [14] Y. C. Ma, *Stud. Appl. Math.* **60**, **43** (1979).
- [15] B. L. Guo, L. M. Ling, and Q. P. Liu, *Phys. Rev. E* **85**, 026607 (2012).

A Comparison of the Undetermined Coefficient Method and the Adomian Decomposition Method for the Solutions of the Sasa-Satsuma Equation

Mir Asma

Abstract

This chapter will talk about the mathematical as well as numerical aspects of the Sasa-Satsuma equation that is the extended nontrivial version of nonlinear Schrödinger's equation. The exact solution will be found out by the undetermined coefficient method. After that, the Adomian decomposition method is secure numerical simulations of computed analytical solutions. The error plots are given to see the accuracy of the results.

Keywords: Sasa-Satsuma equation, solitons, Adomian decomposition method, undetermined coefficient method, telecommunication

1. Introduction

Solitons can be illustrated as special wave packets that are formed as a result of elegant balance among the fiber nonlinearity and dispersion. They have the ability to travel undistorted along trans-continental and trans-oceanic distances. Solitons are narrow pulses with immense peak power and exceptional properties. Mostly, pulses go through by spreading because of group velocity dispersion while propagating through optical fibers. Actually, solitons have the advantage of nonlinear effects that helps to overcome the broadening of pulse with the group velocity dispersion. When the corresponding dispersive effects and nonlinear effects are controlled and get the appropriate shape of the pulse. When these pulses balance compression and broadening and there is no change in the shape of the pulse or there are periodic changes in the shape of the pulse, this phenomenon is called soliton. Solitons are very advantageous for optical communication that they can overcome chromatic dispersion completely. In most Dense Wavelength Division Multiplexing (DWDM) systems, fiber losses are compensated periodically by using fiber amplifiers spaced 60-80 Km apart. Attenuation and higher powers are the indirect properties of solitons that are reimbursed by the optical amplifiers. When solitons and amplifiers are used together, they can assure the very high-bit rate, for the repeater-less data transmission for long distances. This combination can be responsible for the data transmission at a bit rate of 80 Gb/s for 10,000 km and it

was testified in the laboratory. Hasegawa and Tappert in 1973, have discussed the possibilities of propagation of solitons through optical fibers and showed their remarkable stability by numerical computation [1]. Seven years later, Mollenauer, Stolon, and Gordon succeeded in observing soliton propagation experimentally [2].

In this chapter, Sasa-Satsuma equation (SSE) is going to be studied for the sake of optical solitons. SSE is the expansion of nonlinear Schrödinger equation (NLSE). In 1991, Narimasa Sasa and Junkichi Satsuma reported significant results that have a great impact in the field of nonlinear optics and the telecommunication industry [3]. Initially, Sasa and Satsuma displayed a nonlinear complex wave equation that was composed with the aid of inverse scattering transformation [4].

The Sasa-Satsuma equation with the linear temporal evolution is [5]:

$$iq_t + a(|q|^n q)_{xx} + b|q|^2 q + i \left[\beta_3 q_{xxx} + \sigma \left(|q|^2 \right)_x q + \theta |q|^2 q_x \right] = 0 \quad (1)$$

In (1), $q(x, t)$ is the dependent variable, x and t are independent variables and the subscripts serve as partial derivatives. The first term in (1) known as time evolution term, while a is the coefficient of nonlinear chromatic dispersion, b gives the self-phase modulation with Kerr nonlinearity, β_3 is the coefficient of third-order dispersion, σ and θ are the coefficients of nonlinear dispersion. Finally, n gives the nonlinearity parameter of chromatic dispersion and $n > 0$.

2. Method of undetermined coefficients

Method of undetermined coefficients gives the spectrum of soliton solutions. In order to seek the soliton solution of SSE to (1) [6–10]:

$$q(x, t) = P(x, t)e^{i\phi(x, t)} \quad (2)$$

Where $P(x, t)$ is the amplitude segment of the soliton. The phase component is

$$\phi(x, t) = -\kappa x + \omega t + \theta_0 \quad (3)$$

Here, κ , ω and θ_0 are the soliton frequency, wave number and the phase constant respectively. By substituting (2) into (1) and equating real and imaginary parts leads to

$$\begin{aligned} & -a\kappa^2(1+n)^2P^{n+1} + a \left(\frac{\partial}{\partial x} P(x, t) \right)^2 n(1+n)P^{n-1} + (a(1+n)(P(x, t))^n + 3\beta_3\kappa) \frac{\partial^2}{\partial x^2} P(x, t) \\ & P(x, t) \left((-2\sigma - \theta)\kappa - b \right) (P(x, t))^2 + \beta_3\kappa^3 + \omega = 0, \end{aligned} \quad (4)$$

and

$$\begin{aligned} & \left(\frac{\partial^3}{\partial x^3} P(x, t) \right) \beta_3 + \left(-2a\kappa(1+n)^2(P(x, t))^n + (2\sigma + \theta)(P(x, t))^2 - 3\beta_3\kappa^2 \right) \frac{\partial}{\partial x} P(x, t) \\ & + \frac{\partial}{\partial t} P(x, t) = 0. \end{aligned} \quad (5)$$

2.1 Solution of bright soliton

For the solution of bright soliton, the starting hypothesis is [7–10]

$$P(x, t) = \frac{A}{(D + \cosh \tau)^p}, \quad (6)$$

Where

$$\tau = B(x - vt) \quad (7)$$

A is known as amplitude, B is the inverse width of the soliton, and D is the parameter that relates to A and B . The p is an unknown parameter that can be found with the aid of balancing principle. By putting (6) into (4) gives:

$$\begin{aligned} & \frac{A^3(\kappa\theta + b)}{E^{3p}} + \frac{A(a(np^2(n+2)B^2 - \kappa^2) + 3B^2\beta_3\kappa p^2 - \beta_3\kappa^3 - \omega) + AB^2p^2a}{E^p} \\ & + \frac{((n+1)(1+(n+1)p)a + 3\beta_3\kappa(p+1))(D+1)(D-1)ApB^2}{E^{p+2}} \\ & - 2 \frac{DAp((n+1)(1/2 + (n+1)p)a + 3\kappa(p+1/2)\beta_3)B^2}{E^{p+1}} = 0. \end{aligned} \quad (8)$$

where $E = D + (\cosh(\tau))$.

With the balancing principle, the exponents of $3p$ and $p + 2$ gives $p = 1$. By setting the coefficients of linearly independent function in (8) to zero that gives;

$$\omega = ((n+1)^2a + 3\beta_3\kappa)B^2 - \beta_3\kappa^3 - a\kappa^2 \quad (9)$$

$$A = \pm \frac{\sqrt{(\kappa\theta + b)(D-1)(D+1)((n^2 + 3n + 2)a + 6\beta_3\kappa)B}}{\kappa\theta + b}, \quad (10)$$

$$\kappa\theta + b > 0, \quad (11)$$

$$D = \frac{\sqrt{((n^2 + 3n + 2)a + 6\beta_3\kappa)(-B^2(n+2)(n+1)a - 6B^2\beta_3\kappa + (\kappa\theta + b)A^2)}}{((n^2 + 3n + 2)a + 6\beta_3\kappa)B}, \quad (12)$$

$$((n^2 + 3n + 2)a + 6\beta_3\kappa)B > 0. \quad (13)$$

The solution of bright soliton of (1) is

$$q(x, t) = \frac{A}{D + \cosh [B(x - vt)]} e^{i(-kx + \omega t + \theta_0)}, \quad (14)$$

Figure 1 represents the bright optical soliton of SSE. The soliton solution appears with their corresponding constraints conditions.

2.2 Solution of dark solitons

For the solution of dark soliton, the assumption is [7–10]

$$P(x, t) = (A + B \tanh \tau)^p, \quad (15)$$

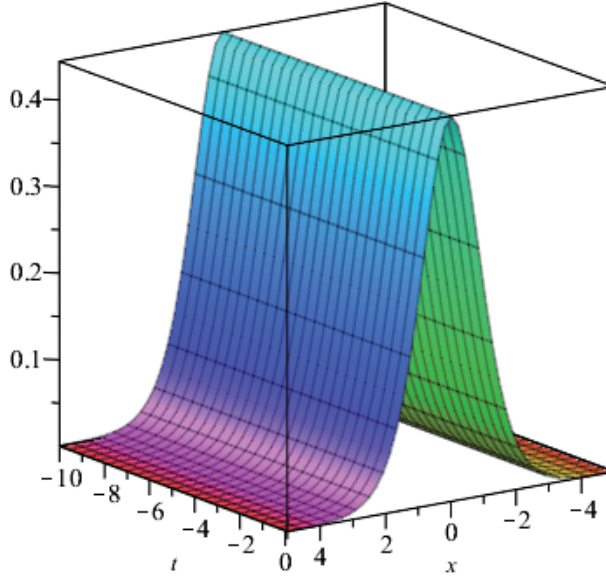


Figure 1.
Bright soliton.

where A and B are free parameters and

$$\tau = \mu(x - vt), \quad (16)$$

Here, p can be found with the balancing principle. By substituting (15) into (4), the real part gives:

$$\begin{aligned} & \mu^2(A(A+B) - B(A+B))^4(a(-1 + (n+1)p)(n+1) + 3\beta_3k(p-1))p E^{p-2} \\ & - 6(A-B)A(a(-1/2 + (n+1)p)(n+1) + 2\beta_3k(p-1/2))(A+B)\mu^2p E^{p-1} \\ & + ((1+2(n+1)p)a(n+1) + 3\beta_3k(2p+1))A\mu^2p E^{p+1} \\ & + ((1+(n+1)p)a(n+1) + 3\beta_3k(1+p))\mu^2p E^{p+2} + B^2(k\theta + b)E^{3p} \\ & + 18 \left((A^2 - 1/3B^2)p^2 \left(1/3(n+1)^2a + \beta_3k \right) \mu^2 - 1/18B^2(\beta_3k^3 + ak^2 + w) \right) E^p = 0 \end{aligned} \quad (17)$$

where $E = (A + B \tanh(\tau))$

The value of p is similar to bright soliton and gives the value of coefficients of linearly independent function as zero that yields to the following relations of soliton parameters.

$$A = \pm B = \pm \frac{\sqrt{(k\theta + b)(an^2 + 3an + 6\beta_3k + 2a)}}{k\theta + b}, \quad (18)$$

$$(k\theta + b) > 0, \quad (19)$$

$$(an^2 + 3an + 6\beta_3k + 2) > 0, \quad (20)$$

$$\mu = \frac{\sqrt{(k\theta + b)(an^2 + 3an + 6\beta_3k + 2a)}}{an^2 + 3an + 6\beta_3k + 2} \quad (21)$$

$$\omega = -ak^2 + 4an^2 - k^3 + 8an + 4a + 12k \quad (22)$$

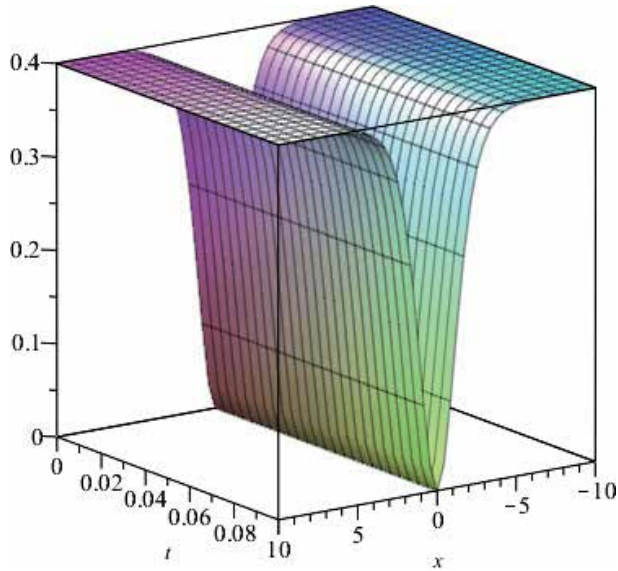


Figure 2.
 Dark soliton.

Hence, the solution of the dark soliton is given as:

$$q(x, t) = A \{1 \pm \tanh [\mu(x - vt)]\} e^{i(-\kappa x + \omega t + \theta_0)}, \quad (23)$$

Figure 2 represents the dark soliton of SSE. The soliton solution appears with their corresponding constraints conditions.

2.3 Solution of singular solitons

For the solution of singular soliton, the starting assumption is [7–10];

$$P(x, t) = \frac{A}{(D + \sinh \tau)^p}, \quad (24)$$

Here, A , B , and D are the free parameters with the unknown p . By putting (25) into (4) gives;

$$\begin{aligned} & \frac{((n+1)(1+(n+1)p)a + 3\beta_3(p+1)k)Ch^2ApB^2}{E^{p+2}} - \frac{AB^2Shp(an + 3\beta_3k + a)}{E^{p+1}} \\ & + \frac{A^3(k\theta + b)}{E^{3p}} - \frac{A(\beta_3k^3 + ak^2 + w)}{E^p} = 0, \end{aligned} \quad (25)$$

where $E = (D + \sinh(\tau))$.

By setting $3p = p + 2$, we get $p = 1$ and the free parameters are related as

$$A = \pm \sqrt{\frac{an^2 + 3an + 6\beta_3k + 2a}{k\theta + b}} B, \quad (26)$$

$$k\theta + b > 0, \quad (27)$$

$$\omega = (a(n+1)^2 + 3\beta_3 k)B^2 - \beta_3 k^3 - ak^2 \quad (28)$$

Hence the solution of singular soliton of (1) is as:

$$q(x, t) = \frac{A}{D + \sinh [B(x - vt)]} e^{i(-kx + \omega t + \theta_0)}, \quad (29)$$

for designated parameters.

2.4 Solution of W-shaped solitons

For the solution of w-shaped soliton, the starting assumption is [7–10];

$$P(x, t) = (\beta + \rho \operatorname{sech}(\tau))^p, \quad (30)$$

$$\tau = \mu(x - vt), \quad (31)$$

Substituting (30) into (4) gives

$$\begin{aligned} & 4\mu^2 p \beta (a(n+1)(1+2(n+1)p) + 3\beta_3 k(2p+1))E^{p+1} \\ & - p(\beta + \rho)\mu^2((-1+(n+1)p)a(n+1) + 3\beta_3 k(p-1))\beta^2(\rho - \beta)E^{p-2} \\ & - 2p((-1/2+(n+1)p)a(n+1) + 3\beta_3 k(p-1/2))(-2\beta^2 + \rho^2)\mu^2 \beta E^{p-1} \\ & + \rho^2(k\theta + b)E^{3p} + (p^2((n+1)^2 a + 3\beta_3 k)\mu^2 - \beta_3 k^3 - ak^2 - w)\rho^2 \\ & - 6\mu^2 \beta^2 p^2 ((n+1)^2 a + 3\beta_3 k)E^p \\ & - ((1+(n+1)p)a(n+1) + 3\beta_3 k(1+p))p\mu^2 E^{p+2} = 0, \end{aligned} \quad (32)$$

where $E = (\beta + \rho \operatorname{sech}(\tau))$

By the aid of balancing principle, the value of $p = 1$ that gives parameters as;

$$\beta = \pm 1/2\sqrt{2}\rho, \quad (33)$$

$$\mu = \pm \sqrt{\frac{k\theta + b}{an^2 + 3an + 6k\beta_3 + 2a}}\rho, \quad (34)$$

$$\rho = \pm \sqrt{\frac{an^2 + 3an + 6k\beta_3 + 2a}{k\theta + b}}, \quad (35)$$

and

$$w = -\frac{6\beta^2 \mu^2 an^2 - \mu^2 an^2 \rho^2 + 12an\mu^2 \beta^2 - 2a\mu^2 n\rho^2 + 18\beta^2 \mu^2 k\beta_3 + \beta_3 k^3 \rho^2 - 3\beta_3 k\mu^2 \rho^2 + 6\mu^2 a\beta^2 + ak^2 \rho^2 - \mu^2 a\rho^2}{\rho^2}. \quad (36)$$

Therefore, W-shaped soliton solution is given by:

$$q(x, t) = (\beta + \rho \operatorname{sech}(\tau))e^{i(-kx + \omega t + \theta_0)}, \quad (37)$$

Figure 3 represents the W-shaped optical soliton of SSE. The soliton solution appears with their corresponding constraints conditions.

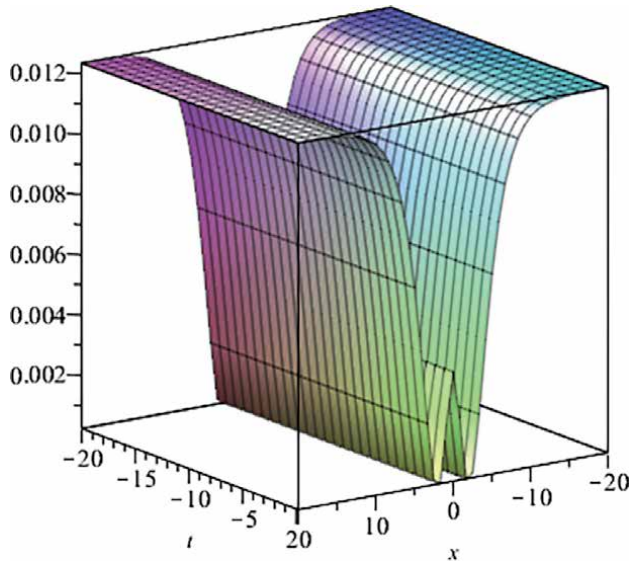


Figure 3.
W-shaped soliton.

3. Numerical investigation of soliton solutions

In this section, the Adomian decomposition method will be implemented. ADM has gained very much popularity in recent times in applied mathematics. This method is very robust, efficient, and effective to grasp a broad range of linear, nonlinear, ordinary or partial differential equations and linear or nonlinear integral equations. This method gives the fast convergence of the solution and has many symbolic advantages.

Geoge Adomian has introduced and developed this method and very well treated it in the literature. A very appreciable amount of work has been explored for the wide range of linear, nonlinear, ordinary differential equations, partial differential equations as well as integral equation [11].

3.1 Recapitulation of Adomian decomposition method

In this section, ADM is used to handle SSE numerically that show the broad spectrum analytically results. This method tackles the problem in a direct way that shows the accuracy of the exact solution of soliton solutions.

$$q(x, t) = q_1(x, t) + iq_2(x, t) \tag{38}$$

By substituting (38) into (4) and breaking it down into real and imaginary parts, respectively

$$\begin{aligned} & -u_{2t} + a(u_1^2 + u_2^2)_{xx} u_{1xx} + u_1^3 + u_1 u_2^2 - \beta_3 u_{2xxx} - \sigma(u_{1x}^2 u_2 + u_{2x}^2 u_1) \\ & -\theta(u_1^2 u_{2x}^2 + u_2^2 u_{1x}^2) = 0, \end{aligned} \tag{39}$$

$$\begin{aligned} & u_{1t} + a(u_1^2 + u_2^2)_{xx} u_{2xx} + u_2^3 + u_1^2 u_2 + \beta_3 u_{1xxx} + \sigma(u_{1x}^2 u_1 + u_{2x}^2 u_1) \\ & +\theta(u_1^2 u_{1x}^2 + u_2^2 u_{1x}^2) = 0, \end{aligned} \tag{40}$$

The solution is decomposed into finite sums of components by decomposition method that is defined as;

$$u_i(z, t) = \sum_{n=0}^{\infty} u_{i,n}(x, t), \quad (41)$$

Here, $i \in \{1, 2\}$. The components $u_{i,n}$, $n \geq 0$ and $i = 1, 2$ will be found out recurrently. By using an operator form $L_t = \frac{\partial}{\partial t}$, Eqs. (39) and (40) becomes

$$-L_t u_2(x, t) + N_2(u_1, u_2) = 0 \quad (42)$$

$$L_t u_1(x, t) + N_1(u_1, u_2) = 0, \quad (43)$$

Where

$$N_2(u_1, u_2) = a(u_1^2 + u_2^2)_{xx} u_{1xx} + u_1^3 + u_1 u_2^2 - \beta_3 u_{2xxx} - \sigma(u_{1x}^2 u_2 + u_{2x}^2 u_1) - \theta(u_1^2 u_{2x}^2 + u_2^2 u_{2x}) = 0, \quad (44)$$

$$N_1(u_1, u_2) = a(u_1^2 + u_2^2)_{xx} u_{2xx} + u_2^3 + u_1^2 u_2 + \beta_3 u_{1xxx} + \sigma(u_{1x}^2 u_1 + u_{2x}^2 u_1) + \theta(u_1^2 u_{1x}^2 + u_2^2 u_{1x}) = 0, \quad (45)$$

By applying an inverse operator $L_t^{-1} = \int_0^t (\cdot) dt$ to Eqs. (42) and (43), we get

$$u_1(x, t) = u_1(x, 0) - L_t^{-1} N_2(u_1(x, t), u_2(x, t)) \quad (46)$$

$$u_2(x, t) = u_2(x, 0) + L_t^{-1} N_1(u_1(x, t), u_2(x, t)), \quad (47)$$

where $u_1(x, 0) = \text{Re}(u(x, 0))$ and $u_2(z, 0) = \text{Im}(q(z, 0))$.

$$u_{1,0}(x, t) = u_1(x, 0)$$

$$u_{2,0}(x, t) = u_2(x, 0)$$

$$u_{1,k+1}(x, t) = -L_t^{-1}(N_{2,k}) \quad (48)$$

$$u_{2,k+1}(x, t) = L_t^{-1}(N_{1,k}),$$

$$A_n = \frac{1}{n!} \frac{d^n}{d\eta^n} N_j \left(\sum_{n=0}^{\infty} \eta^n u_{1,n}(x, t), \sum_{n=0}^{\infty} \eta^n u_{2,n}(x, t) \right). \quad (49)$$

4. Numerical simulations

4.1 Bright solitons

To depict the ability, reliability and the accuracy of the ADM for Sasa-Satsuma equation for bright solitons where, $a = \frac{1}{10}$, $b = \frac{4}{100}$, $\beta_3 = \frac{1}{100}$, $\sigma = \frac{1}{10}$, $\theta = -\frac{173}{200}$, $\theta_0 = 0$, $\omega = \frac{311}{800}$, and $\kappa = \frac{1}{2}$. The results and the profile of bright soliton shown in Table below. **Figures 4–14**, present the plots of exact and approximate solution with their error plots respectively by varying the values of t and x .

t	$ q_e - q_a $
0	$8. \times 10^{-17}$
0.1	$8. \times 10^{-17}$
0.2	8×10^{-17}
0.3	$8. \times 10^{-17}$
1	0.10
2	0.2
3	0.2

x	$ q_e - q_a $
0	$9. \times 10^{-8}$
0.1	$9. \times 10^{-8}$
0.2	$7. \times 10^{-8}$
0.3	$5. \times 10^{-8}$

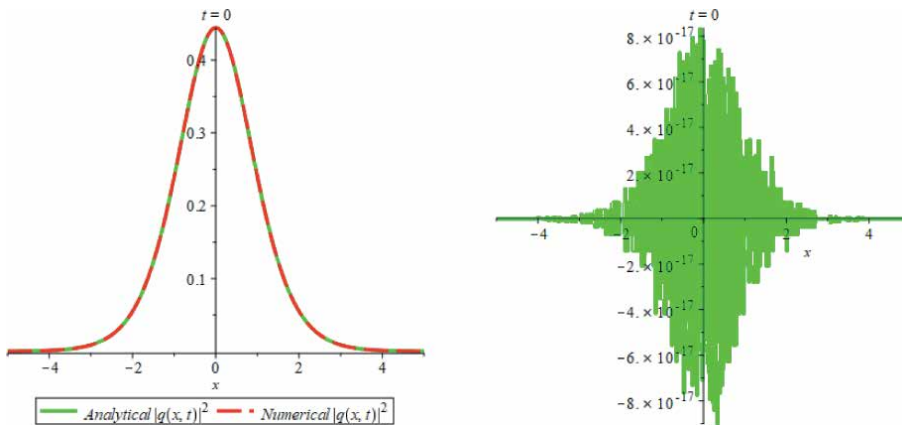


Figure 4. The graph of analytical and numerical solution with absolute error at $t = 0$ and $a = \frac{1}{10^2}$, $b = \frac{4}{100}$, $\beta_3 = \frac{1}{100^2}$, $\sigma = \frac{1}{10^2}$, $\theta = -\frac{173}{200^2}$, $\theta_0 = 0$, $\omega = \frac{311}{800}$, $\kappa = \frac{1}{2}$.

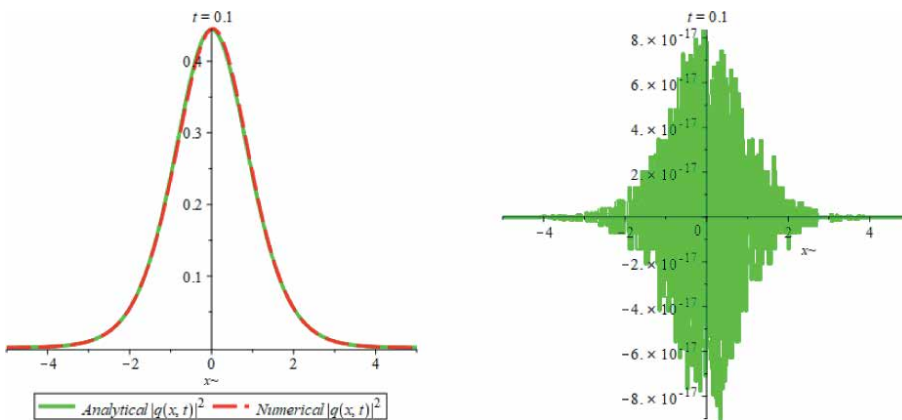


Figure 5. The graph of analytical and numerical solution with absolute error at $t = 0.1$ and $a = \frac{1}{10^2}$, $b = \frac{4}{100}$, $\beta_3 = \frac{1}{100^2}$, $\sigma = \frac{1}{10^2}$, $\theta = -\frac{173}{200^2}$, $\theta_0 = 0$, $\omega = \frac{311}{800}$, $\kappa = \frac{1}{2}$.

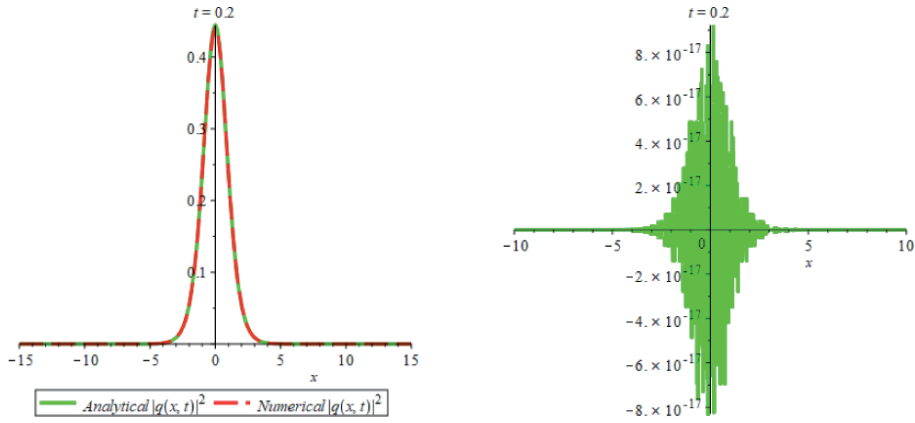


Figure 6. The graph of analytical and numerical solution with absolute error at $t = 0.2$ and $a = \frac{1}{10}$, $b = \frac{4}{100}$, $\beta_3 = \frac{1}{100}$, $\sigma = \frac{1}{10}$, $\theta = -\frac{173}{200}$, $\theta_0 = 0$, $\omega = \frac{311}{800}$, $\kappa = \frac{1}{2}$.

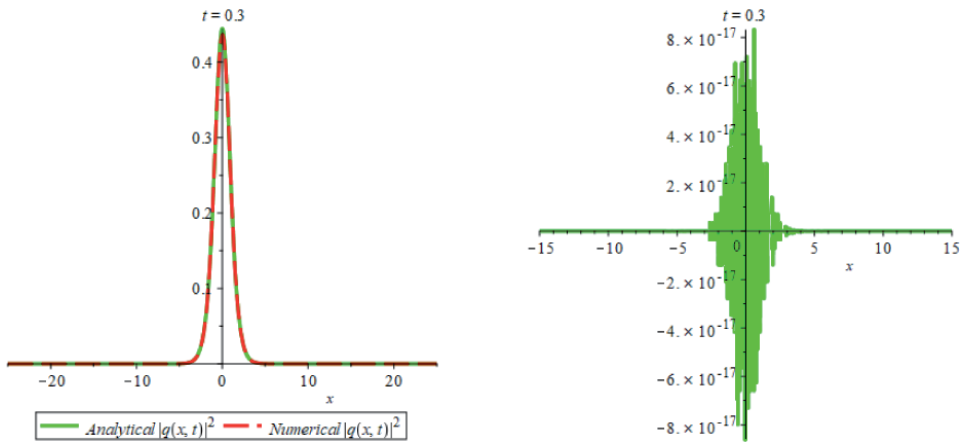


Figure 7. The graph of analytical and numerical solution with absolute error at $t = 0.3$ and $a = \frac{1}{10}$, $b = \frac{4}{100}$, $\beta_3 = \frac{1}{100}$, $\sigma = \frac{1}{10}$, $\theta = -\frac{173}{200}$, $\theta_0 = 0$, $\omega = \frac{311}{800}$, $\kappa = \frac{1}{2}$.

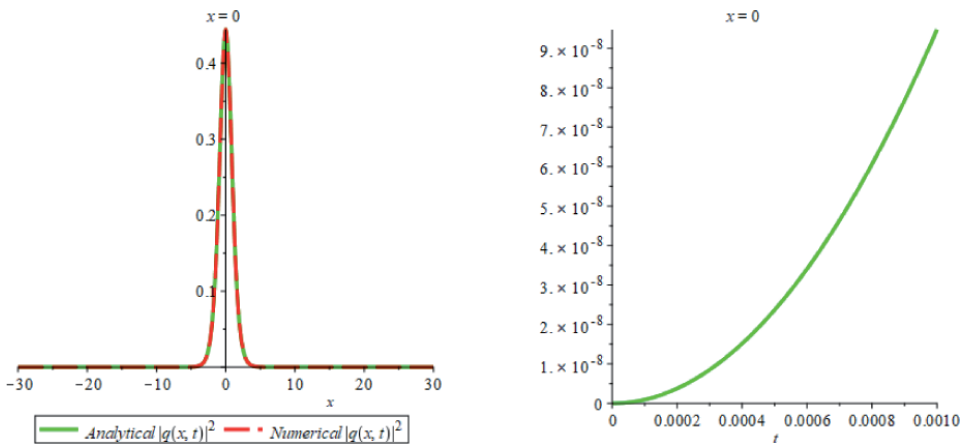


Figure 8. The graph of analytical and numerical solution with absolute error at $x = 0$ and $a = \frac{1}{10}$, $b = \frac{4}{100}$, $\beta_3 = \frac{1}{100}$, $\sigma = \frac{1}{10}$, $\theta = -\frac{173}{200}$, $\theta_0 = 0$, $\omega = \frac{311}{800}$, $\kappa = \frac{1}{2}$.

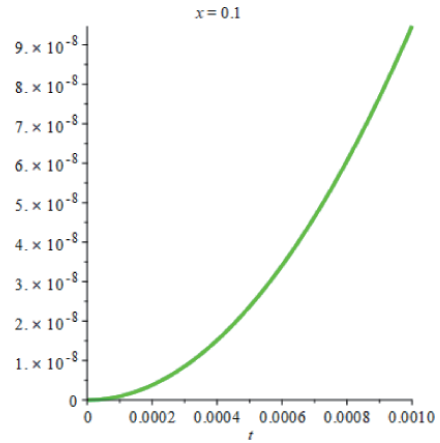
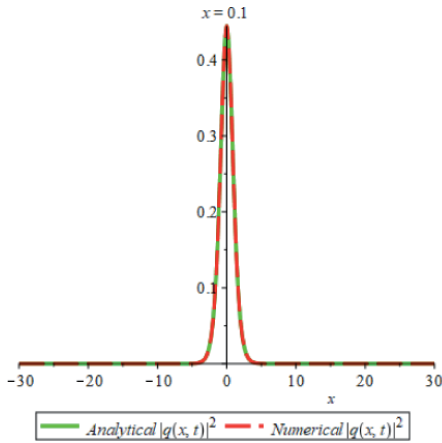


Figure 9.
 The graph of analytical and numerical solution with absolute error at $x = 0.1$ and $a = \frac{1}{10^9}$, $b = \frac{4}{100^9}$, $\beta_3 = \frac{1}{100^9}$
 $\sigma = \frac{1}{10^9}$, $\theta = -\frac{173}{200^9}$, $\theta_0 = 0$, $\omega = \frac{311}{800^9}$, $\kappa = \frac{1}{2}$.

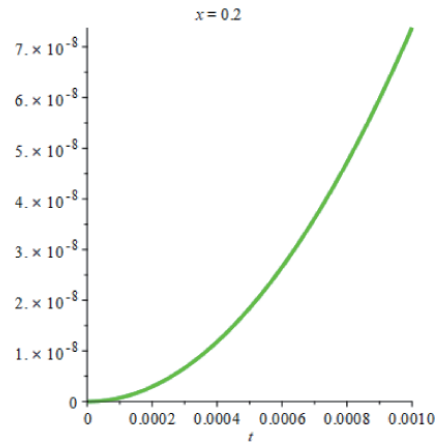
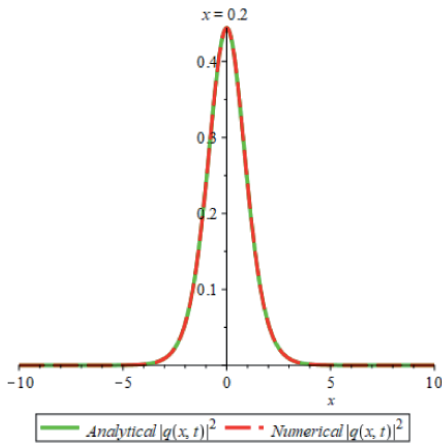


Figure 10.
 The graph of analytical and numerical solution with absolute error at $x = 0.2$ and $a = \frac{1}{10^9}$, $b = \frac{4}{100^9}$, $\beta_3 = \frac{1}{100^9}$
 $\sigma = \frac{1}{10^9}$, $\theta = -\frac{173}{200^9}$, $\theta_0 = 0$, $\omega = \frac{311}{800^9}$, $\kappa = \frac{1}{2}$.

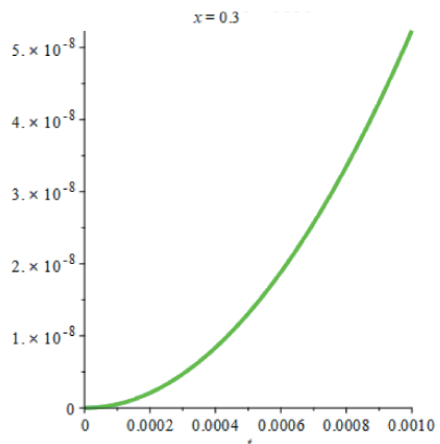
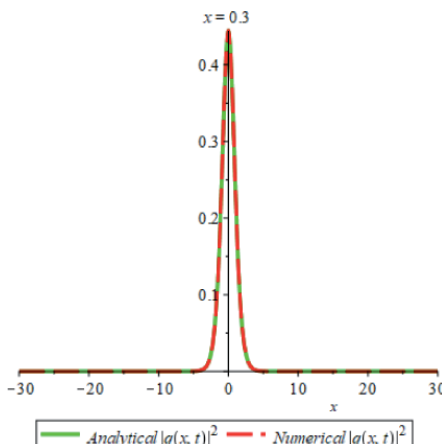


Figure 11.
 The graph of analytical and numerical solution with absolute error at $x = 0.3$ and $a = \frac{1}{10^9}$, $b = \frac{4}{100^9}$, $\beta_3 = \frac{1}{100^9}$
 $\sigma = \frac{1}{10^9}$, $\theta = -\frac{173}{200^9}$, $\theta_0 = 0$, $\omega = \frac{311}{800^9}$, $\kappa = \frac{1}{2}$.

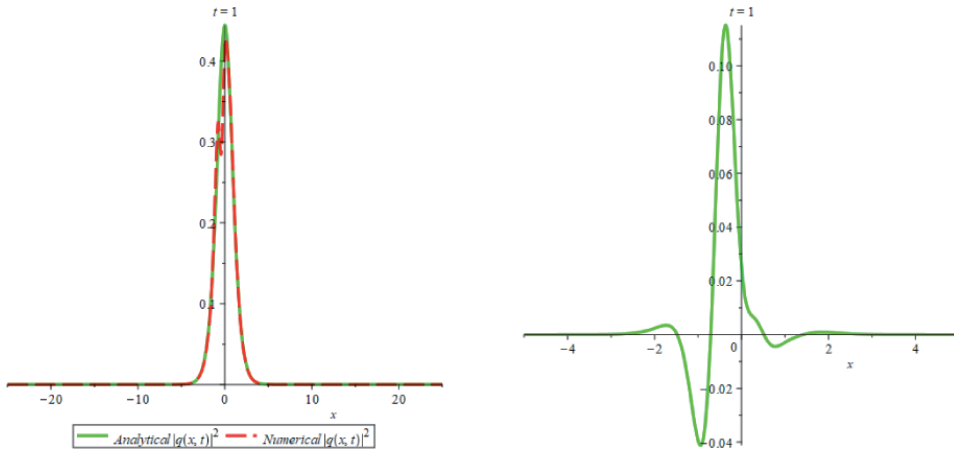


Figure 12.

The graph of analytical and numerical solution with absolute error at $t = 1$ and $a = \frac{1}{10^2}$, $b = \frac{4}{100}$, $\beta_3 = \frac{1}{100^2}$, $\sigma = \frac{1}{10^2}$, $\theta = -\frac{173}{200}$, $\theta_0 = 0$, $\omega = \frac{311}{800}$, $\kappa = \frac{1}{2}$.

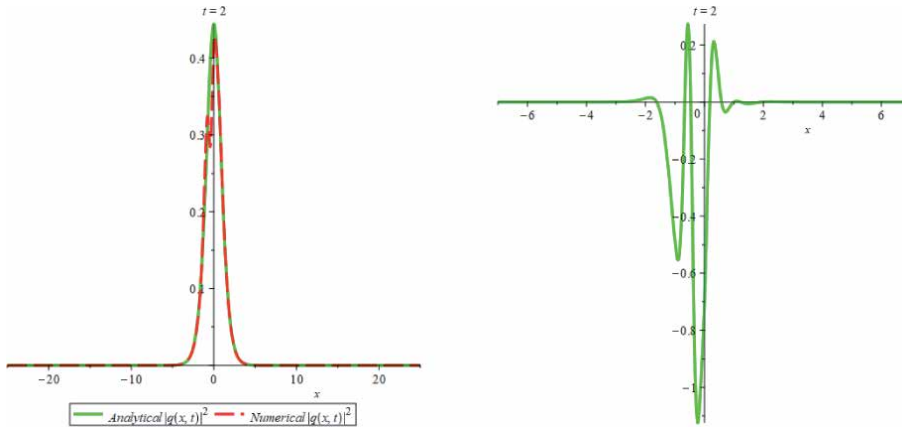


Figure 13.

The graph of analytical and numerical solution with absolute error at $t = 2$ and $a = \frac{1}{10^2}$, $b = \frac{4}{100}$, $\beta_3 = \frac{1}{100^2}$, $\sigma = \frac{1}{10^2}$, $\theta = -\frac{173}{200}$, $\theta_0 = 0$, $\omega = \frac{311}{800}$, $\kappa = \frac{1}{2}$.

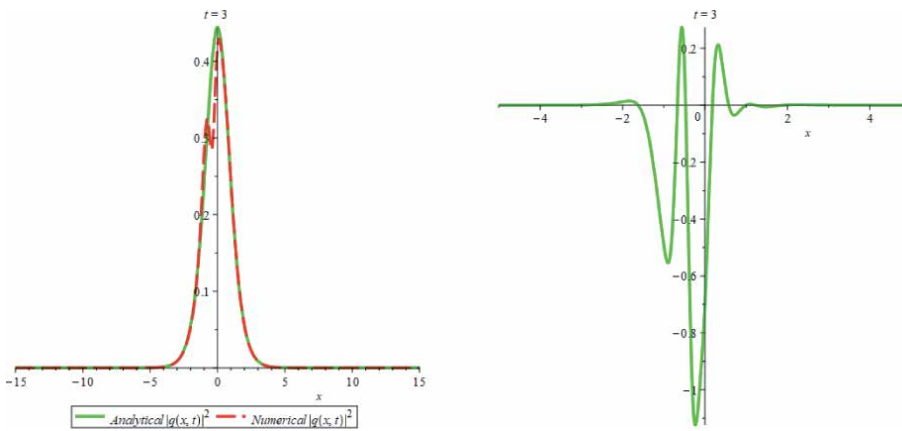


Figure 14.

The graph of analytical and numerical solution with absolute error at $t = 3$ and $a = \frac{1}{10^2}$, $b = \frac{4}{100}$, $\beta_3 = \frac{1}{100^2}$, $\sigma = \frac{1}{10^2}$, $\theta = -\frac{173}{200}$, $\theta_0 = 0$, $\omega = \frac{311}{800}$, $\kappa = \frac{1}{2}$.

4.2 Dark solitons

In order to depict ADM, we acknowledge the Sasa-Satsuma equation in investigated in detail where, $a = \frac{1}{10}$, $b = \frac{1}{2}$, $\beta_3 = \frac{1}{5}$, $\sigma = \frac{1}{10}$, $\theta = -\frac{173}{200}$, $\theta_0 = 0$, $\omega = \frac{311}{800}$, and $\kappa = \frac{1}{2}$. The results and the profile of dark soliton shown in Table below. **Figures 15–22**, present the plots of exact and approximate solution with their error plots respectively by varying the values of t and x .

t	$ q_e - q_a $
0	1.5×10^{-8}
0.1	$1. \times 10^{-16}$
0.2	$1. \times 10^{-16}$
0.3	$1. \times 10^{-16}$
1	$1. \times 10^{-16}$
2	$8. \times 10^{-17}$
4	$6. \times 10^{-17}$
x	$ q_e - q_a $
0.1	$4. \times 10^{-19}$
0.2	1.5×10^{-18}
0.3	$3. \times 10^{-18}$

4.3 W shaped solitons

In order to depict ADM, we acknowledge the Sasa-Satsuma equation in investigated in detail where, $a = \frac{4}{100}$, $b = \frac{1}{2}$, $\beta_3 = \frac{4}{100}$, $\sigma = \frac{1}{10}$, $\rho = \frac{\sqrt{3}}{10}$, $\theta = -\frac{173}{200}$, $\theta_0 = 0$, $\omega = \frac{311}{800}$,

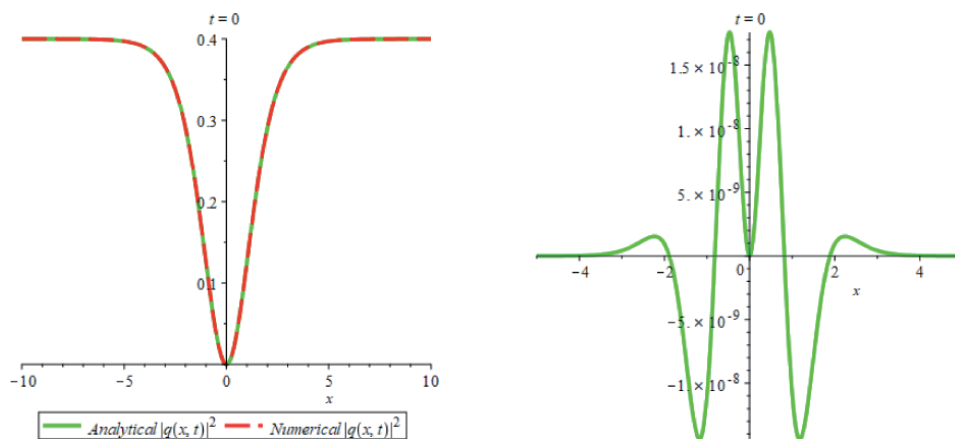


Figure 15.
 The graph of analytical and numerical solution with absolute error at $t = 0$ and $a = \frac{1}{10}$, $b = \frac{1}{2}$, $\beta_3 = \frac{1}{5}$, $\sigma = \frac{1}{10}$, $\theta = -\frac{173}{200}$, $\theta_0 = 0$, $\omega = \frac{311}{800}$, $\kappa = \frac{1}{2}$.

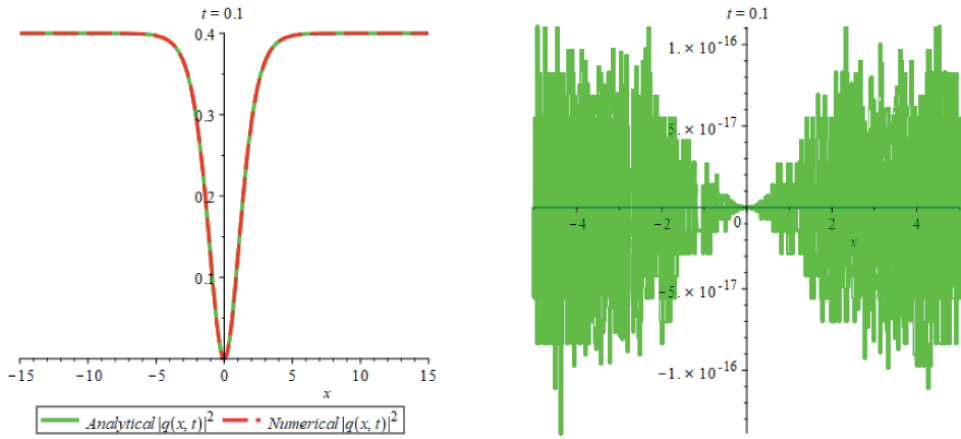


Figure 16.
 The graph of analytical and numerical solution with absolute error at $t = 0.1$ and $a = \frac{1}{10}$, $b = \frac{1}{2}$, $\beta_3 = \frac{1}{5}$, $\sigma = \frac{1}{10}$, $\theta = -\frac{173}{200}$, $\theta_0 = 0$, $\omega = \frac{311}{800}$, $\kappa = \frac{1}{2}$.

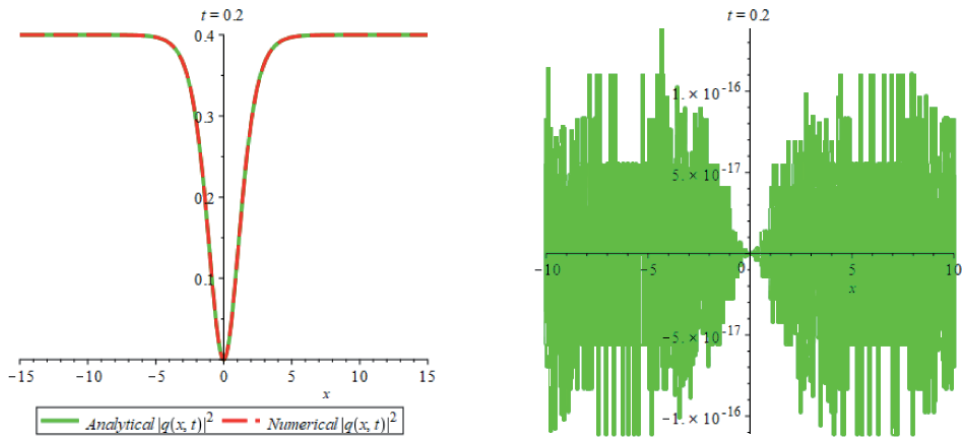


Figure 17.
 The graph of analytical and numerical solution with absolute error at $t = 0.2$ and $a = \frac{1}{10}$, $b = \frac{1}{2}$, $\beta_3 = \frac{1}{5}$, $\sigma = \frac{1}{10}$, $\theta = -\frac{173}{200}$, $\theta_0 = 0$, $\omega = \frac{311}{800}$, $\kappa = \frac{1}{2}$.

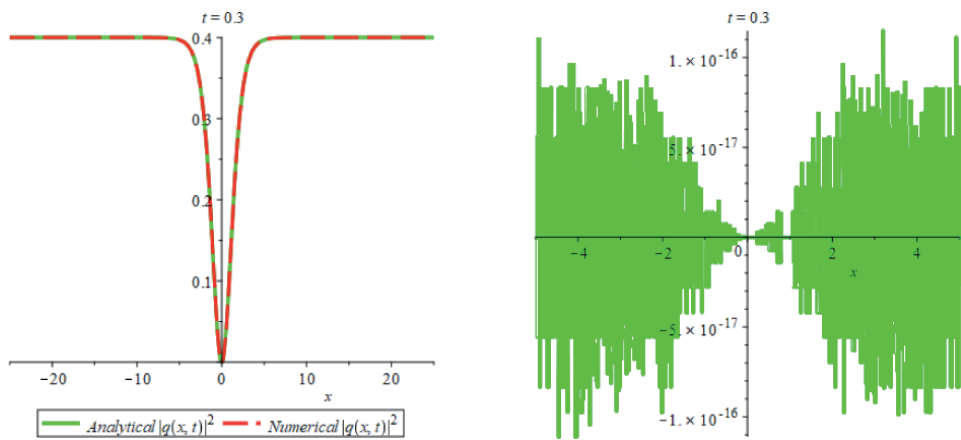


Figure 18.
 The graph of analytical and numerical solution with absolute error at $t = 0.3$ and $a = \frac{1}{10}$, $b = \frac{1}{2}$, $\beta_3 = \frac{1}{5}$, $\sigma = \frac{1}{10}$, $\theta = -\frac{173}{200}$, $\theta_0 = 0$, $\omega = \frac{311}{800}$, $\kappa = \frac{1}{2}$.

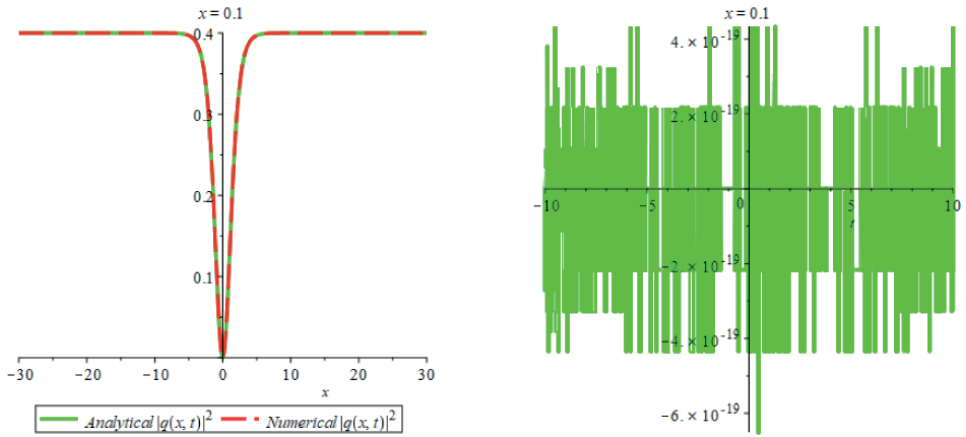


Figure 19.
 The graph of analytical and numerical solution with absolute error at $x = 0.1$ and $a = \frac{1}{10}, b = \frac{1}{2}, \beta_3 = \frac{1}{5}, \sigma = \frac{1}{10}, \theta = -\frac{173}{200}, \theta_0 = 0, \omega = \frac{311}{800}, \kappa = \frac{1}{2}$.

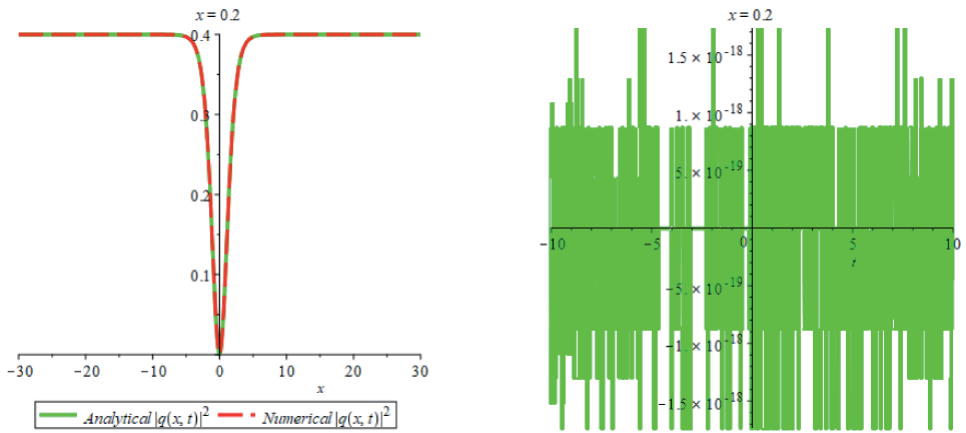


Figure 20.
 The graph of analytical and numerical solution with absolute error at $x = 0.2$ and $a = \frac{1}{10}, b = \frac{1}{2}, \beta_3 = \frac{1}{5}, \sigma = \frac{1}{10}, \theta = -\frac{173}{200}, \theta_0 = 0, \omega = \frac{311}{800}, \kappa = \frac{1}{2}$.

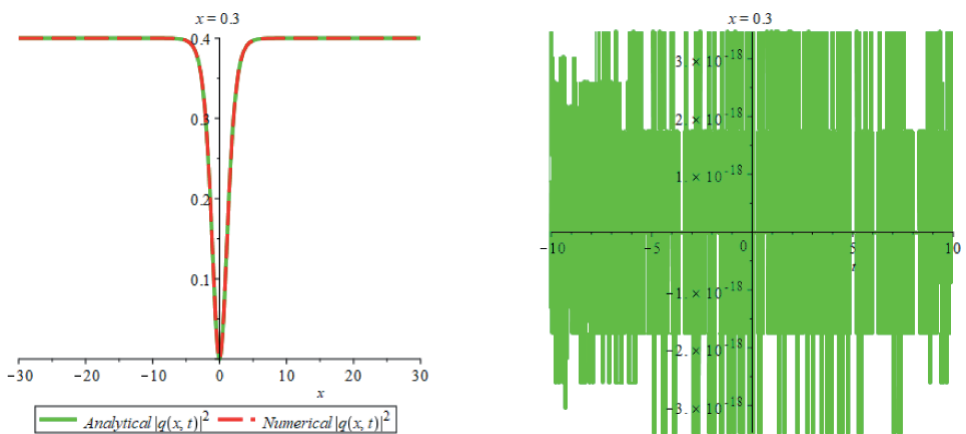


Figure 21.
 The graph of analytical and numerical solution with absolute error at $x = 0.3$ and $a = \frac{1}{10}, b = \frac{1}{2}, \beta_3 = \frac{1}{5}, \sigma = \frac{1}{10}, \theta = -\frac{173}{200}, \theta_0 = 0, \omega = \frac{311}{800}, \kappa = \frac{1}{2}$.

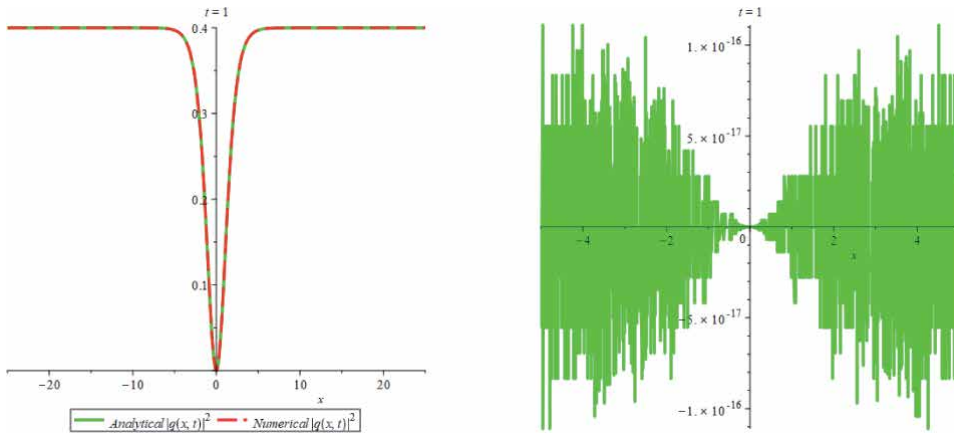


Figure 22. The graph of analytical and numerical solution with absolute error at $t = 1$ and $a = \frac{1}{10}$, $b = \frac{1}{2}$, $\beta_3 = \frac{1}{5}$, $\sigma = \frac{1}{10}$, $\theta = -\frac{173}{200}$, $\theta_0 = 0$, $\omega = \frac{311}{800}$, $\kappa = \frac{1}{2}$.

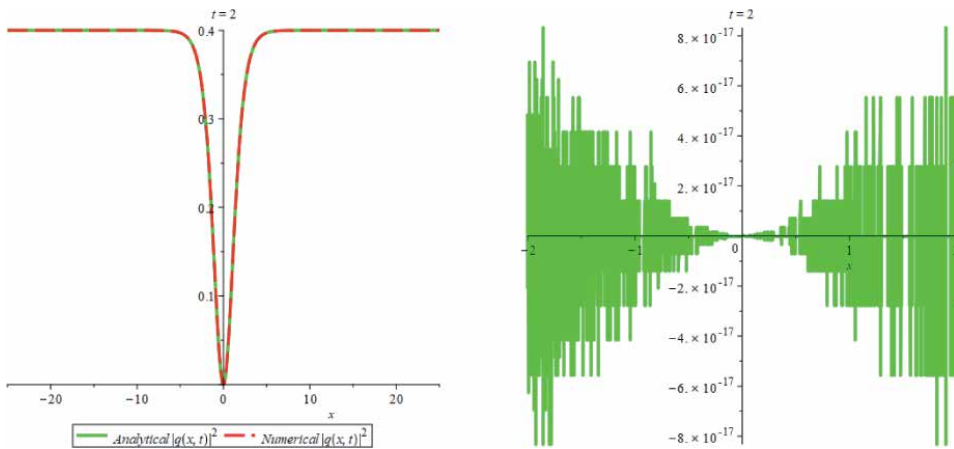


Figure 23. The graph of analytical and numerical solution with absolute error at $t = 2$ and $a = \frac{1}{10}$, $b = \frac{1}{2}$, $\beta_3 = \frac{1}{5}$, $\sigma = \frac{1}{10}$, $\theta = -\frac{173}{200}$, $\theta_0 = 0$, $\omega = \frac{311}{800}$, $\kappa = \frac{1}{2}$.

and $\kappa = \frac{1}{2}$. The results and the profile of W-shaped soliton shown in Table below. **Figures 23–34**, present the plots of exact and approximate solution with their error plots respectively by varying the values of t and x .

t	$ q_e - q_a $
0	1.6×10^{-11}
0.1	1.6×10^{-11}
0.2	1.6×10^{-11}
0.3	1.6×10^{-11}
2	$3. \times 10^{-18}$

t	$ q_e - q_a $
3	$2. \times 10^{-18}$
5	$3. \times 10^{-18}$

x	$ q_e - q_a $
0.1	$8. \times 10^{-19}$
0.2	$8. \times 10^{-19}$
0.3	$8. \times 10^{-19}$

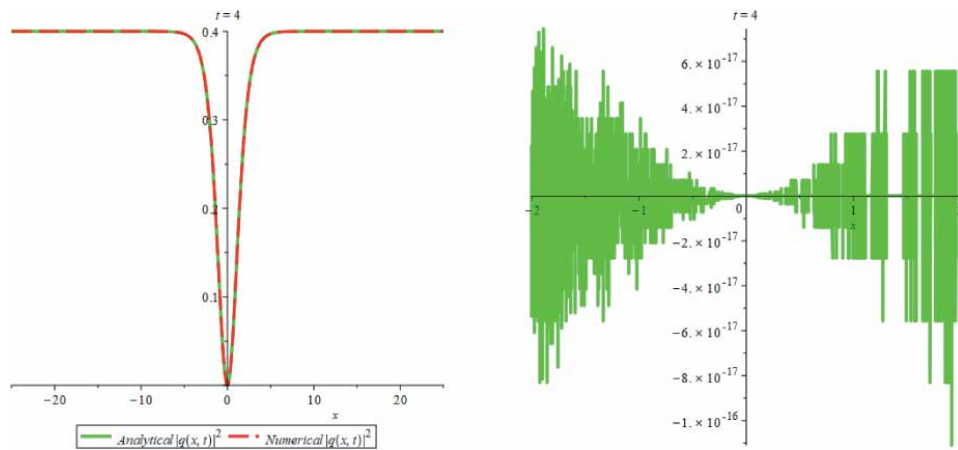


Figure 24.
 The graph of analytical and numerical solution with absolute error at $t = 4$ and $a = \frac{1}{10}$, $b = \frac{1}{2}$, $\beta_3 = \frac{1}{5}$, $\sigma = \frac{1}{10}$,
 $\theta = -\frac{173}{200}$, $\theta_0 = 0$, $\omega = \frac{311}{800}$, $\kappa = \frac{1}{2}$.

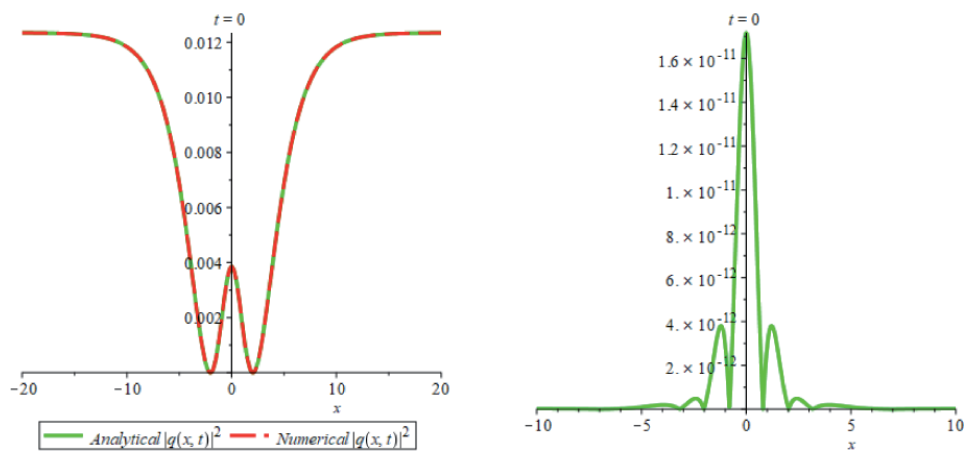


Figure 25.
 The graph of analytical and numerical solution with absolute error at $t = 0$ and $a = \frac{4}{100}$, $b = \frac{1}{2}$, $\beta_3 = \frac{4}{100}$,
 $\sigma = \frac{1}{10}$, $\rho = \frac{\sqrt{3}}{10}$, $\theta = -\frac{173}{200}$, $\theta_0 = 0$, $\omega = \frac{311}{800}$, $\kappa = \frac{1}{2}$.

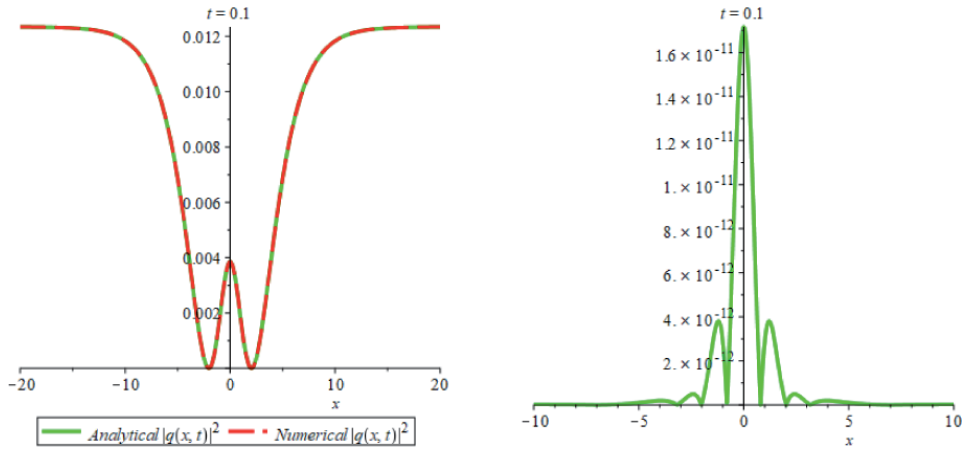


Figure 26.
 The graph of analytical and numerical solution with absolute error at $t = 0.1$ and $a = \frac{4}{100^2}$, $b = \frac{1}{2}$, $\beta_3 = \frac{4}{100^2}$
 $\sigma = \frac{1}{10^2}$, $\rho = \frac{\sqrt{3}}{10^2}$, $\theta = -\frac{173}{200^2}$, $\theta_0 = 0$, $\omega = \frac{311}{800^2}$, $\kappa = \frac{1}{2}$

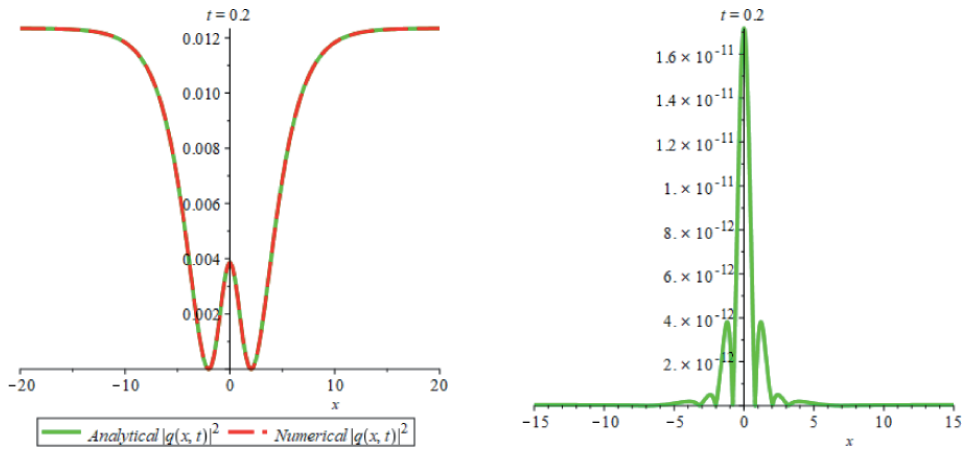


Figure 27.
 The graph of analytical and numerical solution with absolute error at $t = 0.2$ and $a = \frac{4}{100^2}$, $b = \frac{1}{2}$, $\beta_3 = \frac{4}{100^2}$
 $\sigma = \frac{1}{10^2}$, $\rho = \frac{\sqrt{3}}{10^2}$, $\theta = -\frac{173}{200^2}$, $\theta_0 = 0$, $\omega = \frac{311}{800^2}$, $\kappa = \frac{1}{2}$

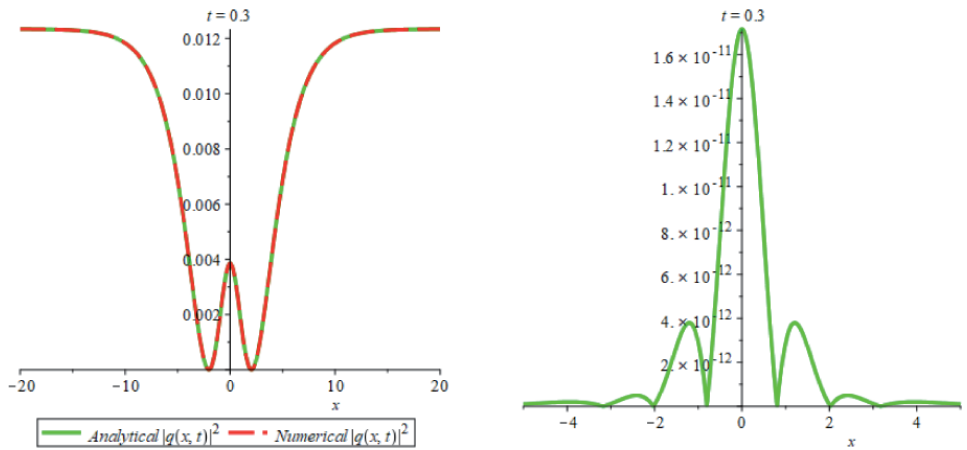


Figure 28.
 The graph of analytical and numerical solution with absolute error at $t = 0.3$ and $a = \frac{4}{100^2}$, $b = \frac{1}{2}$, $\beta_3 = \frac{4}{100^2}$
 $\sigma = \frac{1}{10^2}$, $\rho = \frac{\sqrt{3}}{10^2}$, $\theta = -\frac{173}{200^2}$, $\theta_0 = 0$, $\omega = \frac{311}{800^2}$, $\kappa = \frac{1}{2}$

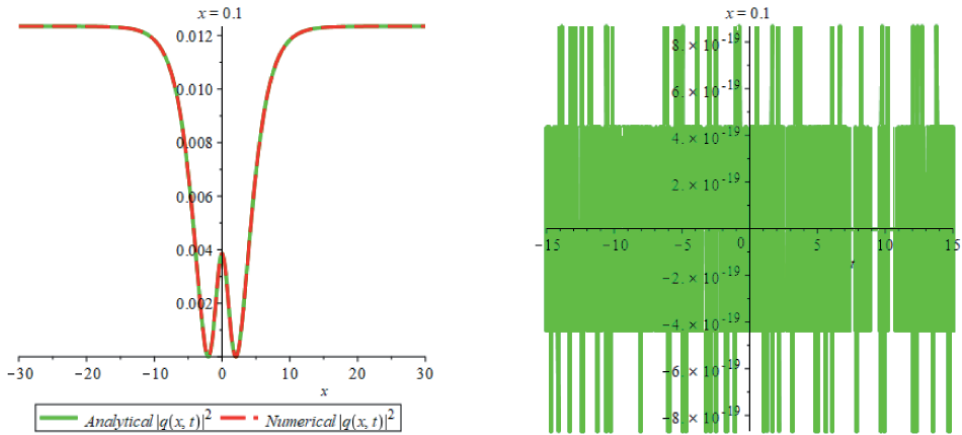


Figure 29.
 The graph of analytical and numerical solution with absolute error at $x = 0.1$ and $a = \frac{4}{100}$, $b = \frac{1}{2}$, $\beta_3 = \frac{4}{100}$,
 $\sigma = \frac{1}{10^2}$, $\rho = \frac{\sqrt{3}}{10^2}$, $\theta = -\frac{173}{200^2}$, $\theta_0 = 0$, $\omega = \frac{311}{800^2}$, $\kappa = \frac{1}{2}$

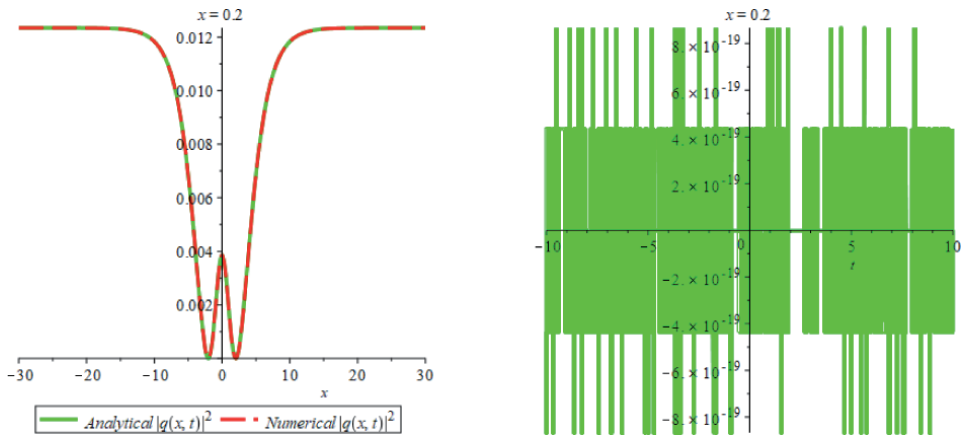


Figure 30.
 The graph of analytical and numerical solution with absolute error at $x = 0.2$ and $a = \frac{4}{100}$, $b = \frac{1}{2}$, $\beta_3 = \frac{4}{100}$,
 $\sigma = \frac{1}{10^2}$, $\rho = \frac{\sqrt{3}}{10^2}$, $\theta = -\frac{173}{200^2}$, $\theta_0 = 0$, $\omega = \frac{311}{800^2}$, $\kappa = \frac{1}{2}$

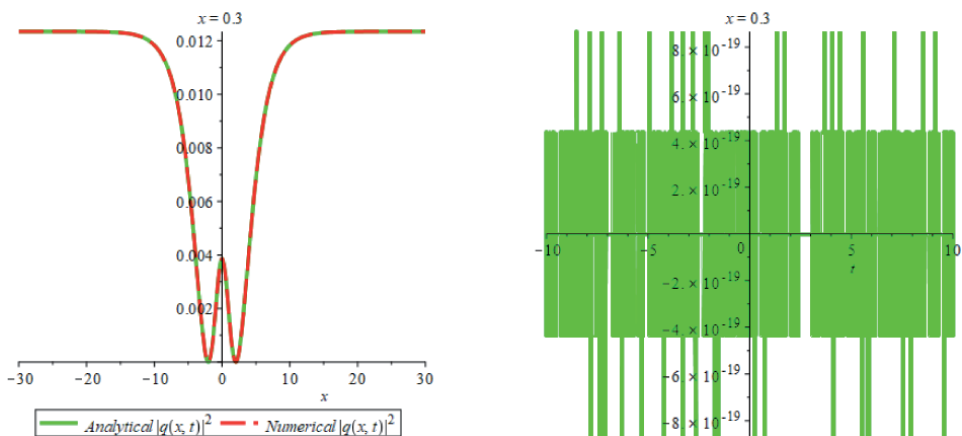


Figure 31.
 The graph of analytical and numerical solution with absolute error at $x = 0.3$ and $a = \frac{4}{100}$, $b = \frac{1}{2}$, $\beta_3 = \frac{4}{100}$,
 $\sigma = \frac{1}{10^2}$, $\rho = \frac{\sqrt{3}}{10^2}$, $\theta = -\frac{173}{200^2}$, $\theta_0 = 0$, $\omega = \frac{311}{800^2}$, $\kappa = \frac{1}{2}$

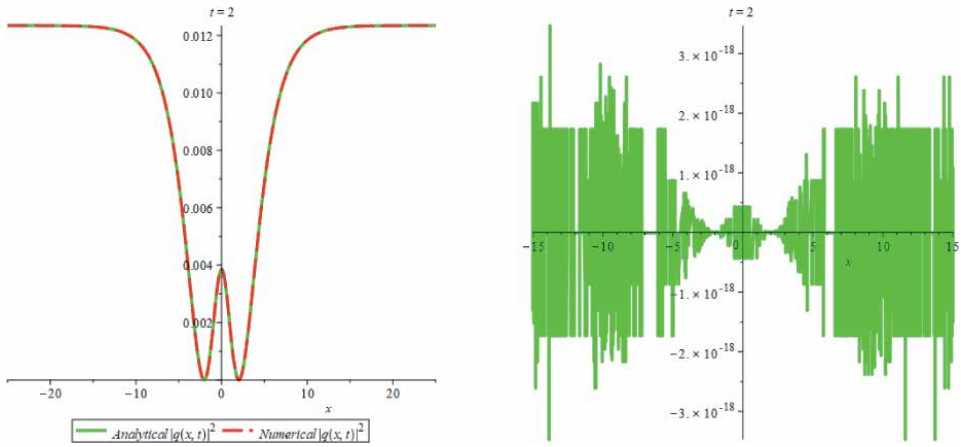


Figure 32.

The graph of analytical and numerical solution with absolute error at $t = 2$ and $a = \frac{4}{100}$, $b = \frac{1}{2}$, $\beta_3 = \frac{4}{100}$

$$\sigma = \frac{1}{10}, \rho = \frac{\sqrt{3}}{10}, \theta = -\frac{173}{200}, \theta_0 = 0, \omega = \frac{311}{800}, \kappa = \frac{1}{2}$$

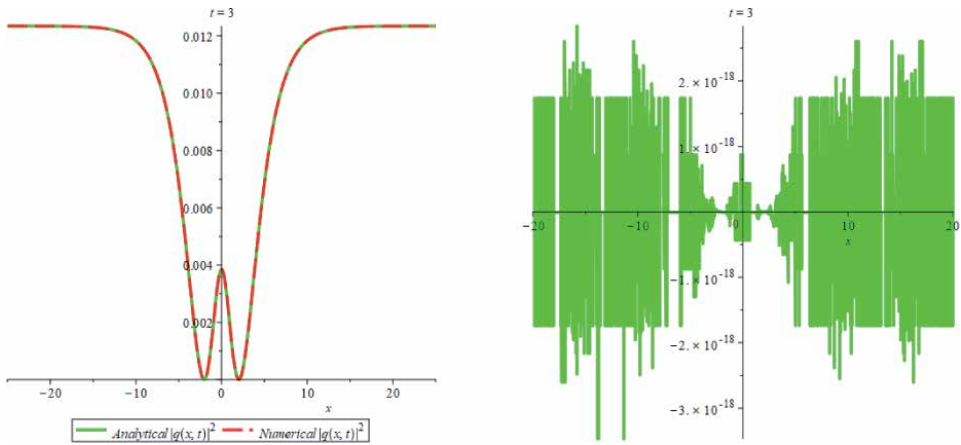


Figure 33.

The graph of analytical and numerical solution with absolute error at $t = 3$ and $a = \frac{4}{100}$, $b = \frac{1}{2}$, $\beta_3 = \frac{4}{100}$, $\sigma = \frac{1}{10}$

$$\rho = \frac{\sqrt{3}}{10}, \theta = -\frac{173}{200}, \theta_0 = 0, \omega = \frac{311}{800}, \kappa = \frac{1}{2}$$

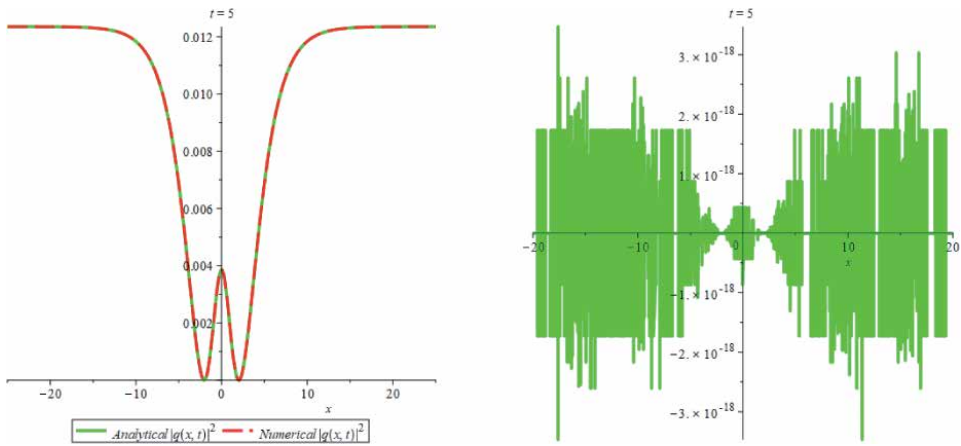


Figure 34.

The graph of analytical and numerical solution with absolute error at $t = 5$ and $a = \frac{4}{100}$, $b = \frac{1}{2}$, $\beta_3 = \frac{4}{100}$

$$\sigma = \frac{1}{10}, \rho = \frac{\sqrt{3}}{10}, \theta = -\frac{173}{200}, \theta_0 = 0, \omega = \frac{311}{800}, \kappa = \frac{1}{2}$$

5. Conclusion

In this chapter, SSE has been discussed. First, the undetermined coefficient method has been used. This method secured bright, dark, singular, and *W*-shaped solitons solutions. The method has given a spectrum of solitons. After that, the Adomian decomposition method has been used for the numerical simulations. This is a very powerful method that has given rapid convergence. Along with, error plots have also been given to witness the accuracy of the exact solution. The graphs have also shown the comparison of exact and absolute solution.

Conflict of interest

“The authors declare no conflict of interest”.

Author details

Mir Asma
Faculty of Science, Institute of Mathematical Science, University of Malaya,
Malaysia

*Address all correspondence to: miraszaka@gmail.com

IntechOpen

© 2022 The Author(s). Licensee IntechOpen. This chapter is distributed under the terms of the Creative Commons Attribution License (<http://creativecommons.org/licenses/by/3.0/>), which permits unrestricted use, distribution, and reproduction in any medium, provided the original work is properly cited. 

References

- [1] Hasegawa A, Tappert F. Transmission of stationary nonlinear optical pulses in dispersive dielectric fibers. I. Anomalous dispersion. *Applied Physics Letters*. 1973;**73**(3):142-144. DOI: 10.1063/1.1654836 [Accessed: November 14, 2016]
- [2] Mollenauer LF, Stolen RH, Gordon JP. Experimental observation of picosecond pulse narrowing and solitons in optical fibers. *Physical Review Letters*. 1980;**45**(13):1095-1098. DOI: 10.1103/PhysRevLett.45.1095 [Accessed: November 14, 2016]
- [3] Sasa N, Satsuma J. New-type of soliton solutions for a higher-order nonlinear Schrödinger equation. *Journal of the Physical Society of Japan*. 1991; **60**(2):409-417. DOI: 10.1143/JPSJ.60.409 [Accessed: November 14, 2016]
- [4] Akhmediev N, Soto-Crespo JM, Devine N, Hoffmann NP. Rogue wave spectra of the Sasa-Satsuma equation. *Physica D: Nonlinear Phenomena*. 2015; **294**:37-42. DOI: 10.1016/j.physd.2014.11.006 [Accessed: November 14, 2016]
- [5] Adem AR, Ntsime BP, Biswas A, Asma M, Ekici M, Moshokoa SP, et al. Stationary optical solitons with Sasa-Satsuma equation having nonlinear chromatic dispersion. *Physics Letters A*. 2020;**384**(27):126721. DOI: 10.1016/j.physleta.2020.126721 [Accessed: November 14, 2016]
- [6] Wright OC III. Sasa-Satsuma equation unstable plane waves and heteroclinic connections. *Chaos, Solitons & Fractals*. 2007;**33**: 374-387. DOI: 10.1016/j.chaos.2006.09.034 [Accessed: November 14, 2016]
- [7] Asma M, Othman WAM, Wong BR, Biswas A. Optical soliton perturbation with quadratic-cubic nonlinearity by semi-inverse variational principle. *Proceedings of the Romanian Academy Series A*. 2017;**18**(4):331-336 [Accessed: November 14, 2016]
- [8] Asma M, Othman WAM, Wong BR, Biswas A. Optical soliton perturbation with quadratic-cubic nonlinearity by traveling wave hypothesis. *Optoelectronics and Advanced Materials—Rapid Communications*. 2017;**11**(9):517-519 [Accessed: November 14, 2016]
- [9] Biswas A, Ullah MZ, Asma M, Zhou Q, Moshokoa SP, Belic M. Optical solitons with quadratic-cubic nonlinearity by semi-inverse variational principle. *Optik*. 2017;**139**:16-19. DOI: 10.1016/j.ijleo.2017.03.111 [Accessed: November 14, 2016]
- [10] Asma M, Othman WAM, Wong BR, Biswas A. Optical soliton perturbation with quadratic-cubic nonlinearity by the method of undetermined coefficients. *Optoelectronics and Advanced Materials*. 2017;**19**(11):699-703 [Accessed: November 14, 2016]
- [11] Wazwaz AM. *Partial Differential Equations and Solitary Waves Theory*. 2nd ed. Springer; 2009. ISBN 978-3-642-00251-9. Available from: <https://link.springer.com/book/10.1007/978-3-642-00251-9>

Resonant Optical Solitons in (3 + 1)-Dimensions Dominated by Kerr Law and Parabolic Law Nonlinearities

Khalil S. Al-Ghafri

Abstract

This study investigates the optical solitons of of (3+1)-dimensional resonant nonlinear Schrödinger (3D-RNLS) equation with the two laws of nonlinearity. The two forms of nonlinearity are represented by Kerr law and parabolic law. Based on complex transformation, the traveling wave reduction of the governing model is derived. The projective Riccati equations technique is applied to obtain the exact solutions of 3D-RNLS equation. Various types of waves that represent different structures of optical solitons are extracted. These structures include bright, dark, singular, dark-singular and combined singular solitons. Additionally, the obliquity effect on resonant solitons is illustrated graphically and is found to cause dramatic variations in soliton behaviors.

Keywords: Optical solitons, 3D-RNLS equation, Kerr law and parabolic law nonlinearities, Projective Riccati equations method, Obliquity influence

1. Introduction

Soliton is one of the important nonlinear waves that has been under intensive investigation in the physical and natural sciences. It has been noticed that solitons play a significant role on describing the physical phenomena in various branches of science, such as optical fibers, plasma physics, nonlinear optics, and many other fields [1–5]. For example, solitons in the field of nonlinear optics are known as optical solitons and have the capacity to transport information through optical fibers over transcontinental and transoceanic distances in a matter of a few femtoseconds [6, 7]. Moreover, it is found that the efficient physical properties of solitons may support the improvement on photonic and optoelectronic devices [8, 9]. Further to this, optical solitons can be exploited widely in optical communication and optical signal processing systems [10, 11].

The formation of solitons is essentially caused due to a delicate balance between dispersion and nonlinearity in the medium. Understanding the dynamics of solitons can be performed through focusing deeply on one model of the nonlinear Schrödinger family of equations with higher order nonlinear terms [12, 13]. Thus, various studies in literatures scrutinized the resonant nonlinear Schrödinger equation which is mainly the governing model that describes soliton propagation and

Madelung fluids in many nonlinear media. Several integration schemes have been implemented to examine the behavior of solitons such as ansatz method, semi-inverse variational principle, simplest equation approach, first integral method, functional variable method, sine-cosine function method, (G'/G) -expansion method, trial solution approach, generalized extended tanh method, modified simple equation method, and improved extended tanh-equation method. For more details, readers are referred to references [14–25].

The present study concentrates on the investigation of resonant optical solitons in $(3 + 1)$ -dimensions with two types of nonlinear influences, namely, Kerr law and parabolic law nonlinearities. In particular, we shed light on the model of $(3 + 1)$ -dimensional resonant nonlinear Schrödinger (3D-RNLS) equation given in the form

$$iQ_t + \eta \nabla^2 Q + \sigma F(s) |Q|^2 Q + s \delta \left(\frac{\nabla^2 |Q|}{|Q|} \right) Q = 0, \quad i = \sqrt{-1}, \quad \nabla^2 = \frac{\partial^2}{\partial x^2} + \frac{\partial^2}{\partial y^2} + \frac{\partial^2}{\partial z^2}, \quad (1)$$

where the dependent variable $Q(x, y, z, t)$ is a complex-valued wave profile and the independent variables x, y and z stand for spatial coordinates while t indicates temporal coordinate. The non-zero constants η, σ , and δ account for the coefficients of the group velocity, non-Kerr nonlinearity, and resonant nonlinearity, respectively. The parameter s plays an important role on manipulating the physical properties of distinct media and consequently affecting the behaviors of constructed solitons, see [26].

Here, we will consider two specific cases for the function $F(s)$ that represent the effect of nonlinearity in the media. These two nonlinear influences include the Kerr law and parabolic law nonlinearities. Hence, Eq. (1) with the two laws of nonlinearity has the following forms

$$iQ_t + \eta \nabla^2 Q + \sigma |Q|^2 Q + \delta \left(\frac{\nabla^2 |Q|}{|Q|} \right) Q = 0, \quad (2)$$

and

$$iQ_t + \eta \nabla^2 Q + (\sigma |Q|^2 + \rho |Q|^4) Q + \delta \left(\frac{\nabla^2 |Q|}{|Q|} \right) Q = 0. \quad (3)$$

The first model given in Eq. (2) is the 3D-RNLS equation dominated by the Kerr law nonlinearity and is found to have applications in the optical fiber and water waves when the refractive index of the light is proportional to the intensity. The second model presented in Eq. (3) is the 3D-RNLS equation with the parabolic law nonlinearity which arises in the context of nonlinear fiber optics.

In literatures, there are some studies that dealt with the 3D-RNLS equation to find exact solutions. For example, Ferdous et al. [27] investigated the conformable time fractional 3D-RNLS equation with Kerr and parabolic law nonlinearities. Different structures of oblique resonant optical solitons have been obtained by using the generalized $\exp(-\Phi(\xi))$ -expansion method. Furthermore, Sedeeg et al. [28] studied the two models of 3D-RNLS equation given in (2) and (3) by applying the modified extended tanh method. Optical soliton solutions including dark, singular and combo solitons are extracted in addition to periodic solutions. Moreover, the exact solutions of the 3D-RNLS equation with Kerr law nonlinearity given in (2) has been examined by Hosseini et al. [29] by exploiting the new expansion methods based on the Jacobi elliptic equation. Recently, Hosseini et al. [30] studied the optical solitons and modulation instability of the models given in (2) and (3).

Various forms of optical solitons are derived with the aid of the \exp_a and hyperbolic function techniques.

The aim of current work is to derive the optical solitons of 3D-RNLS equation presented in (2) and (3). The mathematical technique applied to solve the models is based on a finite series expressed in terms of the solution of projective Riccati equations. The paper is organized as follows. In Section 2, we analyze the idea of implementing the proposed method. In Section 3, the traveling wave reduction of (2) and (3) is extracted. Then, Section 4 displays the derivation of resonant optical solitons in (3 + 1)-dimensions. In Section 5, the main outlook of results and remarks are presented. Finally, the conclusion of work is given in Section 6.

2. Elucidation of solution method

Consider a nonlinear partial differential equation (NLPDE) for $Q(x, y, z, t)$ in the form

$$P(Q, Q_t, Q_x, Q_y, Q_z, Q_{xx}, Q_{yy}, Q_{zz}, \dots) = 0, \quad (4)$$

where P is a polynomial in its arguments.

Since we seek for exact traveling wave solutions, we introduce the wave variables

$$Q(x, t) = q(\xi), \quad \xi = x \cos \alpha + y \cos \beta + z \cos \gamma + ct. \quad (5)$$

Inserting (5) into Eq. (4), one can find the following ordinary differential equation (ODE)

$$H(q, q', q'', q''', \dots) = 0, \quad (6)$$

where prime denotes the derivative with respect to ξ . Then, integrate Eq. (6), if possible, to reduce the order of differentiation.

Now, assume that the solution of Eq. (6) can be expressed in the finite series of the form

$$U(\xi) = a_0 + \sum_{l=1}^m (a_l f^l(\xi) + b_l g^l(\xi)), \quad (7)$$

where $a_0, a_l, b_l, (l = 1, 2, \dots, m)$ are constants to be identified. The parameter m , which is a positive integer, can be determined by balancing the highest order derivative term with the highest order nonlinear term in Eq. (6).

The variables $f(\xi), g(\xi)$ satisfy the equations

$$\begin{aligned} f'(\xi) &= \varepsilon A g^2(\xi), & g'(\xi) &= -A f(\xi) g(\xi) - \frac{B}{A} g(\xi) (R - B f(\xi)), \\ g^2(\xi) &= \varepsilon \left[\frac{1}{A^2} (R - B f(\xi))^2 - f^2(\xi) \right], \end{aligned} \quad (8)$$

where A and B are arbitrary constants and $\varepsilon = \pm 1$. The third equation in the system (8) represents the first integral which gives the relation between the functions $f(\xi)$ and $g(\xi)$.

The set of Eqs. (8) is found to admit the following solutions

$$f_1(\xi) = \frac{R \tanh(R\xi)}{A + B \tanh(R\xi)}, \quad g_1(\xi) = \frac{R \operatorname{sech}(R\xi)}{A + B \tanh(R\xi)}, \quad (9)$$

demands $\varepsilon = 1$.

$$f_2(\xi) = \frac{R \operatorname{coth}(R\xi)}{A + B \operatorname{coth}(R\xi)}, \quad g_2(\xi) = \frac{R \operatorname{csch}(R\xi)}{A + B \operatorname{coth}(R\xi)}, \quad (10)$$

implies $\varepsilon = -1$.

$$f_3(\xi) = \frac{A}{AC + (A^2 - B^2)\xi}, \quad g_3(\xi) = \frac{\sqrt{-\varepsilon(A^2 - B^2)}}{AC + (A^2 - B^2)\xi}, \quad (11)$$

provided $R = 0$, where C is an arbitrary constant.

The substitution of (7) along with (8) into Eq. (6) generates a polynomial in $f^i(\xi)g^j(\xi)$. Equating each coefficient of $f^i(\xi)g^j(\xi)$ in this polynomial to zero, yields a set of algebraic equations for a_i, b_j . Solving this system of equations, we can obtain many exact solutions of Eq. (4) according to (9)–(11).

3. Traveling wave reduction for Eqs. (2) and (3)

In order to tackle the complex models of 3D-RNLS equation with Kerr law and parabolic law nonlinearities given in (2) and (3), we embark on analyzing their structures by using the wave transformation of the form

$$Q(x, t) = q(\xi)e^{i\varphi}, \quad (12)$$

where

$$\xi = x \cos \alpha + y \cos \beta + z \cos \gamma + \nu t, \quad \varphi = \kappa(x \cos \alpha + y \cos \beta + z \cos \gamma) + \omega t. \quad (13)$$

3.1 Traveling wave reduction for Eq. (2)

Applying transformation (12), the 3D-RNLS equation with Kerr law nonlinearity given in (2) is broken down into real and imaginary parts as

$$\begin{aligned} &(\cos^2 \alpha + \cos^2 \beta + \cos^2 \gamma)(\eta + \delta)q'' - (\omega + \eta\kappa^2(\cos^2 \alpha + \cos^2 \beta + \cos^2 \gamma))q + \sigma q^3 \\ &= 0, \end{aligned} \quad (14)$$

and

$$(\nu + 2\eta\kappa(\cos^2 \alpha + \cos^2 \beta + \cos^2 \gamma))q' = 0. \quad (15)$$

From Eq. (15), we obtain

$$\nu = -2\lambda\eta\kappa, \quad (16)$$

where $\lambda = \cos^2\alpha + \cos^2\beta + \cos^2\gamma$. Hence, Eq. (14) reduces to the form

$$\lambda(\eta + \delta)q'' - (\omega + \lambda\eta\kappa^2)q + \sigma q^3 = 0. \quad (17)$$

3.2 Traveling wave reduction for Eq. (3)

Similarly, we utilize the wave transformation (12) to the 3D-RNLS equation with parabolic law nonlinearity given in (3) which is decomposed to real and imaginary parts as

$$\lambda(\eta + \delta)q'' - (\omega + \lambda\eta\kappa^2)q + \sigma q^3 + \rho q^5 = 0, \quad (18)$$

and

$$(\nu + 2\lambda\eta\kappa)q' = 0. \quad (19)$$

From Eq. (19), we come by the expression given in (16). To seek a closed form solution, the structure of Eq. (18) has to be rearranged. Thus, we multiply Eq. (18) by q' and integrate with respect to ξ to arrive at

$$\lambda(\eta + \delta)q'^2 - (\omega + \lambda\eta\kappa^2)q^2 + \frac{\sigma}{2}q^4 + \frac{\rho}{3}q^6 + 2\mu = 0, \quad (20)$$

where μ is the integration constant. For convenience, we make use of the variable transformation given as

$$q^2 = V, \quad (21)$$

which leads to $q'^2 = V'^2/4V$. Thus, Eq. (20), after manipulating, becomes

$$\lambda(\eta + \delta)V'^2 + 8\mu V - 4(\omega + \lambda\eta\kappa^2)V^2 + 2\sigma V^3 + \frac{4}{3}\rho V^4 = 0. \quad (22)$$

4. Optical soliton solutions of 3D-RNLS equation with Kerr law and parabolic law nonlinearities

Now, we aim to employ the projective Riccati equations method given in Section 2 to extract the exact resonant optical soliton solutions with Kerr law and parabolic law nonlinearities for 3D-RNLS equations given in (2) and (3). Basically, the proposed technique will be implemented to Eqs. (17) and (20) and then their obtained solutions will be inserted into (12) so as to derive the optical solitons of the models discussed in this work.

4.1 Oblique resonant solitons of 3D-RNLS equation with Kerr law nonlinearity

According to the expansion given in (7) and the balance between the terms q'' and q^3 , the solution of Eq. (17) reads

$$q(\xi) = a_0 + a_1f(\xi) + b_1g(\xi). \quad (23)$$

Substituting (23) together with Eqs. (8) into Eq. (17) gives rise to an equation having different powers of $f^i g^j$. Collecting all the terms with the same power of $f^i g^j$

together and equating each coefficient to zero, yields a set of algebraic equations. Solving these equations simultaneously leads to the following results.

Set I. If $\varepsilon = 1$, then the following cases of solutions are retrieved.

Case I1. $a_0 = a_1 = 0$, $b_1 = \pm \sqrt{\frac{2\lambda(\eta+\delta)(A^2-B^2)}{\sigma}}$, $\omega = \lambda([\eta + \delta]R^2 - \eta\kappa^2)$.

$$Q(x, y, z, t) = \pm R \sqrt{\frac{2\lambda(\eta+\delta)(A^2-B^2)}{\sigma}} \frac{\operatorname{sech}(R[x \cos \alpha + y \cos \beta + z \cos \gamma - 2\lambda\eta\kappa t])}{A + B \tanh(R[x \cos \alpha + y \cos \beta + z \cos \gamma - 2\lambda\eta\kappa t])} e^{i\varphi}, \quad (24)$$

where $\lambda\sigma(\eta + \delta)(A^2 - B^2) > 0$ and $\varphi = \kappa(x \cos \alpha + y \cos \beta + z \cos \gamma) + \lambda([\eta + \delta]R^2 - \eta\kappa^2)t$.

Case I2. $a_0 = \pm \frac{BR}{A} \sqrt{-\frac{2\lambda(\eta+\delta)}{\sigma}}$, $a_1 = \pm \frac{A^2-B^2}{A} \sqrt{-\frac{2\lambda(\eta+\delta)}{\sigma}}$, $b_1 = 0$,
 $\omega = -\lambda(2[\eta + \delta]R^2 + \eta\kappa^2)$.

$$Q(x, y, z, t) = \pm R \sqrt{-\frac{2\lambda(\eta+\delta)}{\sigma}} \frac{B + A \tanh(R[x \cos \alpha + y \cos \beta + z \cos \gamma - 2\lambda\eta\kappa t])}{A + B \tanh(R[x \cos \alpha + y \cos \beta + z \cos \gamma - 2\lambda\eta\kappa t])} e^{i\varphi}, \quad (25)$$

where $\lambda\sigma(\eta + \delta) < 0$ and $\varphi = \kappa(x \cos \alpha + y \cos \beta + z \cos \gamma) - \lambda(2[\eta + \delta]R^2 + \eta\kappa^2)t$.

Case I3. $a_0 = \pm \frac{BR}{A} \sqrt{-\frac{\lambda(\eta+\delta)}{2\sigma}}$, $a_1 = \pm \frac{A^2-B^2}{A} \sqrt{-\frac{\lambda(\eta+\delta)}{2\sigma}}$, $b_1 = \pm \sqrt{\frac{\lambda(\eta+\delta)(A^2-B^2)}{2\sigma}}$,

$$\omega = -\lambda\left([\eta + \delta] \frac{R^2}{2} + \eta\kappa^2\right).$$

$$Q(x, y, z, t) = \pm R \sqrt{-\frac{\lambda(\eta+\delta)}{2\sigma}} \left\{ \frac{B + A \tanh(R[x \cos \alpha + y \cos \beta + z \cos \gamma - 2\lambda\eta\kappa t])}{A + B \tanh(R[x \cos \alpha + y \cos \beta + z \cos \gamma - 2\lambda\eta\kappa t])} \right. \\ \left. \pm \frac{\sqrt{B^2 - A^2} \operatorname{sech}(R[x \cos \alpha + y \cos \beta + z \cos \gamma - 2\lambda\eta\kappa t])}{A + B \tanh(R[x \cos \alpha + y \cos \beta + z \cos \gamma - 2\lambda\eta\kappa t])} \right\} e^{i\varphi}, \quad (26)$$

where $\lambda\sigma(\eta + \delta) < 0$, $A^2 < B^2$ and $\varphi = \kappa(x \cos \alpha + y \cos \beta + z \cos \gamma) - \lambda([\eta + \delta] \frac{R^2}{2} + \eta\kappa^2)t$.

Set II. If $\varepsilon = -1$, then the following cases of solutions are generated.

Case II1. $a_0 = a_1 = 0$, $b_1 = \pm \sqrt{-\frac{2\lambda(\eta+\delta)(A^2-B^2)}{\sigma}}$, $\omega = \lambda([\eta + \delta]R^2 - \eta\kappa^2)$.

$$Q(x, y, z, t) = \pm R \sqrt{-\frac{2\lambda(\eta+\delta)(A^2-B^2)}{\sigma}} \frac{\operatorname{csch}(R[x \cos \alpha + y \cos \beta + z \cos \gamma - 2\lambda\eta\kappa t])}{A + B \operatorname{coth}(R[x \cos \alpha + y \cos \beta + z \cos \gamma - 2\lambda\eta\kappa t])} e^{i\varphi}, \quad (27)$$

where $\lambda\sigma(\eta + \delta)(A^2 - B^2) < 0$ and $\varphi = \kappa(x \cos \alpha + y \cos \beta + z \cos \gamma) + \lambda([\eta + \delta]R^2 - \eta\kappa^2)t$.

Case II2. $a_0 = \pm \frac{BR}{A} \sqrt{-\frac{2\lambda(\eta+\delta)}{\sigma}}$, $a_1 = \pm \frac{A^2-B^2}{A} \sqrt{-\frac{2\lambda(\eta+\delta)}{\sigma}}$, $b_1 = 0$,
 $\omega = -\lambda(2[\eta + \delta]R^2 + \eta\kappa^2)$.

$$Q(x, y, z, t) = \pm R \sqrt{-\frac{2\lambda(\eta + \delta)}{\sigma}} \frac{B + A \operatorname{coth}(R[x \cos \alpha + y \cos \beta + z \cos \gamma - 2\lambda\eta\kappa t])}{A + B \operatorname{coth}(R[x \cos \alpha + y \cos \beta + z \cos \gamma - 2\lambda\eta\kappa t])} e^{i\varphi}, \quad (28)$$

where $\lambda\sigma(\eta + \delta) < 0$ and $\varphi = \kappa(x \cos \alpha + y \cos \beta + z \cos \gamma) - \lambda(2[\eta + \delta]R^2 + \eta\kappa^2)t$.

Case II3. $a_0 = \pm \frac{BR}{A} \sqrt{-\frac{\lambda(\eta+\delta)}{2\sigma}}$, $a_1 = \pm \frac{A^2-B^2}{A} \sqrt{-\frac{\lambda(\eta+\delta)}{2\sigma}}$, $b_1 = \pm \sqrt{-\frac{\lambda(\eta+\delta)(A^2-B^2)}{2\sigma}}$,

$$\omega = -\lambda \left([\eta + \delta] \frac{R^2}{2} + \eta\kappa^2 \right).$$

$$Q(x, y, z, t) = \pm R \sqrt{-\frac{\lambda(\eta + \delta)}{2\sigma}} \left\{ \frac{B + A \operatorname{coth}(R[x \cos \alpha + y \cos \beta + z \cos \gamma - 2\lambda\eta\kappa t])}{A + B \operatorname{coth}(R[x \cos \alpha + y \cos \beta + z \cos \gamma - 2\lambda\eta\kappa t])} \pm \frac{\sqrt{A^2 - B^2} \operatorname{csch}(R[x \cos \alpha + y \cos \beta + z \cos \gamma - 2\lambda\eta\kappa t])}{A + B \operatorname{coth}(R[x \cos \alpha + y \cos \beta + z \cos \gamma - 2\lambda\eta\kappa t])} \right\} e^{i\varphi}, \quad (29)$$

where $\lambda\sigma(\eta + \delta) < 0$, $A^2 > B^2$ and $\varphi = \kappa(x \cos \alpha + y \cos \beta + z \cos \gamma) - \lambda([\eta + \delta] \frac{R^2}{2} + \eta\kappa^2)t$.

Set III. If $R = 0$, then the following cases of solutions are created.

Case III1. $a_0 = a_1 = 0$, $b_1 = \pm \sqrt{\frac{2\lambda(\eta+\delta)(A^2-B^2)}{\varepsilon\sigma}}$, $\omega = -\lambda\eta\kappa^2$.

Case III2. $a_0 = 0$, $a_1 = \pm \frac{A^2-B^2}{A} \sqrt{-\frac{2\lambda(\eta+\delta)}{\sigma}}$, $b_1 = 0$, $\omega = -\lambda\eta\kappa^2$.

Case III3. $a_0 = 0$, $a_1 = \pm \frac{A^2-B^2}{A} \sqrt{-\frac{\lambda(\eta+\delta)}{2\sigma}}$, $b_1 = \pm \sqrt{\frac{\lambda(\eta+\delta)(A^2-B^2)}{2\varepsilon\sigma}}$, $\omega = -\lambda\eta\kappa^2$.

Herein, these three cases in the Set III provide the solution of the form

$$Q(x, y, z, t) = \pm \sqrt{-\frac{2\lambda(\eta + \delta)}{\sigma}} \frac{(A^2 - B^2)}{AC + (A^2 - B^2)(x \cos \alpha + y \cos \beta + z \cos \gamma - 2\lambda\eta\kappa t)} e^{i\varphi}, \quad (30)$$

where $\lambda\sigma(\eta + \delta) < 0$ and $\varphi = \kappa(x \cos \alpha + y \cos \beta + z \cos \gamma) - \lambda\eta\kappa^2 t$.

4.2 Oblique resonant solitons of 3D-RNLS equation with parabolic law nonlinearity

Based on the expansion given in (7), we consider that the solution to Eq. (22) takes the form

$$q(\xi) = a_0 + \sum_{l=1}^2 (a_l f^l(\xi) + b_l g^l(\xi)). \quad (31)$$

Inserting (31) together with Eqs. (8) into Eq. (22) gives rise to an equation having different powers of $f^i g^j$. Collecting all the terms with the same power of $f^i g^j$ together and equating each coefficient to zero, yields a set of algebraic equations. Solving these equations simultaneously leads to the following results.

Set I. If $\varepsilon = 1$, then the following cases of solutions are obtained.

Case I1. $b_1 = a_2 = b_2 = 0$, $a_0 = \frac{-Ra_1}{(A+B)}$, $a_1 = \pm \frac{A^2-B^2}{2A} \sqrt{-\frac{3\lambda(\eta+\delta)}{\rho}}$,

$$\omega = \frac{\lambda(\eta+\delta)(A+B)^2 a_0^2 - \eta \kappa^2 a_1^2}{a_1^2}, \sigma = \frac{2\lambda(\eta+\delta)(A-B)(A+B)^2 a_0}{A a_1^2}, \mu = 0.$$

$$Q(x, y, z, t) = \left[\mp \frac{R}{2} \sqrt{-\frac{3\lambda(\eta+\delta)}{\rho}} \left\{ 1 - \frac{B + A \tanh(R[x \cos \alpha + y \cos \beta + z \cos \gamma - 2\lambda\eta\kappa t])}{A + B \tanh(R[x \cos \alpha + y \cos \beta + z \cos \gamma - 2\lambda\eta\kappa t])} \right\} \right]^{\frac{1}{2}} e^{i\varphi}, \quad (32)$$

where $\lambda\rho(\eta+\delta) < 0$ and $\varphi = \kappa(x \cos \alpha + y \cos \beta + z \cos \gamma) + \lambda([\eta+\delta]R^2 - \eta\kappa^2)t$.

Case I2. $b_1 = a_2 = b_2 = 0$, $a_0 = \frac{R a_1}{(A-B)}$, $a_1 = \pm \frac{A^2 - B^2}{2A} \sqrt{-\frac{3\lambda(\eta+\delta)}{\rho}}$,

$$\omega = \frac{\lambda(\eta+\delta)(A-B)^2 a_0^2 - \eta \kappa^2 a_1^2}{a_1^2}, \sigma = \frac{2\lambda(\eta+\delta)(A+B)(A-B)^2 a_0}{A a_1^2}, \mu = 0.$$

$$Q(x, y, z, t) = \left[\pm \frac{R}{2} \sqrt{-\frac{3\lambda(\eta+\delta)}{\rho}} \left\{ 1 + \frac{B + A \tanh(R[x \cos \alpha + y \cos \beta + z \cos \gamma - 2\lambda\eta\kappa t])}{A + B \tanh(R[x \cos \alpha + y \cos \beta + z \cos \gamma - 2\lambda\eta\kappa t])} \right\} \right]^{\frac{1}{2}} e^{i\varphi}, \quad (33)$$

where $\lambda\rho(\eta+\delta) < 0$ and $\varphi = \kappa(x \cos \alpha + y \cos \beta + z \cos \gamma) + \lambda([\eta+\delta]R^2 - \eta\kappa^2)t$.

Case I3. $a_1 = a_2 = b_2 = 0$, $a_0 = \pm \frac{R b_1}{\sqrt{A^2 - B^2}}$, $b_1 = \pm \frac{1}{2} \sqrt{\frac{3\lambda(\eta+\delta)(A^2 - B^2)}{\rho}}$,

$$\omega = -\frac{\lambda(5(\eta+\delta)(A^2 - B^2)a_0^2 + 4\eta\kappa^2 b_1^2)}{4b_1^2}, \sigma = -\frac{2\lambda(\eta+\delta)(A^2 - B^2)a_0}{b_1^2}, \mu = -\frac{\lambda(\eta+\delta)(A^2 - B^2)a_0^3}{4b_1^2}.$$

$$Q(x, y, z, t) = \left[\pm \frac{R}{2} \sqrt{\frac{3\lambda(\eta+\delta)}{\rho}} \left\{ 1 \pm \frac{\sqrt{A^2 - B^2} \operatorname{sech}(R[x \cos \alpha + y \cos \beta + z \cos \gamma - 2\lambda\eta\kappa t])}{A + B \tanh(R[x \cos \alpha + y \cos \beta + z \cos \gamma - 2\lambda\eta\kappa t])} \right\} \right]^{\frac{1}{2}} e^{i\varphi}, \quad (34)$$

where $\lambda\rho(\eta+\delta) > 0$, $A^2 > B^2$ and $\varphi = \kappa(x \cos \alpha + y \cos \beta + z \cos \gamma) - \lambda([\eta+\delta]\frac{5R^2}{4} + \eta\kappa^2)t$.

Case I4. $a_2 = b_2 = 0$, $a_0 = -\frac{R b_1}{A(A+B)} \sqrt{A^2 - B^2}$, $a_1 = \pm \frac{b_1}{A} \sqrt{A^2 - B^2}$, $b_1 = \pm \frac{1}{4} \sqrt{\frac{3\lambda(\eta+\delta)(A^2 - B^2)}{\rho}}$, $\omega = -\frac{\lambda(\eta+\delta)(A+B)A^2 a_0^2 + 4\eta\kappa^2(A-B)b_1^2}{4(A-B)b_1^2}$, $\sigma = -\frac{\lambda(\eta+\delta)(A+B)A a_0}{2b_1^2}$, $\mu = 0$.

$$Q(x, y, z, t) = \left[\pm \frac{R}{4A} \sqrt{\frac{3\lambda(\eta+\delta)(A^2 - B^2)}{\rho}} \left\{ \frac{\sqrt{-(A^2 - B^2)} \tanh(R[x \cos \alpha + y \cos \beta + z \cos \gamma - 2\lambda\eta\kappa t])}{A + B \tanh(R[x \cos \alpha + y \cos \beta + z \cos \gamma - 2\lambda\eta\kappa t])} \right. \right. \\ \left. \left. \pm \frac{A \operatorname{sech}(R[x \cos \alpha + y \cos \beta + z \cos \gamma - 2\lambda\eta\kappa t])}{A + B \tanh(R[x \cos \alpha + y \cos \beta + z \cos \gamma - 2\lambda\eta\kappa t])} - \frac{\sqrt{-(A^2 - B^2)}}{(A+B)} \right\} \right]^{\frac{1}{2}} e^{i\varphi}, \quad (35)$$

where $\lambda\rho(\eta+\delta) < 0$, $A^2 < B^2$ and $\varphi = \kappa(x \cos \alpha + y \cos \beta + z \cos \gamma) + \lambda([\eta+\delta]\frac{R^2}{4} - \eta\kappa^2)t$.

Case I5. $a_2 = b_2 = 0$, $a_0 = \pm \frac{R b_1}{A(A-B)} \sqrt{-(A^2 - B^2)}$, $a_1 = \pm \frac{b_1}{A} \sqrt{-(A^2 - B^2)}$, $b_1 = \pm \frac{1}{4} \sqrt{\frac{3\lambda(\eta+\delta)(A^2 - B^2)}{\rho}}$, $\omega = -\frac{\lambda(\eta+\delta)(A-B)A^2 a_0^2 + 4\eta\kappa^2(A+B)b_1^2}{4(A+B)b_1^2}$, $\sigma = -\frac{\lambda(\eta+\delta)(A-B)A a_0}{2b_1^2}$, $\mu = 0$.

$$Q(x, y, z, t) = \left[\pm \frac{R}{4A} \sqrt{\frac{3\lambda(\eta + \delta)(A^2 - B^2)}{\rho}} \left\{ \frac{\sqrt{-(A^2 - B^2)} \tanh(R[x \cos \alpha + y \cos \beta + z \cos \gamma - 2\lambda\eta kt])}{A + B \tanh(R[x \cos \alpha + y \cos \beta + z \cos \gamma - 2\lambda\eta kt])} \right. \right. \\ \left. \left. \pm \frac{A \operatorname{sech}(R[x \cos \alpha + y \cos \beta + z \cos \gamma - 2\lambda\eta kt])}{A + B \tanh(R[x \cos \alpha + y \cos \beta + z \cos \gamma - 2\lambda\eta kt])} + \frac{\sqrt{-(A^2 - B^2)}}{(A - B)} \right\} \right]^{\frac{1}{2}} e^{i\varphi}, \quad (36)$$

where $\lambda\rho(\eta + \delta) < 0$, $A^2 < B^2$ and $\varphi = \kappa(x \cos \alpha + y \cos \beta + z \cos \gamma) + \lambda\left([\eta + \delta]\frac{R^2}{4} - \eta\kappa^2\right)t$.

Case I6. $a_0 = -\frac{(2\lambda(\eta + \delta)A^2 + \sigma b_2)R^2}{\sigma A^2}$, $a_1 = \frac{2BRb_2}{A^2}$, $b_1 = \pm \frac{A^2 a_0 + R^2 b_2}{RA^2} \sqrt{A^2 - B^2}$, $a_2 = \frac{(A^2 - B^2)b_2}{A^2}$, $\omega = -\lambda\left([\eta + \delta]\frac{5R^2}{4} + \eta\kappa^2\right)$, $\rho = \frac{3\sigma^2}{16\lambda(\eta + \delta)R^2}$, $\mu = \frac{\lambda^2(\eta + \delta)^2 R^4}{2\sigma}$.

$$Q(x, y, z, t) = \left[-\frac{2\lambda(\eta + \delta)R^2}{\sigma} \left\{ 1 \pm \frac{\sqrt{A^2 - B^2} \operatorname{sech}(R[x \cos \alpha + y \cos \beta + z \cos \gamma - 2\lambda\eta kt])}{A + B \tanh(R[x \cos \alpha + y \cos \beta + z \cos \gamma - 2\lambda\eta kt])} \right\} \right]^{\frac{1}{2}} e^{i\varphi}, \quad (37)$$

where $A^2 > B^2$ and $\varphi = \kappa(x \cos \alpha + y \cos \beta + z \cos \gamma) - \lambda\left([\eta + \delta]\frac{5R^2}{4} + \eta\kappa^2\right)t$.

Case I7. $b_1 = 0$, $a_0 = \frac{(A^2 a_1 - (A+B)Rb_2)R}{(A-B)A^2}$, $a_1 = \frac{2(\lambda(\eta + \delta)(A^2 - B^2)A + \sigma Bb_2)R}{\sigma A^2}$, $a_2 = \frac{(A^2 - B^2)b_2}{A^2}$, $\omega = \lambda([\eta + \delta]R^2 - \eta\kappa^2)$, $\rho = \frac{3\lambda(\eta + \delta)(A^2 - B^2)^2 A^2}{4(A^2 a_1 - 2BRb_2)^2}$, $\mu = 0$.

$$Q(x, y, z, t) = \left[\frac{2\lambda(\eta + \delta)R^2}{\sigma} \left\{ 1 + \frac{B + A \tanh(R[x \cos \alpha + y \cos \beta + z \cos \gamma - 2\lambda\eta kt])}{A + B \tanh(R[x \cos \alpha + y \cos \beta + z \cos \gamma - 2\lambda\eta kt])} \right\} \right]^{\frac{1}{2}} e^{i\varphi}, \quad (38)$$

where $\varphi = \kappa(x \cos \alpha + y \cos \beta + z \cos \gamma) + \lambda([\eta + \delta]R^2 - \eta\kappa^2)t$.

Case I8. $b_1 = 0$, $a_0 = -\frac{(A^2 a_1 + (A-B)Rb_2)R}{(A+B)A^2}$, $a_1 = -\frac{2(\lambda(\eta + \delta)(A^2 - B^2)A - \sigma Bb_2)R}{\sigma A^2}$, $a_2 = \frac{(A^2 - B^2)b_2}{A^2}$, $\omega = \lambda([\eta + \delta]R^2 - \eta\kappa^2)$, $\rho = -\frac{3\lambda(\eta + \delta)(A^2 - B^2)^2 A^2}{4(A^2 a_1 - 2BRb_2)^2}$, $\mu = 0$.

$$Q(x, y, z, t) = \left[\frac{2\lambda(\eta + \delta)R^2}{\sigma} \left\{ 1 - \frac{B + A \tanh(R[x \cos \alpha + y \cos \beta + z \cos \gamma - 2\lambda\eta kt])}{A + B \tanh(R[x \cos \alpha + y \cos \beta + z \cos \gamma - 2\lambda\eta kt])} \right\} \right]^{\frac{1}{2}} e^{i\varphi}, \quad (39)$$

where $\varphi = \kappa(x \cos \alpha + y \cos \beta + z \cos \gamma) + \lambda([\eta + \delta]R^2 - \eta\kappa^2)t$.

Case I9. $a_0 = \frac{(\lambda(\eta + \delta)(A+B)A - 2\sigma b_2)R^2}{2\sigma A^2}$, $a_1 = \frac{(A-B)A^2 a_0 + (A+B)R^2 b_2}{A^2 R}$, $b_1 = \pm \frac{\lambda(\eta + \delta)R}{2\sigma} \sqrt{-(A^2 - B^2)}$, $a_2 = \frac{(A^2 - B^2)b_2}{A^2}$, $\omega = \lambda\left([\eta + \delta]\frac{R^2}{4} - \eta\kappa^2\right)$, $\rho = -\frac{3\sigma^2}{4\lambda(\eta + \delta)R^2}$, $\mu = 0$.

$$Q(x, y, z, t) = \left[\frac{\lambda(\eta + \delta)R^2}{2\sigma} \left\{ 1 + \frac{B + A \tanh(R[x \cos \alpha + y \cos \beta + z \cos \gamma - 2\lambda\eta\kappa t])}{A + B \tanh(R[x \cos \alpha + y \cos \beta + z \cos \gamma - 2\lambda\eta\kappa t])} \right. \right. \\ \left. \left. \pm \frac{\sqrt{-(A^2 - B^2)} \operatorname{sech}(R[x \cos \alpha + y \cos \beta + z \cos \gamma - 2\lambda\eta\kappa t])}{A + B \tanh(R[x \cos \alpha + y \cos \beta + z \cos \gamma - 2\lambda\eta\kappa t])} \right\} \right]^{\frac{1}{2}} e^{i\varphi}, \quad (40)$$

where $A^2 < B^2$ and $\varphi = \kappa(x \cos \alpha + y \cos \beta + z \cos \gamma) + \lambda \left([\eta + \delta] \frac{R^2}{4} - \eta\kappa^2 \right) t$.

Case I10. $a_0 = \frac{\lambda(\eta+\delta)(A-B)A-2\sigma b_2}{2\sigma A^2} R^2$, $a_1 = -\frac{(A+B)A^2 a_0 + (A-B)R^2 b_2}{A^2 R}$, $b_1 =$
 $\pm \frac{\lambda(\eta+\delta)R}{2\sigma} \sqrt{-(A^2 - B^2)}$, $a_2 = \frac{(A^2 - B^2)b_2}{A^2}$, $\omega = \lambda \left([\eta + \delta] \frac{R^2}{4} - \eta\kappa^2 \right)$, $\rho = -\frac{3\sigma^2}{4\lambda(\eta+\delta)R^2}$, $\mu = 0$.

$$Q(x, y, z, t) = \left[\frac{\lambda(\eta + \delta)R^2}{2\sigma} \left\{ 1 - \frac{B + A \tanh(R[x \cos \alpha + y \cos \beta + z \cos \gamma - 2\lambda\eta\kappa t])}{A + B \tanh(R[x \cos \alpha + y \cos \beta + z \cos \gamma - 2\lambda\eta\kappa t])} \right. \right. \\ \left. \left. \pm \frac{\sqrt{-(A^2 - B^2)} \operatorname{sech}(R[x \cos \alpha + y \cos \beta + z \cos \gamma - 2\lambda\eta\kappa t])}{A + B \tanh(R[x \cos \alpha + y \cos \beta + z \cos \gamma - 2\lambda\eta\kappa t])} \right\} \right]^{\frac{1}{2}} e^{i\varphi}, \quad (41)$$

where $A^2 < B^2$ and $\varphi = \kappa(x \cos \alpha + y \cos \beta + z \cos \gamma) + \lambda \left([\eta + \delta] \frac{R^2}{4} - \eta\kappa^2 \right) t$.

Set II. If $\varepsilon = -1$, then the following cases of solutions are acquired.

Case II1. $b_1 = a_2 = b_2 = 0$, $a_0 = \frac{-Ra_1}{(A+B)}$, $a_1 = \pm \frac{A^2 - B^2}{2A} \sqrt{-\frac{3\lambda(\eta+\delta)}{\rho}}$,
 $\omega = \frac{\lambda((\eta+\delta)(A+B)^2 a_0^2 - \eta\kappa^2 a_1^2)}{a_1^2}$, $\sigma = \frac{2\lambda(\eta+\delta)(A-B)(A+B)^2 a_0}{Aa_1^2}$, $\mu = 0$.

$$Q(x, y, z, t) = \left[\mp \frac{R}{2} \sqrt{-\frac{3\lambda(\eta + \delta)}{\rho}} \left\{ 1 - \frac{B + A \operatorname{coth}(R[x \cos \alpha + y \cos \beta + z \cos \gamma - 2\lambda\eta\kappa t])}{A + B \operatorname{coth}(R[x \cos \alpha + y \cos \beta + z \cos \gamma - 2\lambda\eta\kappa t])} \right\} \right]^{\frac{1}{2}} e^{i\varphi}, \quad (42)$$

where $\lambda\rho(\eta + \delta) < 0$ and $\varphi = \kappa(x \cos \alpha + y \cos \beta + z \cos \gamma) + \lambda \left([\eta + \delta] R^2 - \eta\kappa^2 \right) t$.

Case II2. $b_1 = a_2 = b_2 = 0$, $a_0 = \frac{Ra_1}{(A-B)}$, $a_1 = \pm \frac{A^2 - B^2}{2A} \sqrt{-\frac{3\lambda(\eta+\delta)}{\rho}}$,
 $\omega = \frac{\lambda((\eta+\delta)(A-B)^2 a_0^2 - \eta\kappa^2 a_1^2)}{a_1^2}$, $\sigma = \frac{2\lambda(\eta+\delta)(A+B)(A-B)^2 a_0}{Aa_1^2}$, $\mu = 0$.

$$Q(x, y, z, t) = \left[\pm \frac{R}{2} \sqrt{-\frac{3\lambda(\eta + \delta)}{\rho}} \left\{ 1 + \frac{B + A \operatorname{coth}(R[x \cos \alpha + y \cos \beta + z \cos \gamma - 2\lambda\eta\kappa t])}{A + B \operatorname{coth}(R[x \cos \alpha + y \cos \beta + z \cos \gamma - 2\lambda\eta\kappa t])} \right\} \right]^{\frac{1}{2}} e^{i\varphi}, \quad (43)$$

where $\lambda\rho(\eta + \delta) < 0$ and $\varphi = \kappa(x \cos \alpha + y \cos \beta + z \cos \gamma) + \lambda \left([\eta + \delta] R^2 - \eta\kappa^2 \right) t$.

Case II3. $a_1 = a_2 = b_2 = 0$, $a_0 = \pm \frac{Rb_1}{\sqrt{A^2 - B^2}}$, $b_1 = \pm \frac{1}{2} \sqrt{\frac{3\lambda(\eta+\delta)(A^2 - B^2)}{\rho}}$,
 $\omega = -\frac{\lambda(5(\eta+\delta)(A^2 - B^2)a_0^2 + 4\eta\kappa^2 b_1^2)}{4b_1^2}$, $\sigma = -\frac{2\lambda(\eta+\delta)(A^2 - B^2)a_0}{b_1^2}$, $\mu = -\frac{\lambda(\eta+\delta)(A^2 - B^2)a_0^3}{4b_1^2}$.

$$Q(x, y, z, t) = \left[\pm \frac{R}{2} \sqrt{\frac{3\lambda(\eta + \delta)}{\rho}} \left\{ 1 \pm \frac{\sqrt{-(A^2 - B^2)} \operatorname{csch}(R[x \cos \alpha + y \cos \beta + z \cos \gamma - 2\lambda\eta\kappa t])}{A + B \coth(R[x \cos \alpha + y \cos \beta + z \cos \gamma - 2\lambda\eta\kappa t])} \right\} \right]^{\frac{1}{2}} e^{i\varphi}, \quad (44)$$

where $\lambda\rho(\eta + \delta) > 0$, $A^2 < B^2$ and $\varphi = \kappa(x \cos \alpha + y \cos \beta + z \cos \gamma) - \lambda\left([\eta + \delta] \frac{5R^2}{4} + \eta\kappa^2\right)t$.

Case II4. $a_2 = b_2 = 0$, $a_0 = -\frac{Rb_1}{(A+B)}$, $a_1 = \pm \frac{A^2 - B^2}{4A} \sqrt{-\frac{3\lambda(\eta + \delta)}{\rho}}$, $b_1 = \pm \frac{Aa_1}{A^2 - B^2} \sqrt{A^2 - B^2}$, $\omega = \frac{\lambda(\eta + \delta)(A+B)^2 a_0^2 - 4\eta\kappa^2 a_1^2}{4a_1^2}$, $\sigma = \frac{\lambda(\eta + \delta)(A+B)(A^2 - B^2)a_0}{2Aa_1^2}$, $\mu = 0$.

$$Q(x, y, z, t) = \left[\mp \frac{R}{4} \sqrt{-\frac{3\lambda(\eta + \delta)}{\rho}} \left\{ 1 - \frac{B + A \coth(R[x \cos \alpha + y \cos \beta + z \cos \gamma - 2\lambda\eta\kappa t])}{A + B \coth(R[x \cos \alpha + y \cos \beta + z \cos \gamma - 2\lambda\eta\kappa t])} \right\} \pm \frac{\sqrt{A^2 - B^2} \operatorname{csch}(R[x \cos \alpha + y \cos \beta + z \cos \gamma - 2\lambda\eta\kappa t])}{A + B \coth(R[x \cos \alpha + y \cos \beta + z \cos \gamma - 2\lambda\eta\kappa t])} \right]^{\frac{1}{2}} e^{i\varphi}, \quad (45)$$

where $\lambda\rho(\eta + \delta) < 0$, $A^2 > B^2$ and $\varphi = \kappa(x \cos \alpha + y \cos \beta + z \cos \gamma) + \lambda\left([\eta + \delta] \frac{R^2}{4} - \eta\kappa^2\right)t$.

Case II5. $a_2 = b_2 = 0$, $a_0 = \frac{Rb_1}{(A-B)}$, $a_1 = \pm \frac{A^2 - B^2}{4A} \sqrt{-\frac{3\lambda(\eta + \delta)}{\rho}}$, $b_1 = \pm \frac{Aa_1}{A^2 - B^2} \sqrt{A^2 - B^2}$, $\omega = \frac{\lambda(\eta + \delta)(A-B)^2 a_0^2 - 4\eta\kappa^2 a_1^2}{4a_1^2}$, $\sigma = \frac{\lambda(\eta + \delta)(A-B)(A^2 - B^2)a_0}{2Aa_1^2}$, $\mu = 0$.

$$Q(x, y, z, t) = \left[\pm \frac{R}{4} \sqrt{-\frac{3\lambda(\eta + \delta)}{\rho}} \left\{ 1 + \frac{B + A \coth(R[x \cos \alpha + y \cos \beta + z \cos \gamma - 2\lambda\eta\kappa t])}{A + B \coth(R[x \cos \alpha + y \cos \beta + z \cos \gamma - 2\lambda\eta\kappa t])} \right\} \pm \frac{\sqrt{A^2 - B^2} \operatorname{csch}(R[x \cos \alpha + y \cos \beta + z \cos \gamma - 2\lambda\eta\kappa t])}{A + B \coth(R[x \cos \alpha + y \cos \beta + z \cos \gamma - 2\lambda\eta\kappa t])} \right]^{\frac{1}{2}} e^{i\varphi}, \quad (46)$$

where $\lambda\rho(\eta + \delta) < 0$, $A^2 > B^2$ and $\varphi = \kappa(x \cos \alpha + y \cos \beta + z \cos \gamma) + \lambda\left([\eta + \delta] \frac{R^2}{4} - \eta\kappa^2\right)t$.

Case II6. $a_0 = -\frac{(2\lambda(\eta + \delta)A^2 - \sigma b_2)R^2}{\sigma A^2}$, $a_1 = -\frac{2BRb_2}{A^2}$, $b_1 = \pm \frac{2\lambda(\eta + \delta)R}{\sigma} \sqrt{-(A^2 - B^2)}$, $a_2 = -\frac{(A^2 - B^2)b_2}{A^2}$, $\omega = -\lambda\left([\eta + \delta] \frac{5R^2}{4} + \eta\kappa^2\right)$, $\rho = \frac{3\sigma^2}{16\lambda(\eta + \delta)R^2}$, $\mu = \frac{\lambda^2(\eta + \delta)^2 R^4}{2\sigma}$.

$$Q(x, y, z, t) = \left[-\frac{2\lambda(\eta + \delta)R^2}{\sigma} \left\{ 1 \pm \frac{\sqrt{-(A^2 - B^2)} \operatorname{csch}(R[x \cos \alpha + y \cos \beta + z \cos \gamma - 2\lambda\eta\kappa t])}{A + B \coth(R[x \cos \alpha + y \cos \beta + z \cos \gamma - 2\lambda\eta\kappa t])} \right\} \right]^{\frac{1}{2}} e^{i\varphi}, \quad (47)$$

where $A^2 < B^2$ and $\varphi = \kappa(x \cos \alpha + y \cos \beta + z \cos \gamma) - \lambda\left([\eta + \delta] \frac{5R^2}{4} + \eta\kappa^2\right)t$.

Case II7. $b_1 = 0$, $a_0 = \frac{(A^2 a_1 + (A+B)Rb_2)R}{(A-B)A^2}$, $a_1 = \frac{2(\lambda(\eta + \delta)(A^2 - B^2)A - \sigma Bb_2)R}{\sigma A^2}$, $a_2 = -\frac{(A^2 - B^2)b_2}{A^2}$,

$$\omega = \lambda([\eta + \delta]R^2 - \eta\kappa^2), \rho = -\frac{3\lambda(\eta+\delta)(A^2-B^2)^2A^2}{4(A^2a_1+2BRb_2)^2}, \mu = 0.$$

$$Q(x, y, z, t) = \left[\frac{2\lambda(\eta + \delta)R^2}{\sigma} \left\{ 1 + \frac{B + A \coth(R[x \cos \alpha + y \cos \beta + z \cos \gamma - 2\lambda\eta\kappa t])}{A + B \coth(R[x \cos \alpha + y \cos \beta + z \cos \gamma - 2\lambda\eta\kappa t])} \right\} \right]^{\frac{1}{2}} e^{i\varphi}, \quad (48)$$

where $\varphi = \kappa(x \cos \alpha + y \cos \beta + z \cos \gamma) + \lambda([\eta + \delta]R^2 - \eta\kappa^2)t$.

Case II8. $b_1 = 0, a_0 = -\frac{(A^2a_1-(A-B)Rb_2)R}{(A+B)A^2}, a_1 = -\frac{2(\lambda(\eta+\delta)(A^2-B^2)A+\sigma Bb_2)R}{\sigma A^2},$

$a_2 = -\frac{(A^2-B^2)b_2}{A^2}, \omega = \lambda([\eta + \delta]R^2 - \eta\kappa^2), \rho = -\frac{3\lambda(\eta+\delta)(A^2-B^2)^2A^2}{4(A^2a_1+2BRb_2)^2}, \mu = 0.$

$$Q(x, y, z, t) = \left[\frac{2\lambda(\eta + \delta)R^2}{\sigma} \left\{ 1 - \frac{B + A \coth(R[x \cos \alpha + y \cos \beta + z \cos \gamma - 2\lambda\eta\kappa t])}{A + B \coth(R[x \cos \alpha + y \cos \beta + z \cos \gamma - 2\lambda\eta\kappa t])} \right\} \right]^{\frac{1}{2}} e^{i\varphi}, \quad (49)$$

where $\varphi = \kappa(x \cos \alpha + y \cos \beta + z \cos \gamma) + \lambda([\eta + \delta]R^2 - \eta\kappa^2)t$.

Case II9. $a_0 = \frac{(\lambda(\eta+\delta)(A+B)A+2\sigma b_2)R^2}{2\sigma A^2}, a_1 = \frac{(A-B)A^2a_0-(A+B)R^2b_2}{A^2R}, b_1 =$

$\pm \frac{\lambda(\eta+\delta)R}{2\sigma} \sqrt{A^2 - B^2}, a_2 = -\frac{(A^2-B^2)b_2}{A^2}, \omega = \lambda([\eta + \delta] \frac{R^2}{4} - \eta\kappa^2), \rho = -\frac{3\sigma^2}{4\lambda(\eta+\delta)R^2}, \mu = 0.$

$$Q(x, y, z, t) = \left[\frac{\lambda(\eta + \delta)R^2}{2\sigma} \left\{ 1 + \frac{B + A \coth(R[x \cos \alpha + y \cos \beta + z \cos \gamma - 2\lambda\eta\kappa t])}{A + B \coth(R[x \cos \alpha + y \cos \beta + z \cos \gamma - 2\lambda\eta\kappa t])} \right. \right. \\ \left. \left. \pm \frac{\sqrt{A^2 - B^2} \operatorname{csch}(R[x \cos \alpha + y \cos \beta + z \cos \gamma - 2\lambda\eta\kappa t])}{A + B \coth(R[x \cos \alpha + y \cos \beta + z \cos \gamma - 2\lambda\eta\kappa t])} \right\} \right]^{\frac{1}{2}} e^{i\varphi}, \quad (50)$$

where $A^2 > B^2$ and $\varphi = \kappa(x \cos \alpha + y \cos \beta + z \cos \gamma) + \lambda([\eta + \delta] \frac{R^2}{4} - \eta\kappa^2)t$.

Case II10. $a_0 = \frac{(\lambda(\eta+\delta)(A-B)A+2\sigma b_2)R^2}{2\sigma A^2}, a_1 = -\frac{(A+B)A^2a_0-(A-B)R^2b_2}{A^2R}, b_1 =$

$\pm \frac{\lambda(\eta+\delta)R}{2\sigma} \sqrt{A^2 - B^2}, a_2 = -\frac{(A^2-B^2)b_2}{A^2}, \omega = \lambda([\eta + \delta] \frac{R^2}{4} - \eta\kappa^2), \rho = -\frac{3\sigma^2}{4\lambda(\eta+\delta)R^2}, \mu = 0.$

$$Q(x, y, z, t) = \left[\frac{\lambda(\eta + \delta)R^2}{2\sigma} \left\{ 1 - \frac{B + A \coth(R[x \cos \alpha + y \cos \beta + z \cos \gamma - 2\lambda\eta\kappa t])}{A + B \coth(R[x \cos \alpha + y \cos \beta + z \cos \gamma - 2\lambda\eta\kappa t])} \right. \right. \\ \left. \left. \pm \frac{\sqrt{A^2 - B^2} \operatorname{csch}(R[x \cos \alpha + y \cos \beta + z \cos \gamma - 2\lambda\eta\kappa t])}{A + B \coth(R[x \cos \alpha + y \cos \beta + z \cos \gamma - 2\lambda\eta\kappa t])} \right\} \right]^{\frac{1}{2}} e^{i\varphi}, \quad (51)$$

where $A^2 > B^2$ and $\varphi = \kappa(x \cos \alpha + y \cos \beta + z \cos \gamma) + \lambda([\eta + \delta] \frac{R^2}{4} - \eta\kappa^2)t$.

5. Results and remarks

To give a clear insight into the behavior of resonant optical solitons, the graphical representations for some of the extracted soliton solutions are presented. Besides, the obliqueness influence on the resonant solitons is examined. Thus, we

display the 3D and 2D plots of the absolute of these solutions by selecting different values of the model parameters. For example, **Figure 1(a)-(b)** present the 3D and 2D plots of resonant soliton for the solution given in (24) of 3D-RNLS equation with Kerr-law nonlinearity. It is clear from the graph that the wave profile represents bright soliton. **Figure 1(c)-(d)** display the 3D plot for the effect of obliquity on the resonant soliton given in (24), where **Figure 1(c)** shows the relation between x and α while **Figure 1(d)** illustrates the relation between x and γ . **Figure 2(a)-(b)** exhibit the 3D and 2D plots of resonant dark soliton given in the solution (29) of 3D-RNLS equation with Kerr-law nonlinearity. The obliqueness influence on the solution (29) is shown in **Figure 2(c)-(d)**. Additionally, **Figure 3(a)-(b)** demonstrate the 3D and 2D plots of resonant soliton given in the solution (40) of 3D-RNLS equation with parabolic-law nonlinearity, where the wave profile describes a kink-shape soliton. It can be seen that **Figure 3(c)-(d)** present the obliquity impact on the solution (40). **Figure 4(a)-(b)** depict the 3D and 2D plots of resonant singular soliton given in the solution (48) of 3D-RNLS equation with parabolic-law nonlinearity, where the effect of obliqueness on this wave is illustrated in **Figure 4(c)-(d)**.

One can obviously see from **Figures 1–4** that the obliqueness influences the behavior of resonant solitons, where the structure of solitons is changed remarkably with the variation of obliqueness parameters. Further to this, it is noticed that the

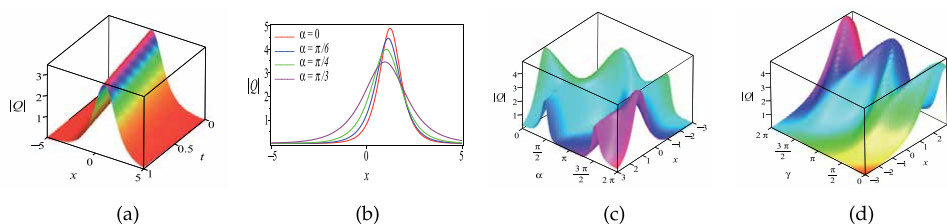


Figure 1. (a)-(b) Resonant soliton and (c)-(d) obliqueness effect on resonant soliton corresponding to solution (24) with $\kappa = 0.5, \eta = \delta = \sigma = 1, R = A = 2, B = 1, \alpha = \beta = \gamma = \pi/3, y = z = 0, t = 1$.

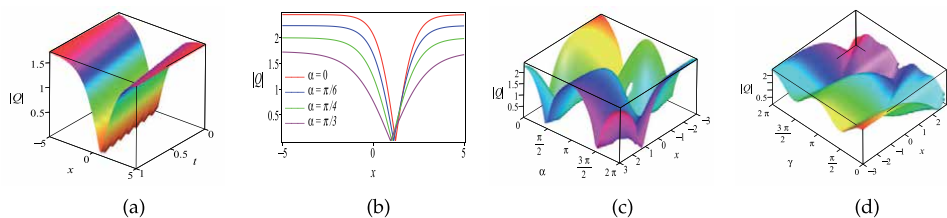


Figure 2. (a)-(b) Resonant soliton and (c)-(d) obliqueness effect on resonant soliton corresponding to solution (29) with the same values of parameters in **Figure 1** except $\sigma = -1$.

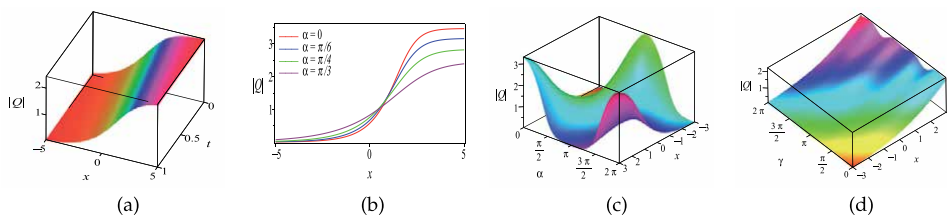


Figure 3. (a)-(b) Resonant soliton and (c)-(d) obliqueness effect on resonant soliton corresponding to solution (40) with the same values of parameters in **Figure 1** except $A = 1, B = -2$.

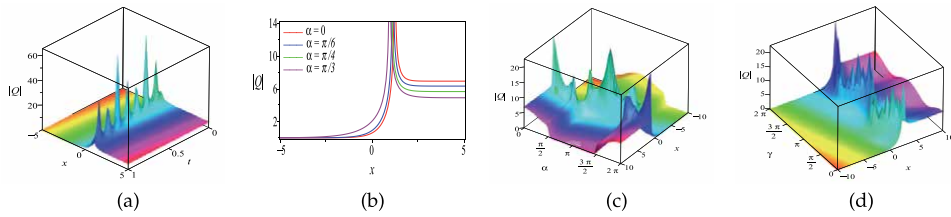


Figure 4. (a)-(b) Resonant soliton and (c)-(d) obliqueness effect on resonant soliton corresponding to solution (48) with the same values of parameters in **Figure 1**.

amplitude of the resonant solitons decreases and the width rises with the increase of obliqueness as shown in the 2D graphs.

6. Conclusions

This work scoped the behavior of optical solitons of 3D-RNLS equation. The dominant nonlinearity in the model is considered to have two forms which are Kerr law and parabolic law. The resonant solitons are derived with the aid of projective Riccati equations method. Various forms of wave structures are retrieved such as bright, dark, singular, kink, dark-singular and combined singular solitons. The influence of obliquity on resonant solitons is also examined. It is found that the change in the obliqueness parameters leads to a noticeable variation on the behavior of optical soliton waves. In addition to this, the amplitude of the resonant solitons undergoes a reduction, but their width is enhanced as the obliqueness is increased. The results obtained in this work are entirely new and it may be useful to understand the dynamics of resonant solitons affected by obliqueness in different nonlinear media such as optical fiber and Madelung fluids.

Conflict of interest

The author declares no conflict of interest.

Author details

Khalil S. Al-Ghafri
University of Technology and Applied Sciences, Ibri, Oman

*Address all correspondence to: khalil.ibr@cas.edu.om

IntechOpen

© 2021 The Author(s). Licensee IntechOpen. This chapter is distributed under the terms of the Creative Commons Attribution License (<http://creativecommons.org/licenses/by/3.0>), which permits unrestricted use, distribution, and reproduction in any medium, provided the original work is properly cited. 

References

- [1] Lonngren KE. Soliton experiments in plasmas. *Plasma Physics*. 1983;25(9): 943–982.
- [2] Agrawal GP. *Nonlinear fiber optics: quantum electronics—principles and applications*. Academic Press, New York; 1995.
- [3] Mollenauer LF, Gordon JP. *Solitons in optical fibers: fundamentals and applications*. Elsevier; 2006.
- [4] Biswas A, Konar S. *Introduction to non-Kerr law optical solitons*. CRC Press; 2006.
- [5] Bao W. The nonlinear Schrödinger equation and applications in Bose-Einstein condensation and plasma physics. *Dynamics in Models of Coarsening, Coagulation, Condensation and Quantization* (IMS Lecture Notes Series, World Scientific). 2007;9:141–240.
- [6] Gedalin M, Scott T, Band Y. Optical solitary waves in the higher order nonlinear Schrödinger equation. *Physical review letters*. 1997;78(3):448.
- [7] Hong WP. Optical solitary wave solutions for the higher order nonlinear Schrödinger equation with cubic-quintic non-kerr terms. *Optics Communications*. 2001;194(1-3):217–223.
- [8] Liu W, Pang L, Han H, et al. Tungsten disulphide for ultrashort pulse generation in all-fiber lasers. *Nanoscale*. 2017;9(18):5806–5811.
- [9] Liu W, Zhu YN, Liu M, et al. Optical properties and applications for MoS₂-Sb₂Te₃-MoS₂ heterostructure materials. *Photonics Research*. 2018;6(3):220–227.
- [10] Singer A. *Signal processing and communication with solitons [dissertation]*. Massachusetts Institute of Technology; 1996.
- [11] Song Y, Shi X, Wu C, et al. Recent progress of study on optical solitons in fiber lasers. *Applied Physics Reviews*. 2019;6(2):021313.
- [12] Porsezian K. Soliton propagation in nonlinear optics with higher-order effects. *Journal of Modern Optics*. 1997; 44(2):387–394.
- [13] Radhakrishnan R, Kundu A, Lakshmanan M. Coupled nonlinear Schrödinger equations with cubic-quintic nonlinearity: integrability and soliton interaction in non-kerr media. *Physical Review E*. 1999;60(3): 3314.
- [14] Triki H, Hayat T, Aldossary OM, et al. Bright and dark solitons for the resonant nonlinear Schrödinger's equation with time-dependent coefficients. *Optics & Laser Technology*. 2012;44(7):2223–2231.
- [15] Triki H, Yildirim A, Hayat T, et al. 1-soliton solution of the generalized resonant nonlinear dispersive Schrödinger's equation with time-dependent coefficients. *Advanced Science Letters*. 2012;16(1):309–312.
- [16] Biswas A. Soliton solutions of the perturbed resonant nonlinear Schrödinger's equation with full nonlinearity by semi-inverse variational principle. *Quantum Phys Lett*. 2012;1(2):79–89.
- [17] Eslami M, Mirzazadeh M, Biswas A. Soliton solutions of the resonant nonlinear Schrödinger's equation in optical fibers with time-dependent coefficients by simplest equation approach. *Journal of Modern Optics*. 2013;60(19):1627–1636.
- [18] Eslami M, Mirzazadeh M, Vajargah BF, et al. Optical solitons for the resonant nonlinear Schrödinger's equation with time-dependent

- coefficients by the first integral method. *Optik*. 2014;125(13):3107–3116.
- [19] Mirzazadeh M, Eslami M, Vajargah BF, et al. Optical solitons and optical rogons of generalized resonant dispersive nonlinear Schrödinger's equation with power law nonlinearity. *Optik*. 2014;125(16):4246–4256.
- [20] Mirzazadeh M, Eslami M, Milovic D, et al. Topological solitons of resonant nonlinear Schrödinger's equation with dual-power law nonlinearity by G'/G -expansion technique. *Optik*. 2014;125(19): 5480–5489.
- [21] Mirzazadeh M, Arnous A, Mahmood M, et al. Soliton solutions to resonant nonlinear Schrödinger's equation with time-dependent coefficients by trial solution approach. *Nonlinear Dynamics*. 2015;81(1):277–282.
- [22] Kilic B, Inc M. On optical solitons of the resonant Schrödinger's equation in optical fibers with dual-power law nonlinearity and time-dependent coefficients. *Waves in Random and Complex Media*. 2015;25(3):334–341.
- [23] Arnous AH, Mirzazadeh M, Zhou Q, et al. Soliton solutions to resonant nonlinear schrodinger's equation with time-dependent coefficients by modified simple equation method. *Optik*. 2016;127(23): 11450–11459.
- [24] Mirzazadeh M, Ekici M, Zhou Q, et al. Exact solitons to generalized resonant dispersive nonlinear Schrödinger's equation with power law nonlinearity. *Optik*. 2017;130:178–183.
- [25] Al-Ghafri KS. Different physical structures of solutions for a generalized resonant dispersive nonlinear schrödinger equation with power law nonlinearity. *Journal of Applied Mathematics*. 2019;2019:1–8.
- [26] Pashaev OK, Lee JH. Resonance solitons as black holes in madelung fluid. *Modern Physics Letters A*. 2002;17(24):1601–1619.
- [27] Ferdous F, Hafez MG, Biswas A, et al. Oblique resonant optical solitons with Kerr and parabolic law nonlinearities and fractional temporal evolution by generalized $\exp(-\phi(\xi))$ -expansion. *Optik*. 2019;178:439–448.
- [28] Sedeeg AKH, Nuruddeen R, Gomez-Aguilar J. Generalized optical soliton solutions to the $(3+1)$ -dimensional resonant nonlinear schrödinger equation with kerr and parabolic law nonlinearities. *Optical and Quantum Electronics*. 2019;51(6):1–15.
- [29] Hosseini K, Matinfar M, Mirzazadeh M. A $(3+1)$ -dimensional resonant nonlinear Schrödinger equation and its jacobi elliptic and exponential function solutions. *Optik*. 2020;207:164458.
- [30] Hosseini K, Ansari R, Zabihi A, et al. Optical solitons and modulation instability of the resonant nonlinear Schrödinger equations in $(3+1)$ -dimensions. *Optik*. 2020;209:164584.

Traveling Wave Solutions and Chaotic Motions for a Perturbed Nonlinear Schrödinger Equation with Power-Law Nonlinearity and Higher-Order Dispersions

Mati Youssoufa, Ousmanou Dafounansou,

Camus Gaston Latchio Tiofack and Alidou Mohamadou

Abstract

This chapter aims to study and solve the perturbed nonlinear Schrödinger (NLS) equation with the power-law nonlinearity in a nano-optical fiber, based upon different methods such as the auxiliary equation method, the Stuart and DiPrima's stability analysis method, and the bifurcation theory. The existence of the traveling wave solutions is discussed, and their stability properties are investigated through the modulational stability gain spectra. Moreover, the development of the chaotic motions for the systems is pointed out *via* the bifurcation theory. Taking into account an external periodic perturbation, we have analyzed the chaotic behavior of traveling waves through quasiperiodic route to chaos.

Keywords: nano-optical fibers, perturbed nonlinear Schrödinger equation, auxiliary equation method, exact traveling wave solutions, modulational instability, planar dynamic system, chaotic motions

1. Introduction

The wave process is innumerable in nature. Such familiar examples include water waves, plasma waves, and optical waves and are governed by nonlinear partial differential equations. The study of nonlinear evolution equations helps a lot in understanding certain interesting physical properties posed by themselves, in several physical systems. Recently, an important amount of studies has been related to nonlinear systems having multidegrees of freedom: The well-known nonlinear Schrödinger (NLS) equation is a particular example. The idea behind the NLS equation was originated from the work of Erwin Schrödinger, an Austrian physicist, in 1926 [1]. This equation governs weakly nonlinear and dispersive wave packets in one-dimensional (1D) physical systems. It was first derived, in a general setting, by Benney and Newell in 1967 [2]. Also, it was derived in the study of modulational stability of deep-water waves by Zakharov in 1968 [3]. Afterward, Hasegawa and Tappert (1973) showed that the same equation governs light-pulse

propagation in optical fibers [4]. For instance, the cubic-NLS has been widely used to model the propagation of light pulse in material's systems involving third-order susceptibility $\chi^{(3)}$ [5–7]. In the same context, the nonlinear interaction between the high-frequency Langmuir waves and the ion-acoustic waves by ponderomotive forces [8, 9] in a region of reduced plasma density, and the nonlinear interaction between Langmuir waves and electrons, were described by the “*parabolic law nonlinearity*” (cubic-quintic CQ) that existing in nonlinear media such as the CdS_xSe_{1-x} -doped glass [10, 11], the poly-toluene sulfonate (PTS) crystals, special semiconductor waveguides (e.g., AlGaAs, CdS) [12]. Furthermore, Serkin et al. [13], Dai et al. [14], and others have devoted pioneering works in order to analyze the dynamical propagation of light pulse in CQ-nonlinear media, by considering the CQ-NLS equation.

Generally, the NLS-type models are important classes of nonlinear evolution equations that play a crucial role in the study of nonlinear dynamical problems in several areas of nonlinear sciences such as nonlinear optics, plasmas and Bose-Einstein condensates, and nano-optical fibers among others [15–18]. Although these equations explain the pulse dynamics in optical fibers [19–22], some of these nonlinear models are non-integrable. In this context, various computational and analytical methods have been proposed and used in the past few decades, to examine many classes of Schrödinger equation [23–42]. Nonetheless, these investigations reveal that the dynamic of solutions in non-integrable systems can be important and more complex.

Our study will be focused on a nano-optical fiber-system, described by the following extended perturbed NLS equation (integrable equation named as Biswas-Arshed model), involving power-law nonlinearity and higher-order dispersions [20–22]:

$$i\psi_z + a_1\psi_{xx} + a_2\psi_{xt} + b_1|\psi|^{2n}\psi + b_2|\psi|^{4n}\psi - i\left[\alpha\psi_x + \gamma(|\psi|^{2n}\psi)_x + \sigma(|\psi|^{2n})_x\psi + \delta(|\psi|^{4n}\psi)_x + \lambda(|\psi|^{4n})_x\psi + \theta|\psi|^{2n}\psi_x\right] = 0, \quad (1)$$

where the complex-valued function $\psi(z, x)$ is designated for waveform, which depends on the temporal variable z and the spatial variable x ; a_1 and a_2 are, respectively, the group velocity dispersion (GVD) and spatiotemporal dispersion coefficients (STD). b_1 and b_2 correspond to the coefficient of power-law nonlinearity; α accounts for the inter-modal dispersion. γ and δ account for the self-steepening perturbation terms, while σ , λ , and θ provide the effect of nonlinear dispersion coefficient. Finally, n denotes the strength of the power-law nonlinearity.

This model is relevant to some applications in which higher-order nonlinearities are important and describe the dynamics of solitary-wave propagation through optical fibers and other forms of waveguides, and contains, under different circumstances, several integrable NLS-types such as the Hirota equation [43], the Sasa Satsuma model [44], Gerdjikov-Ivanov equation, Lakshmanan-Porsezian-Daniel model, Schrödinger-Hirota equation, and a variety of other such models. More specially, Eq. (1) with $b_2 = \sigma = \delta = \lambda = \theta = 0$ and $0 < n < 2$ was used to study chaotic motions for the perturbed NLS equation with the power-law nonlinearity based on the equilibrium points by Yin et al. [20] and was also considered by Savescu et al. [45] to analyze nonlinear dynamical problems in the nano-optical fibers. Here, we study the model Eq. (1) with arbitrary parameters that are valid for several types of highly nonlinear mediums and give rise to some new results. For this purpose, we would like to obtain the exact solutions of Eq. (1) by using the auxiliary equation method [46–48] and the bifurcation theory of planar dynamical systems [49, 50].

The auxiliary equation method is a powerful solution method for the computation of exact traveling wave and soliton solutions. It is a one of the most direct and effective algebraic methods for finding exact solutions of nonlinear partial differential equations. This method is applicable to a large class of equations and does not need therefore to make strong assumptions about the nonlinear equations, as compared to the well-known inverse scattering transform, which uses powerful analytical methods and therefore makes strong assumptions.

The bifurcation theory of planar dynamical systems plays a crucial role in the study of the evolution of higher-order nonlinear equations. The bifurcation analysis can be used to obtain chaotic motions for Eq. (1) based on the equilibrium points.

We will discuss model Eq. (1) and explore the dynamics of traveling wave solutions by employing the auxiliary equation method. In addition, using the linear stability analysis formulation, we will analyze and report the typical outcomes of the nonlinear development of the modulational instability (MI). Finally, we will point out the development of the chaotic motions for systems described by Eq. (1) through the bifurcation theory.

2. Exact solutions

2.1 The auxiliary equation method

In order to obtain the exact analytic traveling wave solutions of Eq. (1), we can employ the auxiliary equation method by considering the following transformation:

$$\psi(z, x) = U(\zeta)e^{i\phi(\zeta)}, \quad \zeta = k_1x - k_2z. \quad (2)$$

Here, k_1 and k_2 are real constants, $U(\zeta)$ denotes the amplitude and $\phi(\zeta)$ characterizes the phase component of the soliton.

Putting Eq. (2) into Eq. (1) and separating the real and imaginary parts, one obtains

$$\begin{aligned} b_1U^{2n+1} + (b_2 + k_1\phi_\zeta)U^{4n+1} + k_1(\gamma + \theta)\phi_\zeta U^{2n+1} + (k_2 + \alpha k_1)\phi_\zeta U \\ - k_1(a_1k_1 - a_2k_2)(\phi_\zeta^2 U + U_{\zeta\zeta}) = 0, \end{aligned} \quad (3)$$

and

$$\begin{aligned} -k_1[\delta + 4n(\delta + \lambda)]U_\zeta U^{4n} - (k_2 + \alpha k_1)U_\zeta - k_1[\gamma + \theta + 2n(\gamma + \sigma)]U_\zeta U^{2n} \\ + k_1(a_1k_1 - a_2k_2)(2\phi_\zeta U_\zeta + \phi_{\zeta\zeta} U) = 0. \end{aligned} \quad (4)$$

We set:

$$\phi_\zeta = p_1 - p_2 U^{2n}, \quad \phi_{\zeta\zeta} = -2np_2 U_\zeta U^{2n-1}. \quad (5)$$

The substitution of Eq. (5) into Eq. (4) gives

$$p_1 = \frac{k_2 + \alpha k_1}{2k_1(a_1k_1 - a_2k_2)}, \quad p_2 = -\frac{\gamma + \theta + 2n(\gamma + \sigma)}{2(n+1)(a_1k_1 - a_2k_2)}, \quad (6)$$

under the restraint relation

$$\lambda = -(4n + 1)\delta. \quad (7)$$

Plugging Eq. (5) into Eq. (3) with respect to Eqs. (6) and (7), we get

$$\begin{aligned} & k_1(a_1k_1 - a_2k_2)U_{\zeta\zeta} + [p_1(k_2 + \alpha k_1) - p_1^2k_1(a_1k_1 - a_2k_2)]U \\ & + [b_1 + k_1p_1(\gamma + \theta) + p_2(k_2 + \alpha k_1) - 2p_1p_2k_1(a_1k_1 - a_2k_2)]U^{2n+1}. \\ & + [b_2 + k_1p_1 + k_1p_2(\gamma + \theta) - p_2^2k_1(a_1k_1 - a_2k_2)]U^{4n+1} + k_1p_2U^{6n+1} = 0. \end{aligned} \quad (8)$$

The substitution of

$$U(\zeta) = V^{\frac{1}{2n}}(\zeta), \quad (9)$$

in Eq. (8) yields:

$$\begin{aligned} & k_1(a_1k_1 - a_2k_2) \left[2nVV_{\zeta\zeta} + (1 - 2n)(V_{\zeta})^2 \right] + 4n^2k_1p_2V^5 \\ & + 4n^2[b_2 + k_1p_1 + k_1p_2(\gamma + \theta) - p_2^2k_1(a_1k_1 - a_2k_2)]V^4 \\ & + 4n^2[b_1 + k_1p_1(\gamma + \theta) + p_2(k_2 + \alpha k_1) - 2p_1p_2k_1(a_1k_1 - a_2k_2)]V^3 \\ & + 4n^2[p_1(k_2 + \alpha k_1) - p_1^2k_1(a_1k_1 - a_2k_2)]V^2 = 0. \end{aligned} \quad (10)$$

We consider the trial equation as [46, 47]:

$$(V_{\zeta})^2 = F(V) = \sum_{l=0}^N \mu_l V^l, \quad (11)$$

where $\mu_l (l = 0, 1, \dots, N)$ are constants to be determined according to the balance principle. The previous Eq. (11) can be rewritten by the integral form

$$\pm(\zeta - \zeta_0) = \int \frac{dV}{\sqrt{F(V)}}. \quad (12)$$

Balancing $VV_{\zeta\zeta}$ and V^5 in Eq. (10), we get $N = 5$. Using the solution procedure of the trial equation method [46, 47], a system of algebraic equations is obtained (see Appendix) and the resolution of this obtained system yields the following:

$$\begin{aligned} \mu_0 &= 0, \mu_1 = 0, \mu_2 = 4n^2 \left[p_1^2 - \frac{p_1(k_2 + \alpha k_1)}{k_1(a_1k_1 - a_2k_2)} \right], \\ \mu_3 &= \frac{4n^2}{n+1} \left[2p_1p_2 - \frac{b_1 + k_1p_1(\gamma + \theta) + p_2(k_2 + \alpha k_1)}{k_1(a_1k_1 - a_2k_2)} \right], \\ \mu_4 &= \frac{4n^2}{2n+1} \left[p_2^2 - \frac{b_2 + k_1p_1 + k_1p_2(\gamma + \theta)}{k_1(a_1k_1 - a_2k_2)} \right], \\ \mu_5 &= -\frac{4n^2p_2}{(a_1k_1 - a_2k_2)(3n+1)}. \end{aligned} \quad (13)$$

Now, from Eqs. (11) and (12), we can write

$$\pm(\zeta - \zeta_0) = \int \frac{dV}{V \sqrt{\mu_2 + \mu_3V + \mu_4V^2 + \mu_5V^3}}. \quad (14)$$

The integral Eq. (14) admits many types of solutions that can be listed in accordance with [51–53].

Since $\mu_2 = 4n^2 \left[p_1^2 - \frac{p_1(k_2 + \alpha k_1)}{k_1(a_1 k_1 - a_2 k_2)} \right] = -\frac{n^2(k_2 + \alpha k_1)^2}{k_1^2(a_1 k_1 - a_2 k_2)^2} < 0$, and in order to highlight our analysis, we consider the following parametric setting $\gamma = -\sigma = -\theta$. After these considerations, the phase component of the soliton can be written as follows:

$$\phi(z, x) = \frac{k_2 + \alpha k_1}{2k_1(a_1 k_1 - a_2 k_2)} (k_1 x - k_2 z) + c, \quad (15)$$

where c is a real constant number.

a. If $4\mu_2\mu_4 - \mu_3^2 = 0$ and $\mu_4 > 0$, we have the following exact traveling solution.

$$\psi_a(z, x) = \left\{ \frac{\mu_3}{4\mu_4} \left[1 \pm \operatorname{cotanh} \left(\frac{\mu_3 \sqrt{\mu_4}}{4\mu_4} (k_1 x - k_2 z) \right) \right] \right\}^{\frac{1}{2n}} e^{i\phi(z, x)}, \quad (16)$$

under the constraint $\mu_4 > 0$.

b. If $\mu_3^2 - 4\mu_2\mu_4 > 0$ and $\mu_2 < 0$ we get a singular periodic solution

$$\psi_b(z, x) = \left\{ \frac{2\mu_2}{-\mu_3 \pm \sqrt{\mu_3^2 - 4\mu_2\mu_4} \sin [\sqrt{-\mu_2} (k_1 x - k_2 z)]} \right\}^{\frac{1}{2n}} e^{i\phi(z, x)}. \quad (17)$$

2.2 Stability analysis method: Modulational instability (MI) of the continuous wave (CW) background

Modulational instability (MI) is a fundamental and ubiquitous phenomenon originating from the interplay between nonlinear self-interaction of wave fields and linear dispersion or diffraction. This process appears in most nonlinear systems [42, 52–57]. Unlike the well-known pulse kinds, the solitons are relatively stable, even in a perturbed environment.

In this section, we investigate the stability of the previous solutions that are sitting on a CW background, which may be subject to MI. To do so, we apply the standard linear stability analysis [52, 53, 56] on a generic CW (steady-state solution)

$$\psi_0(z, x) = P_0 e^{i(c_1 x + c_2 z)}, \quad (18)$$

where P_0 , c_1 , and c_2 are real constants.

Putting Eq. (18) into Eq. (1), we get:

$$c_2 = \frac{1}{1 + a_2 c_1} \{ (\alpha - a_1 c_1) c_1 + [b_1 + (\gamma + \theta) c_1] P_0^{2n} + (b_2 + \delta c_1) P_0^{4n} \}. \quad (19)$$

Adding infinitesimal perturbation field v on CW solutions by introducing the following expansion

$$\tilde{\psi}(z, x) = [P_0 + v(z, x)] e^{i(c_1 x + c_2 z)}, \quad (20)$$

one can find the linearized equation satisfied by the complex perturbation v as:

$$ir_1v_z + ir_2v_x + a_1v_{xx} + a_1v_{xz} + r_3(v + v^*) + ir_4(v_x + v_x^*) = 0, \quad (21)$$

where

$$\begin{aligned} r_1 &= 1 + a_2c_1, \\ r_2 &= 2a_1c_1 + a_2c_2 - \alpha - (\gamma + \theta)P_0^{2n} - \delta P_0^{4n}, \\ r_3 &= nP_0^{2n} [b_1 + (\gamma + \theta)c_1 + 2(b_2 + \delta c_1)P_0^{2n}], \\ r_4 &= -nP_0^{2n} [\gamma + \sigma + 2(\delta + \lambda)P_0^{2n}]. \end{aligned} \quad (22)$$

The solution of Eq. (21) is given by collecting the Fourier modes as

$$v(z, x) = v_+e^{i(Kz - \Omega x)} + v_-e^{-i(Kz - \Omega x)}, \quad (23)$$

where Ω accounts for the wavenumber and K represents the frequency of perturbation. v_+ and v_- are much less than the background amplitude P_0 ($|v(z, x)| \ll P_0$). In this case, the instability of the steady state (CW) is achieved by the exponential growth of the perturbed field.

Deputing the expression of perturbed nonlinear background Eq. (23) into Eq. (21), we obtain after linearization, a system of homogeneous equations satisfied by v_+ and v_- :

$$\begin{pmatrix} (a_2\Omega - r_1)K + (r_2 + r_4)\Omega + r_3 - a_1\Omega^2 & r_3 + \Omega r_4 \\ r_3 - \Omega r_4 & (a_2\Omega + r_1)K - (r_2 + r_4)\Omega + r_3 - a_1\Omega^2 \end{pmatrix} \begin{pmatrix} v_+ \\ v_- \end{pmatrix} = \begin{pmatrix} 0 \\ 0 \end{pmatrix}. \quad (24)$$

This set has a nontrivial solution only when the previous 2×2 determinant matrix vanishes. By requiring the determinant of the associated matrix to be zero, we get the dispersion relation:

$$\begin{aligned} (a_2^2\Omega^2 - r_1^2)K^2 + 2\Omega[a_2(r_3 - a_1\Omega^2) + r_1(r_2 + r_4)]K + (r_3 - a_1\Omega^2)^2 \\ - \Omega^2(r_2 + r_4)^2 = 0. \end{aligned} \quad (25)$$

In order to observe MI, one of the two roots of the previous dispersion relation should possess a negative imaginary part, which corresponds to an exponential growth of the perturbation amplitude. So, the MI is measured by power gain, and it is defined at any pump frequency as [52, 53]:

$$g(\Omega) = 2|Im(K_{max})|, \quad (26)$$

where the factor 2 converts $g(\Omega)$ to power gain, and $Im(K_{max})$ denotes the imaginary part of the polynomial root with the largest value K_{max} .

Figure 1 depicts the MI gain spectra as a function of the modulation frequency (Ω) and second-order dispersion (a_1), for a fixed value of the initial power ($P_0 = 10kW$), the other parameter values being $a_2 = 0.005$, $b_1 = b_2 = \alpha = 0.2$, $c_1 = 2$, $\gamma = -\theta = -\sigma = 1$, $\delta = 0.5$. Firstly, we consider the strength of the power-law nonlinearity $n = 1$, which yields to symmetrical sidelobes of instability around the zero-perturbation frequency $\Omega = 0$ in **Figure 1(a)**. In this map, the width and magnitude of the two sidelobes remain constant in the normal group velocity dispersion ($a_1 < 0$), while they increase in the anomalous dispersion regime ($a_1 > 0$). For the nonlinearity power index $n = 2$, we obtain in **Figure 1(b)**, two similar sidelobes due to MI, which stand symmetrically around the line $\Omega = 0$. In this case,

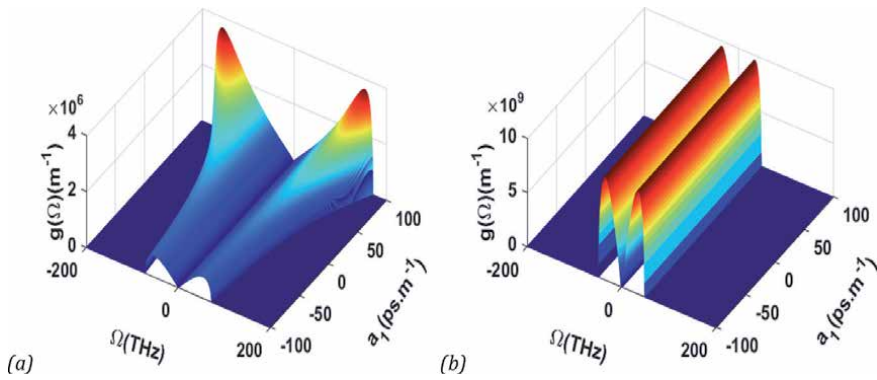


Figure 1. MI gain spectra $g(\Omega)$ versus frequency shift Ω and second-order dispersion a_1 for parameter values: $a_2 = 0.005$, $b_1 = b_2 = \alpha = 0.2$, $c_1 = 2$, $\gamma = -\theta = -\sigma = 1$, $\delta = 0.5$, $P_0 = 10$: (a) $n = 1$; (b) $n = 2$.

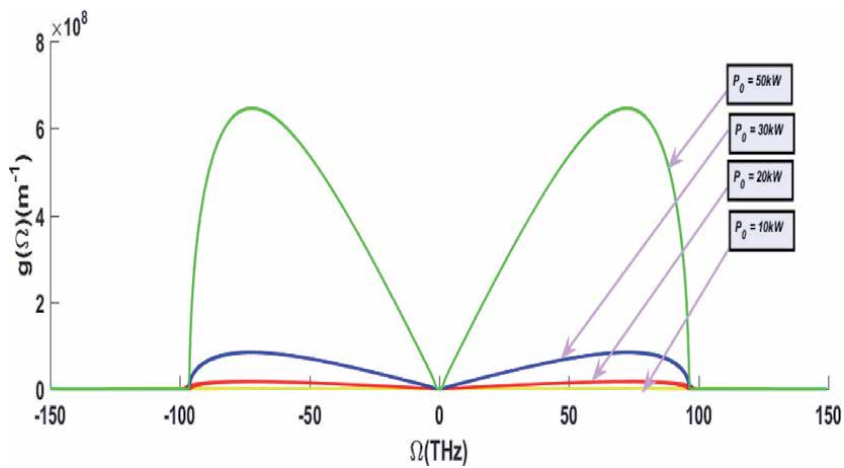


Figure 2. 2D plot showing the variation of the MI gain spectra $g(\Omega)$ versus frequency Ω at a four-power level P_0 [for yellow solid line ($P_0 = 10\text{kW}$), red solid line ($P_0 = 20\text{kW}$), blue solid line ($P_0 = 30\text{kW}$), and green solid line ($P_0 = 50\text{kW}$)], with the same parameter values as in **Figure 1**.

the magnitude and width of the sidelobes remain constant in the normal as well as the anomalous dispersion regimes.

Figure 2 exhibits the enlarged MI gain spectra in 2D-plot at four power levels ($P_0 = 10\text{kW}$; 20kW ; 30kW ; 50kW) with the same values of parameters as in **Figure 1**. The MI gain profile, indicated by colored solid curves, is constitutive of two gain bands in the Stokes frequency shift region ($\Omega < 0$) and in the anti-Stokes frequency shift region ($\Omega > 0$). We can see that the MI gain exists only within a limited range of frequency ($|\Omega| < 100$) and the maximum gain increases with the increasing input power P_0 .

3. Planar dynamical system and Hamiltonian: Phase portraits

In this section, we transform Eq. (8) to a dynamical system by introducing new variables X and Y , in order to investigate the equilibrium points, the periodic, quasiperiodic, and chaotic motions of systems in the presence of an external periodic perturbation, *via* the bifurcation method [49, 50, 58].

3.1 Formation of a dynamical system

Now, we rewrite Eq. (8) as

$$U_{\zeta\zeta} = AU + BU^{2n+1} + CU^{4n+1} + DU^{6n+1}, \quad (27)$$

where

$$\begin{aligned} A &= p_1^2 - \frac{p_1(k_2 + \alpha k_1)}{k_1(a_1 k_1 - a_2 k_2)} = -\frac{(k_2 + \alpha k_1)^2}{4k_1^2(a_1 k_1 - a_2 k_2)^2} < 0, \\ B &= 2p_1 p_2 - \frac{b_1 + k_1 p_1(\gamma + \theta) + p_2(k_2 + \alpha k_1)}{k_1(a_1 k_1 - a_2 k_2)}, \\ C &= p_2^2 - \frac{b_2 + k_1 p_1 + k_1 p_2(\gamma + \theta)}{k_1(a_1 k_1 - a_2 k_2)}, \\ D &= -\frac{k_1 p_2}{k_1(a_1 k_1 - a_2 k_2)}. \end{aligned} \quad (28)$$

By setting

$$X = U, Y = U_{\zeta}, \quad (29)$$

we can rewrite Eq. (27) as a planar dynamical system

$$\begin{cases} X_{\zeta} = Y, \\ Y_{\zeta} = f(X) = AX + BX^{2n+1} + CX^{4n+1} + DX^{6n+1}. \end{cases} \quad (30)$$

The Hamiltonian of the dynamical system Eq. (30) is defined as

$$H(X, Y) = \frac{1}{2}Y^2 - \frac{A}{2}X^2 - \frac{B}{2(n+1)}X^{2n+2} - \frac{C}{2(2n+1)}X^{4n+2} - \frac{D}{2(3n+1)}X^{6n+2}, \quad (31)$$

and satisfy to

$$\frac{dH}{d\zeta} = \frac{\partial H}{\partial \zeta} X_{\zeta} + \frac{\partial H}{\partial \zeta} Y_{\zeta} = 0. \quad (32)$$

This result implies that the Hamiltonian is a constant of motion [i.e., $H(X, Y) \equiv Cst$] and the system Eq. (30) is an integrable Hamiltonian system.

3.2 Chaotic motion analysis

3.2.1 Equilibrium state derivation

Using the bifurcation analysis and qualitative theory, we analyze equilibrium points for system Eq. (30). We consider the following Jacobian matrix of system (30) at the equilibrium points (X_k, Y_k) :

$$J = \begin{pmatrix} \frac{\partial X_\zeta}{\partial X} & \frac{\partial X_\zeta}{\partial Y} \\ \frac{\partial Y_\zeta}{\partial X} & \frac{\partial Y_\zeta}{\partial Y} \end{pmatrix} = \begin{pmatrix} 0 & 1 \\ A + (2n+1)BX_k^{2n} + (4n+1)CX_k^{4n} + (6n+1)DX_k^{6n} & 0 \end{pmatrix}, \quad (33)$$

where X_k are the zeros (solutions) of $f(X)$, and the determinant of J is expressed by $M \equiv \det(J)$ as

$$M = -A - (2n+1)BX_k^{2n} - (4n+1)CX_k^{4n} - (6n+1)DX_k^{6n}. \quad (34)$$

We research equilibrium points that satisfy $X_\zeta = Y_\zeta = f(X) = 0$, and we find

$$\begin{cases} Y = 0, \\ X(A + BX^{2n} + CX^{4n} + DX^{6n}) = 0. \end{cases} \quad (35)$$

It is obvious to notice that $\text{Trace}(J) = 0$, and through the bifurcation theory [49, 50, 58], we know that, the solution (X_j, Y_j) of Eq. (35) is a:

- center point, if $M > 0$;
- saddle point, if $M < 0$;
- degenerate point, if $M = 0$.

From Eq. (35), firstly, we have one equilibrium point $(X, Y) = (0, 0)$ for the dynamical system Eq. (30), which is a center point, and hence stable.

- If we consider $A = 0$, we have

$$\begin{cases} Y = 0, \\ X^{2n+1}(B + CX^{2n} + DX^{4n}) = 0, \end{cases} \quad (36)$$

and by setting $\Delta = C^2 - 4BD$, we can discuss the following situations:

- If $\Delta < 0$, Eq. (36) has only one real root, which indicates that the dynamical system Eq. (30) has one equilibrium point $(X, Y) = (0, 0)$, which is a center point.
- If $\Delta = 0$ and $-\frac{C}{2D} > 0$, Eq. (36) has three real roots, which indicates that the dynamical system Eq. (30) has three equilibrium points: $(X, Y) \equiv (0, 0); \left(\sqrt[2n]{-\frac{C}{2D}}, 0\right); \left(-\sqrt[2n]{-\frac{C}{2D}}, 0\right)$. The first equilibrium point $(0, 0)$ is a center point; the second $\left(\sqrt[2n]{-\frac{C}{2D}}, 0\right)$ and third $\left(-\sqrt[2n]{-\frac{C}{2D}}, 0\right)$ points are also center points if $M > 0$. Else, if $M < 0$, they are saddle points and hence unstable.
- If $\Delta > 0$, $C < 0$, and $D < 0$, Eq. (36) has just one root; we find one equilibrium point $(0, 0)$, which indicates a stable center point.

- For $A \neq 0$, we get

$$\begin{cases} Y = 0, \\ A + BX^{2n} + CX^{4n} + DX^{6n} = 0. \end{cases} \quad (37)$$

We consider an evident root of the polynomial equation $A + BX^{2n} + CX^{4n} + DX^{6n} = 0$, as X_0 [i.e., $A + BX_0^{2n} + CX_0^{4n} + DX_0^{6n} = 0$] and setting $\Delta' = (C + DX_0^{2n})^2 - 4D[B + X_0^{2n}(C + DX_0^{2n})]$. After this consideration, we can discuss the equilibrium points for the dynamical system Eq. (30):

- If $\Delta' < 0$, we get a first equilibrium point as $(X_0, 0)$, which is a center point.
- If $\Delta' = 0$ and $-\frac{C+DX_0^{2n}}{2D} > 0$, there are three equilibrium points: one center point $(X_0, 0)$, and two saddle points $\left(\sqrt[2n]{-\frac{C+DX_0^{2n}}{2D}}, 0\right)$ and $\left(-\sqrt[2n]{-\frac{C+DX_0^{2n}}{2D}}, 0\right)$ for $M < 0$. In contrast for $M > 0$, the three equilibrium points are center points.
- If $\Delta' > 0$, $C > 0$, and $D > 0$, the dynamical system Eq. (30) has just equilibrium point $(X_0, 0)$, which indicates a stable center point.

Figure 3 shows the phase portrait of the dynamical system (30) for $a_1 = 1.4$, $a_2 = 1$, $b_1 = b_2 = \alpha = 2$, $\gamma = 3$, $\theta = 0.0005$, $\sigma = -4$, $k_1 = 0.51$, $k_2 = 3.5$, and $n = 1$. We observe one limit cycle about the origin $(0, 0)$. This implies that the waves are stable, and there are no noises to disturb them.

The periodicity of X and Y , based on system (30) with the same values of parameters as in **Figure 3**, is shown in **Figure 4**.

3.2.2 Quasiperiodic and chaotic motions of the perturbed system

In this section, we will study the quasiperiodic and chaotic motions for Eq. (1) under the external perturbation. As in the previous process, we find the following perturbed dynamical system:

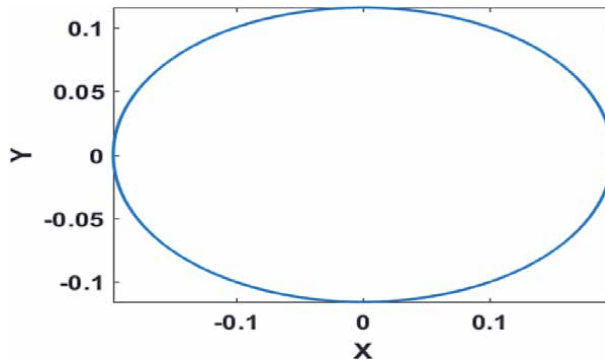


Figure 3. Phase portrait of the system (30) for parameter values: $a_1 = 1.4$, $a_2 = 1$, $b_1 = b_2 = \alpha = 2$, $\gamma = 3$, $\theta = 0.0005$, $\sigma = -4$, $k_1 = 0.51$, $k_2 = 3.5$, and $n = 1$.

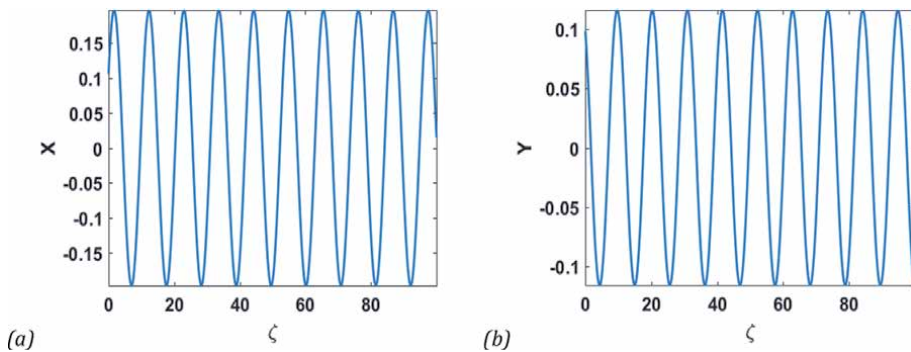


Figure 4. Periodicity of X and Y based on system Eq. (30), with the same values of parameters as **Figure 3**.

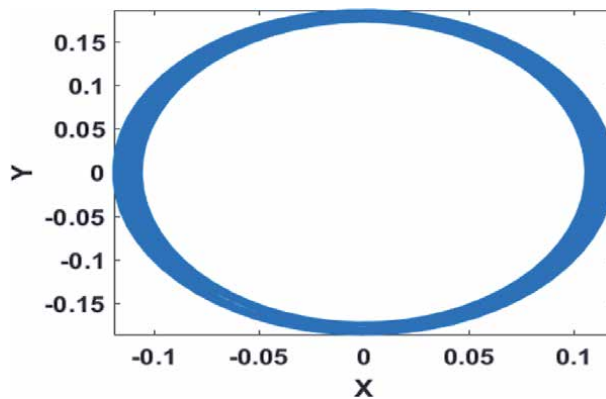


Figure 5. Phase portrait of the perturbed system (38) for the same parameter values as those in **Figure 3**, under external perturbation $R(\zeta) = E_0 \cos(\omega\zeta)$, where $E_0 = 0.01$ and $\omega = 1$.

$$\begin{cases} X_\zeta = Y, \\ Y_\zeta = g(X) = AX + BX^{2n+1} + CX^{4n+1} + DX^{6n+1} - \frac{R(\zeta)}{k_1(a_1k_1 - a_2k_2)}, \end{cases} \quad (38)$$

where $X, Y, A, B, C,$ and D are given by Eqs. (28) and (29); $R(\zeta) = R_0 \cos(\omega\zeta)$ is an external periodic perturbation, R_0 is a strength of the external perturbation, and ω is the frequency. The difference between the system (30) and the system (38) is that only external periodic perturbation is added with the system (38).

In **Figure 5**, we have presented a phase portrait of the perturbed system (38) under the conditions of parameter values as those in **Figure 3**, except those fixed $E_0 = 0.01$ and $\omega = 1$. For the same parameter values as **Figure 5**, we plotted in **Figure 6** the quasiperiodicity of X and Y versus ζ . From this plot, it is obvious to notice that the perturbed system (38) has quasiperiodic motion even with the consideration of the external periodic perturbation.

If we increase the strength of the periodic perturbation by considering $E_0 = 0.01$, the other parameter values remain as in **Figure 5**, the perturbed system (38) shows quasiperiodic route to chaos as it is shown in **Figure 7**. In this case, the solutions ignore the periodic motions and represent random sequences of uncorrelated oscillations (see **Figures 7** and **8**).

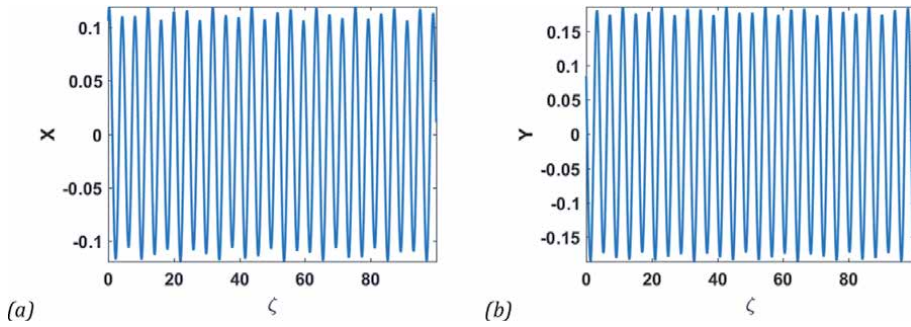


Figure 6. Variation of X and Y with respect to ζ of the perturbed system (38), for the same values of parameters as in Figure 5.

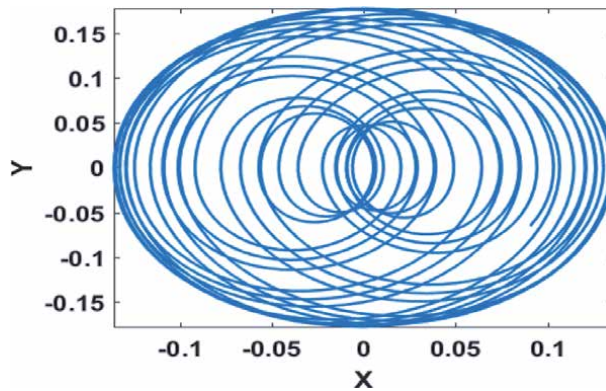


Figure 7. Phase portrait of the perturbed system (38) for the same parameter values as those in Figure 5 with $E_0 = 0.1$.

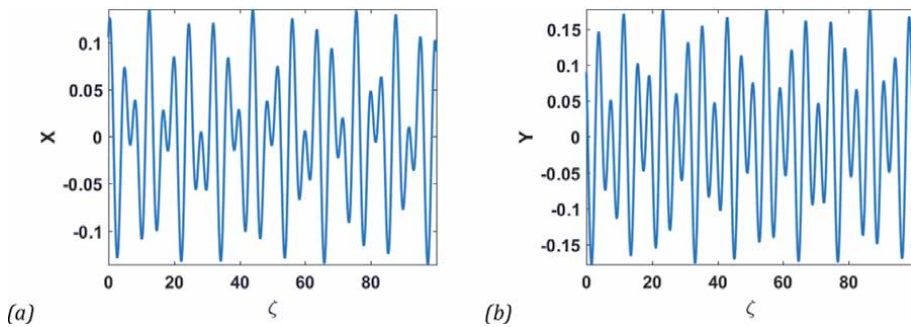


Figure 8. Quasi-periodicity of X and Y based on system (38), for same values of parameters as Figure 7.

From the above observations, it is straightforward to notice that the strength of the periodic perturbation significantly enhances the development of the quasi-periodic motion of the perturbed system (38) and quasi-periodic route to chaotic motion of the system (38). Thus, the perturbed NLS Eq. (1) with the power-law nonlinearity in a nano-optical fiber not only has solitonic and periodic wave solutions but could also possess quasi-periodic and chaotic motions.

4. Conclusion

In this chapter, we have investigated the perturbed nonlinear Schrödinger equation involving power-law nonlinearity and higher-order dispersions. We have constructed exact traveling wave solutions of the model by means of the well-known auxiliary equation method. We showed the existence of a family of traveling wave solutions and we have reported the parametric conditions on the physical parameters for the existence of these propagating solutions. Moreover, by employing Stuart and DiPrima's stability analysis method, a dispersion relation for the MI gain has been obtained. The outcomes of the instability development depend upon the nonlinearity, the power levels, and the dispersion parameters; the instability region increases regardless of the dispersion regime. The results may find straightforward applications in nonlinear optics, particularly in fiber-optical communication. Afterward, equivalent two-dimensional planar dynamic system and Hamiltonian have been derived and equilibrium points of the corresponding system have been gotten through the bifurcation theory. In addition, we have addressed the periodic, quasiperiodic, and chaotic behaviors of the traveling waves considering an external periodic perturbation. It has been observed that the perturbed system shows quasiperiodic route to chaos as a result of the strength of the periodic perturbation enhancement.

Conflict of interest

The authors declare no conflict of interest.

Appendix

The system of algebraic equations obtained by balancing $VV_{\zeta\zeta}$ and V^5 in Eq. (10) is as follows:

- V^5 coeff :

$$k_1(a_1k_1 - a_2k_2)(3n + 1)\mu_5 + 4n^2k_1p_2 = 0,$$

- V^4 coeff :

$$4n^2 [b_2 + k_1p_1 + k_1p_2(\gamma + \theta) - p_2^2k_1(a_1k_1 - a_2k_2)] \\ + k_1(a_1k_1 - a_2k_2)(2n + 1)\mu_4 = 0,$$

- V^3 coeff :

$$4n^2 [b_1 + k_1p_1(\gamma + \theta) + p_2(k_2 + \alpha k_1) - 2p_1p_2k_1(a_1k_1 - a_2k_2)] \\ + k_1(a_1k_1 - a_2k_2)(n + 1)\mu_3 = 0,$$

- V^2 coeff :

$$4n^2 [p_1(k_2 + \alpha k_1) - p_1^2k_1(a_1k_1 - a_2k_2)] \\ + k_1(a_1k_1 - a_2k_2)\mu_2 = 0,$$

- V^1 coeff :

$$k_1(a_1k_1 - a_2k_2)(1 - n)\mu_1 = 0,$$

- V^0 coeff :

$$k_1(a_1k_1 - a_2k_2)(1 - 2n)\mu_0 = 0.$$

Author details

Mati Youssoufa^{1*}, Ousmanou Dafounansou¹, Camus Gaston Latchio Tiofack²
and Alidou Mohamadou²

1 Faculty of Science, Department of Physics, University of Douala, Douala,
Cameroon

2 Faculty of Science, Department of Physics, University of Maroua, Maroua,
Cameroon

*Address all correspondence to: mati.youss@yahoo.fr

IntechOpen

© 2021 The Author(s). Licensee IntechOpen. This chapter is distributed under the terms of the Creative Commons Attribution License (<http://creativecommons.org/licenses/by/3.0>), which permits unrestricted use, distribution, and reproduction in any medium, provided the original work is properly cited. 

References

- [1] Schrödinger E. An undulatory theory of the mechanics of atoms and molecules. *Physical Review*. 1926;**28**: 1049-1070
- [2] Benney DJ, Newell AC. Nonlinear wave envelopes. *Journal of Mathematical Physics*. 1967;**46**:133-139
- [3] Zakharov VE. Stability of periodic waves of finite amplitude on the surface of a deep fluid. *Zhurnal Prikladnoj Mekhaniki i Tekhnicheskoy Fiziki*. 1968; **9**:86-94
- [4] Hasegawa A, Tappert FD. Transmission of stationary nonlinear optical pulses in dispersive dielectric fibers. I. Anomalous dispersion. *Applied Physics Letters*. 1973;**23**:142
- [5] Peregrine DH. Water waves, nonlinear Schrödinger equations and their solutions. *The Journal of the Australian Mathematical Society Series B Applied Mathematics*. 1983;**25**:16
- [6] Belmonte-Beitia J, Perez-Garcia VM, Vekslerchik V, Konotop VV. Localized nonlinear waves in systems with time- and space-modulated nonlinearities. *Physical Review Letters*. 2008;**100**: 164102
- [7] Chabchoub A, Hoffmann N, Onorato M, Slunyaev A, Sergeeva A, Pelinovsky E, et al. Observation of a hierarchy of up to fifth-order rogue waves in a water tank. *Physical Review E*. 2012;**86**:056601
- [8] Zhou Q, Liu L, Zhang H, Wei C, Lu J, Yu H, et al. Analytical study of Thirring optical solitons with parabolic law nonlinearity and spatio-temporal dispersion. *The European Physical Journal Plus*. 2015;**130**:138
- [9] Jiang Q, Su Y, Nie H, Ma Z, Li Y. New type gray spatial solitons in two-photon photorefractive media with both the linear and quadratic electro-optic effects. *Journal of Nonlinear Optical Physics & Materials*. 2017;**26**(1): 1750006
- [10] Topkara E, Milovic D, Sarma AK, Zerrad E, Biswas A. Optical solitons with non-Kerr law nonlinearity and inter-modal dispersion with time-dependent coefficients. *Communications in Nonlinear Science and Numerical Simulation*. 2010;**15**: 2320-2330
- [11] Jovanoski Z, Roland DR. Variational analysis of solitary waves in a homogeneous cubic-quintic nonlinear medium. *Journal of Modern Optics*. 2001;**48**:1179
- [12] Kivshar YS, Luther-Davies B. Dark optical solitons: Physics and applications. *Physics Reports*. 1998;**298**:81-197
- [13] Serkin VN, Belyaeva TL, Alexandrov IV, Melchor GM. Optical pulse and beam propagation III. In: Band YB, editor. *SPIE Proceedings*. Vol. 4271. Bellingham: SPIE; 2001. p. 292
- [14] Dai CQ, Wang YY, Zhang JF. Analytical spatiotemporal localizations for the generalized (3+1)-dimensional nonlinear Schrödinger equation. *Optics Letters*. 2010;**35**:1437
- [15] Jubgang D, Dikande AM, Sunda-Meya A. Elliptic solitons in optical fiber media. *Physical Review A*. 2015;**92**: 053850
- [16] Younis M, Rizvi S. Optical solitons for ultrashort pulses in nano fibers. *Journal of Nanoelectronics and Optoelectronics*. 2015;**10**:179
- [17] Tsatourian V, Sergeev SV, Mou C, Rozhin A, Mikhailov V, Rabin B, et al. Polarisation dynamics of vector soliton molecules in mode locked fibre laser. *Scientific Reports*. 2013;**3**:3154

- [18] Herink G, Kurtz F, Jalali B, Solli DR, Ropers C. Real-time spectral interferometry probes the internal dynamics of femtosecond soliton molecules. *Science*. 2017;**356**:50
- [19] Chernysheva M, Bednyakova A, Araithi MA, Howe R, Hu G, Hasan T, et al. Double-wall carbon nanotube hybrid mode-locker in tm-doped fibre laser: A novel mechanism for robust bound-state solitons generation. *Scientific Reports*. 2017;**7**:44314
- [20] Yin HM, Tian B, Hu CC, Zhao XC. Chaotic motions for a perturbed nonlinear Schrödinger equation with the power-law nonlinearity in a nano optical fiber. *Applied Mathematics Letters*. 2019;**93**:139-146
- [21] Tahir M, Awan AU, Rehman HU. Dark and singular optical solitons to the Biswas-Arshed model with Kerr and power law nonlinearity. *Optik - International Journal for Light and Electron Optics*. 2019;**185**:777-783
- [22] Biswas A, Ekici M, Sonmezoglu A, Alqahtani RT. Sub-pico-second chirped optical solitons in mono-mode fibers with Kaup-Newell equation by extended trial function method. *Optik*. 2018;**168**: 208-216
- [23] Rogers C, Chow KW. Localized pulses for the quintic derivative nonlinear Schrödinger equation on a continuous-wave background. *Physical Review E*. 2012;**86**:037601
- [24] Yang B, Zhang W-G, Zhang H-Q, Pei S-B. Generalized Darboux transformation and rational soliton solutions for Chen-Lee-Liu equation. *Applied Mathematics and Computation*. 2014;**242**:863-876
- [25] Zhang J, Liu W, Qiu D, Zhang Y, Porsezian K, He J. Rogue wave solutions of a higher-order Chen-Lee-Liu equation. *Physica Scripta*. 2015;**90**: 055207
- [26] Bakodah H, Qarni AA, Banaja M, Zhou Q, Moshokoa SP, Biswas A. Bright and dark Thirring optical solitons with improved adomian decomposition method. *Optik*. 2017;**130**:1115-1123
- [27] Triki H, Babatin M, Biswas A. Chirped bright solitons for Chen-Lee-Liu equation in optical fibers and PCF. *Optik*. 2017;**149**:300-303
- [28] Arshad M, Seadawy A, Lu D, Wang J. Travelling wave solutions of Drinfel'd-Sokolov-Wilson, Whitham-Broer-Kaup and $(2 + 1)$ -dimensional Broer-Kaup-Kupershmit equations and their applications. *Chinese Journal of Physics*. 2017;**55**:780-797
- [29] Banaja M, Qarni A, Bakodah H, Zhou Q, Moshokoa SP, Biswas A. The investigate of optical solitons in cascaded system by improved adomian decomposition scheme. *Optik*. 2017;**130**: 1107-1114
- [30] González-Gaxiola O, Biswas A. W-shaped optical solitons of Chen-Lee-Liu equation by Laplace-Adomian decomposition method. *Optical and Quantum Electronics*. 2018;**50**:314
- [31] Triki H, Zhou Q, Moshokoa SP, Ullah MZ, Biswas A, Belic M. Chirped wshaped optical solitons of Chen-Lee-Liu equation. *Optik*. 2018; **155**:208-12
- [32] Triki H, Hamaizi Y, Zhou Q, Biswas A, Ullah MZ, Moshokoa SP, et al. Chirped dark and gray solitons for Chen-Lee-Liu equation in optical fibers and PCF. *Optik*. 2018;**155**:329-33
- [33] Triki H, Hamaizi Y, Zhou Q, Biswas A, Ullah MZ, Moshokoa SP, et al. Chirped singular solitons for Chen-Lee-Liu equation in optical fibers and PCF. *Optik*. 2018;**157**:156-60
- [34] Kara A, Biswas A, Zhou Q, Moraru L, Moshokoa SP, Belic M. Conservation laws for optical solitons

with Chen–Lee–Liu equation. *Optik*. 2018;**174**:195-8

[35] Youssoufa M, Dafounansou O, Mohamadou A. W-shaped, dark and grey solitary waves in the nonlinear Schrödinger equation competing dual power-law nonlinear terms and potentials modulated in time and space. *Journal of Modern Optics*. 2019;**66**(5): 530-540

[36] Jawad AJAM, Biswas A, Zhou Q, Alfiras M, Moshokoa SP, Belic M. Chirped singular and combo optical solitons for Chen–Lee–Liu equation with three forms of integration architecture. *Optik*. 2019;**178**:172-7

[37] Kudryashov NA. General solution of the traveling wave reduction for the perturbed Chen-Lee-Liu equation. *Optik*. 2019;**186**:339-49

[38] Xie XY, Meng GQ. Dark solitons for the $(2+ 1)$ -dimensional Davey–Stewartson-like equations in the electrostatic wave packets. *Nonlinear Dynamics*. 2018;**93**:779

[39] Mohammed ASHF, Bakodah HO, Banaja MA. Approximate Adomian solutions to the bright optical solitary waves of the Chen-Lee-Liu equation. *MATTER: International Journal of Science and Technology*. 2019;**5**:110-20

[40] Ahmed I, Seadawy AR, Lu D. M-shaped rational solitons and their interaction with kink waves in the Fokas–Lenells equation. *Physica Scripta*. 2019;**94**:055205

[41] Arshad M, Lu D, Rehman M-U, Ahmed I, Sultan AM. Optical solitary wave and elliptic function solutions of the Fokas–Lenells equation in the presence of perturbation terms and its modulation instability. *Physica Scripta*. 2019;**94**:105202

[42] Youssoufa M, Dafounansou O, Mohamadou A. *Nonlinear Optics –*

From Solitons to Similaritons. London: IntechOpen; 2020

[43] Hirota R. Exact envelope-soliton solutions of a nonlinear wave equation. *Journal of Mathematical Physics*. 1973; **14**:805-809

[44] Sasa N, Satsuma J. New-type of soliton solutions for a higher-order nonlinear Schrödinger equation. *Journal of the Physical Society of Japan*. 1991; **60**:409-9

[45] Savescu M, Khan KR, Kohl RW, Moraru L, Yildirim Y, Biswas A. Wavelength selective supercontinuum signal generated from photonic crystal fibers for microscopic object detection. *Journal of Nanoelectronics and Optoelectronics*. 2013;**8**:208

[46] Mirzazadeh M, Ekici M, Sonomezoglu A, Eslami M, Zhou Q, Kara AH, et al. Optical solitons with complex Ginzburg–Landau equation. *Nonlinear Dynamics*. 2016;**5**(3): 1979-2016

[47] Biswas A, Yildirim Y, Yasar E, Triki H, Alshomrani AS, Ullah MZ, et al. Optical soliton perturbation with complex Ginzburg–Landau equation using trial solution approach. *Optik*. 2018;**160**:44-60

[48] Abdoukary S, Mohamadou A, Beda T, Gambo B, Doka SY, Alim, Mahamoudou A. Exact traveling wave solutions to the nonlinear Schrödinger equation. *Applied Mathematics and Computation*. 2014;**233**:109-115

[49] Saha A. Bifurcation of travelling wave solutions for the generalized KP-MEW equations. *Communications in Nonlinear Science and Numerical Simulation*. 2012;**17**:3539

[50] Guckenheimer J, Holmes PJ. *Nonlinear Oscillations, Dynamical Systems and Bifurcations of Vector Fields*. New York: Springer-Verlag; 1983

[51] Gradshteyn IS, Ryzhik IM. Table of Integrals, Series, and Products. 7th ed. London: Academic Press; 2007

[52] Agrawal GP. Nonlinear Fiber Optics. New York: Academic Press; 2013

[53] Kivshar YS, Agrawal GP. Optical Solitons: From Fibers to Photonic Crystal. San Diego: Academic Press; 2003

[54] Shukla PK, Rasmussen JJ. Modulational instability of short pulses in long optical fibers. Optics Letters. 1986;**11**:171

[55] Potasek MJ. Modulation instability in an extended nonlinear Schrödinger equation. Optics Letters. 1987;**12**:921

[56] Mohamadou A, Latchio Tiofack CG, Kofané TC. Wave train generation of solitons in systems with higher-order nonlinearities. Physical Review E. 2010; **82**:016601

[57] Porsezian K, Nithyanandan K, Vasantha Jayakantha Raja R, Shukla PK. Modulational instability at the proximity of zero dispersion wavelength in the relaxing saturable nonlinear system. Journal of the Optical Society of America. 2012;**B29**:2803

[58] Infeld E, Rowlands G. Nonlinear Waves, Solitons and Chaos. Cambridge: Cambridge University Press; 1990

Non-Manakovian Propagation in Optical Fiber

Lothar Moeller

Abstract

Solving the nonlinear Schrödinger equation or similar calculus is essential for designing today's long-haul optical communication systems. Associated numerical and analytical approaches were extensively studied over the past four decades; simplifications and adaptations for various applications and purposes have been introduced. Optical fibers installed in long-haul systems possess nonideal features such as birefringence, which some of these adaptations partially address to improve the simulation accuracy. But as the fiber birefringence frequently and randomly changes along a link, finding a mathematical solution is a more complex problem and beyond the task of dealing with the nonlinear nature of the corresponding equations. Recently, a novel propagation phenomenon related to the polarization evolution of a signal has been observed. In links with considerable length, i.e., bridging transatlantic or transpacific distances, the polarization state of a light wave is impacted by neighboring signals via the Kerr nonlinearity in glass. Established formalisms for describing polarization effects based on the nonlinear Schrödinger equation cannot fully capture this phenomenon. Here we discuss a first-order calculus for this problem. We start with high-level reviews of experimental observations to introduce the phenomenon and ways to model regular nonlinear propagation. Then we present a first-order calculus to describe the statistics behind the phenomenon by specifically discussing the interplay between fiber birefringence and fiber nonlinearities.

Keywords: nonlinear depolarization, Kerr nonlinearity, polarization, single-mode fiber, Manakov equation, Manakov-PMD equation, coupled NL Schrödinger equations

1. Introduction

Long-distance optical telecommunications using standard single-mode fiber (SSMF) is economically [1] one of the most important industrial applications, which requires an accurate solution to the nonlinear (NL) Schrödinger equations for developing competitive products. Modern fiber communications, the basis of all backbone networks, enable global long-reach and high-capacity data exchange such as the WWW and state-of-the-art systems provide 10s of Tb/s capacity per fiber over transpacific distances without electrical signal regeneration [2, 3].

By simulating the NL Schrödinger equation or similar approaches, the industry assesses potential commercial link design options for network operations [4, 5]. The chosen optical power levels balance the generated NL signal distortions with sufficiently high optical signal-to-noise ratios (OSNR) to guarantee certain bit error rates (BERs) on the receive side.

Throughout the half-century-long history of SSMF, various mathematical approaches for describing NL signal propagation have been proposed where all of them are somewhat related to the (coupled) NL Schrödinger equation(s) [6, 7]. These models vary in terms of complexity, their intended purposes, and user friendliness. For example, a more refined analysis of light propagation in SSMF for telecom application requires a polarization dependent field representation. Today's coherent signaling technique, which exploits two orthogonal polarization states at same optical frequency to encode data information and the unavoidable birefringence of SSMF, requires a vector field representation of the light mode. But simultaneously considering both aspects, the polarization of light and its random changes along a regular link due to fiber birefringence lead to an extended set of equations that are for most applications impractical to solve exactly.

The high end of the “manageable” equation sets, the “Manakov-PMD equation” addresses NL propagation in a fiber with randomly varying birefringence [8]. For the current generation of communication systems, it provides quite accurate results for expected NL signal distortions. But recently, a fiber phenomenon, to which we refer to as nonlinear depolarization (NLDP) of light in fiber, has been observed and does not conform to the Manakov-polarization mode dispersion (PMD) equation. Here we discuss some relevant experimental aspects of this phenomenon and its impact on the mathematical description of NL propagation in realistic, i.e., birefringent fiber. The Manakov-PMD equation is in some ways an advanced form of the NL Schrödinger equation as it additionally considers PMD effects [9, 10], and on the other hand, a simplification as it uses averaged quantities over distance to describe the randomly changing fiber birefringence.

In this chapter, we describe an algorithm for solving the NL Schrödinger equation in vector form when the field variables are randomly and rapidly alternated by the stationary and linear properties (birefringence) of the channel. In other words, some coefficients of the coupled NL Schrödinger equation (CNLS) become distance dependent and describe the changing features of the glass medium along the propagation path.

We start with a brief overview on commonly used modeling for NL signal propagation (Manakovian propagation) in SSMF, report on a high-level view of experimental results that do not conform to such formalism (non-Manakovian propagation) and discuss an algorithm that yields some analytic quantities for a theoretical description of the later. Although not fully technically correct, we use the SSMF terminology in our chapter [11] even when we also mean other fiber types such as large effective area fiber (LEAF [12]) that are often installed in long-haul communication systems.

Our focus is to develop a mathematical formalism for NLDP that yields quantities that are observable in typical industrial test beds. Certainly, more sophisticated experimental setups can be built to characterize other features of NLDP. We report the experimental conditions to a degree that produces a qualitative understanding of the phenomenon and will reference further details in the literature.

2. Nonlinear propagation equations

Back in 1972 and far before commercial applications of optical communications became relevant, Sergey Manakov¹ suggested that a careful consideration of NL pulse propagation is required for accurate signal modeling in fiber. He proposed a set of coupled differential equations that to a large degree can capture the impact of the fiber's Kerr nonlinearity on a signal's evolution [13]. A slowly varying envelope

¹ Sergey Valentinovich Manakov, Russian mathematician, *1948–†2012.

constituted by the two orthogonal variables A_x and A_y represents the pulse in space and time domains:

$$\frac{\partial A_x}{\partial z} + \beta_1 \frac{\partial A_x}{\partial t} + \frac{j\beta_2}{2} \frac{\partial^2 A_x}{\partial t^2} + \frac{\alpha}{2} A_x = j\gamma \left(|A_x|^2 + |A_y|^2 \right) A_x \quad (1)$$

$$\frac{\partial A_y}{\partial z} + \beta_1 \frac{\partial A_y}{\partial t} + \frac{j\beta_2}{2} \frac{\partial^2 A_y}{\partial t^2} + \frac{\alpha}{2} A_y = j\gamma \left(|A_x|^2 + |A_y|^2 \right) A_y \quad (2)$$

where z and t are the propagation direction and time, respectively. The optical features of the fiber are characterized by α, β_1, β_2 , and γ , which refer to the fiber attenuation, propagation constant, group velocity, and Kerr nonlinearity [14], respectively. By multiplying A_x and A_y with the optical carrier, which typically resides around 194 THz (1.5 μm wavelength), the optical field can be obtained.

In the field of telecom the above listed formulas are called the Manakov Equation (ME). Literature uses this name for both its scalar version and a two-dimensional version for polarization representation of a signal. The ME was heuristically found in the sense that the left side, known from linear transmission theory, has been extended by a source term on its right side describing the Kerr nonlinearity. It assumes that the nonlinearities are weak and proportional to the signal's intensity.

The ME has been highly successfully applied to NL signal propagation and can explain phenomena such as optical solitons and nonlinear polarization rotation (NLPR [15, 16]) that were subjects of intensive research until about the end of the 1990 [17–20]. But the ME in the form outlined above is restricted in twofold aspects compared with a more accurate propagation modeling that modern telecom applications require:

- (a) It assumes a rotational symmetry of the fiber, i.e., without birefringence. But commercial SSMFs, even those with the lowest amounts of birefringence, demand for modeling that adapts the ME's left side (the linear propagation features) to simulate typical evolutions of a signal's state of polarization (SOP). We address this issue by substituting β_1 and β_2 with polarization-dependent constants $\beta_{1x}, \beta_{1y}, \beta_{2x}$ and β_{2y} and
- (b) other than the ME hypothesizes, the fiber Kerr NL of glass is significantly polarization dependent. The impact of an orthogonal polarization component needs to be weighted by a factor of 2/3.

Both adjustments in the ME lead to a simplified version of the so-called coupled NL Schrödinger equations (CNLSs):

$$\frac{\partial A_x}{\partial z} + \beta_{1x} \frac{\partial A_x}{\partial t} + \frac{j\beta_2}{2} \frac{\partial^2 A_x}{\partial t^2} + \frac{\alpha}{2} A_x = j\gamma \left(|A_x|^2 + \frac{2}{3} |A_y|^2 \right) A_x \quad (3)$$

$$\frac{\partial A_y}{\partial z} + \beta_{1y} \frac{\partial A_y}{\partial t} + \frac{j\beta_2}{2} \frac{\partial^2 A_y}{\partial t^2} + \frac{\alpha}{2} A_y = j\gamma \left(|A_y|^2 + \frac{2}{3} |A_x|^2 \right) A_y \quad (4)$$

The extended version differs by terms on the right side, which model fast oscillations of the nonlinearity (not shown). In our further considerations, those terms can be neglected; and the polarization dependence of β_2 is small and can be ignored. Strictly speaking, the CNLSs hold only for a single piece of fiber with linear birefringence, referred to in the literature as waveplate. Different velocities of light in both optical axes (principal states) of a waveplate lead in general to SOP changes for a cw tone passing through a single plate and complicate the calculus.

A model of a realistic fiber link would typically involve a concatenation of many waveplates, each with their optical axes randomly oriented. Solving the CNLS becomes for such a scenario a cumbersome process. On the other hand, it had been observed that NL differential equations of Manakovian type (Eqs. (1) and (2)) sufficiently capture experimental results such as soliton propagation. This led to the assumption that the ME can be derived from the CNLS when its polarization-dependent NL source term is averaged in a way that it simulates polarization scrambling caused by fiber birefringence [21, 22]. Several derivations have been published, which yield an ME with an 8/9 reduced Kerr nonlinearity as fitting parameter:

$$\frac{\partial A_x}{\partial z} + \beta_1 \frac{\partial A_x}{\partial t} + \frac{j\beta_2}{2} \frac{\partial^2 A_x}{\partial t^2} + \frac{\alpha}{2} A_x = j\gamma \frac{8}{9} \left(|A_x|^2 + |A_y|^2 \right) A_x \quad (5)$$

$$\frac{\partial A_y}{\partial z} + \beta_1 \frac{\partial A_y}{\partial t} + \frac{j\beta_2}{2} \frac{\partial^2 A_y}{\partial t^2} + \frac{\alpha}{2} A_y = j\gamma \frac{8}{9} \left(|A_y|^2 + |A_x|^2 \right) A_y \quad (6)$$

Note, the fiber birefringence does not appear anymore in the form of polarization-dependent propagation constants, and the x, y -indexes should not be identified with the coordinates of the lab frame. Nevertheless, advanced effects such as NL polarization rotation of two cw tones can be quantitatively described by such equations.

The heuristically determined ME with and without reduced Kerr nonlinearity has become an integral part of soliton theory and is often used in today's system modeling due to its relatively simple form and highly accurate results. Based on this success, the published attempts for deriving the ME from the more fundamental CNLSs have gained wide acceptance [21]. Here, however, we challenge their formalism as they rely on an elusively compelling mathematical argument and show that the solution spaces of the ME with reduced Kerr nonlinearity and of the section-wise solved CNLS for long birefringent fibers diverge from each other. This difference matters in case of NLDP.

The Manakov-PMD equation developed toward the end of the 1990 is cumbersome but allows to separate the principal effects by terms such as the Kerr nonlinearity, chromatic dispersion, nonlinear PMD, and linear PMD that contribute to the signal's evolution. Its nonlinear PMD term can be ignored in applications for today's regular telecom fibers, thus the remaining NL source term of the Manakov-PMD equation simplifies to the same form as known from the ME (Eqs. (5) and (6)). It differs from the latter by an additional term that accounts for linear PMD contributions. Nonlinear PMD refers to a situation where the fiber birefringence does not sufficiently scramble the SOP of a cw signal when it linearly propagates over distances that are comparable to the NL propagation length of the path. In our following considerations, we can (to good approximation) assume that a signal's SOP gets strongly scrambled represented by a homogeneous coverage on the Poincare sphere while it propagates just a few kilometers. We can therefore neglect NL PMD.

Nevertheless, due to the same method of averaging that had been applied when deriving from the CNLS the ME with an 8/9 reduced Kerr nonlinearity, the Manakov-PMD equation does not represent NLDP fully correctly, regardless if it includes NL PMD or not.

3. Comparative polarimetry for detecting NLDP

The undersea communication industry continuously aims for a more precise modeling of signal propagation in fiber to enable longer unrepeated system spans

and higher transport capacities, hence more cost-effective solutions. However, a noticeable discrepancy in channel capacity between measurable performance and predictions from the most advanced simulation tools remains, which attracts significant research in propagation modeling mostly focusing on pure optical effects [23] but lately also considering weak acousto-optic interactions [24, 25]. Here we discuss NL depolarization of light (NLDP), a recently observed non-Manakovian transmission phenomenon as a potential candidate to narrow down this discrepancy [26]. Unpolarized optical noise rapidly changes via the fiber's Kerr nonlinearity the SOP from a fully polarized cw light by inducing antisymmetric phase noise in both of its orthogonal polarization states. These fluctuations become resolvable with a new generation of high-speed polarimeters [27] and do not average out over wide noise bandwidths but grow with propagation distance.

Prior to applying the CNLS to NLDP, we introduce the phenomenon by providing some experimental evidence that will prompt the discussion of quantities needed for developing our algorithm. Back in 2017, two measurements were performed on an undersea cable that connects Brazil and Florida to demonstrate NLDP (**Figure 1a**) on a real communication link [26, 28]. A cw light launched from Brazil and looped back in Florida propagates via the opposite fiber link to its origin. There are about 200 optical amplifiers in each direction to compensate for fiber attenuation but cause weak NL propagation in the first few tens of kilometer fiber length directly after each repeater.

Undersea cables on the ocean floor undergo environmental impact such as motion due to water currents, seismic vibrations, and temperature fluctuations, etc. These environmental factors lead to small SOP motions on the receive side, trackable with a low-speed polarimeter, and represented as velocities in histograms. We define the amount of the time derivative from the corresponding normalized Stokes vector as "SOP speed." Typical SOP speeds range on the order of a few rad/s (**Figure 1b**). In this experiment, a cw light (ECL, External Cavity Laser) also referred to as probe (or signal) is launched together with unpolarized Amplified Spontaneous Emission (ASE, loading) into the cable input. The ASE spectrum covers the whole repeater bandwidth (~ 4.5 THz) except for a narrow central gap with ~ 100 GHz width where the probe resides (**Figure 1c**). Without loading, the probe would pick up almost the entire repeater output power resulting in strong NL propagation, mainly self phase modulation (SPM) [29], which can produce unstable SOPs. With loading, the probe contributes less than 1% of the total repeater output power and NL effects such as Brillouin scattering [30] are avoided. The electrical detection bandwidth of the low-speed polarimeter (a few 10s of Hz) averages out all fast SOP motions; while increasing its bandwidth (a few 10s of MHz) produces much wider SOP speed histograms under identical experimental conditions (**Figure 1d**).

It would be incorrect to attribute the entire width of this histogram solely to NL interactions between the loading and the probe, as any noise during the detection corrupts the polarimeter, leading to artifacts in SOP speeds. In our experiment, signal-ASE beat noise is the main contributor and [31] biases the SOP detection. Every repeater adds small amounts of ASE that raise the noise floor within the spectral gap. This ASE then mixes with the probe on the four photodiodes of the polarimeter. Even a hypothetical constant SOP of the probe on the receive side will appear in a histogram with nonzero width due to the omnipresent signal-ASE beat noise. We refer to this noise-induced SOP speed (NISS) as an artifact since improving the optical signal-to-noise ratio (OSNR) at the polarimeter input would reduce the width of its histogram. However, probe power constraints, inevitable added repeater noise during transmission, and practical limitations on tighter filtering yield OSNR levels, which result in artificially broadened SOP speed histograms that partially obscure NLDP.

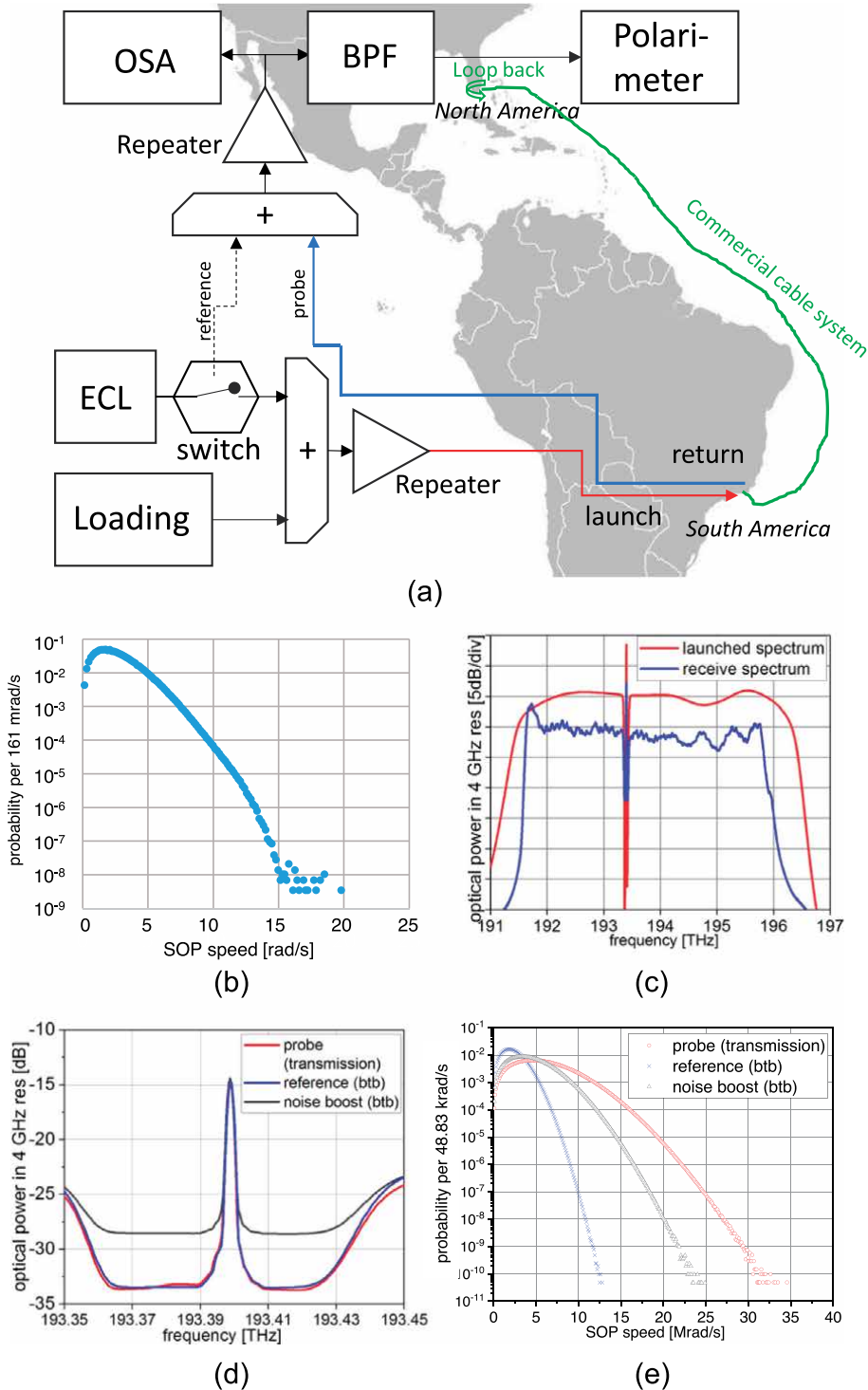


Figure 1. (a) Comparative polarimetry on a commercial undersea cable system. A cw tone and unpolarized ASE propagate together from Brazil to the USA and back. The probe's SOP speed is measured after propagation and compared with a local reference (not transmitted through the cable, dashed path); (b) SOP speed histogram recorded over 24 h showing environmental impact on SOP stability; (c) spectra of transmitted and received signals; (d) matched optical spectra of the probe and reference, taken with an OSA, look similar, but the corresponding SOP speed histograms (e) differ significantly and prove the existence of NLDP (noise boost explained in text).

Instead, we demonstrate NLDP-induced fast SOP changes by means of a comparison technique. We contrast the SOP speed histograms from the transmitted probe with one from a reference signal that possesses equal power, equal ASE, and equal OSNR but bypasses the undersea cable (reference, btb). This reference is obtained by superimposing the transmitter signal with the noise output of the cable in Brazil and launched btb into the receiver (ECL switched to reference path, **Figure 1a**). Within the resolution capabilities (~ 2 GHz) of our optical spectrum analyzer (OSA), both the transmitted probe and the reference spectra are identical (**Figure 1d**). However, the SOP speed histogram for the probe is significantly wider compared with the histogram for the reference (**Figure 1e**) as NL interactions fluctuated the probe's SOP. Even when the optical noise floor in the btb experiment is subject to added ASE (~ 5 dB, **Figure 1d**), the corresponding histogram does not expand to the same width of the probe's plot (**Figure 1e**).

It is reasonable to assume a scaling of the NLDP magnitude with the probe's transmission length and the loading power, as both determine the strength of the Kerr nonlinearity. Such parametric NLDP studies become feasible with a lab test bed based on a recirculating fiber loop (RFL, **Figure 2a**) [32]. In RFLs, a fast optical switch allows to launch a signal into a fiber link whose output is coupled back into its input. After a programmable number of round trips inside the loop, the signal is released via the switch and analyzed.

Our RFL comprises 11 transmission spans each with an output power-adjustable repeater followed by SSMF (specs see **Figure 2a**). The transmitter (**Figure 2b**) inserts the probe via a variable optical attenuator (VOA) in path I into the RFL (VOA_I open, VOA_II blocked). After leaving the RFL, a narrow bandwidth amplified filter cascade selects the probe from the wide band loading prior to its detection by the polarimeter. To acquire the reference for determining NISS (btb measurement), VOA_I blocks the access to path I for the ECL while the reference reaches the receiver via path II. In both scenarios, loading enters the RFL via path I. We fine-tune VOA_II to match the spectra from probe and reference within 0.1 dB across a bandwidth of approx. 50 GHz. A central clock synchronizes the gates from loop switch, kicker (loop synchronous polarization controller), OSA, and polarimeter. It periodically activates the latter's data acquisition at 100 MS/s typically for a ~ 3 ms long interval per transmission. A spectrally programmable ASE source delivers unpolarized loading (Degree of Polarization (DOP) $< 1\%$) with flat spectrum (constant power density) across the repeater gain bandwidth of about 4.5 THz except for a narrow gap (100 GHz wide, ~ 50 dB ASE suppression) centered at 193.9 THz to contain the probe. Here we chose a flat launch spectrum for the loading and a flat transfer function for the RFL, adjusted via its GEF (Gain Equalizing Filter, **Figure 2a**), to simplify a mathematical treatment of NLDP [26]. In reality, every system component such as repeaters, fibers, etc., possesses small amounts of PDL [33] and PMD. Due to the large number and the random orientation of their optical axes in Stokes space, the results follow a "smooth distribution." But in an RFL, a signal passes the same components several times, which causes filtering and different PDL and PMD statistics. To counteract this effect and emulate scenarios such as those in real systems, a triggered loop synchronous polarization controller [34] (kicker) randomizes PMD and PDL inside the loop. After the signal has traversed the device and before its return, the kicker is set to a different mode within a few nanoseconds to randomize the output SOP. The kicker does not directly impact the SOP speed as it is stationary when the probe is passing through, but it emulates more realistic propagation paths.

By programming the loop's timing gate, SOP speed histograms are determined (**Figure 2c**) for propagation lengths of approx. 1023 km, 3069 km, 5115 km, 10,230 km, and 20,460 km further referred to as 1 Mm, 3 Mm, ..., 20 Mm transmissions and correspond to 1, 3, 5, 10, and 20 loop circulations, respectively. For

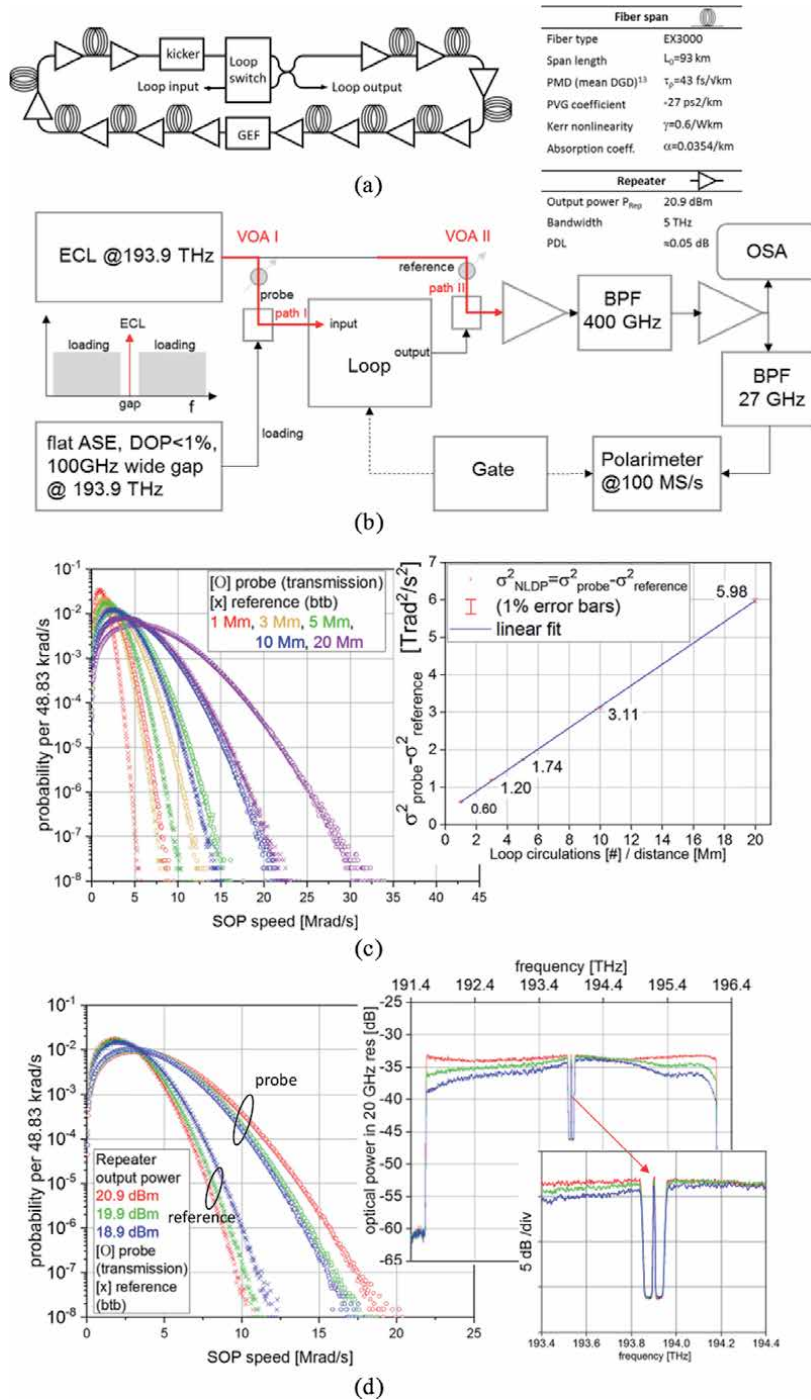


Figure 2. Characterizing NLDP in a lab setup using a recirculating fiber loop: (a) block diagram of an RFL design and its fiber specifics. (b) Setup for experimental comparative polarimetry embedding an RFL. The RFL allows economically emulating differently long transmission paths, which impacts the magnitude of NLDP. The propagation time is determined by a central clock that synchronizes the gates of the RFL, the high-speed polarimeter, and the OSA. (c) Visualization of a typical NLDP dependence on transmission distances; the histograms widen for the probe and reference with increased transmission distances. Their difference σ^2_{NLDP} shows the NLDP magnitude and grows nearly linearly with the transmission distance. (d) Repeater output power dependence of NLDP at 10 mm transmission. The power-dependent Kerr effect mediates the cross-phase modulation between loading and the probe. Lowering the repeater output power reduces the width of the probe's histograms but deforms the spectral shape of the loading as the gain shape of the individual EDFA changes.

longer transmissions, the corresponding btb measurements show wider NISS histograms as the received OSNRs decay. The probe's SOP speed histograms broaden with propagation length due to NISS and NLDP. We hypothesize both as statistically independent processes and visualize NLDP by subtracting the reference's NISS from the probe's SOP speed variance (**Figure 2c**, inset). This quantity monotonically increases, indicating a growing NLDP with transmission distance. A linear fit reasonably resembles the measured NLDP variances as a function of the propagation length. Each recording consists of about 100 MSamples and was repeated multiple times to verify stable measurement readings. We found experimentally for the short-term reproducibility of all measured SOP speed variances a relative error smaller than 1%.

Without NL interaction with the loading, the probe would linearly propagate. Altering the nominal probe power of ~ -5.2 dBm at the repeater output by ± 3 dB has shown an insignificant dependence of σ_{NLDP}^2 on SPM-based effects at 10 Mm transmission distance. Hence, Brillouin scattering or modulation instability (known to be the weakest NL fiber process) can be ruled out as origin for NLDP.

The repeater output power inside our RFL can be to some degree controlled without strongly tilting and distorting the spectral shape of the loading. At maximum repeater output power (20.9 dBm into transmission fiber) and at 1 and 2 dB down, we record SOP speed histograms over 10 Mm transmission distance following the same methodology. As three different phenomena need to be considered, NLDP, receive OSNR degradation, and spectral distortions of the loading, the data analysis becomes more complex. Increasing widths of the reference's NISS histograms with decreasing repeater power (**Figure 2d**) can be explained by receive OSNR reduction. To a good approximation, the ASE that an optical amplifier adds to a boosted signal is proportional to the repeater's gain. Since our repeaters operate in constant gain mode (as the span loss stays constant the repeater gain must do the same), altering the output power does not affect their ASE contributions. Consequently, lower repeater output power means smaller probe power and degraded OSNR after transmission (at constant ECL power), which enhances NISS. Remarkably, after transmission, and despite improved receive OSNR, the corresponding SOP speed histograms trend oppositely and widen with stronger repeater power. This broadening stems from NLDP, which even exceeds a theoretically expected narrowing of the histograms when only the enhanced receive OSNRs are considered as in case of the reference. Other than in the NLDP versus transmission distance—study, the received spectra diverge from an ideal boxcar shape and deform at different test conditions (**Figure 2d**, inset). While around 194.4 THz, the spectral density remains about constant, it drops disproportionately toward the spectral edges with reduced repeater power, making a quantitative analysis more challenging. But the noise floor surrounding the probe (zoom-in **Figure 2d**) remains relatively constant, which supports our previous OSNR argument.

As discussed in Section 4.7, NLDP is formed on long-range nonlinear optical interactions that become observable in the spectral domain. Distortions mainly generated within the first section of a transmission fiber connected to a repeater output substantially interfere among each other when propagating along a multi span link. Qualitatively spoken, the spectral features of the probe's Stokes vector depend on the transmission distance—more precisely, the further the signal propagates, the leaner the Stokes vector spectrum becomes. In our study, we define as the probe's spectrum the Fourier transform of the autocorrelation of its normalized, three-dimensional Stokes vector.

In our experimental verification, we utilize the same RFL as in the aforementioned setup. But instead of using a polarimeter, a polarization scrambling

20 Mm spectral width (FWHM), between 16.1 and 3.3 MHz, respectively, were observed. This demonstrates the spectral contraction over propagation length (**Figure 3b**).

An analogy to Fabry-Perot etalons [36] whose filter width narrows with the number of interfering rays inside its cavity maybe helpful for understanding the spectral shaping of the Stokes vector spectrum with transmission distance. While a higher reflectivity of the etalon's mirrors produces more interfering rays, more link spans lead to more coherently superimposing distortions in the receiver plane that cause spectral compression.

4. Applying the coupled NL Schrödinger equations to NLDP

Techniques for solving the CNLS for a short piece of fiber with constant linear birefringence have been extensively discussed in the literature [37]. SSMF can be envisioned as a concatenation of many fiber pieces with linear birefringence. The length of each piece and the orientation of its optical axes follow known statistics. Our goal is to calculate closed-form solutions for quantities that describe the underlying statistics of the reported NLDP effects based on the aforementioned fiber models. For the sake of simplicity, we take advantage of certain experimental conditions that justify a significantly reduced formalism. The conceptual simplifications relate to NL propagation, the repeater functionality, and the fiber model.

We assume NL signal propagation but consider its impact as relatively weak, which effectively addresses the operational range of today's telecom systems. This allows us to model NL distortions as first-order perturbations that propagate linearly through the path once they have been generated.

Every repeater adds small amounts of ASE to the loading. While this extra noise does not significantly change the spectral shape of the loading, it slightly impacts its temporal correlation features, which will be ignored.

We will partially diverge from the picture of discrete and concatenated waveplates that form a fiber. For SSMF, it is appropriate to imagine smooth transitions between the single waveplates. However, we will consider a discrete waveplate model to discuss local SOP rotations and apply the theory of PMD statistics to cope with long-distance SOP correlations. These assumptions should not impact our main conclusions.

4.1 Sorting the Kerr nonlinearity in even and odd operators

For simplicity, we consider a weak cw field $a_{x(y)}$ (probe) residing in a narrow spectral gap of a surrounding, fully unpolarized and co-propagating strong ASE field $A_{x(y)}$ (loading) with a boxcar-shaped spectrum (**Figure 4a**). As stated, significantly less than 1% of the total signal power stems from the probe. The known CNLS [38] for propagation in z direction within a waveplate, given here in complete form, can approximate this scenario well:

$$\frac{\partial A_x^\Sigma}{\partial z} + \beta_{1x} \frac{\partial A_x^\Sigma}{\partial t} + \frac{j\beta_2}{2} \frac{\partial^2 A_x^\Sigma}{\partial t^2} + \frac{\alpha}{2} A_x^\Sigma = j\gamma \left(|A_x^\Sigma|^2 + \frac{2}{3} |A_y^\Sigma|^2 \right) A_x^\Sigma + j\gamma \frac{1}{3} A_x^{\Sigma*} A_y^{\Sigma^2} e^{-j2\Delta\beta z} \quad (7)$$

$$\frac{\partial A_y^\Sigma}{\partial z} + \beta_{1y} \frac{\partial A_y^\Sigma}{\partial t} + \frac{j\beta_2}{2} \frac{\partial^2 A_y^\Sigma}{\partial t^2} + \frac{\alpha}{2} A_y^\Sigma = j\gamma \left(|A_y^\Sigma|^2 + \frac{2}{3} |A_x^\Sigma|^2 \right) A_y^\Sigma + j\gamma \frac{1}{3} A_y^{\Sigma*} A_x^{\Sigma^2} e^{+j2\Delta\beta z} \quad (8)$$

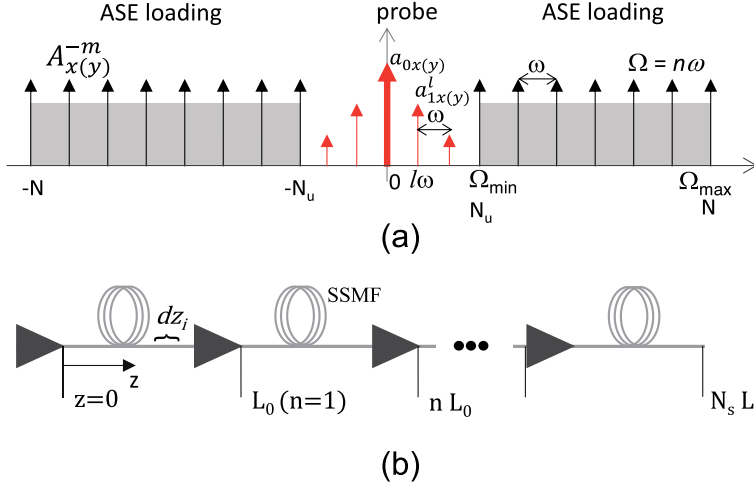


Figure 4. (a) Spectral grid for boxcar-shaped ASE spectrum with a probe residing in its center gap. (b) Single and multiple span link design for NLDP study.

$$\text{with } A_{x(y)}^\Sigma = A_{x(y)} + a_{x(y)}; |a_{x(y)}| \ll |A_{x(y)}|, \quad (9)$$

where the wavelength-independent α , $\beta_{1x(y)}^{-1}$, β_2 , and γ denote the attenuation, polarization-dependent group velocities, dispersion coefficient, and the Kerr nonlinearity of a waveplate, respectively. As previously mentioned, the high modal birefringence $\Delta\beta$ of regular SMF induces fast oscillating of the terms at the far-right side, which leads to ineffective NL interference. This has been discussed in great detail for the derivation of the Manakov-PMD equation [8]; however, it is negligible in our analysis and thus left out in the following.

We assume that the loading modulates the probe, but the probe has no impact on the loading. In the limit of a negligibly small probe power, such interaction can be justified and simplifies the Kerr nonlinearity. Two sets of equation pairs follow, for the two cases $a_{x(y)} = 0$ and $1 \gg |a_{x(y)}| \neq 0$. Subtracting both sets, neglecting second-order terms, and considering coupling conditions yield an equation set that describes the motion of the probe induced by the loading

$$\frac{\partial a_x}{\partial z} + \beta_{1x} \frac{\partial a_x}{\partial t} + \frac{j\beta_{2x}}{2} \frac{\partial^2 a_x}{\partial t^2} + \frac{\alpha}{2} a_x = j\gamma \left(2|A_x|^2 + \frac{2}{3}|A_y|^2 \right) a_x \quad (10)$$

$$\frac{\partial a_y}{\partial z} + \beta_{1y} \frac{\partial a_y}{\partial t} + \frac{j\beta_{2y}}{2} \frac{\partial^2 a_y}{\partial t^2} + \frac{\alpha}{2} a_y = j\gamma \left(2|A_y|^2 + \frac{2}{3}|A_x|^2 \right) a_y. \quad (11)$$

The remaining stochastic perturbation on the right side is decomposed into a symmetric and an antisymmetric term (Eqs. (12) and (13)) with respect to the loading's field

$$\frac{\partial a_x}{\partial z} + \beta_{1x} \frac{\partial a_x}{\partial t} + \frac{j\beta_{2x}}{2} \frac{\partial^2 a_x}{\partial t^2} + \frac{\alpha}{2} a_x = j\gamma \left[\frac{4}{3} \left(|A_x|^2 + |A_y|^2 \right) a_x + \frac{2}{3} \left(|A_x|^2 - |A_y|^2 \right) a_x \right] \quad (12)$$

$$\frac{\partial a_y}{\partial z} + \beta_{1y} \frac{\partial a_y}{\partial t} + \frac{j\beta_{2y}}{2} \frac{\partial^2 a_y}{\partial t^2} + \frac{\alpha}{2} a_y = j\gamma \left[\frac{4}{3} \left(|A_y|^2 + |A_x|^2 \right) a_y + \frac{2}{3} \left(|A_y|^2 - |A_x|^2 \right) a_y \right]. \quad (13)$$

While both describe weak and independently treatable NL interactions in a first-order perturbation calculus, the polarization-dependent sign of the antisymmetric perturbation (right sides of Eqs. (12) and (13) root-causes opposite phase noises in both principal axes that manifests experimentally as NLDP. Identical phase changes in both polarizations as produced by the symmetric perturbation do not alter the probe's SOP but lead to NL phase noise. In the following, we discuss solutions for the pair

$$\frac{\partial a_x}{\partial z} + \beta_1 \frac{\partial a_x}{\partial t} + \frac{j\beta_2}{2} \frac{\partial^2 a_x}{\partial t^2} + \frac{\alpha}{2} a_x = j\gamma \frac{2}{3} \left(|A_x|^2 - |A_y|^2 \right) a_x \quad (14)$$

$$\frac{\partial a_y}{\partial z} + \beta_1 \frac{\partial a_y}{\partial t} + \frac{j\beta_2}{2} \frac{\partial^2 a_y}{\partial t^2} + \frac{\alpha}{2} a_y = j\gamma \frac{2}{3} \left(|A_y|^2 - |A_x|^2 \right) a_y. \quad (15)$$

The impact of birefringence has been disregarded in Eqs. (14) and (15) by replacing $\beta_{1x(y)}$ with a polarization-independent group velocity β_1^{-1} but will be revisited at a later stage. That is, Eqs. (14) and (15) captures nonlinear SOP changes along a waveplate but does not include the much larger SOP changes caused by linear birefringence. The linear SOP changes are static and do not contribute to the measured SOP speeds. In practical applications, the right side represents a very fast fluctuating term as the noise components A_x and A_y stem from stochastically independent processes with bandwidths in the range of several THz. Since we assume unpolarized loading, the quantity $\left(|A_{x(y)}|^2 - |A_{y(x)}|^2 \right)$ is on average zero. For our algorithm, we represent it on an evenly spaced frequency grid, which yields experimentally observable quantities to describe some statistical features of the probe $a_{x(y)}$.

4.2 Asymmetric phase noise in first-order approximation

The right side of Eqs. (14) and (15) weakly perturbs the probe by adding a first-order correction term $a_{1x(y)}(z,t)$ to it. We write the perturbation by means of the undistorted fields of the probe $a_{x(y)}(z)$ and the loading $A_{x(y)}(z,t)$. The latter's components with amplitudes $A_{x(y)}$ form a comb Eqs. (16) and (17) on an evenly spaced grid with an infinitesimally small angular frequency pitch ω (**Figure 4a**). For a single span system, the probe $a_{x(y)}(z,t)$ in first-order development and the ASE field read

$$A_{0x}(z,t) = \sum_{m=-N}^N A_x^m e^{j(k_m z - m\omega t)} e^{-\frac{\alpha}{2}z} \quad (16)$$

$$A_{0y}(z,t) = \sum_{m=-N}^N A_y^m e^{j(k_m z - m\omega t)} e^{-\frac{\alpha}{2}z} \quad (17)$$

$$a_x(z,t) \approx (a_{0x} + a_{1x}(z,t)) e^{-\frac{\alpha}{2}z} = \left(a_{0x} + \sum_l A_{1x}^l(z) e^{-j l \omega t} \right) e^{-\frac{\alpha}{2}z} \quad (18)$$

$$a_y(z,t) \approx (a_{0y} + a_{1y}(z,t)) e^{-\frac{\alpha}{2}z} = \left(a_{0y} + \sum_l A_{1y}^l(z) e^{-j l \omega t} \right) e^{-\frac{\alpha}{2}z} \quad (19)$$

with $A_{x(y)}^m = 0$ for $|m| < N_u$, $|m| > N$, $z \geq 0$ and $A_{0x}(z,t) = a_x(z,t) = 0$ for $z < 0$ (20)

where $k_m = \beta_1 m \omega + \frac{\beta_2}{2} (m\omega)^2$ stands for the propagation constant of a component at 'm ω '. We synthesize the Kerr nonlinearity in Eqs. (14) and (15) as a sum to address the impact of low-frequency beat noises among its terms. Due to phase matching conditions, this noise alone can efficiently interact with the probe and is used to redefine the perturbation term in Eqs. (14) and (15) as

$$|A_x|^2 - |A_y|^2 \stackrel{\text{def}}{=} \sum_{m,l} \mathcal{A}_x^{l,m} e^{-\alpha z} e^{j((\beta_1 l \omega + \beta_2 l m \omega^2)z - l \omega t)} \quad (21)$$

$$|A_y|^2 - |A_x|^2 \stackrel{\text{def}}{=} \sum_{m,l} \mathcal{A}_y^{l,m} e^{-\alpha z} e^{j((\beta_1 l \omega + \beta_2 l m \omega^2)z - l \omega t)} \quad (22)$$

$$\text{with } \mathcal{A}_{x(y)}^{l,m} = A_{x(y)}^{m+\frac{1}{2}} A_{x(y)}^{m-\frac{1}{2}*} - A_{y(x)}^{m+\frac{1}{2}} A_{y(x)}^{m-\frac{1}{2}*}, |l| \ll N_u. \quad (23)$$

Here $m\omega$ stands for the angular frequency spacing between the two beating ASE tones at $\omega(m \pm \frac{1}{2})$ and the probe, which is typically in the THz range. Due to coupling inefficiency, any beating among the two noise tones can be neglected when its frequency $l\omega$ resides beyond a few tens of MHz. Eqs. (21) and (22) hold separately for every l and m , and its solution for a single span system can be written by means of a Green's function

$$a_{1x(y)}^{l,m}(z, t) = j \frac{2}{3} \gamma \int_0^z e^{jk_l(z-z_i) - \alpha z_i} \mathcal{A}_{x(y)}^{l,m} e^{j((\beta_1 l \omega + \beta_2 l m \omega^2)z_i - l \omega t)} a_{0x(y)} dz_i \quad (24)$$

According to this Ansatz, the NL distortions are generated as a kind of “wave packet” in fiber sections of incremental length dz_i , propagate thereafter linearly through the span, and coherently superimpose in the receiver plane. We portion out the integral of Eq. (24) into a sum of infinitesimal short waveplates dz_i (Eq. (25)) to analyze NL interactions in the presence of Polarization Mode Dispersion (PMD), which originates from fiber birefringence. At the span output at L_0 holds

$$\delta_{1x(y)}^{l,m}(L_0, t) = \frac{a_{1x(y)}^{l,m}(L_0, t)}{a_{0x(y)}} = j \frac{2}{3} \gamma e^{j(\beta_1 l \omega L_0 - l \omega t)} \sum_i \mathcal{A}_{x(y)}^{m,l} e^{-\alpha z_i} e^{j\beta_2 l m \omega^2 z_i} e^{j\frac{1}{2}\beta_2 l^2 \omega^2 (L_0 - z_i)} dz_i. \quad (25)$$

Alternating the sign of l conjugates its right side, except for its last and typically negligible small exponent ($a_{1x(y)}^{l,m}(L_0, t) \approx a_{1x(y)}^{-l,m}(L_0, t)^*$). Hence, pairing contributions at $\pm l$ results into a correction with a 90° phase offset relative to the undistorted probe. Therefore, all pairs of NL distortions stemming from single waveplates generate pure phase oscillations in the receiver plane $\varepsilon(L_0, t) = \left(\delta_{1x(y)}^{l,m}(L_0, t) + \delta_{1x(y)}^{-l,m}(L_0, t) \right)$ at an angular frequency $l\omega$. As $\mathcal{A}_{x(y)}^{m,l} = -\mathcal{A}_{y(x)}^{m,l}$ holds, the oscillations in both orthogonal polarizations are 180° out of phase and cause SOP fluctuations. We define for later purposes a temporal autocorrelation as

$$\varphi_{i,k}^{l,m}(\tau) = \left\langle \delta_{1x,i}^{l,m}(L_0, t + \tau) \delta_{1x,k}^{l,m}(L_0, t)^* \right\rangle + \left\langle \delta_{1y,i}^{l,m}(L_0, t + \tau) \delta_{1y,k}^{l,m}(L_0, t)^* \right\rangle, \quad (26)$$

where the indices i, k denote different waveplates and $\langle \rangle$ denotes the averaging over time and fields, which involves reestablishing the birefringent fiber features in our model as detailed below.

4.3 Correlations of asymmetric phase noise in birefringent fiber

For deriving correlations between phase noises generated at different propagation distances of the probe, we focus on a single span system and extend the results to a multiple span link. Modeling a birefringent fiber as a concatenation of

waveplates uses Eq. (25) to determine the correlation among incremental distortions stemming from two different plates. Our $x(y)$ -coordinate system is congruent with the fast (slow) axis of a waveplate, i.e., it rotates and follows the plates' orientations along the propagation path. Our model incorporates birefringence, originating from, e.g., axis-specific group velocities ($\beta_{1x} \neq \beta_{1y}$), by means of a Jones matrix that transforms the input SOPs from the probe and the noise components $A_{x(y)}^m$ when traversing a waveplate. A Jones matrix \bar{R}_i of a waveplate shall be given by a unitary matrix

$$\bar{R}_i = \begin{bmatrix} R_{11}^i & R_{12}^i \\ -R_{12}^{i*} & R_{11}^{i*} \end{bmatrix} \text{ with } |R_{11}^i|^2 + |R_{12}^i|^2 = 1. \quad (27)$$

With $a_{0x(y)} := \vec{a}_0 = \begin{pmatrix} a_{0x} \\ a_{0y} \end{pmatrix}$ and $\bar{I} = \begin{bmatrix} 1 & 0 \\ 0 & -1 \end{bmatrix}$, an NL distortion generated in waveplate k with length dz_k concisely reads at the span output

$$\vec{a}_{1,k}^{m,l}(L_0, t) = \begin{pmatrix} a_{1x,k}^{m,l}(L_0, t) \\ a_{1y,k}^{m,l}(L_0, t) \end{pmatrix} = j \frac{2}{3} \gamma e^{j(\beta_{1l}\omega L_0 - l\omega t)} e^{j\beta_{2l}m\omega^2 z_k} dz_k \times \left(\prod_{k=i}^{M_{L_0}} \bar{R}_i \right) A_{x,k}^{m,l} \bar{I} e^{-\alpha z_k} \left(\prod_{i=1}^{k-1} \bar{R}_i \right) \vec{a}_0, \quad (28)$$

where $A_{x,k}^{m,l}$ and M_{L_0} stand for the undepleted noise components inside of waveplate k constituted by Eq. (23), and the total number of waveplates, respectively. The correlation between contributions from two consecutive waveplates follows as

$$\langle \vec{a}_{1,k+1}^{m,l}(L_0) | \vec{a}_{1,k}^{m,l}(L_0) \rangle = \frac{4}{9} \gamma^2 e^{j\beta_{2l}m\omega^2(z_k - z_{k+1})} e^{-\alpha(z_k + z_{k+1})} dz_k dz_{k+1} \times \langle A_{x,k+1}^{m,l} \bar{I} \bar{R}_k \vec{a}_{0,k} | A_{x,k}^{m,l} \bar{R}_k \bar{I} \vec{a}_{0,k} \rangle, \quad (29)$$

where $\vec{a}_{0,k}$ and $\langle \rangle$ represent the undistorted and undepleted probe field within waveplate k and the field-averaged scalar product, respectively. We restore PMD in our fiber model by using matrices \bar{R}_i, \bar{R}_i' obeying Eq. (27) and transforming wavelength-dependent the probe and ASE fields:

$$\langle A_{x,k+1}^{m,l} \bar{I} \bar{R}_k \vec{a}_{0,k} | \bar{R}_k A_{x,k}^{m,l} \bar{I} \vec{a}_{0,k} \rangle = \langle (|R_{11}^k|^2 - |R_{12}^k|^2) (|R_{11}^{k'}|^2 - |R_{12}^{k'}|^2) \rangle \mathcal{H}^m |\vec{a}_{0,k}|^2 \quad (30)$$

$$\text{with } \mathcal{H}^m = \langle |A_x^{m''}|^2 |A_x^{m''}|^2 + |A_y^m|^2 |A_y^{m''}|^2 \rangle, \quad (31)$$

where double primes indicate statistically independent noises. Since $m \gg l$ holds, we can evaluate Eq. (30) just at m but must treat the original two noise components at frequencies $(m \pm l/2)\omega$ as uncorrelated. The theory of PMD statistics [39] specifies the distance-dependent decorrelation from two SOPs of two co-propagating cw tones at different wavelengths, which provides a correlation between the matrix elements

$$\langle (|R_{11}^k|^2 - |R_{12}^k|^2) (|R_{11}^{k'}|^2 - |R_{12}^{k'}|^2) \rangle = \frac{1}{3} e^{-\frac{1}{3}(m\omega)^2 \tau_\rho^2 \Delta L}, \quad (32)$$

where $m\omega$, τ_ρ , and $\Delta L = |z_{k+1} - z_k|$ are the angular frequency spacing between the probe and the two noise components, the mean fiber DGD per $\sqrt{\text{length}}$ (Differential Group Delay), and the propagation distance, respectively. PMD effects

across frequency intervals of size $\sim l \omega$ such as the spectral width of the received and distorted probe or spacings between two efficiently beating noise components are negligibly small. Hence, the sum of all incremental phase oscillations correlates as defined by Eq. (26) at the span output like

$$\varphi^{l,m}(\tau) = \frac{4}{27} \gamma^2 e^{-j l \omega \tau} \mathcal{H}^m \sum_{i,k} e^{j \beta_2 l m \omega^2 (z_i - z_k) - \alpha (z_i + z_k)} e^{-\frac{1}{3} (\omega m)^2 \tau_\rho^2 |z_i - z_k|} dz_i dz_k. \quad (33)$$

The above outlined calculus assumes two consecutive birefringent waveplates $k, k + 1$. But it holds for any pair of further spaced waveplates, indexed i, k with $i \neq k + 1$, as well. Since a matrix product $\bar{R} = \bar{R}_i \dots \bar{R}_{k+2} \bar{R}_{k+1}$ of intermediately located waveplates can be expressed by a single unitary matrix that fulfills Eq. (27), the conclusion from Eq. (30) will equally hold and leads to Eq. (33).

4.4 Fiber PMD constitutes NLDP

System PMD imposes cutoff conditions via the Gaussian for the number of interacting waveplates addressed by the double sum of Eq. (33). Without this constrain, the sum tends to zero as its complex exponential function causes averaging for sufficiently small α . For a single span system with $L_0 \gg \alpha^{-1}$ (typically tens of kilometers) and relatively short waveplates ($\ll \alpha^{-1}$, typically tens of meters), we will replace the double sum with an integral.

Experimentally observed NLDP-caused SOP features such as scattering angles and speed as their time derivatives are detected after O/E conversion of the optical fields and conveniently reported in Stokes space (Section 3). To derive such quantities, we will confine the optical autocorrelation density by introducing electrical low-pass filtering, which represents the detection process, and then convert the result into Stokes space. In Jones space, the density of the optical autocorrelation (Eq. (33)) at $l\omega$ reads for sufficiently long propagation distances ($L_0 \rightarrow \infty$)

$$\begin{aligned} \varphi^{l,m}(\tau) &= \frac{4}{27} \gamma^2 \mathcal{H}^m \frac{e^{-j l \omega \tau}}{2\alpha} \int_{-\infty}^{+\infty} e^{-(\alpha + \frac{1}{3} (\omega m)^2 \tau_\rho^2) |z|} e^{j \beta_2 l m \omega^2 z} dz \\ &= \frac{4}{27} \gamma^2 \mathcal{H}^m \frac{e^{-j l \omega \tau}}{\alpha} \frac{\alpha + \frac{1}{3} (\omega m)^2 \tau_\rho^2}{\left(\alpha + \frac{1}{3} (\omega m)^2 \tau_\rho^2\right)^2 + (\beta_2 l m \omega^2)^2} \end{aligned} \quad (34)$$

and its integration over m, l' yields the autocorrelation for the total phase noise.

So far, we have considered a single span system, i.e., one optical amplifier boosts the probe and loading prior of their launch into an as infinite long assumed transmission fiber. Today's undersea communication cables can consist of a few hundred spans to bridge transpacific distances of up to about 15 Mm length. In contrast to terrestrial systems, they are strictly modularly designed, which eases our modeling. To keep the calculation effort at an introductory level, we further assume a large enough fiber attenuation α , thus all NL propagation fades away far before the span end. Additionally, our amplification is assumed to be a noiseless process. For a cable with N_s spans, the autocorrelation then reads

$$\varphi_{N_s}^{l,m}(\tau) = \frac{4}{27} \gamma^2 e^{-j l \omega \tau} \mathcal{H}^m \times \sum_{p=0, q=0}^{N_s, N_s} \sum_{i,k} e^{j \beta_2 l m \omega^2 (z_i - z_k + L_0(p-q)) - \alpha (z_i + z_k)} e^{-\frac{1}{3} (\omega m)^2 \tau_\rho^2 |z_i - z_k + L_0(p-q)|} dz_i dz_k \quad (35)$$

with $z_i + L_0p$ and $z_k + L_0q$ as the positions of two interacting waveplates.

For approximating the interleaved summations, we take advantage of the assumed large fiber attenuation, which forms cutoff conditions for the z_i and z_k . When one of the two coordinates or both are large enough but still significantly smaller than L_0 , the corresponding summands do not substantially contribute to the overall sum. Thus, a replacement of the amount in the exponents by

$$|z_i - z_k + L_0(p - q)| \rightarrow |z_i - z_k| + L_0|p - q| \quad (36)$$

can be justified and yields

$$\begin{aligned} \varphi_{N_s}^{l,m}(\tau) &\cong \frac{4}{27} \gamma^2 e^{-j\omega\tau} \mathcal{H}^m \times \sum_{i,k} e^{j\beta_2 l m \omega^2 (z_i - z_k) - \alpha(z_i + z_k)} e^{-\frac{1}{3}(\omega m)^2 \tau_\rho^2 |z_i - z_k|} dz_i dz_k \\ &\times \sum_{p=0, q=0}^{N_s, N_s} e^{j\beta_2 l m \omega^2 L_0(p-q)} e^{-\frac{1}{3}(\omega m)^2 \tau_\rho^2 L_0 |p-q|} \end{aligned} \quad (37)$$

$$\begin{aligned} &= \frac{4}{27} \gamma^2 \frac{e^{-il\omega\tau}}{\alpha} \mathcal{H}^m \times \frac{\alpha + \frac{1}{3}(\omega m)^2 \tau_\rho^2}{\left(\alpha + \frac{1}{3}(\omega m)^2 \tau_\rho^2\right)^2 + (\beta_2 l m \omega^2)^2} \\ &\times N_s \sum_{n=-N_s}^{N_s} e^{j\beta_2 l m \omega^2 L_0 n} e^{-\frac{1}{3}(\omega m)^2 \tau_\rho^2 L_0 |n|} \Lambda\left(\frac{n}{N_s}\right), \end{aligned} \quad (38)$$

where $\Lambda(\cdot)$ denotes the triangular function. For the degree of accuracy, we follow in our modeling, it is sufficient to approximate it with an exponential function of even area and substitute both sums by integrals to obtain at least trends that show how NLDP qualitatively depends on system parameters.

$$\begin{aligned} \varphi_{N_s}^{l,m}(\tau) &\approx \frac{4}{27} \gamma^2 \frac{e^{-il\omega\tau}}{\alpha} \mathcal{H}^m \frac{\alpha + \frac{1}{3}(\omega m)^2 \tau_\rho^2}{\left(\alpha + \frac{1}{3}(\omega m)^2 \tau_\rho^2\right)^2 + (\beta_2 l m \omega^2)^2} \\ &\times N_s \sum_{n=-\infty}^{\infty} e^{j\beta_2 l m \omega^2 L_0 n} e^{-\left(\frac{1}{3}(\omega m)^2 \tau_\rho^2 L_0 + \frac{2}{N_s}\right)|n|}. \end{aligned} \quad (39)$$

Further we approximate the sum with a Fourier integral and find for the density of the optical correlation

$$\varphi_{N_s}^{l,m}(\tau) \approx \frac{8}{27} \gamma^2 \mathcal{H}^m N_s \frac{e^{-j\omega\tau}}{\alpha L_0} \frac{1}{\alpha + \frac{1}{3}(\omega m)^2 \tau_\rho^2} \frac{2}{\frac{1}{3}(\omega m)^2 \tau_\rho^2 + \frac{2}{N_s L_0}} \frac{1}{1 + \left(\frac{\beta_2 l m \omega^2}{\alpha + \frac{1}{3}(\omega m)^2 \tau_\rho^2}\right)^2} \frac{1}{1 + \left(\frac{\beta_2 l m \omega^2}{\frac{1}{3}(\omega m)^2 \tau_\rho^2 + \frac{2}{N_s L_0}}\right)^2}. \quad (40)$$

4.5 Detecting optical fields in the electrical domain

For the sake of simplicity, we consider two extreme cases for the electrical detection bandwidth Ω_e of our polarimeter. In one scenario its bandwidth tends to infinity and in the other, it strongly filters the photocurrents. In both cases $\tau_S^{-1} \gg \Omega_e$ should hold for its sampling rate. In typical lab experiments, the electrical detection bandwidth is the only parameter that can be practically tuned over a larger range

without the need for readjusting other model assumptions. For example, reducing the optical bandwidth of a system (~ 4.5 THz) at launch or the launch power into a span usually distorts the assumed boxcar-shaped spectrum of the loading.

We model the low-pass characteristic of the polarimeter with a Lorentzian curve, thus the autocorrelations in the optical and electrical domain interrelate as

$$\varphi_{N_s}^{elec}(\tau) = \int_{-\infty}^{\infty} \int_{-\infty}^{\infty} \frac{1}{1 + \left(\frac{l\omega}{\Omega_e}\right)^2} \varphi_{N_s}^{l,m}(\tau) d\omega d\omega, \quad (41)$$

Provided sufficiently short sampling periods τ_S , compared with the inverse of the autocorrelation's spectral width², the exponential in Eq. (40) ($e^{-j\omega\tau} \approx 1 - j\omega\tau - \frac{1}{2}(l\omega\tau)^2$) can be approximated in τ . Its linear term vanishes after the integration (Eq. (41)) due to symmetry aspects. The second order in τ_S of $\varphi_{(\tau_S)}^{elec}$ determines the variance of the stochastic SOP speed as shown below and reads

$$\varphi_{N_s}^{elec}(0) - \varphi_{N_s}^{elec}(\tau_S) = \int_{-\infty}^{\infty} \int_{-\infty}^{\infty} \frac{1}{1 + \left(\frac{l\omega}{\Omega_e}\right)^2} \left(\varphi_{N_s}^{l,m}(0) - \varphi_{N_s}^{l,m}(\tau_S)\right) d\omega d\omega, \quad (42)$$

which tends for the case of wide bandwidth detection ($\Omega_e \rightarrow \infty$) and under the assumptions of typical system parameters as explained in Section 3 toward

$$\varphi_{N_s}^{elec}(0) - \varphi_{N_s}^{elec}(\tau_S) \approx \frac{\pi}{81} \gamma^2 \frac{N_s}{\alpha L_0} \beta_2^{-3} \tau_S^2 \tau_{\rho}^2 P_{\text{rep}}^2 \frac{1}{(\Omega_{\text{max}} - \Omega_{\text{min}})^2} \ln\left(\frac{\Omega_{\text{max}}}{\Omega_{\text{min}}}\right), \quad (43)$$

where P_{rep} represents the total launch power of the loading at the fiber input.

For the case of detection at a reduced electrical bandwidth ($\Omega_e \ll \frac{1}{3}\Omega_{\text{min}}\frac{\tau_S^2}{\beta_2}$), we find

$$\varphi_{N_s}^{elec}(0) - \varphi_{N_s}^{elec}(\tau_S) \approx \frac{\pi}{27} \gamma^2 \frac{N_s}{\alpha L_0} \frac{\Omega_e^2}{\Omega_{\text{max}}^2} \frac{\tau_S^2}{\beta_2 \alpha} P_{\text{rep}}^2 \ln\left(\sqrt{\frac{3\alpha}{2}} \frac{1}{\tau_{\rho} \Omega_{\text{min}}}\right). \quad (44)$$

As Eq. (44) rapidly declines for small Ω_e^2 , NLDP stays hidden in the study of environmentally driven SOP fluctuations in undersea cables (**Figure 1b**), which had been performed at a detection bandwidth below 100 Hz.

4.6 Transforming phase noise from Jones space to stokes space

So far, NLDP has been characterized in Jones space for which the CNLSs hold. But for convenience in general, quantities such as the SOP speed and the SOP scattering angle [40] are usually discussed and experimentally obtained in Stokes space. To transform the incremental field distortions, determined by means of the Jones calculus and the CNLS, into Stokes space, we represent the assumed normalized probe's Jones vector $\overrightarrow{a_{\text{norm}}}(N_s L_0, t) = [a_x(N_s L_0, t), a_y(N_s L_0, t)]^T$ at the fiber output by

² With the current generation of commercially available high-speed polarimeters sampling periods ~ 10 ns can be achieved while spectral widths of the autocorrelation typically reside in the few MHz range.

$$\vec{a}_{\text{norm}}(N_s L_0, t) = \begin{bmatrix} a_x(N_s L_0, t) \\ a_y(N_s L_0, t) \end{bmatrix} = \begin{bmatrix} \cos \vartheta \cos \theta + j \sin \vartheta \sin \theta \\ \sin \vartheta \cos \theta - j \cos \vartheta \sin \theta \end{bmatrix} \quad (45)$$

with $\vartheta = \vartheta_0 + \delta\vartheta(t)$, $|\delta\vartheta| < \pi$ and $\theta = \theta_0 + \delta\theta(t)$, $|\delta\theta| < \pi$ where ϑ_0, θ_0 obey known distributions [41] to uniformly cover the Poincare sphere. For the SOP density Ψ holds

$$\Psi(2\vartheta_0, 2\theta_0) d2\vartheta_0 d2\theta_0 = \frac{1}{4\pi} \text{rect}\left(\frac{2\vartheta_0}{2\pi}\right) \text{rect}\left(\frac{2\theta_0}{\pi}\right) \cos(2\theta_0) d2\vartheta_0 d2\theta_0. \quad (46)$$

NLDP causes small temporal fluctuations $\delta\vartheta(t)$, $\delta\theta(t)$ whose autocorrelations must equal $\langle \delta\vartheta(t + \tau_S) \delta\vartheta(t) \rangle = \langle \delta\theta(t + \tau_S) \delta\theta(t) \rangle = \varphi_J(\tau_S)$ due to averaging caused by birefringence fluctuations along the long propagation path. The corresponding three-dimensional Stokes vector with unity length ($S_0 = 1$) to Eq. (45) reads

$$\vec{S}(N_s L_0, t) = \begin{bmatrix} |a_x|^2 - |a_y|^2 \\ +2 \Re\{a_x a_y^*\} \\ -2 \Im\{a_x a_y^*\} \end{bmatrix}_{(N_s L_0, t)} = \begin{bmatrix} \cos(2\vartheta) \cos(2\theta) \\ \sin(2\vartheta) \cos(2\theta) \\ -\sin(2\theta) \end{bmatrix}_{(N_s L_0, t)} \quad (47)$$

and can be analyzed with respect to the impact of $\delta\vartheta(t)$ and $\delta\theta(t)$. One finds

$$\left\langle \left| \vec{S}(t + \tau_S) - \vec{S}(t) \right|^2 \right\rangle = \frac{40}{3} (\varphi_J(0) - \varphi_J(\tau_S)). \quad (48)$$

In Jones space we get

$$\left\langle \left| \vec{a}_{\text{norm}}(t + \tau_S) - \vec{a}_{\text{norm}}(t) \right|^2 \right\rangle = 4 (\varphi_J(0) - \varphi_J(\tau_S)). \quad (49)$$

Thus, combing both results add up to

$$\left\langle \left| \vec{S}(t + \tau_S) - \vec{S}(t) \right|^2 \right\rangle = \frac{10}{3} \left\langle \left| \vec{a}_{\text{norm}}(t + \tau_S) - \vec{a}_{\text{norm}}(t) \right|^2 \right\rangle \quad (50)$$

Identifying $\left\langle \left| \vec{a}_{\text{norm}}(t + \tau_S) - \vec{a}_{\text{norm}}(t) \right|^2 \right\rangle = 2 (\varphi_{N_s}^{\text{elec}}(0) - \varphi_{N_s}^{\text{elec}}(\tau_S))$ yields the variance of the NLDP-induced SOP speed in Stokes space

$$\frac{\left\langle \left| \vec{S}(t + \tau_S) - \vec{S}(t) \right|^2 \right\rangle}{\tau_S^2} \approx \frac{2\pi}{81} \gamma^2 \frac{N_s}{\alpha L_0} \beta_2^{-3} \tau_{\rho}^2 P_{\text{rep}}^2 \frac{1}{(\Omega_{\text{max}} - \Omega_{\text{min}})^2} \ln\left(\frac{\Omega_{\text{max}}}{\Omega_{\text{min}}}\right), \quad (51)$$

which depends on the PMD of the link and differentiates NLDP from NL polarization rotation (NLPR) [15]. NLPR is a phenomenon between two cw tones where one impacts the SOP of the other. However, its fundamental equations do not include fiber features such as PMD and chromatic dispersion.

4.7 NLDP-induced stokes vector spectrum of the probe

In analogy to the relationship between temporal and spectral features of an electrical signal in time and frequency domain, we define the spectrum of the probe's Stokes vector by the Fourier transform of its temporal autocorrelation

$$\langle \vec{S}(t + \tau_S) \cdot \vec{S}(t) \rangle = 1 - \frac{20}{3} \varphi_J(0) + \frac{20}{3} \varphi_J(\tau_S) \approx 1 + \frac{20}{3} \varphi_J(\tau_S) - \Phi(f). \quad (52)$$

For our following derivations, we revisit Eq. (52). It does not include several approximations we have meanwhile applied in our calculus and can therefore be considered as a more accurate starting point. But we simplify the integration over the loading's optical spectrum by neglecting its central gap and assume infinite integral bounds, i.e., $\mathcal{H}^m = \bar{\mathcal{H}}^m = \text{const}$ holds

$$\begin{aligned} \varphi_{N_s}^{l,m}(\tau) &= \frac{4}{27} \gamma^2 \frac{e^{-il\omega\tau}}{\alpha^2} \bar{\mathcal{H}}^m \frac{1}{1 + \frac{1}{3\alpha} (\omega m)^2 \tau_\rho^2} \frac{1}{1 + \left(\frac{\beta l m \omega^2}{\alpha + \frac{1}{3} (\omega m)^2 \tau_\rho^2} \right)^2} \\ &\times N_s \sum_{n=-N_s}^{N_s} e^{j\beta_2 l m \omega^2 L_0 n} e^{-\frac{1}{3} (\omega m)^2 \tau_\rho^2 L_0 |n|} \Lambda\left(\frac{n}{N_s}\right). \end{aligned} \quad (53)$$

For typical system parameters, Eq. (53) is dominated by the term $e^{-\frac{1}{3} (\omega m)^2 \tau_\rho^2 L_0 |n|}$, which sets even for low fiber PMD (~ 50 fs/ $\sqrt{\text{km}}$) and small $|n| > 0$ a strong cutoff criterion for the integration. In this case the first two fractions on the right side will be ignored and the integration yields

$$\varphi_{N_s}^l(\tau) \sim e^{-jl\omega\tau} \sum_{n=-N_s, n \neq 0}^{N_s} \frac{1}{\sqrt{|n|}} e^{-\frac{3\beta_2^2}{4\tau_\rho} (\omega l)^2 L_0 |n|} \Lambda\left(\frac{n}{N_s}\right). \quad (54)$$

A narrowing of the probe's Stokes vector spectrum with an increasing number of system spans can be qualitatively understood by defining its spectral width as

$$\frac{1}{\varphi_{N_s}^l(0)} \int \varphi_{N_s}^l(0) d\omega l \approx \frac{\ln(N_s) - 1}{\sqrt{N_s} - 1}. \quad (55)$$

This quantity decreases for large enough and increasing N_s . NL distortions generated along the transmission link interfere, which leads to spectral shaping of the Stokes vector spectrum. Such kind of spectral compression has been experimentally observed (Section 3). The more spans a link consists of, the more nonlinear distortions in form of wave packets superpose in the receiver plane and steepen the pedestal of the averaged RF spectra (**Figure 3b**) [35].

5. Non-Manakovian transmission

We continue to assume that the CNLSs provide a sufficiently accurate basis for signal modeling in a single birefringent waveplate and will compare in the following their nonlinearity with corresponding terms of often-used simplifications such as the Manakov equation [13], the Manakov-PMD equation [8], and GN theory [23]. It turns out that the nonlinearity used in our NLDP calculus differs significantly from simplified forms often exploited in today's system simulations. For this purpose, we examine a known transformation of the CNLS into the ME for regular birefringent fiber, which leads to an inconsistency in the foundation of nonlinear propagation theory. This commonly applied assumption biases microscopic NL polarization effects. As for non-Manakovian effects such as the NLDP, we like to refer to when propagating signals cannot be sufficiently accurately described by applying

equations of Manakovian type or the Manakov-PMD equation, which possess averaged and symmetric Kerr nonlinearities.

5.1 Shortfalls of an averaged Kerr nonlinearity

Here we review key steps for introducing an averaged Kerr nonlinearity into the CNLS and point out the associated shortfalls. The two main concepts [22, 41] to derive an averaged Kerr nonlinearity can be found in the literature. We follow a well-documented scheme in [41], which considers a piece of isotropic fiber (with zero birefringence) and neglect for now linear propagation effects such as attenuation and all forms of dispersion. Furthermore, like all published derivations we assume for $A_{x(y)}^\Sigma$ monochromatic fields at $\omega = 0$, which some papers paraphrase as fully polarized light³. In this case Eqs. (7) and (8) reduces to polarization-dependent differentials that equal small NL distortions

$$\frac{\partial A_x^\Sigma}{\partial z} = j\gamma \left(|A_x^\Sigma|^2 + \frac{2}{3} |A_y^\Sigma|^2 \right) A_x^\Sigma + j\gamma \frac{1}{3} A_x^{\Sigma*} A_y^{\Sigma^2} \quad (56)$$

$$\frac{\partial A_y^\Sigma}{\partial z} = j\gamma \left(|A_y^\Sigma|^2 + \frac{2}{3} |A_x^\Sigma|^2 \right) A_y^\Sigma + j\gamma \frac{1}{3} A_y^{\Sigma*} A_x^{\Sigma^2}. \quad (57)$$

For normalized variables

$$|A_x^\Sigma|^2 + |A_y^\Sigma|^2 = 1 \quad (58)$$

Eqs. (56) and (57) can concisely be written as

$$\frac{\partial A_x^\Sigma}{\partial z} = j\gamma \left(2A_x^\Sigma + A_x^{\Sigma*} \left(A_x^{\Sigma^2} + A_y^{\Sigma^2} \right) \right) \quad (59)$$

$$\frac{\partial A_y^\Sigma}{\partial z} = j\gamma \left(2A_y^\Sigma + A_y^{\Sigma*} \left(A_x^{\Sigma^2} + A_y^{\Sigma^2} \right) \right). \quad (60)$$

Similar as in Section 4.6, we evaluate the magnitude of the polarization state-dependent NL distortion by expressing the field with a Jones vector

$$\begin{bmatrix} A_x^\Sigma \\ A_y^\Sigma \end{bmatrix} = \begin{bmatrix} \cos\vartheta \cos \varepsilon + j \sin\vartheta \sin \varepsilon \\ \sin\vartheta \cos \varepsilon - j \cos\vartheta \sin \varepsilon \end{bmatrix} e^{i\psi}. \quad (61)$$

But here, the time-independent variables $\vartheta, \varepsilon, \psi$ are functions of the distance z . As empirically observed, the SOP of a cw light propagating through randomly and rapidly changing fiber birefringence is uniformly distributed on the Poincare sphere with corresponding densities for the angles ϑ, ε as assumed for Eq. (46).

Inserting Eq. (61) into the left sides of Eqs. (59) and (60) leads to a differential term for the phase

$$\begin{bmatrix} A_x^\Sigma & A_y^\Sigma \end{bmatrix}^\dagger \partial_z \psi \quad (62)$$

³ Note, in the given derivation [22] on p. 29 it should read shortly above Eq. (3) “converts $s_3 \sigma_3 \mathbf{U}$ to $1/3 s_0 \mathbf{U}$.”

that can be evaluated as scalar when multiplying both sides of the equation by $\left[A_x^\Sigma A_y^\Sigma\right]^*$. Averaging the differentials across the Poincare sphere by means of Eq. (46) must equate to zero for terms including $\partial_z \vartheta$ and $\partial_z \varepsilon$ due to symmetry considerations. Thus, on the left only a term in $\partial_z \psi$ remains. On the right, $\left(|A_x^\Sigma|^2 + |A_y^\Sigma|^2\right)$ is factored out, which is no longer assumed to be limited to unity, but represents time- and distance-dependent power levels of a signal. When adding the time-dependent differentials on the left sides that describe linear propagation effects and including the absorption term, then the ME as stated in form of Eqs. (5) and (6) with an averaged Kerr NL follows. As this derivation assumes an isotropic fiber, β_1, β_2 must be defined as x -, y -independent. Some closed-form solutions of Eqs. (5) and (6) are known (solitons). Its nonlinearity is symmetric in the field components. But strictly speaking, the above derivation holds only for cw light and so Eqs. (5) and (6). The reintroduction of Eq. (58) as time- and distance-dependent quantity without expanding term (62) by additional corresponding differentials violates the derivation's assumptions and complicates it. Literature justifies the above derivation with lacking phase matching of mixing terms that can be neglected. However, if the field contains components that are closely separated, a low-frequency beat tone can occur. When sufficient phase matching is present (as in the case of NLDP), measurable modulation of the probe can appear. Additionally, the derivation does not mirror correlations among differentials in $\partial_z \vartheta$ or $\partial_z \varepsilon$ taken at two different positions separated by PMD. But as such, they are essential for understanding the spectral properties of NLDP.

When choosing Eqs. (5) and (6) as starting point for the splitting of the overall NL operator as explicated by Eqs. (12) and (13), the symmetric and asymmetric NL perturbation terms change their relative weights. Hence, both phenomena NLDP and NL phase noise cannot be represented at the same time using the same effective average Kerr nonlinearity.

5.2 Manakovian simulators in telecom

A common technique in modern optical communications is to polarization multiplex two orthogonal channels at same wavelength, which maximizes the spectral efficiency of a system. When representing in a simplified picture transmitted data symbols per channel by optical wave packets, their instantaneous common receive SOP is equally blurred by NLDP in both azimuth and polar angles on the Poincare sphere. Especially, fast SOP motions in azimuthal direction (assuming the individual channels possess polarizations aligned with the x - y coordinates) impair coherent cross talk at high receive OSNR for advanced modulation formats and reduce established limits for the channel capacity. Current research on capacity limits of fiber channels has not explicitly considered NLDP. These theories apply Shannon's theorem while computing NL signal distortions by means of the Manakov equation [42–49]. They need to be revisited when more accurate estimates are required.

To ease computations, most of the industrial link simulations resort to a type of ME when estimating NL transmission penalties. For signals with low-density constellation (e.g., PM-QPSK), the small NLDP-induced SOP scattering has little performance impact and a Manakovian simulation can be a good approximation. As reference, for a link with moderate Kerr nonlinearity and transpacific transmission distance, we experimentally found an apex angle $\sim 11^\circ$ for NLDP-induced scattering on the Poincare sphere [40].

The Manakov-PMD equation as defined in [8] includes the 8/9 factor for an averaged Kerr nonlinearity. For regular birefringent fiber, its NL PMD term

becomes irrelevant and only its linear PMD term distinguishes it from an ordinary ME. However, the averaging of its Kerr nonlinearity that yields its 8/9 weighting questions its claim of universal acceptance as a governing model.

The GN model, another widely discussed approach for simulating optical communication channels, is a technique to analytically solve the ME for a weakly NL WDM system with D+ propagation [23, 50]. Its main advantage resides in the derivation of variances for NL field distortions that can be linearly added to noise powers (repeater ASE) in the SNR formula to determine a BER. Note, these NL field distortions should not be confused with polarization state noise generated by NLDP. The GN model does not include PMD effects, which lead to a linear SOP decorrelation between the probe and the beating ASE components [39]; but this decorrelation is essential for the foundation of the probe's NLDP-induced Stokes vector spectrum, which is interferometrically formed by long-range NL interactions (Section 3 [35]).

6. Conclusions

Precise modeling of NL signal propagation in optical fibers is critical for maximizing the data capacity of long-haul communication systems. It balances signal powers and received OSNR to mitigate nonlinearities. Over the past five decades, simplified techniques have been developed to efficiently compute NL propagation in fiber. They adapt models for ideal or piece-wise linear birefringent fiber to simulate propagation paths with randomly varying birefringence.

Recently, a novel transmission phenomenon in fiber to which we refer to as NL DePolarization (NLDP) has been introduced. Unpolarized ASE depolarizes a co-propagating probe in long-haul communication systems and lab test beds due to the fiber Kerr nonlinearity. This phenomenon has proven elusive to simpler propagation modeling.

We have described NLDP by means of propagation-dependent SOP speed histograms. And under some simplifying assumptions, our outlined analytical model yields a closed-form solution for NLDP-induced SOP speed in single and multiple span systems. Although small compared with other polarization effects, this phenomenon leads to a qualitatively different microscopic understanding of nonlinear light propagation in fiber. An antisymmetric perturbation operator in the CNLS generates phase noises that produce the SOP fluctuations. A major aspect of our model forms the PMD dependence of NLDP, which fundamentally differentiates it from other NL polarization phenomena such as NL polarization rotation. NLDP is based on long-range NL interactions where contributions from Kerr nonlinearities interfere over long transmission distances. Counterintuitively, the NL-generated Stokes vector spectrum of a signal's polarization narrows with increasing propagation length.

Our derivations show that in the case of NLDP (non-Manakovian propagation), the solution spaces of the CNLS and the Manakov equation do not converge as suggested by earlier work. Under consideration of NLDP, reassessing fiber channel capacity simulations that are utilizing Manakovian-type equations can be beneficial for scientific purposes and could show small performance offsets.

Author details

Lothar Moeller
SubCom LLC, Eatontown, New Jersey, USA

*Address all correspondence to: lmoeller@subcom.com

IntechOpen

© 2022 The Author(s). Licensee IntechOpen. This chapter is distributed under the terms of the Creative Commons Attribution License (<http://creativecommons.org/licenses/by/3.0>), which permits unrestricted use, distribution, and reproduction in any medium, provided the original work is properly cited. 

References

- [1] Markets and Markets. Optical Communication and Networking Equipment Market, Online Report. 2021. Available from: <https://www.marketsandmarkets.com/Market-Reports/Optical-networking-communications-market-227693036.html>
- [2] Chesnoy J. Undersea Fiber Communication Systems. Netherlands: Elsevier Science; 2015. ISBN 9780128043950
- [3] Cai JX et al. 51.5 Tb/s capacity over 17,107 km in C+L bandwidth using single-mode fibers and nonlinearity compensation. *Journal of Lightwave Technology*. 2009;**36**:2135-2141
- [4] Hartling ER et al. Design, acceptance and capacity of subsea open cables. *Journal of Lightwave Technology*. 2021;**39**:742-756
- [5] Pecci P et al. Subsea open cables: A practical perspective on the guidelines and gotchas. *SubOptic*. 2019
- [6] Menyuk CR. Nonlinear pulse propagation in birefringent optical fibers. *IEEE Journal of Quantum Electronics*. 1987;**QE-23**:174-176
- [7] Menyuk CR, Marks BS. Interaction of polarization mode dispersion and nonlinearity in optical fiber transmission systems. *Journal of Lightwave Technology*. 2006;**24**:2806-2826
- [8] Marcuse D, Menyuk CR, Wai PKA. Application of the Manakov-PMD equation to studies of signal propagation in optical fibers with randomly varying birefringence. *Journal of Lightwave Technology*. 1997;**15**:1735-1746
- [9] Damask JN. *Polarization Optics in Telecommunications*. New York: Springer; 2005. ISBN 9780387263021
- [10] Brodsky M, Frigo NJ, Boroditsky M, Tur M. Polarization mode dispersion of installed fibers. *Journal of Lightwave Technology*. 2006;**24**:4584-4599
- [11] ITU-T Recommendations, ITU-T G.652. Available from: <https://www.itu.int/itu-t/recommendations/rec.aspx?rec=13076>
- [12] Liu Y. Novel optical fibers for WDM transmission and dispersion management. In: *Nanostructures and Quantum Dots/WDM Components/VCSELs and Microcavities/RF Photonics for CATV and HFC Systems* (Cat. No.99TH8455). LEOS Summer Topical Meeting, San Diego, CA, USA: IEEE; 1999. DOI: 10.1109/LEOSST.1999.794648. Available from: <https://ieeexplore.ieee.org/document/794648>. ISBN: 0-7803-5633-0
- [13] Manakov SV. On the theory of two-dimensional stationary self-focusing of electromagnetic waves. *Journal of Experimental and Theoretical Physics*. 1974;**38**:248-253
- [14] Boyd RW. *Nonlinear Optics*. Cambridge, Massachusetts: Academic Press; 2003. ISBN 0-12-121682-9
- [15] Collings BC, Boivin L. Nonlinear polarization evolution induced by cross-phase modulation and its impact on transmission systems. *IEEE Photonics Technology Letters*. 2002;**12**:1582-1584
- [16] Winter M, Bunge CA, Setti D, Petermann K. A statistical treatment of cross-polarization modulation in DWDM systems. *Journal of Lightwave Technology*. 2009;**27**:3739-3751
- [17] Millot G, Wabnitz S. Nonlinear polarization effects in optical fibers: Polarization attraction and modulation instability. *Journal of the Optical Society of America A*. 2014;**B31**:2754-2768
- [18] Lu F, Lin Q, Knox WH, Agrawal GP. Vector soliton fission.

Physical Review Letters. 2004;**93**:
183901

[19] Ferreira MFS. Nonlinear Effects in
Optical Fibers. Hoboken: Wiley; 2011

[20] Mollenaur LF, Gordon JP,
Heismann F. Polarization scattering by
soliton-soliton collisions. Optics Letters.
1995;**16**:2060-2062

[21] Wai PKA, Menyuk CR, Chen HH.
Stability of solitons in randomly varying
birefringent fibers. Optics Letters. 1991;
16:1231-1233

[22] Evangelides SG, Mollenauer LF,
Gordon JP, Bergano NS. Polarization
multiplexing with solitons. Journal of
Lightwave Technology. 1992;**10**:28-35

[23] Poggiolini P. The GN model of non-
linear propagation in uncompensated
coherent optical systems. Journal of
Lightwave Technology. 2012;**24**:
3857-3879

[24] Nakazawa M, Terayama M,
Okamoto S, Yoshida M, Kasai K,
Hirooka T. Observation of guided
acoustic-wave Brillouin scattering and its
digital compensation in coherent QAM
transmission. In: Proceedings of Optical
Fiber Communications Conference
(OFC), Paper M4B.2. London: IEEE; 2018

[25] Bolshtyansky A, Cai J-X,
Davidson C, Mazurczyk M, Wang D,
Paskov M, et al. Impact of spontaneous
guided Acoustic-wave Brillouin
scattering on long-haul transmission. In:
Proceedings of Optical Fiber
Communications Conference (OFC),
Paper M4B.3. London: IEEE; 2018

[26] Moeller L. Nonlinear depolarization
of light in optical communication fiber.
APL Photonics. 2020;**5**(5):050801

[27] Noe R, Koch B, Mirvoda V.
Polarimetry of Polarization-Modulated
Signals Based on Polarization-Selective

RF Power Detection. Los Angeles, CA,
USA: OFC; 2017

[28] Moeller L. Experimentally observed
nonlinear depolarization of cw light in
long-haul transmission. In: European
Conf. on Optical Communications
(ECOC). CLEO, TOPS: Dublin, Ireland;
2019

[29] Stolen RH, Lin C. Self-phase-
modulation in silica optical fibers.
Physical Review A. 1978;**17**(4):1448

[30] Chi S, Lee CC, Chiang PW, Li CH,
Tsai FY, Tu YK. Measurement of
stimulated-Brillouin-scattering
thresholds for various types of fibers
using Brillouin optical-time-domain
reflectometer. In: Conference on Lasers
and Electro-Optics (CLEO), TOPS. Vol.
39. CLEO, TOPS: San Jose, California,
USA; 2000

[31] Agrawal GP. Fiber-Optics
Communication Systems. Hoboken,
New Jersey, United States: Wiley; 1997.
ISBN 0-47-17540-4

[32] Bergano NS, Davidson CD.
Circulating loop transmission
experiments for the study of long-haul
transmission systems using erbium-
doped fiber-amplifiers. Journal of
Lightwave Technology. 1995;**13**:879-888

[33] Dumenil A, Awwad E, Méasson C.
PDL in optical links: A model analysis
and a demonstration of a PDL-resilient
modulation. Journal of Lightwave
Technology. 2020;**38**(18):5017-5025

[34] Yu Q, Yan LS, Lee S, Xie Y,
Willner AE. Loop-synchronous
polarization scrambling technique for
simulating polarization effects using
recirculating fiber loops. Journal of
Lightwave Technology. 2003;**21**:
1593-1600

[35] Moeller L. Stokes vector
spectroscopy of nonlinear depolarized
light. In: 45th European Conference on

Optical Communication (ECOC).
ECOC: Brussels, Belgium; 2019

[36] Saleh BEA, Teich MC.
Fundamentals of Photonics. Hoboken,
New Jersey, United States: John Wiley
& Sons; 1991. ISBN 0-471-83965-5

[37] Sinkin O, Holzlohner R, Zweck J,
Menyuk CR. Optimization of the split-
step Fourier method in modeling
optical-fiber communications systems.
Journal of Lightwave Technology. 2003;
21:61-68

[38] Agrawal GP. *Nonlinear Fiber
Optics*. 3rd ed. San Diego: Academic
Press; 2001

[39] Karlsson M, Brentel J,
Anderkson PA. Long-term
measurement of PMD and polarization
drift in installed fibers. *Journal of
Lightwave Technology*. 2000;**18**:
941-951

[40] Moeller L. Stokes vector scattering
induced by nonlinear depolarization of
light in fiber. In: 46th European
Conference on Optical Communication
(ECOC). ECOC: Brussels, Belgium; 2020

[41] Noe R. *Essentials of Modern Optical
Fiber Communication*. Berlin, Germany:
Springer; 2010. ISBN 978-3-662-49623-7

[42] Essiambre R, Foschini G, Kramer G,
Winzer P. Capacity limits of
information transport in fiber-optic
networks. *Physical Review Letters*.
2008;**101**:163901-163904

[43] Tang J. The Shannon channel
capacity of dispersion-free nonlinear
optical fiber transmission. *Journal of
Lightwave Technology*. 2001;**19**:
1104-1109

[44] Tang J. A comparison study of the
Shannon channel capacity of various
nonlinear optical fibers. *Journal of
Lightwave Technology*. 2006;**24**:
2070-2075

[45] Turitsyn KS, Derevyanko SA,
Yurkevich IV, Turitsyn SK. Information
capacity of optical fiber channels with
zero average dispersion. *Physical
Review Letters*. 2003;**91**:203901

[46] Mitra PP, Stark JB. Nonlinear limits
to the information capacity of optical
fibre communications. *Nature
(London)*. 2001;**411**:1027-1030

[47] Narimanov EE, Mitra P. The
channel capacity of a fiber optics
communication system: Perturbation.
*Theory Journal of Lightwave
Technology*. 2002;**20**:530-537

[48] Mecozzi A, Essembré RJ. Nonlinear
shannon limit in pseudolinear coherent
systems. *Journal of Lightwave
Technology*. 2012;**30**:2011-2024

[49] Poggiolini P, Bosco G, Carena A,
Curri V, Jiang Y, Forghieri F. Analytical
results on channel capacity in
uncompensated optical links with
coherent detection. In: *The Proceedings
Under European Conference on Optical
Communication*. Geneva: IEEE; 2011

[50] Poggiolini P, Carena A, Curri V,
Bosco G, Forghieri F. Analytical
modeling of nonlinear propagation in
uncompensated optical transmission
links. *IEEE Photonics Technology
Letters*. 2011;**23**:742-744

Nonlinear Generalized Schrödinger's Equations by Lifting Hamilton-Jacobi's Formulation of Classical Mechanics

Gérard Gouesbet

Abstract

It is well known that, by taking a limit of Schrödinger's equation, we may recover Hamilton-Jacobi's equation which governs one of the possible formulations of classical mechanics. Conversely, we may start from the Hamilton-Jacobi's equation and, by using a lifting principle, we may reach a set of nonlinear generalized Schrödinger's equations. The classical Schrödinger's equation then occurs as the simplest equation among the set.

Keywords: Schrödinger's equation, Hamilton-Jacobi's equation, correspondence principle, lifting principle

1. Introduction

Schrödinger's equation is the fundamental equation of quantum mechanics. Using a correspondence principle, we may recover the classical limit of mechanics under the form of the Hamilton-Jacobi's equation. This is a up-down process, from a general theory to a limit restricted theory, i.e. from quantum mechanics to classical mechanics. We may use another principle, that I call a lifting principle, which, starting from Hamilton-Jacobi's equation allows one, through a bottom-up process, to reach a set of generalized Schrödinger's equations, encompassing nonlinear terms. From this generalized set, we may turn back to a up-bottom process. In a first step, we recover the classical Schrödinger's equation as, in some sense, the simplest equation in the set and, in a second step, we recover again classical mechanics from quantum mechanics, using again a correspondence principle.

The chapter is organized as follows. Section 2 recalls the Hamilton-Jacobi's equation of classical mechanics which, in the present chapter, may be viewed as a turning equation, both the end of a up-bottom process and the beginning of a bottom-up process. Section 3 exemplifies a way to obtain Schrödinger's equation by using an analogy relying on Hamilton-Jacobi's equation. Section 4 expounds the bottom-up process from Hamilton-Jacobi's equation to a set of generalized Schrödinger's equations. Section 5 provides a complementary discussion while Section 6 is a conclusion.

2. Hamilton-Jacobi's formulation of classical mechanics

We know that classical mechanics can be declined under four different formulations, which are mathematically and empirically equivalent. These are the Newton's, Lagrange's, Hamilton's and Hamilton-Jacobi's formulations. In the present chapter, we rely on the Hamilton-Jacobi's formulation, see for instance Louis de Broglie [1], Blotkhintsev [2], Landau and Lifchitz [3], and Holland [4]. This formulation of nonrelativistic classical mechanics of a matter point relies on an equation, that I shall call Hamilton-Jacobi's equation, reading as:

$$-\frac{\partial S}{\partial t} = \frac{1}{2m} \left(\frac{\partial S}{\partial x_j} \right)^2 + V \quad (1)$$

This equation allows one to study the motions of a particle of mass m in a potential $V = V(x_j, t)$. The x_j 's denote Cartesian coordinates and t is the time. The field $S = S(x_j, t)$ is a real field that I shall call the Jacobi's field. Eq. (1) has to be complemented by two other equations reading as:

$$W = -\frac{\partial S}{\partial t} \quad (2)$$

$$p_j = \frac{\partial S}{\partial x_j} \quad (3)$$

in which W is the energy and p_j is the momentum. From Eq. (2), we see that S is an action (energy multiplied by time) and, from now on, we may call it the action. Also, inserting Eqs. (2) and (3) in Eq. (1), we see that we obtain $W = T + V$, which should be enough to convince us of the equivalence between Newton's and Hamilton-Jacobi's formulations. For a conservative motion, the energy (that we denote E in that case) is constant along each particular motion, and Eq. (2) implies:

$$S(x_j, t) = S_0(x_j) - Et \quad (4)$$

Inserting Eq. (4) into Eq. (1), we obtain:

$$\left(\frac{\partial S_0}{\partial x_j} \right)^2 = 2m(E - V) \quad (5)$$

We now consider the locus of the points for which S_0 possesses a given value C_0 :

$$S_0(x_j) = C_0 \quad (6)$$

Eq. (6) shows that the locus is a time-independent surface. There is one surface, and only one, containing a point P of space, according to $C_0 = S_0(x_j(P))$. The whole space is therefore filled by a set of motionless surfaces forming what I call the Jacobi's static field. From Eqs. (3) and (4), we have:

$$p_j = \left(\frac{\partial S}{\partial x_j} \right) = \left(\frac{\partial S_0}{\partial x_j} \right) \quad (7)$$

Therefore, p_j is the gradient of S (and of S_0). This means that trajectories are orthogonal to the surfaces S (and to the surfaces S_0). Next, we consider the locus of the points for which the action S possesses a given value C :

$$S(x_j, t) = C \quad (8)$$

Eq. (8) shows that the locus is still a surface but which now depends on time. When times goes on, the surface moves and, in general, experiences a deformation. For a given time t , the moving surface $S(x_j, t) = C$ coincides with a motionless surface $S_0(x_j) = C_0$, according to, from Eq. (4): $C = C_0 - Et$. Therefore, when time goes on, the moving surface $S = C$ sweeps over all motionless surfaces $S_0 = C_0$.

We now consider a fictitious point P, pertaining to the surface $S = C$, and therefore moving with it, with the constraint that its displacement remains orthogonal to the swept surfaces $S_0 = C_0$. The velocity of the moving surface may then be defined as:

$$w_j = \frac{dx_j}{dt} \quad (9)$$

in which dx_j is an infinitesimal displacement of the point P. But we have:

$$\frac{dS}{dt} = \frac{dC}{dt} = 0 \quad (10)$$

that is to say:

$$\frac{\partial S}{\partial x_j} \frac{dx_j}{dt} + \frac{\partial S}{\partial t} = 0 \quad (11)$$

leading to:

$$p_j w_j = E \quad (12)$$

But w_j (modulus: w) is colinear to p_j (modulus: p). Hence, with E positive, we obtain:

$$w = \frac{E}{p} = \frac{E}{\sqrt{2m(E - V)}} \quad (13)$$

We are therefore facing two different velocities (i) the velocity $v = p/m$ of the material point and (ii) the velocity $w = E/p$ of the fictitious point P. Finally, inserting Eq. (13) into Eq. (5), we obtain:

$$\left(\frac{\partial S_0}{\partial x_j} \right)^2 = \frac{E^2}{w^2} = p^2 \quad (14)$$

We then remark that Newton's formulation relies on the existence of trajectories while Hamilton-Jacobi's formulation relies both on trajectories and on a field filling the space. Hamilton-Jacobi's formulation is the first one in which the motion of a localized object has been associated with a space filling field. In other words, Hamilton-Jacobi's formulation is nonlocal. This nonlocality actually anticipates the nonlocality of quantum mechanics and the space filling field S is an anticipation as well of a space filling field of quantum mechanics. It has furthermore been argued that Newton's and Hamilton-Jacobi's formulation, although empirically equivalent, are ontological contradictory, representing an example of the Duhem-Quine ontological underdetermination of theory by experience [5, 6].

3. Guessing Schrödinger's derivation

Strictly speaking, there is no derivation of Schrödinger's equations but a variety of guessing approaches, with different flavors depending on the preferences of the authors. Basically, however, Schrödinger's equation has been introduced in [7, 8] under its stationary form and in [9] under its time-dependent form. English translation is available from [10] and French translation from [11]. The derivation relies on an analogy between Hamilton-Jacobi's formulation of classical mechanics and geometrical optics. As rather usual when something new is exposed for the first time, Schrödinger's argument is more complicated than necessary. For instance, it relies on the use of non-Cartesian coordinates and on a non-Euclidean interpretation of the configuration space, requiring the use of covariant and contravariant components of vectors (more generally, of tensors), which may be unfamiliar to some readers. Feynman even commented that some arguments invoked by Schrödinger are erroneous [12]. Without showing any disrespect to Schrödinger's work, I prefer to present a more recent exposition extracted from Winogradski [13] who defended her thesis under the supervision of Louis de Broglie.

We begin with scalar wave optics and with the corresponding wave equation reading as:

$$\frac{\partial^2 \Psi}{\partial x_j^2} - \frac{1}{u^2} \frac{\partial^2 \Psi}{\partial t^2} = 0 \quad (15)$$

in which $u = u(x_j, t)$ is the velocity of the wave $\Psi(x_j, t)$. We may also introduce the refractive index n of the medium according to $n = c/u$ in which c is the speed of light. We now consider a steady medium ($\partial n / \partial t = 0$) which may support monochromatic waves of angular frequency ω , reading as:

$$\Psi(x_j, t) = \Psi_0(x_j) \exp(-i\omega t) \quad (16)$$

Because Ψ and Ψ_0 are, in general, complex fields, we set:

$$\Psi_0 = A \exp(i\phi_0) \quad A, \phi_0 \in \mathcal{R} \quad (17)$$

leading to:

$$\Psi = A \exp(i\phi) \quad (18)$$

with:

$$\phi(x_j, t) = \phi_0(x_j) - \omega t \quad (19)$$

In these expressions, Ψ_0 is a complex amplitude, A a real amplitude, $\phi(x_j, t)$ and $\phi_0(x_j)$ are phases. We may then introduce the wave-number vector reading as:

$$k_j = \frac{\partial \phi}{\partial x_j} = \frac{\partial \phi_0}{\partial x_j} \quad (20)$$

The wave-number k is defined as $\sqrt{k_j^2}$ and the wave-length λ is defined by $\lambda = 2\pi/k$. Also, we have:

$$\omega = -\frac{\partial \phi}{\partial t} \quad (21)$$

Inserting Eq. (16) into Eq. (15), we obtain:

$$\frac{\partial^2 \Psi_0}{\partial x_j^2} + \frac{\omega^2}{u^2} \Psi_0 = 0 \quad (22)$$

Next, inserting Eq. (17) into Eq. (22), we obtain two equations relating the real amplitude A and the phase ϕ_0 :

$$\frac{1}{A} \frac{\partial^2 A}{\partial x_j^2} - \left(\frac{\partial \phi_0}{\partial x_j} \right)^2 + \frac{\omega^2}{u^2} = 0 \quad (23)$$

$$\frac{2}{A} \frac{\partial A}{\partial x_j} \frac{\partial \phi_0}{\partial x_j} + \frac{\partial^2 \phi_0}{\partial x_j^2} = 0 \quad (24)$$

If the medium, besides being steady, is homogeneous ($\partial n / \partial x_j = 0$), the wave equation admits plane wave solutions reading as:

$$\Psi(x_j, t) = A \exp i(k_j x_j - \omega t) \quad (25)$$

in which A , k_j , ω are constant quantities, and λ becomes the spatial period of the wave along the direction of propagation.

We are now equipped enough to turn to a discussion of geometrical optics which is an approximation to wave optics. This approximation is valid whenever the optical wave approximately behaves as a plane wave over a distance of the order of the wave-length λ , that is to say when $A(x_j)$ and $k_j = \partial \phi_0 / \partial x_j$ are approximately constant over λ . Equivalently, we may take the limit $\lambda \rightarrow 0$. There is a rigorous but tedious way to take this limit by examining the relative variations of $\Delta A / A$ and $\Delta k_j / k$ over λ , in the direction $x_{(k)}$, relying on Taylor expansions. I shall rather use heuristic and convincing enough arguments which furthermore lead to the correct results. Because A is approximately a constant, Eq. (23) reduces to:

$$-\left(\frac{\partial \phi_0}{\partial x_j} \right)^2 + \frac{\omega^2}{u^2} = 0 \quad (26)$$

Furthermore, because $k_j = \partial \phi_0 / \partial x_j$ is approximately a constant too, Eq. (24) reduces to an identity $0 \equiv 0$. Therefore, Eq. (26) is the geometrical optics version of the wave optics. Eqs. (23) and (24), i.e. two equations, have collapsed into a single one. We observe that Eq. (26) contains the phase ϕ_0 , but does not contain any more the amplitude A . This means that the concept of amplitude has no meaning, in a strict sense defined by the above derivation, in geometrical optics (this does not prevent to build geometrical optics models using the concept of amplitude).

Also, from Eqs. (20) and (26), we have:

$$k^2 = \frac{\omega^2}{u^2} \quad (27)$$

Now, similarly as for S_0 and S , ϕ_0 and ϕ are equiphase surfaces satisfying the following obvious analogous results. The locus of the points for which ϕ_0 possesses a given value C_0 , i.e. $\phi_0(x_j) = C_0$, is a time-independent equiphase surface. There is one surface, and only one, containing a point P of space, given by $C_0 = \phi_0(x_j(P))$. The whole space is therefore filled by a set of motionless surfaces forming the static phase field. The trajectories orthogonal to these surfaces are called rays. The locus of the points for which ϕ possesses a given value C , i.e. $\phi(x_j, t) = C$, is a

time-dependent equiphase surface. For a given time t , the moving equiphase surface $\phi = C$ coincides with a motionless equiphase surface $\phi_0 = C_0$. When time goes on, the moving surface $\phi = C$ sweeps over all motionless surfaces $\phi_0 = C_0$.

Assembling the results obtained for the conservative Hamilton-Jacobi's classical mechanics and for geometrical optics, we obtain a remarkable analogy exhibited in **Table 1**.

This analogy has been discovered by Hamilton, about one century (!) before its use to the discovery of Schrödinger's equations, see Refs. [14, 15], references therein and prior references from Hamilton. Formally, we may express the same structure by using a mechanical language or an optical language. Both languages may be translated, from one to the other, by using a dictionary D exhibited in **Table 2**, where the newly introduced constant G has the dimension of an action.

An analogy is not necessarily significant but any analogy should be, at least tentatively, taken seriously. If the analogy is fully meaningless, then the value of the constant G does not matter, and any value for G would do. *A contrario*, if the analogy is somehow meaningful, that is to say if the motion of a material point can be somehow associated with the propagation of a certain scalar field (the point of view taken *very seriously* by Louis de Broglie in his double solution), then the constant G should be a new fundamental constant of nature. We now know that the analogy under study may be taken seriously enough, and that it eventually leads to $G = \hbar$. Lines (c) and (d) of **Table 2** then lead to:

$$p_j = \hbar k_j \tag{28}$$

$$E = \hbar \omega \tag{29}$$

Classical mechanics	Geometrical optics
$S = S_0 - Et$	$\Phi = \Phi_0 - \omega t$
$S_0 = S_0(x_j)$	$\Phi_0 = \Phi_0(x_j)$
$E = \text{constant}$	$\omega = \text{constant}$
$p_j = \frac{\partial S}{\partial x_j} = \frac{\partial S_0}{\partial x_j}$	$k_j = \frac{\partial \Phi}{\partial x_j} = \frac{\partial \Phi_0}{\partial x_j}$
$E = -\frac{\partial S}{\partial t}$	$\omega = -\frac{\partial \Phi}{\partial t}$
$\left(\frac{\partial S_0}{\partial x_j}\right)^2 = \frac{E^2}{u^2} = p^2$	$\left(\frac{\partial \Phi_0}{\partial x_j}\right)^2 = \frac{\omega^2}{u^2} = k^2$
$w = E/p$	$u = \omega/k$
Trajectory	Ray

Table 1.
Analogy between Hamilton-Jacobi's classical mechanics and geometrical optics.

$S = G\Phi$	(a)
$S_0 = G\Phi_0$	(b)
$p_j = \frac{\partial S}{\partial x_j} = G \frac{\partial \Phi}{\partial x_j} = Gk_j$	(c)
$E = -\frac{\partial S}{\partial t} = -G \frac{\partial \Phi}{\partial t} = G\omega$	(d)
$w = \frac{E}{p} = \frac{G}{k} = u$	(e)
trajectory \leftrightarrow ray	

Table 2.
The dictionary.

which we call de Broglie, or Einstein-de Broglie relations. Eq. (28) expresses an equivalence between momentum (mechanical language) and wave-number (optical language), while Eq. (29) expresses an equivalence between energy (mechanical language) and angular frequency (optical language).

The situation we are facing is now sketched in the **Figure 1** below. First, we possess an analogy between Hamilton-Jacobi's classical mechanics and geometrical optics, expressed by a dictionary D. Second, geometrical optics is an approximation to scalar wave optics. The **Figure 1** then exhibits three filled rectangles, and we may feel intuitively but clearly that something is lacking, corresponding to the fourth empty rectangle. To fill this rectangle, we apply the dictionary D to wave optics. From the dictionary of **Table 2**, with $G = \hbar$, we have:

$$\frac{\omega^2}{u^2} = k^2 = \frac{p^2}{\hbar^2} = \frac{2m(E - V)}{\hbar^2} \quad (30)$$

We may then translate Eq. (22) to:

$$\frac{\partial^2 \Psi_0}{\partial x_j^2} + \frac{2m}{\hbar^2} (E - V) \Psi_0 = 0 \quad (31)$$

which is exactly the time-independent (stationary) Schrödinger's equation. Therefore, Eq. (16) is translated to:

$$\Psi = \Psi_0 \exp(-iEt/\hbar) \quad (32)$$

and we readily establish that Ψ also satisfies Eq. (31) that we better rewrite as:

$$-\frac{\hbar^2}{2m} \frac{\partial^2 \Psi}{\partial x_j^2} + V\Psi = E\Psi \quad (33)$$

Next, we can eliminate E from Eq. (33) by using Eq. (32). The "simplest" way to do it is to write:

$$E\Psi = i\hbar \frac{\partial \Psi}{\partial t} \quad (34)$$

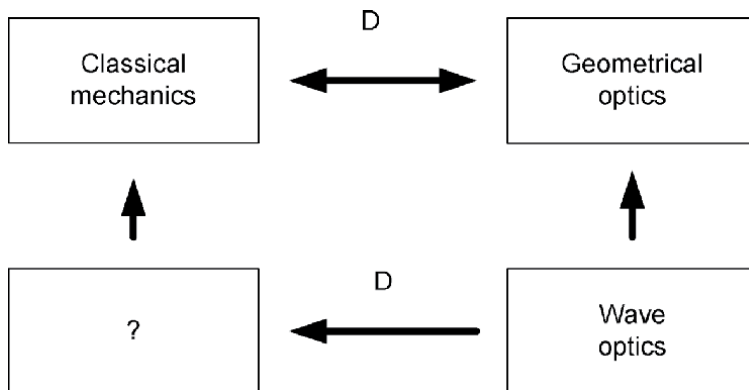


Figure 1.
 Guessing Schrödinger's equation.

leading to:

$$i\hbar \frac{\partial \Psi}{\partial t} = -\frac{\hbar^2}{2m} \frac{\partial^2 \Psi}{\partial x_j^2} + V\Psi \quad (35)$$

which is the general time-dependent Schrödinger's equation. Invoking the “simplest” way to obtain Eq. (34) rules out awkward expressions such as the one obtained by deriving Eq. (32) twice with respect to time, i.e.:

$$E\Psi = i\hbar \sqrt{\Psi \frac{\partial^2 \Psi}{\partial t^2}} \quad (36)$$

4. Deriving a set of generalized Schrödinger's equations

There are good reasons to believe that classical mechanics is suspicious. One of them is the existence of singularities in classical mechanics such as exhibited in the mechanical rainbow [16, 17]. If we trust a non-singularity principle stating that “local infinity in physics is not admissible” [18], we arrive to the conclusion that we must build a wave mechanics (nowadays better known as “quantum mechanics”). For this, we decide to start from what we know (actually what we are supposed to know), namely classical mechanics. We are looking for a wave mechanics based on a wave $\Psi(x_j, t)$ which should have the virtue of washing out the singularities exhibited by classical mechanics. The most general form for a wave reads as:

$$\Psi = e^{iT} \quad (37)$$

in which $T = T(x_j, t)$ is a complex dimensionless phase. At this stage, our amount of knowledge is supposed to be very weak. We only possess one field $S(x_j, t)$ for classical mechanics and two fields $\Psi(x_j, t)$ and $T(x_j, t)$ for wave mechanics. These fields are the only quantities involved in the problem. Therefore, we have to search for a relationship between Ψ and S (first option), or between T and S (second option). Because T and S possess the same nature (they are fields without being waves), I preferably choose the second option. Of course, the first option is likely to be valid as well, but it would certainly lead to more complicated derivations and equations.

For the relationship between T and S , we could search for $T(S)$ or for $S(T)$. Because wave mechanics (T) is assumed to be more general than classical mechanics (S), it is apparent that we better have to try to determine $T(S)$ rather than the inverse version $S(T)$. We therefore have to explicitly consider $T(x_j, t) = T(S(x_j, t))$. However, this is to be slightly corrected. Indeed, T is dimensionless while S is an action (the action). This will require us to introduce a new constant, that will be denoted g .

Now, I invoke a principle that I call the lifting principle (later to be commented a bit more when the demonstration is completed). This principle tells us something very simple, even looking a bit like tautological, as follows: classical mechanics is an approximation to wave mechanics. Rather than simply using the argument S in $T(S)$, we then have to look for a function $T(\bar{S})$ in which the functional argument $\bar{S} = \bar{S}(x_j, t)$ reads as:

$$\bar{S} = \frac{1}{g}(S + i\epsilon S_1) \quad (38)$$

in which g is a constant having the dimension of an action, S_1 is a correcting function, and ε is a small parameter. To recover classical mechanics from wave mechanics, we shall have to take the limit $\varepsilon \rightarrow 0$ so that, the constant g being dismissed, we are left with the field S (and with its equation). Also, we can take $\varepsilon \in \mathcal{R}$. Indeed, if ε were complex, it would exhibit a phase factor which could be absorbed in S_1 . Similarly, the prefactor “ i ” which is introduced for convenience could be absorbed in S_1 .

The function $T(\bar{S})$ may be explicitly written as:

$$T = T_\varepsilon \left(\frac{S + i\varepsilon S_1}{g} \right) \quad (39)$$

in which we used a subscript ε to insist on the fact that T depends on ε . Eq. (39) may give the feeling that we are dealing with a restricted first-order perturbation approach. However, instead of Eq. (38), let us assume:

$$\bar{S} = \frac{1}{g} \left(S + i\varepsilon \bar{S}_1 + (i\varepsilon)^2 \bar{S}_2 + \dots \right) \quad (40)$$

This can be rewritten as:

$$\bar{S} = \frac{1}{g} \left[S + i\varepsilon (\bar{S}_1 + i\varepsilon \bar{S}_2 + \dots) \right] \quad (41)$$

which, relabelling, identifies with Eq. (38).

We are now looking for a differential equation satisfied by the wave Ψ , involving partial derivatives with respect to x_j and t . This equation must be fundamental, that is to say it must contain lowest-order derivatives compatible with the constraints imposed by the problem under study. Once the fundamental equation is obtained, we can of course generate other equations by further differentiating with respect to x_j and t , but such extra-equations are said to be non-fundamental.

We begin with the assumption that, besides derivatives with respect to x_j , the wave equation only contains the first derivative $\partial\Psi/\partial t$ with respect to time. We shall later comment on the use of higher-order derivatives with respect to time.

The derivative $\partial\Psi/\partial t$ may always be written as:

$$\frac{\partial\Psi}{\partial t} = f_\varepsilon(K, \{\partial\Psi\}) \quad (42)$$

in which we again use a subscript ε to insist on the dependence on ε . Also, K is an extra-field (i.e. a function of time and space, but not a dynamical field possessing its own differential equation), possibly a constant, and $\{\partial\Psi\}$ represents a set of arguments formed from various derivatives of Ψ with respect to x_j :

$$\Psi_{i_1 i_2 i_3 \dots i_r} = \frac{\partial}{\partial x_{i_1}} \frac{\partial}{\partial x_{i_2}} \frac{\partial}{\partial x_{i_3}} \dots \frac{\partial}{\partial x_{i_r}} \Psi \quad (43)$$

The set $\{\partial\Psi\}$ is infinite and there is a systematic way to generate all arguments of the set. For instance, the subset generated by Ψ_{ijk} contains $\Psi_{ijk}\Psi_i\Psi_j\Psi_k$, $\Psi_{ijk}\Psi_{ij}\Psi_k$, ..., and other arguments obtained by using complex conjugations.

We may also express the derivative $\partial\Psi/\partial t$ from Eqs. (37) and (39), so that we obtain:

$$\frac{\partial \Psi}{\partial t} = i \frac{dT_\varepsilon}{dS} \frac{1}{g} \left(\frac{\partial S}{\partial t} + i\varepsilon \frac{\partial S_1}{\partial t} \right) \Psi \quad (44)$$

We rewrite Eq. (44) as:

$$-\frac{\partial S}{\partial t} = i\varepsilon \frac{\partial S_1}{\partial t} - \frac{g}{i \frac{dT_\varepsilon}{dS} \Psi} \frac{\partial \Psi}{\partial t}, \quad \Psi \neq 0 \quad (45)$$

or, invoking Eq. (42):

$$-\frac{\partial S}{\partial t} = i\varepsilon \frac{\partial S_1}{\partial t} - \frac{g}{i \frac{dT_\varepsilon}{dS} \Psi} f_\varepsilon(K, \{\partial \Psi\}) \quad (46)$$

But, Hamilton-Jacobi's equation (and the lifting principle) implies that the r.h.s. of Eq. (46) must contain a term with no derivative associated with V in Eq. (1), and a term involving $(\partial S / \partial x_j)^2$, associated with the first term in the r.h.s. of Eq. (1). These terms have to be involved in the function f_ε . Upon investigation, we find that the term involving $(\partial S / \partial x_j)^2$ can only be generated by Ψ_{jj} which indeed is found to be:

$$\begin{aligned} \Psi_{jj} = & \frac{i\Psi}{g} \left\{ \frac{T}{g} \left(\frac{\partial S}{\partial x_j} \right)^2 + \frac{2i\varepsilon T}{g} \frac{\partial S}{\partial x_j} \frac{\partial S_1}{\partial x_j} \right. \\ & \left. - \frac{\varepsilon^2 T}{g} \left(\frac{\partial S_1}{\partial x_j} \right)^2 + \frac{dT_\varepsilon}{dS} \left(\frac{\partial^2 S}{\partial x_j^2} + i\varepsilon \frac{\partial^2 S_1}{\partial x_j^2} \right) \right\} \end{aligned} \quad (47)$$

in which:

$$T = i \left(\frac{dT_\varepsilon}{dS} \right)^2 + \frac{d^2 T_\varepsilon}{dS^2} \quad (48)$$

We therefore set, without any loss of generality:

$$f_\varepsilon(K, \{\partial \Psi\}) = a \frac{\partial^2 \Psi}{\partial x_j^2} + b\Psi + h_\varepsilon(K, \{\partial \Psi\}) \quad (49)$$

in which h_ε is a complementary function, possibly including non-linear terms, and which also could possibly annihilate the terms $a\partial^2 \Psi / \partial x_j^2$ and $b\Psi$ if, eventually, we would find that they should be zero.

The evolution Eq. (42) then takes the form:

$$\frac{\partial \Psi}{\partial t} = a \frac{\partial^2 \Psi}{\partial x_j^2} + b\Psi + h_\varepsilon(K, \{\partial \Psi\}) \quad (50)$$

and our next task is to evaluate a and b .

To this purpose, we now return to Eq. (46) and insert in it Eqs. (49) and (47), leading to:

$$-\frac{\partial S}{\partial t} + \frac{a}{g} \left(\frac{\partial S}{\partial x_j} \right)^2 \left(i \frac{dT_\varepsilon}{dS} + \frac{d^2 T_\varepsilon / dS^2}{dT_\varepsilon / dS} \right) + \frac{gb}{i \frac{dT_\varepsilon}{dS}} = \mathcal{A} + \mathcal{B} + \mathcal{C} \quad (51)$$

with:

$$\begin{aligned}
 A &= -a \frac{\partial^2 S}{\partial x_j^2} - g \frac{h_\epsilon}{i \frac{dT_\epsilon}{d\bar{S}}} \Psi \\
 B &= \epsilon \left[i \frac{\partial S_1}{\partial t} - \frac{2ia}{g} \left(i \frac{dT_\epsilon}{d\bar{S}} + \frac{d^2 T_\epsilon / d\bar{S}^2}{dT_\epsilon / d\bar{S}} \right) \frac{\partial S}{\partial x_j} \frac{\partial S_1}{\partial x_j} - ia \frac{\partial^2 S_1}{\partial x_j^2} \right] \\
 C &= \epsilon^2 \frac{a}{g} \left(\frac{\partial S_1}{\partial x_j} \right)^2 \left(i \frac{dT_\epsilon}{d\bar{S}} + \frac{d^2 T_\epsilon / d\bar{S}^2}{dT_\epsilon / d\bar{S}} \right)
 \end{aligned}$$

In the classical limit ($\epsilon \rightarrow 0$), Eq. (51) simplifies to:

$$-\frac{\partial S}{\partial t} + \frac{a}{g} \left(\frac{\partial S}{\partial x_j} \right)^2 \left(i \frac{dT_0}{d\bar{S}} + \frac{d^2 T_0 / d\bar{S}^2}{dT_0 / d\bar{S}} \right) + \frac{gb}{i \frac{dT_0}{d\bar{S}}} = -a \frac{\partial^2 S}{\partial x_j^2} - g \frac{h_0}{i \frac{dT_0}{d\bar{S}}} \Psi \quad (52)$$

which must identify with Hamilton-Jacobi's equation. Under the proviso to be checked later that the r.h.s. of Eq. (52) must be vanishingly small, we then obtain, from the l.h.s.:

$$\frac{gb}{i \frac{dT_0}{d\bar{S}}} = -V \quad (53)$$

$$\frac{a}{g} \left(i \frac{dT_0}{d\bar{S}} + \frac{d^2 T_0 / d\bar{S}^2}{dT_0 / d\bar{S}} \right) = -\frac{1}{2m} \quad (54)$$

in which $T_0 = T_0(S/g)$ and \bar{S} therefore reduces to S/g . Eq. (53) implies:

$$b = -\frac{iV \frac{dT_0}{d\bar{S}}}{g} \quad (55)$$

We must now recall that the coefficient b has been actually set as a function $b(x_j, t)$, and Eq. (50) shows that it must pertain to the wave mechanical level. In other words, it does not pertain to the classical mechanical level, that is to say, as a rational demand, we would not like it to depend on S . Therefore, $dT_0/d\bar{S}$ must be a constant that we denote as C_1 .

From Eq. (55), we then have:

$$b = \frac{-iV}{g} C_1 \quad (56)$$

With $d^2 T_0 / d\bar{S}^2 = 0$ (since the first derivative is a constant), Eq. (54) then implies:

$$a = \frac{ig}{2mC_1} \quad (57)$$

Inserting Eqs. (56) and (57) into Eq. (50), we then obtain:

$$ig \frac{\partial \Psi}{\partial t} = -\frac{g^2}{2mC_1} \frac{\partial^2 \Psi}{\partial x_j^2} + VC_1 \Psi + igh_\epsilon \quad (58)$$

Concerning the constant C_1 , I have (at least at the present time) no theoretical reason to assign a value to it.

Let R denote the r.h.s. of Eq. (52). We still have to check that it is vanishingly small. With Eq. (57), we obtain:

$$R = -\frac{g}{C_1} \left(\frac{i}{2m} \frac{\partial^2 S}{\partial x_j^2} + \frac{h_0}{i\Psi} \right) \quad (59)$$

which is indeed 0 in the limit $g \rightarrow 0$. This implies that g is a small action, actually so small that it could not be detected in a classical framework.

Eq. (58) is the main result of this subsection. It provides a set of generalized Schrödinger's equations, being admitted that they are evolution equations (first derivative with respect to time), obtained by a deformation of Hamilton-Jacobi's equation, according to the lifting principle. The classical Schrödinger's equation is, in a certain sense, the simplest equation in the set. It is obtained by setting the nonlinear term h_e to 0 and C_1 to 1, while the constant g identifies with the Planck's constant \hbar . This is equivalent to saying that in Eqs. (49) and (50), only the a - and b -terms in the r.h.s. of the equations, required to match Hamilton-Jacobi's equation in the classical limit, are retained.

Let us note that the function h_e in Eq. (58) may be significant because it allows one to introduce non-linear wave equations. Non-linear Schrödinger's equations in quantum theory are considered in the literature in many papers. For example, they are comprehensively discussed by Doebner and Goldin in [19], and in many references therein. We may also meet such equations in the Bohm-Bub hidden-variables theory [20], or with the Ghirardi-Rimini-Weber equation for spontaneous collapse of the wave function [21]. More generally, non-linear equations may provide a solution to the measurement problem insofar as linear equations, in utmost rigor, do not allow one to get rid of quantum superpositions. This fact has been recently heavily emphasized by R. Penrose in one of his books [22]. A word of caution is however required, namely that, according to Gisin [23], "the Schrödinger evolution is the only quantum evolution that is deterministic and compatible with relativity". Hence, "the fact that a deterministic evolution compatible with relativity must be linear puts heavy doubts on the possibility to solve the measurement problem [...] by adding non linear terms to the Schrödinger equation".

5. Complementary discussion

From the generalized Schrödinger's Eq. (58) we may recover the classical Schrödinger's equation, as we have commented, by setting $h_e = 0$, $C_1 = 1$ and $g = \hbar$, leading to:

$$i\hbar \frac{\partial \Psi}{\partial t} = -\frac{\hbar^2}{2m} \frac{\partial^2 \Psi}{\partial x_j^2} + V\Psi \quad (60)$$

This is a first application of the correspondence principle. A second application of this correspondence principle afterward allows one to recover the classical Hamilton-Jacobi's equation from Schrödinger's equation, as discussed for instance by Blotkhintsev [2]. From the generalized Schrödinger's equation, we therefore recover the classical Hamilton-Jacobi's equation by a two-step up-bottom process, applying twice the correspondence principle. Another approach is to use Eq. (58) as an Ansatz under the form:

$$i\hbar \frac{\partial \Psi}{\partial t} = A(x_j, t) \frac{\partial^2 \Psi}{\partial x_j^2} + B(x_j, t) \Psi + H_\varepsilon$$

and to pursue the game with the correspondence principle to recover, using again a two-step approach, Hamilton-Jacobi's equation. But the use of an Ansatz is less rigorous than the lifting principle because it contains the risk to make the Ansatz too simple, and therefore to omit significant terms. Note, however, that we have implicitly made the assumption that the state of the wave is defined by the wave ψ itself so that we have obtained what is called an evolution equation. The use of a second-order derivative with respect to time would require, for integration, to have the state defined by ψ and by its first derivative (and similar considerations for higher order derivatives with respect to time) so that the result would not be an evolution equation. Therefore, in utmost rigor, what we have demonstrated is that Schrödinger's equation is the simplest evolution equation satisfying the lifting principle.

To clearly emphasize the difference between the correspondence and the lifting principles, let us consider two theories, denoted T_G (G standing for "general") and T_A (A standing for "approximate"). By taking some kind of limit on T_G , we must recover T_A , a up-down process (\downarrow) that may be denoted as $T_G \rightarrow T_A$. We then say that T_G satisfies a correspondence principle with respect to T_A . If T_G is unknown and under construction, any valid candidate, say $T_{G1}, T_{G2} \dots$ must satisfy the correspondence principle: $T_{G1} \rightarrow T_A, T_{G2} \rightarrow T_A \dots$. If it does not, it is not valid and must be rejected. If several valid candidates are retained, then the discrimination among the candidates may need to rely on other considerations, or even remaining undecidable, such as when dealing with the Duhem-Quine underdetermination of theories by experiments. The lifting principle is a down-up process (\uparrow): $T_A \rightarrow T_G$. It starts from a theory relying on an equation (or a set of equations) which is acknowledged to be valid within a certain domain of applicability and extends this domain of validity by extending the original equation (or set of equations) under conditions defined by physical requirements.

For example, the lifting principle tells us that classical mechanics is an approximation to quantum mechanics. Therefore, quantum mechanics must indeed satisfy a correspondence principle, meaning that the correspondence principle is contained in the lifting principle. However, as we have seen, it does not identify with it. What we have done to use it is to start from T_A and find a way to reach candidates for T_G . However, the word "lifting" may have other meanings, for instance in the theory of nonlinear dynamics when, to study a low-dimensional system it can be easier to study its elevation in a higher dimensional system [24, 25]. On the one hand, the higher-dimensional system must satisfy a correspondence principle. On the other hand, it is said that it is obtained as a result of the "lifting" of the low-dimensional system. My choice of the word "lifting" in the context of the present chapter is the result of my borrowing it to the context of chaos theory.

Another point of view may be taken by using a metaphor from Feynman [12] according to which the correspondence principle proceeds from one object to its shadow (and there is one shadow for one object) while the lifting principle proceeds from a shadow to objects (and there are several possible objects for a given shadow). Our results agree with this expectation. We did not reach Schrödinger's equation, but rather a set of generalized Schrödinger's equation. The derivation of Schrödinger, and all Schrödinger-like derivations, reach a single result because they used analogies, guesses and trials, with more or less implicit assumptions. Conversely, the use of the lifting principle simultaneously provides the whole set of admissible possibilities with a minimal number of assumptions (namely that we have to deal with an evolution equation). All candidates are reached in a single step.

6. Conclusion

The realm of nonlinear Schrödinger's equations is very rich, with many applications such as to fluid mechanics, solitons, nonlinear optics and Bose-Einstein condensates. In the present chapter, we have demonstrated, using a lifting principle, that such equations occur naturally as a generalization of Hamilton-Jacobi's formulation of classical mechanics, without however pretending that nonlinear equations obtained by the lifting process identify with nonlinear Schrödinger's equations used in other different contexts (this would require another specific study outside of the scope of the present chapter). The material presented in this chapter is extracted from a book, namely [26]. It is here however presented under a single roof and might then attract the interest of other readers.

Author details

Gérard Gouesbet
CORIA-UMR 6614, Normandie Université, CNRS-Université et INSA de Rouen,
Saint-Etienne-du Rouvray, France

*Address all correspondence to: gouesbet@coria.fr

IntechOpen

© 2021 The Author(s). Licensee IntechOpen. This chapter is distributed under the terms of the Creative Commons Attribution License (<http://creativecommons.org/licenses/by/3.0>), which permits unrestricted use, distribution, and reproduction in any medium, provided the original work is properly cited. 

References

- [1] de Broglie L. Introduction à l'étude de la mécanique ondulatoire. Paris: Hermann; 1930
- [2] Blokhintsev DI. Mécanique quantique. Paris: Masson; 1967
- [3] Landau LD, Lifchitz EV. Mécanique (English translation of: Mechanics, Pergamon Press, Oxford, England, 1969). Moscow: Mir; 1966
- [4] Holland PR. The Quantum Theory of Motion: An Account of the de Broglie-Bohm Causal Interpretation of Quantum Mechanics. Cambridge, England: Cambridge University Press; 1993
- [5] G. Gouesbet. From theories by Lorenz and Mie to ontological underdetermination of theories by experiments. Invited book chapter. Thomas Wriedt, Wolfram Hergert, editors. Mie Theory 1908-2008, Springer-Verlag, 73-100, 2012.
- [6] G. Gouesbet. On empirically equivalent systems of the world with conflicting ontologies; three case-studies. International Journal of Philosophy and Theology, 4, 1, 22-41, 2016.
- [7] E. Schrödinger. Quantisierung als Eigenwertproblem. Annalen der Physics. 79, 4: 361-376, 1926.
- [8] E. Schrödinger. Quantisierung als Eigenwertproblem. Annalen der Physics. 79, 4: 489-527, 1926.
- [9] E. Schrödinger. Quantisierung als Eigenwertproblem. Annalen der Physics. 81, 18: 109-139, 1926.
- [10] Schrödinger E. Collected Papers on Wave Mechanics. Glasgow: Blackie; 1928
- [11] Schrödinger E. Mémoires sur la mécanique quantique. Paris: Jacques Gabay; 1988
- [12] R.P. Feynman. Le cours de physique de Feynman, mécanique quantique, Dunod, Paris, 2000. French translation of: The Feynman Lectures on Physics, 1965,
- [13] Winogradski J. Lecture notes and "An imaginary history of the making of nonrelativistic quantum mechanics". Unpublished personal communication.
- [14] Hamilton WR. On a general method of expressing the paths of light and of the planets by the coefficients of a characteristic function. Dublin University Review and Quarterly Magazine. 1833;1:795-826
- [15] Hamilton WR. On a general method in dynamics. Philosophical Transactions of the Royal Society, Part II. 1834;247-308
- [16] Newton RG. Scattering Theory of Waves and Particles. New-York: Dover; 2002
- [17] Nussenzveig HM. Diffraction Effects in Semiclassical Scattering. Cambridge, England: Cambridge University Press; 1992
- [18] G. Gouesbet. Hypotheses on the a priori rational necessity of quantum mechanics. Principia, an international journal of epistemology, 14, 3, 393-404, 2010.
- [19] H.D. Doebner and G.A. Goldin. Introducing nonlinear gauge transformation in a family of nonlinear Schrödinger equations. Physical Review A, 54, 5: 3764-3771, 1996.
- [20] D. Bohm and J. Bub. A proposed solution of the measurement problem in quantum mechanics by a hidden variable theory. Review of Modern Physics. 38, 3: 453-469, 1966.
- [21] G.C. Ghirardi, A. Rimini and T. Weber. Unified dynamics for

microscopic and macroscopic systems.
Physical Review D, 34, 2:470-491, 1986.

[22] Penrose R. A la découverte des lois de l'univers, la prodigieuse histoire des mathématiques et de la physique (French translation of: The Road to Reality, a Complete Guide to the Laws of the Universe). Paris: Odile Jacob; 2007

[23] Gison N. Stochastic quantum dynamics and relativity. Helvetica Physica Acta. 1989;62:363-371

[24] J. Guckenheimer and P. Holmes. Nonlinear oscillations, dynamical systems, and bifurcations of vector fields. Applied Mathematical Sciences, 42, Springer-Verlag, Berlin, 1983.

[25] Thompson JMT, Stewart HB. Nonlinear Dynamics and Chaos. New-York: Wiley; 1986

[26] Gouesbet G. Hidden Worlds in Quantum Physics. Mineola, New-York: Dover Publications; 2013

From Schrödinger Equation to Quantum Conspiracy

Francis T.S. Yu

Abstract

Schrödinger's quantum mechanics is a legacy of Hamiltonian's classical mechanics. But Hamiltonian mechanics was developed from an empty space paradigm, for which Schrödinger's equation is a timeless ($t = 0$) or time-independent deterministic equation, which includes his fundamental principle of superposition. When one is dealing Schrödinger equation, it is unavoidable not to mention about Schrödinger's cat. Which is one of the most elusive cats in modern science since disclosed the half-life cat hypothesis in 1935. The cat is alive or not had been debated by score of world renowned scientists it is still debating. Yet I will show Schrödinger's hypothesis is not a physically realizable hypothesis, for which it has nothing for us to debate about. But quantum communication and computing rely on qubit information algorithm, I will show that qubit information logic is as elusive as Schrödinger's cat. It exists only within an empty space, but not exists within our temporal ($t > 0$) universe. Since there is always a price to pay within our universe, I will show that every physical subspace needs a section of time Δt and an amount of energy ΔE to create and it is not free. Although, double slit hypothesis had been fictitiously confirmed that superposition principle exists, but I will show that double-slit postulation is another non-physically realizable hypothesis that had let us to believing superposition principle is actually existed within our time-space. Yet one of the worst coverup must be particles behaved differently within a micro space to justify the spooky superposition principle, which is one of greatest quantum conspiracy in modern science. Nevertheless, the art of quantum mechanics is all about a physically realizable equation, we see that everything existed within our universe, no matter how small it is, it has to be temporal ($t > 0$) which includes all the laws, principles, and equations. Otherwise, it is virtual as mathematics is since Schrödinger equation is mathematics, but mathematics is not equaled to science. Finally, when science turns to virtual reality for solution it is not a reliable answer. But when science turns to physical reality for an answer it is a reliable solution.

Keywords: Schrödinger equation, quantum mechanics, Schrödinger's cat, qubit information, physical realizable, timeless space, temporal space, quantum theory, double-slit hypothesis, superposition principle

1. Introduction

In modern physics there are two most important pillars of disciplines: It seems to me one is dealing with macro scale objects of Einstein [1] and the others is dealing with micro scale particle of Schrödinger [2]. Instead of speculating that micro and macro-object behaves differently, but they share a common denominator; temporal

($t > 0$) subspace. In other words, regardless how small the particle is it has to be temporal ($t > 0$), otherwise it cannot exist within our temporal ($t > 0$) universe. Nevertheless, as science changes from Newtonian [3] mechanics to statistical [4], to relativistic [1], and to quantum mechanics [2], time had always been regarded as an independent variable with respect to substance or subspace. And this is precisely what modern physics had been used the same empty space platform, which they had have treated time as an independent variable for centuries. Since Heisenberg was one of the earlier starters in quantum theory [5], I have found his principle was derived on the same empty space platform as depicted in **Figure 1** which is in fact the “same” platform used for developing Hamiltonian classical mechanics [6]. For which this is the same reason why Schrödinger’s quantum mechanics is timeless ($t = 0$) or time independent because quantum mechanics is the legacy of Hamiltonian. And this is the same reason that Heisenberg uncertainty principle is time independent, instead of changes with time [7].

Nevertheless, **Figure 1** is not a physically realizable paradigm by virtue of temporal exclusive principle. In other words, emptiness and temporal ($t > 0$) are mutually exclusive. Strictly every substance or subspace has to be temporal ($t > 0$) within our temporal ($t > 0$) universe. For simplicity we assumed momentarily that mass m is a constant and I shall come for this temporal issue in a subsequent discussion.

Yet, total energy of a Hamiltonian particle in motion is equal to its kinetic energy plus the particle’s potential energy as given by [6],

$$\mathcal{H} = p^2/(2m) + V \tag{1}$$

which is the well-known Hamiltonian equation, where p and m represent the particle’s momentum and mass respectively, V is the particle’s potential energy. Equivalently Hamiltonian equation can be written in the following form as applied for a subatomic particle.

$$\mathcal{H} = -\left[\frac{\hbar^2}{8\pi^2m}\right] \nabla^2 + V \tag{2}$$

which is the well-known “Hamiltonian Operator” in classical mechanics. Where \hbar is the Planck’s constant, m and V are the mass and potential energy of the particle and ∇^2 is a Laplacian operator;



A piece of paper Timeless ($t=0$) Subspace

Figure 1.
Shows a particle in motion within a timeless ($t = 0$) subspace. v is the velocity of the particle.

$$\nabla^2 = \frac{\partial^2}{\partial x_i \partial x_j}$$

By virtue of “energy conservation”, Hamiltonian equation can be written as,

$$\nabla \psi = \left\{ - \left[\frac{h^2}{8\pi^2 m} \right] \nabla^2 + V \right\} \psi = E \psi \quad (3)$$

where ψ is the wave function that remains to be determined, E and V are the energy factor and potential energy that need to be incorporated within the equation. And this is precisely where Schrödinger’s equation was derived from, by using the energy factor $E = h\nu$ (i.e., a quanta of light energy) adopted from Bohr’s atomic model [8], Schrödinger equation can be written as [6];

$$\frac{\partial^2 \psi}{\partial x^2} + \frac{8\pi^2 m}{h^2} (E - V) \psi = 0 \quad (4)$$

In view of this Schrödinger’s equation, but it is essentially identical to the Hamiltonian equation. Where ψ is the wave function has to be determined, m is the mass of a photonic-particle (i.e., photon), E and V are the dynamic quantum state energy and potential energy of the particle, x is the spatial variable and h is the Planck’s constant.

Since Schrödinger’s equation is the core of quantum mechanics, but without Hamiltonian’s mechanics it seems to me; we would not have the quantum mechanics. The fact is that quantum mechanics is essentially identical to Hamiltonian mechanics. The major difference between them is that; Schrödinger used a dynamic quantum energy $E = h\nu$ as obtained from a quantum leap energy of Bohr’s hypothesis which changes from classical mechanics to quantum leap mechanics or quantum mechanics. In other words, Schrödinger used a package of wavelet quantum leap energy $h\nu$ to equivalent a particle (or photon) as from wave-particle dynamics of de Broglie’s hypothesis [9], although photon is not actually a real particle [10]. Nevertheless, where the mass m for a photonic particle in the Schrödinger’s equation remains to be “physically reconciled”, after all science is a law of approximation. Furthermore, without the adoption of Bohr’s quantum leap $h\nu$, quantum physics would not have started. It seems to me that; quantum leap energy $E = h\nu$ has played a viable role as transforming from Hamiltonian classical mechanics to quantum mechanics which Schrödinger had done to his quantum theory.

2. Timeless (t = 0) Schrödinger equation

Nevertheless, Schrödinger equation is a point singularity approximated deterministic time-independent equation, for which we see that any solution and principle come out from Schrödinger equation will be deterministic time-independent. But science is supposed to change naturally with time or approximated. And this is precisely the reason that quantum scientists had have committed for decades without knowing that solution or principle as obtained from Schrödinger equation is not physically realizable. For which his fundamental principle of superposition is one of them. The reason why Schrödinger equation is not a physically realizable equation is trivial; firstly, since Schrödinger equation is the legacy of Hamiltonian, which is a timeless (t = 0) or time independent classical machine. Secondly, the quantum leap $E = h\nu$ is not a time limited physically realizable assumption, since Bohr’s atomic was developed from an empty subspace platform, which has no time and no space. And

this empty virtual subspace had been using it for centuries. Although Schrödinger equation has given scores of viable solutions for practical applications but at the same time it had also produced a number of fictitious and irrational principles and theories that are not actually existed within our temporal ($t > 0$) universe, such as the paradox of Schrödinger’s Cat [11], string theory [12], superposition principle, and others.

In order to understand why Schrödinger equation is a timeless ($t = 0$) or time-independent equation, we have to understand what is a temporal ($t > 0$) space paradigm since physically realizable solution comes from a physically realizable subspace. For which every physically realizable subspace must be a subspace within our temporal ($t > 0$) universe, which changes naturally with time. This includes all the laws, principles, and theories must changes naturally with time, as from strictly physical realizability standpoint. Particularly we are in the era of asking our science to response as instantaneously, for instance as the fundamental principle of Schrödinger equation.

For which let me epitomize the nature of our temporal ($t > 0$) universe as depicted in **Figure 2**. It shows that our universe was started from a big bang creation theory about 14 billion light years ago. Since past certainty’s consequences (i.e., memory subspaces) were happened at specified time within the negative time domain (i.e., $t < 0$), we see that every specific past time event has been determined with respect to a precise past certainty subspace. For which time can be treated as an independent variable with respect to the past certainty consequences within the pass-time domain ($t < 0$) as from mathematical standpoint. Which is precisely where Schrödinger equation is, as well all the laws and theories were developed.

However, it is reasonable to predict any hypothesis and principle based on our past certainty knowledges, but it is the nature of our time–space tells us that prediction cannot be absolute deterministic, since every physical aspect changes

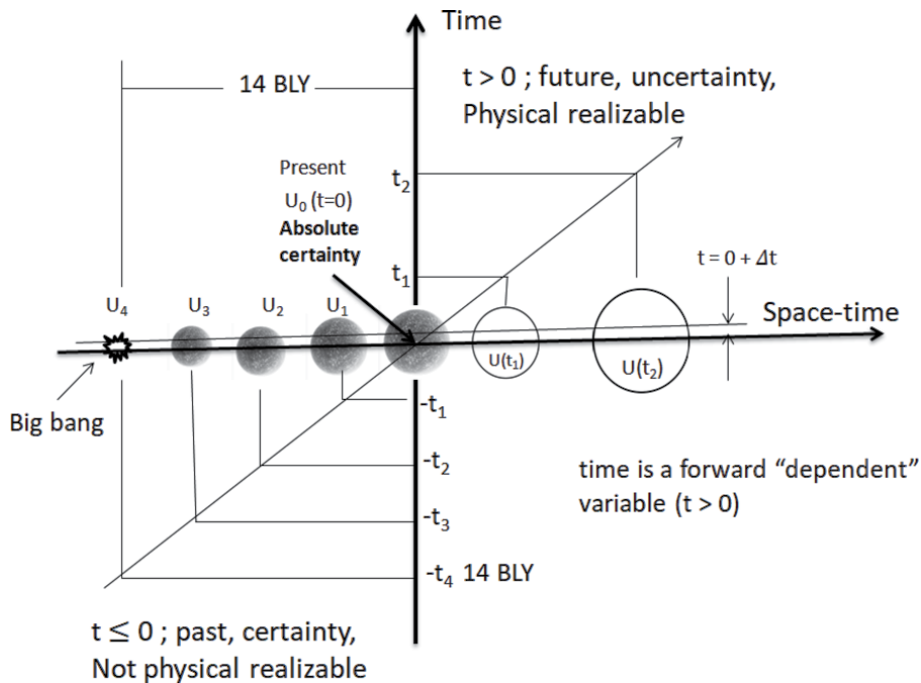


Figure 2. Shows a composited temporal ($t > 0$) time–space diagram to epitomize the nature of our temporal universe. BLY is billion of light years.

with time. In other words, a deterministic Schrödinger equation should not be used to predict future reality without the constrain of temporal ($t > 0$) condition, since future physical reality changes naturally with time. And this is the timeless ($t = 0$) or time-independent past-time certainty subspace that many scientists had used to predict the future out-come with absolute certainty, even though consciously they knew it is incorrect. Although this was the issue that Einstein and his colleagues were strongly opposed Schrödinger's fundamental principle of superposition [13], but Einstein had also committed the same error as Schrödinger did, his general and special theory of relativity are also deterministic theories. Nevertheless, the major difference between Schrödinger's fundamental principle and Einstein's theories is that, Schrödinger's principle is essentially to stop the time, such as applied to quantum computing and communication [14, 15]. While Einstein's theory is basically to move ahead or behind the pace of time, for instance as applied to wormhole time traveling [16]. Nevertheless, Schrödinger equation is a non-physically realizable equation which is not encouraged to be used without the constrain of temporal ($t > 0$) condition, particularly as applied on instantaneously and simultaneously supersession position. Since the fundamental principle exists only within an empty space, but not within our temporal ($t > 0$) space where empty space is not an inaccessible subspace within our temporal universe. From which we see that those application of Schrödinger equation to quantum space-time would have problem to prove that they exist within our temporal ($t > 0$) universe, since Schrödinger equation is a time-independent equation.

Although using past certainties to predict future outcome is a reasonable method that had have been used for centuries, but it is physically wrong if we treated time as an independent variable within our temporal ($t > 0$) universe. And this is the reason scores of irrational and fictitious solutions emerged, that has already been dominated the world-wide scientific community. This includes Schrödinger's fundamental principle of superposition, Einstein's special and general relativity theories, and many others, since they were all based on past certainties to predict a deterministic future, which is not a temporal ($t > 0$) solution that changes with time (i.e., non-deterministic).

Nevertheless, the section of time Δt shown in **Figure 2** represents an incremental moment after instant $t = 0$ moved to a new $t = 0 + \Delta t$. In which Δt can be squeeze as small as we wish (i.e., $\Delta t \rightarrow 0$), but it cannot be squeezed to zero (i.e., $\Delta t = 0$) even we have all the energy ΔE to pay for it. In fact, this is the section of time that cannot be delay or moved ahead the pace of time (i.e., $t < 0 + \Delta t$ or $t > 0 + \Delta t$). From which the possibility for time traveling either ahead or behind the pace of time is not conceivable, since we are coexisted with time.

Since our temporal ($t > 0$) universe shows that science is supposed to be approximated but not exact or deterministic, any deterministic solution is not physically real as from absolute certainty of the present. In other words, further away from the absolute certainty the more ambiguous the prediction or uncertainty is. And this exactly why uncertainty principle should have developed based on temporal ($t > 0$) standpoint, instead Heisenberg principle was derived by observation which is independent from time [7].

3. Temporal ($t > 0$) Schrodinger equation

As any physical substance or subspace requires to be temporal ($t > 0$), otherwise it cannot be existed within our temporal universe, this includes all the laws, principles, and theories, otherwise those principles and theories would be as virtual as mathematics. For example, as we had shown in the preceding section. Schrödinger

equation is essentially the legacy of Hamiltonian, where Hamiltonian is a timeless ($t = 0$) or time-independent equation. To avoid the ambiguity of timeless and time-independent equation, that means that timeless and time independent are equivalent, since within a virtual empty space it has no time and no physical space. Which is precisely why we had hijacked by an empty space inadvertently for centuries, for not knowingly that empty space paradigm is not a physically realizable paradigm.

Since the application of all those timeless ($t = 0$) principles and theories were never encountered with serious irrationality, it was because we had never thought that temporal ($t > 0$) issue of those timeless ($t = 0$) principles, although we knew science is approximated. Which was in part due to our own analytical incline that paradoxes can be alleviated by rigorous mathematics that all theoretical scientists adored. For which we felt that without complicated mathematics it has no theoretical physics. But mathematics is not equaled to science, although science needs mathematics. It turns out to be wrong with theoretical physicists, physically realizable science depends on a physically realizable platform but not on the severity of mathematics. Nevertheless, as we have seen it is mathematics currently leads the theoretical physics, but not science directs mathematics. In other words, if it not how rigorous mathematics is, but it is the physically realizable science that we are searching for.

Nevertheless, it must be the demand for instantaneous information-transmission and simultaneous computing, that had motivated me found that the fundamental principle of Schrodinger had violated the nature of temporal ($t > 0$) condition of our universe. Since every subspace within our universe changes with time, but not the subspace stops the time. In other words, it is time changes us yet we are coexisted with time. Since time changes subspace, then the respond from subspace cannot be instantaneously ($t = 0$), but it takes a section of time Δt no matter as small it is (i.e., $\Delta t \rightarrow 0$), but never able to make it to zero (i.e., $\Delta t = 0$), to response. Which is a well-known causality constraint [17], that we may have forgotten.

Since Schrödinger equation is one of my typical examples to shown that flaw and limitation as it is implemented within our temporal ($t > 0$) time-space. Firstly, Schrodinger equation is a time-independent deterministic equation, which is precisely why superposition is a timeless ($t = 0$) principle. Nevertheless, if we imposed a temporal ($t > 0$) constraint on the equation as given by,

$$\frac{\partial^2 \psi}{\partial x^2} + \frac{8\pi^2 m}{h^2} (E - V) \psi = 0, t > 0 \quad (5)$$

From which we see that any solution comes out from this equation will be temporal ($t > 0$), since temporal equation produces temporal solution. Nevertheless, as from strict temporal ($t > 0$) standpoint, mass m , quantum leap energy $E = h\nu$, and potential energy V should be temporal. Nevertheless, ($t > 0$) imposition is showing that solution or principle as derived from this equation should be temporal. For example, fundamental principle of superposition is one of the evidences, since the principle was not constrained by temporal condition. In other words, the adopted quantum leap energy $E = h\nu$ is not a physically realizable assumption to be used, since it is not a time limited quantum leap. This means the wave function ψ as obtained from Schrödinger equation without the temporal constraint is given by [6];

$$\psi(t) = \psi_0 \exp[-i 2\pi \nu (t-t_0)/h] \quad (6)$$

Which is the well-known Schrödinger wave equation, where ψ_0 is an arbitrary constant, ν is the frequency of the quantum leap $h\nu$ and h is the Planck's constant.

As anticipated, Schrödinger wave equation is also a time unlimited solution with no bandwidth, which is not a physical realizable solution. Yet many quantum scientists had used this wave solution to pursuing their dream for quantum supremacy computing and communication [14, 15]. But not knowing the dream they are pursuing is not a physical realizable dream.

It is trivial where the source of the unlimited quantum leap came from, it is from Bohr atomic model as depicted in **Figure 3**. Where an atomic model is embedded within a non-physically realizable empty space paper paradigm, it has no time and no space. Yet quantum physicists can implant virtual time and coordinates within the paradigm but not knowing that piece of paper does not actually represents a physically real subspace. From which we see that Bohr's model strictly speaking it is not a physically realizable paradigm should be used. Firstly it is an empty subspace paradigm, secondly $E = h\nu$ is not a physically realizable quantum leap energy.

On the other hand, if we put a temporal ($t > 0$) constraint on the time unlimited wave equation as given by,

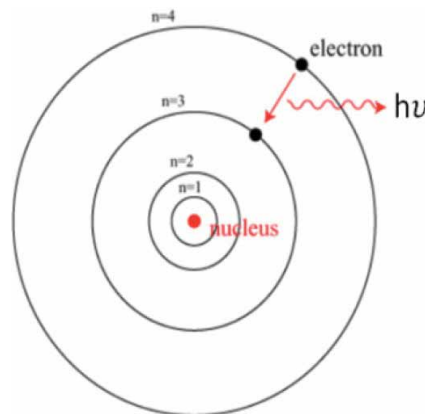
$$\psi(t) = \psi_0 \exp.[-i 2\pi \nu (t-t_0)/h], t > 0 \quad (7)$$

From which we have,

$$\psi(t) = \psi_0 \exp.[-\alpha_0 (t - t_0)^2] \cos(2\pi\nu t), t > 0, \quad (8)$$

where $t > 0$ denotes equation is subjected to temporal ($t > 0$) condition (i.e., exists only within positive time domain). From which we see that a narrow package of wavelet as shown in **Figure 4** is temporal ($t > 0$) and time limited. Thus, we see that it is unlikely simultaneous wavelets will instantaneously occur at same time. From which we have shown that Schrödinger's fundamental principle of superposition fails to exist within our temporal ($t > 0$) universe.

Nevertheless, major problem of Schrödinger equation is its time-independent or timeless issue, since the equation was derived from an empty space platform as



**A piece of paper
 Timeless ($t = 0$) subspace**

Figure 3.
 Shows a Bohr atomic model embedded in a timeless ($t = 0$) platform (i.e., a piece of paper).

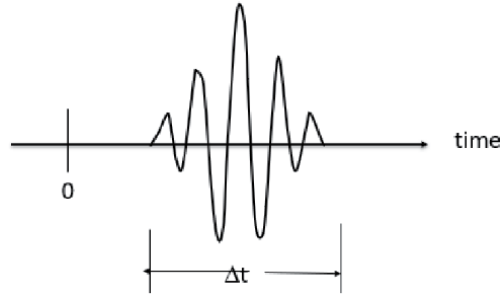


Figure 4. Shows a time-limited temporal ($t > 0$) equation exists in positive time domain. Which can be implemented within our temporal ($t > 0$) universe.

Hamiltonian. From which we see that, Schrodinger equation is not a physically realizable equation, which is precisely why quantum world behaves weirdly as within a timeless wonderland. Since string theory [12] in part was developed from Schrödinger equation, it is trivial to see that string theory is deterministic which is not a physically realizable theory. From which we see that it is not how sophisticated a theory is, but it is the temporal ($t > 0$) subspace platform that produces physically realizable theories.

There is however another essential physical limit cannot be ignored. Within our temporal ($t > 0$) universe every aspect has a price to pay; a section of time Δt and an amount of energy ΔE [i.e., $\Delta t, \Delta E$], where $\Delta E(t)$ is temporal. In other words, every physically realizable theory or principle needs a section of time Δt to spare and an amount of energy ΔE to realize or to transmit. For instance, every bit of information needs a section of time Δt to create. But without an amount of energy ΔE it is impossible to physically realize a bit of information. For which we have the following by uncertainty relationship as given by [18],

$$\Delta t \Delta E \geq h \quad (9)$$

where h is the Planck's constant. From which we see that we need to pay a higher amount of energy ΔE for a narrower section of Δt for every bit of information-transmission.

On the other hand, if we want to curve a particle into a string-like shape within our quantum world [12], which is not a physically realizable theory since string theory is a deterministic principle while our universe is temporal ($t > 0$). Yet, my question is that how long it will take to change a particle to string like equivalent, even though assume we have all the energy (i.e., ΔE) we need. And this is a trivial question that we have to answer, since every physical aspect within our universe has a price (i.e., $\Delta t, \Delta E$) to pay. In other words, particle-string dynamic is a mathematical equivalent, but physically they are not equaled since every particle is a temporal ($t > 0$) particle, which has a mass with time.

4. What timeless space does to wavelets?

On the other hand, if we take a set physically realizable wave functions as given by,

$$\psi_{o1}(t) = \psi_{o1} \exp[-\alpha_{o1}(t - t_{o1})^2] \cos(2\pi\nu_{o1}t), t > 0, \quad (10)$$

$$\psi_{o2}(t) = \psi_{o2} \exp[-\alpha_{o2}(t - t_{o2})^2] \cos(2\pi\nu_{o2}t), t > 0, \quad (11)$$

Which are depicted respectively in **Figure 5(a)**, where we see that wavelets are physically separated. However, if this set of wavelets are submerged within an empty subspace, although physically not realizable as illustrated in **Figure 5(b)**, we see that the wavelets superimposed at $t = 0$ within an empty space, since within an empty space it has no time and no distance. And this is precisely what a virtual empty space can do for all substances as from mathematical standpoint.

Before we move on, let me stress that wave-particle duality is a non-physical realizable dynamic, since it is from statistical mechanics standpoint that a package wavelet energy is equivalent to a particle in motion where momentum of a particle $p = h/\lambda$ is conserved [6]. However, one should not treat wave or a package of wavelet energy $h\Delta\nu$ as a particle or particle as wave. But it is a package of wavelet energy equivalent to a particle dynamic (i.e., photon), but they are not equaled. Similar to mass to energy equation, mass is equivalent to energy and energy is equivalent to mass, but mass is not equaled to energy and energy is not mass. For which a quantum of $h\nu$ or a photon is a virtual particle. From which we see that a photon has a momentum $p = h/\lambda$ but no mass, although many quantum scientists regard a photon as a physical real particle.

Similarly, we can show that a set of separated particles in motion is situated within a temporal ($t > 0$) subspace as depicted in **Figure 6(a)**. Since they are embedded within a time-space platform, their locations can be precisely determined. However, if this set moving particles are situated within an empty space as illustrated in **Figure 6(b)**, then particles lost their temporal ($t > 0$) identities (e.g., such as size, location, and motion), since within an empty space it has no time and

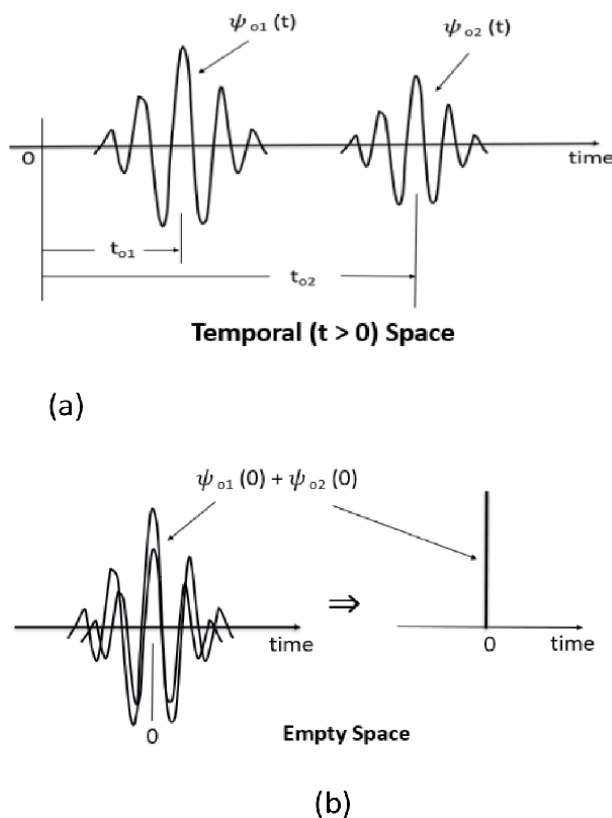


Figure 5. (a) Shows a set of time-limited temporal wavelets. (b) Shows the set of time-limited wavelets is embedded within an empty space. We see superposition principle holds within an empty space since it has no time and no space.

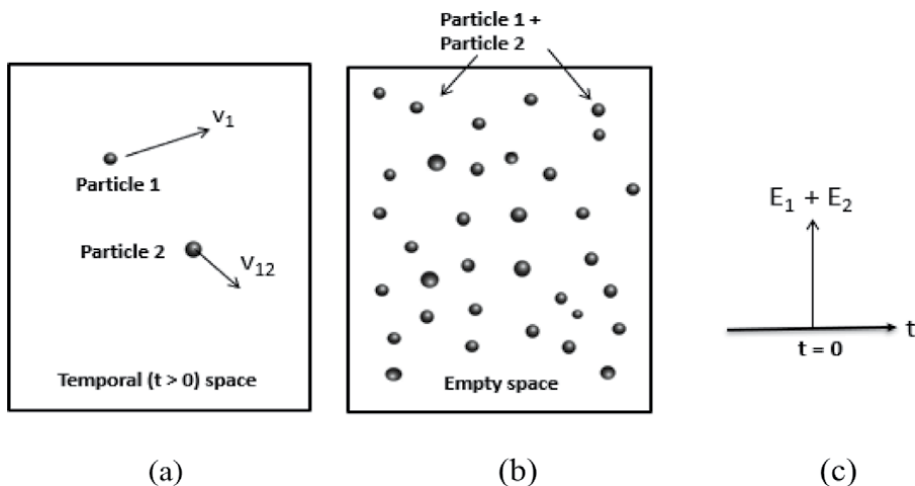


Figure 6.

(a) Shows particles within a timeless ($t = 0$) subspace can do to particles. (b) Shows particle 1 and 2 are superimposing at everywhere within an empty space. (c) Shows energy of particle 1 and 2 converged at $t = 0$, in view of energy conservation. But empty space is a virtual mathematical space which does not exist within our universe.

no space. For which all the particles' dynamic energy converged at $t = 0$. From which we see that empty space is a virtual space which does not exist within our temporal ($t > 0$) universe. But we had used this virtual space for ages since the dawn of our science. And this reason that why we need to change to temporal ($t > 0$) science otherwise we will forever be trapping within the empty wonderland of timeless ($t = 0$) science, which does not need to pay a price (i.e., Δt , ΔE).

Nevertheless, Schrödinger equation is a non-physical realizable equation, which can be traced back to the development of Hamiltonian mechanics. From which we see that it is the background subspace (i.e., a piece of paper) that we had inadvertently treated as an empty space paradigm. And it is also the same empty space paradigm that Bohr's atomic model was embedded, from which we see that quantum state energy $h\nu$ is not a physically physical assumption. From which I had shown any application of Schrödinger equation has to be constrained within the temporal ($t > 0$) condition. Otherwise, the solution would be virtual and fictitious, which cannot be implemented within our time-space. From which I had shown that it is not how rigorous mathematics is, it is the physical realizable paradigm determines her solution is physical realizable.

5. Schrödinger's cat

When we are dealing with quantum mechanics, it is inevitable not to mention Schrödinger's cat since it is one of the most elusive cats in the modern science since Schrödinger's disclosed it in 1935 at a Copenhagen forum. Since then, his half-life cat has intrigued by a score of scientists and has been debated by Einstein, Bohr, Schrödinger, and many others as soon Schrödinger disclosed his hypothesis. And the debates have been persisted for over eight decades, and still debating. For example, I may quote one of the late Richard Feynman quotations as: "After you have leaned quantum mechanics, you really "do not" understand quantum mechanics ...".

It is however not the fate of the Schrödinger's half-life cat, but it is the paradox that quantum scientists had have treated the fate of the cat as a physically realizable

paradox. In other words, many scientists believed the paradox of Schrödinger's cat is actually existed within our universe, without any hesitation. Or literally accepted superposition is a physically realizable principle, although fictitious and irrational solutions had emerged, it seems like looking into the Alice wonderland. In order to justify some of their believing some quantum scientists even come-up with their own logic; particle behaves weirdly within a microenvironment as in contrast within a macro space. Yet some of their potential applications, such as quantum computing and quantum entanglement communication are in fact in macro sub-space environment. Nevertheless, I have found many of those micro behaviors are not existed within our universe, from which paradox of Schrödinger's cat is one of them, as I shall discuss.

Let us start with the Schrödinger's box as shown in **Figure 7**. Inside the box we have equipped a bottle of poison gas and a device (i.e., a hammer) to break the bottle, triggered by the decaying of a radio-active particle, to kill the cat. Since the box is assumed totally opaque of which no one knows that the cat will be killed or not, as imposed by the Schrödinger's superposition principle until we open his box. From which we see that the fate of Schrödinger 's cat is dependent upon the beholder, or consciousness.

Nevertheless, as we investigate Schrödinger 's hypothesis, immediately we see that his hypothesis is not a physical realizable postulation, since within the box it has a timeless ($t = 0$) or time independent radioactive particle in it. As we know that; any particle within our universe subspace has to be a temporal ($t > 0$) particle or has time with it, otherwise the proposed radioactive particle cannot be existed within Schrödinger's temporal ($t > 0$) box. It is therefore, the paradox of Schrödinger's cat is not a physical realizable hypothesis and we should not have treated Schrödinger's cat as a physically real paradox.

Since every problem has multi solutions, I can change the scenarios of Schrödinger's box a little bit, such as allow a small group of individuals take turn to open the box. After each observation close the box before passing on to the next observer. My question is that; how many times the superposition has to collapse? With all those apparent contradicted logics, we see that Schrödinger 's cat is not a paradox after all. And the root of timeless ($t = 0$) superposition principle as based on Bohr's quantum leap $h\nu$, represents a time unlimited radiator, which is a singularity approximated wave solution. But time-unlimited quantum leap is a non-physically realizable radiator that cannot exist within our universe.

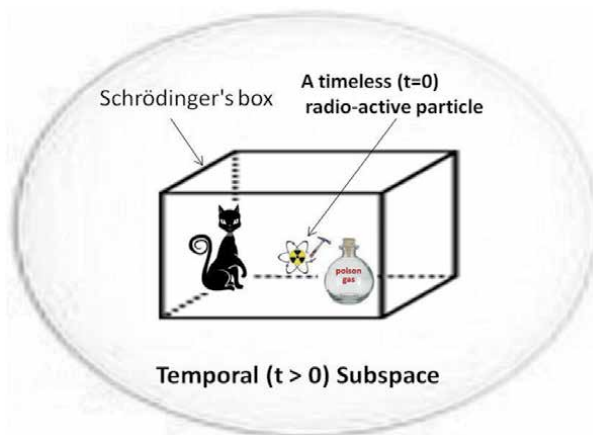


Figure 7. Shows Paradox of Schrodinger's Cat: Inside the box we equipped a bottle of poison gas and a device (i.e., hammer) to break the bottle, triggered by the decaying of a radio-active particle, to kill the cat.

6. Micro space coverup

Two of the important pillars in modern physics must be Einstein's relativity and Schrödinger's Quantum theory; one is dealing with very large object, and the other is dealing with small particles. Since both of Einstein's theories and Schrödinger's mechanics were developed from an empty subspace, they are not physically realizable principles. But it was those theories that had given us the fantasy promises that had led us to believe that physical behaves within a macro and a micro are different, otherwise relativistic theory and quantum mechanics cannot be reconciled. Nevertheless, either was inadvertently or not, it remains to be found. Nevertheless, this is the objective that I will show that particles behave within a macro and a micro space are basically the same regardless of their sizes. From which I wonder that particle behaves differently within a micro space must be a major cover up but not inadvertently in modern scientific history.

Although Einstein was strongly opposing Schrödinger's quantum theory [13], but his relativity theory had also committed the same error for using the same empty space paradigm. For which I will show that particle behaves basically the same within a macro and a micro space, regardless of their size. Nevertheless, the major difference between Einstein's theory and Schrödinger's principle is that, one is to move ahead or behind the pace of time and the other is to stop the time. Yet neither move ahead nor stop time is possible, since our universe changes with time, but not change the time.

As commonly agreed, that a picture is worth more than a thousand words, then a viable diagram is worth more hundreds of equations. Once again let me epitomize the creation of our temporal ($t > 0$) universe as summarized in **Figure 8**.

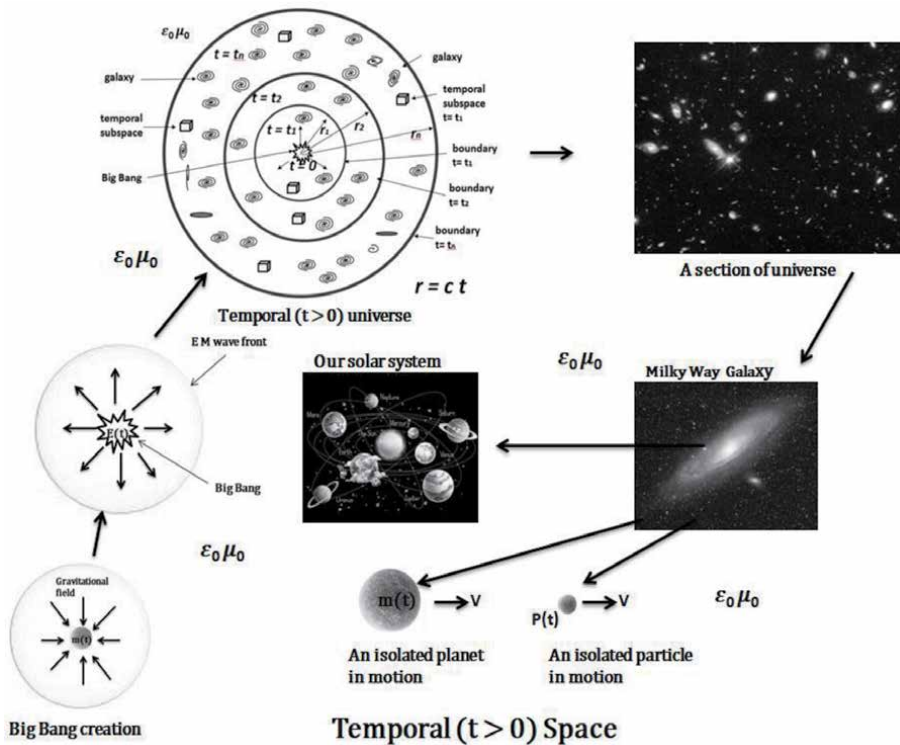


Figure 8. Shows our universe was originated by a big bang explosion from a singularity temporal mass $m(t)$ triggered by her own intensive gravitational force within a preexisted temporal ($t > 0$) space. In which we see that our universe, subspace, galaxy, planet, particle regardless the size changes naturally with time. From which we see that the behaviors within micro and macro are basically the same.

In which it shows that the origin of our temporal ($t > 0$) universe was started by a big bang explosion within a preexisted temporal ($t > 0$) space that allows a singularity mass $M(t)$ to exist and to grow over time. Such that her induced gravitational pressure will eventually trigger the thermo-nuclei explosion of mass M that enables creation of our universe. From which we see that every substance regardless the size changes with time. Where time is the only invisible real variable runs at a constant pace, for which nothing can move ahead or even stop time. And this a physically realizable time-space we live in. Which is different from the Einstein's space-time continuum where he had treated time as an independent variable [1]. The fact is that temporal ($t > 0$) universe is a newly discovered realizable time-space that closer to truth. From which I would anticipate temporal ($t > 0$) space will eventually take over the time-independent universe of Einstein. For which we would have a viable physically realizable paradigm for years to come, because principle and theory developed from a temporal ($t > 0$) space platform will be physically realizable.

In view of our temporal ($t > 0$) universe, it is not possible for particle behavior differently within a micro space, since every particle is temporal that changes naturally with time. Since it is time changes the particle, but not particle changes time, time is neither can be stop momentarily as superposition principle stated or changed momentarily as relativistic theory promised. In other words, every substance regardless of the size needs a section of time Δt and an amount of energy ΔE to create. And it cannot allow micro-space behaves like a timeless space since every subspace within our universe has to be temporal, by virtue of temporal exclusive principle.

7. Qubit information conspiracy

Qubit information-transmission is basically exploiting Wiener's communication strategy for the purpose of qubit transmission [19]. For which the receiver would anticipate a more ambiguous digital signal (e.g., either 0 or 1) from an anticipated sender. In other words, qubit communication has treated at receiving end entropy $H(B)$ as a source entropy $H(A)$ to determine the intended signal was sent. Since signal was originated by the sender, by maximizing entropy $H(B)$ under noiseless condition the receiver can interpret the received signal (e.g., 0 or 1) as equals to a qubit information. And this is precisely the qubit information principle that currently is using for quantum communication and computing.

For example, a receiver is not certain about an enclosed message is either yes or no, until the receiver opens the envelope to find out is yes or no message but not both. Which is a similar the scenario to the paradox of Schrödinger's cat before opening his box. But the fate of Schrödinger's cat or the information within the envelope had been determined before we look into the Schrödinger's box or the receiver opens the envelope. From which we see that it is not our consciousness changing the outcome of the enclosed message or the fate of the cat, as superposition principle had implied. For which to guarantee that the envelope will not be contaminated during transmission, if and only if the transmission time is instantaneously (i.e., $\Delta t = 0$) which is equivalently that message is sent within timeless ($t = 0$) channel, that has no time.

Therefore, it is the physically realizable qubit information whether it exists within our temporal ($t > 0$) universe. Since everything within our universe has a price to pay, namely a section of time Δt and an amount of energy ΔE , for which qubit information transmission cannot be the exception. Firstly, quantum communication relies on fundamental principle of superposition, but we had shown that

superposition principle cannot exist within our temporal ($t > 0$) universe. Then it has no sense to talk about all the possible capability of qubit information can offer.

Nevertheless, let us assume a quantum communication channel which is situated within an empty space paradigm shown in the **Figure 9**, where a binary source ensemble of $A = \{0, 1\}$ is capable of transmitting 0 and 1 instantaneously and simultaneously within an empty space. Notice that this is precisely the same sub-space platform that Schrödinger's fundamental principle of superposition derived from. From which we see that qubit information can only exist within an empty space platform which is not a physically realizable information hypothesis, since platform has no time to represent a transmitting signal. The fact is that every temporal information (i.e., 0 or 1) needs a section of time (i.e., Δt) to presents a time-signal. In other words, if a time-signal has no section of time, it has no carrier to represent and to transmit within our temporal ($t > 0$) universe since qubit information is timeless ($t = 0$) space transmission algorithm.

Aside it is not a physically realizable paradigm, let me show how a qubit information channel works as depicted by a block box diagram shown in **Figure 10**, which is a timeless ($t = 0$) noise free channel. Where $A = \{0, 1\}$ represents an input binary source, $H(A) = 1$ bit is the input entropy, $B\{\text{qubit}\}$ is output quantum bit, $H(B) = \text{qubit}$ is the output entropy. Since quantum qubit information transmission has treated the input binary source $A = \{0, 1\}$ and the output ensemble as qubit $B = \{\text{qubit}\}$, such that at the receiving ending information can be presented in quantum bit (i.e., qubit). But qubit channel is embedded within a timeless ($t = 0$) subspace, it has no noise and no time, we see that it has no channel noise entropy [i.e., $H(A/B) = 0$]. From which mutual information of the qubit channel can be written as,

$$I(A; B) = H(B) = H(A) \tag{12}$$

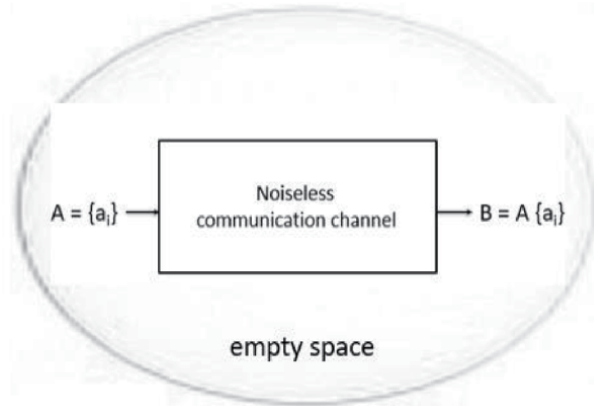


Figure 9. Shows a conventional noiseless communication channel is embedded within an empty space. But it is not a physically realizable paradigm since substance (i.e., signal) and emptiness cannot coexist.

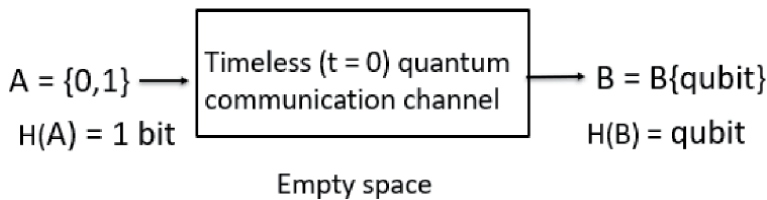


Figure 10. Shows a binary timeless ($t = 0$) quantum qubit-information channel.

where the output end entropy $H(B)$ is equaled to the input entropy $H(A)$ [i.e., $H(B) = H(A)$]. Thus, the intended sent signal either 1 or 0, but not by both, is receiving at the receiving end. This is equivalently to recovering the intended input signal that was corrupted within a noisy channel of Wiener's information-transmission, but in this case is a noiseless channel. In fact, a noiseless channel only exists within an empty virtual space, which cannot be existed within our temporal ($t > 0$) universe.

Since quantum information is dependent on Schrodinger's superposition principle such that binary transmission of 0 and 1 can be transmitted instantaneously and simultaneously. This presents a quantum bit or a qubit to determine the input source ensemble of either 1 or 0. But quantum information channel is assumed within an empty space paradigm, we see that the operation is instantaneous and simultaneous but only exists within timeless ($t = 0$) space. Since qubit information is the anchor principle for quantum computing and communication, but unfortunately qubit information cannot exist within our temporal ($t > 0$) universe, by virtue of temporal exclusive principle.

A similar scenario to qubit information transmission is the paradox of Schrodinger's cat, where a received signal is dependent upon on observation. For example, the observer (i.e., the receiver) did not know the cat within the Schrödinger's box is either alive or dead until the observer opens up the box. In which we see that it is the observer confirms the outcome after the observation. But the physical fact is that the cat is alive, or dead had been determined before the observer opens up Schrödinger's box. Similarly, we never know a boiled egg is either hard or soft-boiled until we crack open it. But hard- or soft-boiled egg had been determined before we crack the egg.

Although paradox of Schrödinger's cat had been debated since the disclosure of the hypothesis in 1935, it seems to me that no one had have found the real reason where the paradox comes from until recent discovery of the temporal ($t > 0$) universe [20, 21]. From which I had shown that paradox came from an empty subspace (i.e., a piece commonly used paper) where Schrödinger's equation was derived from. From which I had shown that his fundamental principle of superposition is timeless ($t = 0$), fails to exist within our universe.

On the other hand, if qubit information channel is situated within a temporal ($t > 0$) subspace as shown in **Figure 11**, then the responds of a supposed qubit channel is subjected to the boundary condition within temporal ($t > 0$) space.

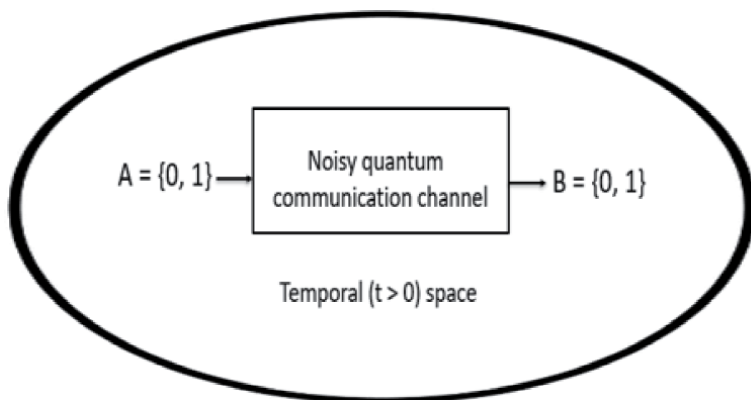


Figure 11. Shows a binary noisy quantum communication channel embedded within a temporal ($t > 0$) space. For which output entropy is always larger than the input entropy, that is $H(B) > H(A)$. Note: For a noise-free channel we have $H(B) = H(A)$. But noiseless channel is equivalent to a timeless channel, which is not a physically realizable communication channel.

For which simultaneous and instantaneous superposition of binary digital transmission (i.e., 0, 1) fails to exist. Thus, output entropy $H(B)$ at the transmitted end cannot be treated as a qubit information since superposition principle does not hold within our temporal ($t > 0$) space. Of which output ensemble is $B = \{0, 1\}$ that is identical to a conventional noisy binary channel, instead of $B = \{\text{qubit}\}$.

Before departing this section, I would stress that within our universe everything needs a price to pay, a section of time Δt and an amount of energy ΔE and it is not free. However, quantum qubit information pays no price since it does not have a section of time Δt . Yet, qubit information had created a worldwide qubit conspiracy, from which it is hard to tell when this conspiracy would be ended. But I am confidence to say that this fictitious qubit information supremacy would be ended soon since information-transmission is supposed to be physically realizable.

8. Double slit paradox

Instead of getting into the argument of simultaneous existence particles at double-slit using Young's experiment, which is a non-physical realizable paradigm as from temporal exclusive principle standpoint. Particle-wave dynamics is a mathematical equivalent duality principle as described; particle in motion is equivalent to wave dynamics or wave propagation is equivalent to particle dynamics. However, particle is not equaled to wave and wave is not equal to particle. Particularly as from De Broglie-Bohm theory as I quote: particles have "precise locations" at all times ... [9]. But, in contrast within a temporal ($t > 0$) subspace, particle changes with time but not at precise location since future prediction is not deterministic. As we have shown earlier particle existed within a temporal ($t > 0$) space is quite difference as assumed within a virtual non-physically realizable subspace. For example, particle existed within our temporal ($t > 0$) universe, no matter how small it is, it has to be temporal ($t > 0$). Since temporal subspace is not empty, from which we see that particle cannot be totally isolated. For example, mass particle induces gravitational field, charged particle induces electric field, and others which cannot be ignored. Without the preexistent substances such as permittivity and permeability, wave dynamics has no way to exist. From which we see that particle-wave dynamics is a mathematical postulation existed only within an empty timeless ($t = 0$) or time independent virtual mathematical subspace, since the assumption of wave dynamics is not a time and band limited physically realizable wavelet.

Nevertheless, let me show a double slit set-up as depicted in **Figure 12(a)**, which is a commonly accepted paradigm that has been used in decades, but it is not a physically realizable paradigm. Yet a photonic particle can be shown simultaneously and instantaneously existed at the double slits, since within an empty space it has no time and no distance. And this is precisely the same subspace that Schrödinger's superposition principle derived from, but we had shown that superposition principle can only exist within an empty timeless ($t = 0$) virtual subspace.

However, if the double-slit hypothesis is situated within a temporal ($t > 0$) subspace as depicted in **Figure 12(b)**, then it is very unlikely two particles will be instantaneously and simultaneously existing at both slits because time is distance and distance is time. Since wave is equivalent to particle as from particle-wave dynamics standpoint, but within our temporal ($t > 0$) universe any physical wave dynamic has to be time and band limited otherwise it is a virtual wave-dynamic. From which we see that it is very unlikely two wavelets (or particles) will be simultaneously arrived at both slits at the same time.

Yet, a question remains to be asked, why it works for a continuous emitting laser. It is apparently that a continuous light emitter has a longer time-limited

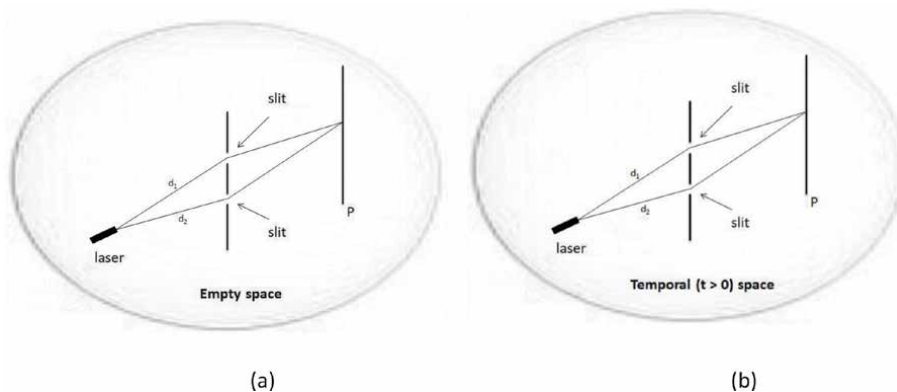


Figure 12. Shows a hypothetical double-slit experiment. (a) Shows a non-physically realizable empty space paradigm, (b) shows a physically realizable paradigm.

duration. For example, if we assume that human has a 300-year life expectance, then it has a good chance that we may coexist with Einstein, Schrödinger, and may be coexisted with Newton at some time, but may not at the same place. On the other hand, if our universe is a time-independent (i.e., timeless) space, then in principle we can time-traveling back to visit them. What I have just given is that within our temporal ($t > 0$) universe everything has a price; an amount of energy ΔE and a section of time Δt (i.e., $\Delta E, \Delta t$) to pay. But this is the necessary cost, and it is not sufficient. From which we see that superposition principle is limited by a section of time Δt , although ΔE and Δt are coexisted.

Nevertheless, we can hypothetically show that instantaneously and simultaneously superposition phenomenon does not hold by a postulated set-up shown in **Figure 13**, which is a physically realizable paradigm since substance and temporal ($t > 0$) space are mutually inclusive.

However, if the difference path length between d_1 and d_2 is beyond the coherence length D of the coherent illuminator (i.e., laser) as given by.

$$D = d_2 - d_1 = c (\Delta t_2 - \Delta t_1) = c \Delta t' < D \quad (13)$$

where d_s are the distances, Δt_s are the incremental times and c is the velocity of light. Then interference pattern cannot be observed at the diffraction screen of P.

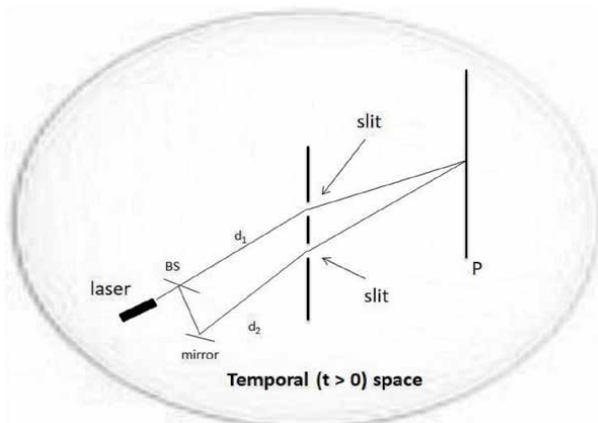


Figure 13. Shows a double-slit experimental setup using a band limited coherent light source.

This means that photonic-particles (i.e., photons) emitted from the laser are not simultaneously and instantaneously arriving at the double-slit as from the coherence theory standpoint.

Let me further note that if one submerges any scientific model within a temporal ($t > 0$) subspace, then it is rather easy to find out any paradox as observed within an empty subspace is not existed. Notice that whenever a scientific model is submerged within a temporal ($t > 0$) subspace, the model becomes a part of the temporal ($t > 0$) space for analysis, from which many of the timeless ($t = 0$) paradoxes can be resolved rather easily, for instance such as Schrödinger's Cat and Einstein's theories. Nonetheless this is an inadvertently error that all scientists had committed for centuries. For instance, all the laws, principles, theories, and paradoxes were developed from the same empty timeless subspace. For which most of the scientists believe that we can travel ahead and behind the pace of time, as Einstein's special theory has suggested. Similarly, we can simultaneously and instantaneously exploit photonic particles for computing and communication as Schrödinger's fundamental principle of superposition has indicated.

For example, if one plunge two moving spaceships within an empty space, we cannot tell which one is moving with respect to the other. However, if we submerge the same scenario within a temporal ($t > 0$) subspace, inevitably we can figure out the relative position between them, since time is space, and space is time within a temporal ($t > 0$) subspace while within an empty space there has no time and no distance to distinguish. And this is precisely why Einstein's special theory is relativistic-directional independent and as well his general theory of relativity is a deterministic principle. From which it is trivial for us to submerge a pair of entangled particles within a temporal ($t > 0$) subspace, then we would find out the instantaneous (i.e., $\Delta t = 0$) entanglement is not existed, since within our universe there is always a section of time Δt to pay aside an amount of energy ΔE , and there are not free.

Let me further stress that time speed is one of the most esoteric variables existed with our universe that cannot be changed, but it is the section of time Δt we have to spend that can somewhat manipulate. From which we see that the section of Δt that we will spend can be squeezed as small as we wish yet we can never be able to squeeze it to zero (i.e., $t = 0$), even we have all the energy ΔE (i.e., $\Delta E \rightarrow \infty$) willing to pay for. And this is the well-known causality constraint within our temporal ($t > 0$) universe that cannot be violated.

Furthermore, a question remains to be asked; if the width of Young's experiment is smaller than the wavelength of the illuminator, would you able to observe the diffraction pattern. If the answer is no, then we see that wave dynamics is equivalent to particle in motion but not equaled to particle since photonic particle has no size. From which we see that particle in motion is equivalent to wave-dynamic, but wave-dynamic is not particle and particle is not wave. Finally, I would say that when science turns to virtual reality for solution it is not a reliable answer. But when science turns to physical reality for an answer it is a reliable solution.

9. Conclusion

I would conclude that quantum scientists used amazing mathematical analyses added with their fantastic computer simulations provide very convincing virtual evidences. But mathematical analyses and computer animations are virtual and fictitious, and many of their animations are not physically realizable for example such as superimposing principle for quantum computing is not actually existed within our universe. One of the important aspects within our universe is that one

cannot get something from nothing there is always a price to pay; an amount of energy ΔE and a section of time Δt and they are not free! Since science within our universe is temporal ($t > 0$), in which we see that any scientific law, principle, theory, and paradox has to comply with temporal ($t > 0$) condition within our universe, otherwise it is unlikely be physically realizable. Since science is mathematics but mathematics is not equaled to science. Yet, Schrödinger equation is a legacy of Hamiltonian classical mechanics, I had shown that Schrödinger equation is a timeless ($t = 0$) or time-independent formula which includes his superposition is not a physical realizable principle. Since Schrödinger's cat is one of the most controversial paradoxes in modern science, I had shown that the paradox of Schrödinger's cat is not a physical realizable paradox, which should not have been postulated.

Nevertheless, the most esoteric nature of our universe must be time, for which every fundamental law, principle, and theory is associated with a section of time Δt . I had shown that it is the section of Δt we had expended that cannot bring it back. For which I had shown that we can squeeze a section of time Δt closes to zero (i.e., $\Delta t \rightarrow 0$) but it is not possible reach zero (i.e., $\Delta t = 0$) even though that we have all the energy ΔE to pay for it. In which we see that we can change a section of Δt , but we cannot change the pace of time. Since quantum computing and communication rely on qubit information logic, but qubit information can only exist within a timeless ($t = 0$) subspace. I had shown that qubit information is virtual and illusive as Schrödinger's cat. Which is not a physically realizable qubit information that can be used for quantum supremacy communication and computing.

Although double-slit hypothesis is a well-accepted postulation for showing the superposition principle holds, but unfortunately the postulation only holds within empty space paradigm, and it is not existed within our temporal ($t > 0$) universe. What I meant is that double-slit postulation is another false hypothesis aside the Schrödinger's cat that had led us to believing superposition is actually existed within our universe. Since quantum supremacy relies on qubit information-transmission, which has caused a worldwide quantum conspiracy. I hope this conspiracy will be ended soon, otherwise we will forever trap within a timeless wonderland of quantum supremacy. From which we see that it is not how rigorous the mathematics is, it is the temporal ($t > 0$) subspace paradigm that produces viable realizable solution.

Author details

Francis T.S. Yu

Emeritus Evan Pugh (University) Professor of Electrical Engineering, Penn State University, University Park, USA

*Address all correspondence to: fty1@psu.edu

IntechOpen

© 2021 The Author(s). Licensee IntechOpen. This chapter is distributed under the terms of the Creative Commons Attribution License (<http://creativecommons.org/licenses/by/3.0>), which permits unrestricted use, distribution, and reproduction in any medium, provided the original work is properly cited. 

References

- [1] A. Einstein. *Relativity, the Special and General Theory*, New York: Crown Publishers, 1961.
- [2] E. Schrödinger, "An Undulatory Theory of the Mechanics of Atoms and Molecules," *Phys. Rev.*, vol. 28, no. 6, 1049 (1926).
- [3] J. M. Knudsen, and P. Hjorth, *Elements of Newtonian Mechanics*, Springer Science & Business Media. (2012)
- [4] R. C. Tolman, *The Principles of Statistical Mechanics*. London: Dover Publication. (1938)
- [5] W. Heisenberg, "Über den anschaulichen Inhalt der quantentheoretischen Kinematik und Mechanik," *Zeitschrift Für Physik*, vol. 43, no 3–4, 172 (1927)
- [6] D. F. Lawden, *The Mathematical Principles of Quantum mechanics*, London: Methuen & Co Ltd., (1967).
- [7] F. T. S. Yu, "Chapter 8: Nature of Temporal ($t > 0$) Quantum Theory: Part I". In: *Quantum Mechanics*, Edited by P. Bracken, pp, 139-160, London: Intech Open (2020).
- [8] N. Bohr, "On the Constitution of Atoms and Molecules", *Philos. Mag.*, Vol. 26, No. 1, 1-23, 1913.
- [9] E. Mac Kinnon, De Broglie's thesis: a critical retrospective, *Am. J. Phys.* 44: 1047-1055 (1976).
- [10] F.T.S. Yu, "Aspect of Particle and Wave Dynamics". In: *Origin of Temporal ($t > 0$) Universe: Correcting with Relativity, Entropy, Communication and Quantum Mechanics*, Appendix. New York: CRC Press, pp. 145-147 (2019).
- [11] F. T. S. Yu, *The Fate of Schrodinger's Cat*, *Asian J. Phys.*, vol. 28, no 1, 63-70 (2019).
- [12] B Zweibach, *A First Course in String Theory*. Cambridge University Press. p. 582 (2009).
- [13] A. Einstein, B. Podolsky, and N. Rosen, "Can Quantum-Mechanics Description of Physical Reality Be Considered Complete?" *Phys. Rev. Vol.* 47, No. 10, 777-780, 1935.
- [14] C. H. Bennett, *Quantum information and computation*. *Phys. Today*, Vol. 48, No. 10, 24–30, 1995.
- [15] K. Życzkowski, P. Horodecki, M. Horodecki, and R. Horodecki, "Dynamics of quantum entanglement". *Phys. Rev. A* 65, 1-10, 2001.
- [16] M. S. Morris and K.S. Thorne, "Wormholes in spacetime and their use for interstellar travel: A tool for teaching general relativity" *Am. J. of Physics*, 56 (5), 395-412 (1988).
- [17] M. Bunge, *Causality: the place of the causal principle in modern science*. Cambridge: Harvard University Press (1959).
- [18] F. T. S. Yu, "Chapter 9: Nature of Temporal ($t > 0$) Quantum Theory: II". In: *Quantum Mechanics*, Edited by P. Bracken, 161-188, London: Intech Open, (2020).
- [19] B. Schumacher, "Quantum coding" *Physical Review A*, 51 (4): 2738–2747, 1995.
- [20] F.T.S. Yu, "Time: The Enigma of Space", *Asian Journal of Physics*, Vol. 26, No. 3, 143-158, 2017.
- [21] F.T.S. Yu, "Chapter 1: From Relativity to Discovery of Temporal ($t > 0$) Universe". In: *Origin of Temporal ($t > 0$) Universe: Correcting with Relativity, Entropy, Communication and Quantum Mechanics*, New York: CRC Press, pp. 1-26 (2019).

Edited by Nalan Antar and İlkey Bakırtaş

The nonlinear Schrödinger equation is a prototypical dispersive nonlinear partial differential equation that has been derived in many areas of physics and analyzed mathematically for many years. With this book, we aim to capture different perspectives of researchers on the nonlinear Schrödinger equation arising from theoretical, numerical, and experimental aspects. The eight chapters cover a variety of topics related to nonlinear optics, quantum mechanics, and physics. This book provides scientists, researchers, and engineers as well as graduate and post-graduate students working on or interested in the nonlinear Schrödinger equation with an in-depth discussion of the latest advances in nonlinear optics and quantum physics.

Published in London, UK

© 2022 IntechOpen
© DocsR / iStock

IntechOpen

